Flow of Particulate Solids in Silos

by

Kefeng Zhang

A thesis submitted for the degree of
Doctor of Philosophy

The University of Edinburgh

1997

TO

my wife: Yiqing Liu

and

daughter: Shuhui Zhang

ABSTRACT

The flow of particulate solids is a complex phenomenon which is not well understood, but has important applications in many industries. This thesis presents a study of particulate or granular solids flow in silos. The flow of solids can often be divided into zones of flowing and stationary material, with the dividing line between them being termed the "flow channel boundary". Observing and predicting the locus of this boundary is a major goal of granular solids flow research. The main work of the thesis consists of three parts: an experimental study of the granular solids flow in a laboratory model silo, an engineering mathematical model for predicting solids flow, and a deduction technique to infer the changing flow channel boundary during discharge from measurements of the residence times of markers placed within the solid during filling.

The experimental study was conducted to explore the flow behaviour of particulate solids in silos and to provide the experimental data for the theoretical work. Silo discharge tests using polypropylene pellets in a half cylindrical model silo were conducted under different discharge eccentricities. In addition, some experimental data from a research project on a full scale silo at the University of Edinburgh were also analysed and used in this thesis. In these tests, the main observations relating to flow were the residence times of the markers seeded in the solid during filling (residence time is the time a particle takes to move from its initial position to the outlet). The top surface profile was also measured at regular intervals during discharge. The residence time measurements are analysed using several approaches to infer the approximate location of the flow channel boundary in both silos. These techniques demonstrate how residence time measurements can be used to infer the flow patterns in silo discharge.

In addition to the above, the transparent front wall in the half cylindrical model silo enabled a record to be made of the development of the flow channel boundary and the trajectories of individual particles. This data provided further insight into the complex flow patterns. The direct measurements of the changing flow channel boundary are also used in the thesis to evaluate the dilation of the solid which occurred in the flowing material. The dilation, or decrease in the bulk density, is believed to play a significant role in determining the solids flow pattern.

The theoretical work presented starts with the development of a simple engineering model to predict solids flow in funnel flow silos. This model uses the kinematic theory for steady state flow, subject to simple assumptions concerning the top surface profile, top surface flow geometry and particle trajectory. The flow of iron ore pellets in the full scale silo and polypropylene pellets in the model silo during concentric emptying are predicted using the simple engineering model. The predictions for both silos are plausible and are in good agreement with the experimental observations.

At present, there appears to be no model which can accurately predict the locus of the changing flow channel boundary during the complete emptying of a silo. Indeed, measurement of such a boundary in an experiment is quite challenging. The last part of this thesis therefore aims to develop a deduction technique to infer the time-dependent flow channel boundary from residence time measurements. An inverse analysis method is used. In this deduction technique, the residence time field is treated as the output, and the solids flow is required to satisfy the continuity equation to provide the working mechanism of the system. The unknown velocities and trajectory paths of particles are identified by applying an optimisation algorithm. The deduction technique is applied to the model silo under concentric discharge. The flow channel boundary at different instants, the trajectory paths of particles, and the particle velocities are deduced. There is very good agreement between the deduced and the observed flow channel boundaries, which suggests that the technique can be used reliably to infer the solids flow pattern during concentric discharge of cylindrical silos.

PREFACE

This thesis is submitted to the University of Edinburgh for the degree of Doctor of Philosophy. The work described in this thesis was carried out by the candidate during the years 1993-1997 under the supervision of Dr Jin Y. Ooi. All the work was carried out in the Department of Civil and Environmental Engineering at the University of Edinburgh, Scotland, UK. The candidate submits that the thesis has been composed by himself and that the work described herein is his own unless otherwise stated in the text.

The candidate has published following papers related to the thesis during the course of research.

1. Zhang, K. F. and Ooi, J. Y., A kinematic model for solid flow in flat bottomed silos, *Geotechnique,* to appear;

2. Zhang, K. F. and Ooi, J. Y., Engineering modelling of flow in a flat bottom silo, *CHISA'96 Conference*, Prague, Czech Republic, August 1996;

3. Chen, J. F., Zhang, K. F., Ooi, J. Y. and Rotter, J, M., Visualisation of solids flow in a full scale silo, *PARTEC 95, 3rd European symposium storage and flow of particulate solids*, Nurnberg, Germany, 21-23 March 1995;

4. Chen, J. F., Zhang, K. F., Ooi, J. Y. and Rotter, J. M., Numerical predictions of wall pressures in cylindrical silos, *Second structural engineering conference*, Shanghai, China, January, 1995.

Kefeng Zhang

ACKNOWLEDGEMENTS

First of all, the author would like to express his deep and sincere gratitude to his supervisor, Dr Jin Y. Ooi for his continuous guidance, friendship and inspiration over the last four years. Also, the author is indebted to his second supervisor, Prof. J. Michael Rotter for his guidance and encouragement.

Next, I would like to thank my friends Tim Dalaney and Des Blake for their friendship, the constant help during the testing stages and partial analysis of the measured experimental results. I wish them all the best for the future.

I would also like to thank Jim Hutcheson for his supervision and concern for safety during the testing stage, Ian Fowler for his innovation and skill in preparing the model silo for testing, and Chris Burnside for his help in keeping my computer in good working condition.

I am very grateful for the financial supports from the British Government and the University of Edinburgh through an ORS award and a studentship.

Thanks also go to my friends at the University of Edinburgh in particular, Dr Jianfei Chen and Dr Zhijun Zhong for their help during my study; Richard Boyd for many happy memories and help over the past years. I wish them and their families happy and safe futures.

Thanks are also due to my wife Yiqing Liu and my daughter Shuhui Zhang for their love and understanding. Without them, I would not have finished my study. To them, I dedicate this thesis.

CONTENTS

NOTATION

The definitions of the symbols used in this thesis are listed below. Roman characters are given first, followed by Greek characters, subscripts and superscripts. The symbols are also defined where they first appear in the text. In a few cases, more than one definition has been assigned to a symbol.

Roman Characters:

A: constant in Eq. (6.8) dependent on effective angle of friction.

B: kinematic constant

$\mathbf{C}(\mathbf{x}^k)$: gradient vector $\nabla h_r(\mathbf{x}^k)$ with n-*l* constraints

c: void concentration

constant in Eqs. (7.5) and (7.6)

D: diameter of silo

d: diameter of outlet

$\mathbf{d}^k$: search direction

d_k: horizontal distance to the height measurement position k

E^n: N-dimensional Euler domain

F_p: particle constant in Eq (4.7)

F: objective function

f_i: function to evaluate travelling time of particle, shown in Eq. (7.8)

$g_j(\mathbf{x})$: inequality constraint function

H: height of fill

h_c: distance between inverted conical apex to initial top surface

$h_i(\mathbf{x})$: equality constraint function

h_t: thickness of top flow layer

h: height for each increment to calculate volume of flowing solid

$\mathbf{J}(\mathbf{x}^k)$: gradient vector $\nabla h_r(\mathbf{x}^k)$ with l constraints

J_o: Bessel function of first kind

J_1: first derivative of Bessel function J_o

k: particle shape constant in Eq. (5.20)

l: number of equality constraints

m: number of inequality constraints

N_i: mapping function

n: number of increments used to evaluate volume of flowing solid

n: total number of straight lines of trajectory path of particle

n: number of design variables

P: probability of particle leaving its cage

Q_{cone}: displaced volume at top solid boundary

Q_{exit}: volume of exiled solid

Q_{flow}: volume of solid in flow zone

$Q_r(t)$: remaining volume of solid at time t

q: influx of solid flowing through level

q_1: converted flow influx through level

q_{exit}: volumetric discharge rate

R: radius of the silo

$\mathbf{r}(\mathbf{x}_N)$: reduced gradients

$\bar{r}$: radius of flow channel boundary (FCB)

r_o: initial radial coordinate of particle

r: radial coordinate

T_i: residence time of particle at position i

T_{tot}: total discharge time

$\mathbf{T}_s$: matrix indicating times for particles to start moving

T_s: remaining time of particle before moving

T: residence time of particle

t_{tot}: total moving time of particle

t: time during discharge

u: horizontal velocity of particle

$|v_z|$: normalised vertical velocity of particle

$\mathbf{V}$: vector of vertical velocity distribution

v_r: radial velocity of particle

v_{zo}: vertical velocity of particle at initial position

v_z: vertical velocity of particle

v: vertical velocity of particle

W: mass flow discharge

w_i: weight percentage of particles in size interval i

$\mathbf{X}$: matrix consisting of a group of design variables

$\bar{\mathbf{x}}$: vector of partial design variables

$\mathbf{x}^0$: first design estimate

$\mathbf{x}$: vector of design variables

$\mathbf{x}_B$: vector of independent design variables

$\mathbf{x}_N$: vector of dependent design variables

$\mathbf{x}_{opt}$: optimum design variables

$\mathbf{x}^p$: vector of design variables in p^{th} cycle of Newton-Raphson (NR) iteration

x_o: initial horizontal coordinate of particle in 2-D silo

$\overline{\overline{x_i}}$: weight percentage of particles in size interval i

$\bar{x}$: mean particle diameter

x_{il}: largest allowed value of design variable x_i

x_{is}: smallest allowed value of design variable x_i

x: horizontal coordinate

$\mathbf{y}^p$: solution to Eq. (7.45)

y_o: initial vertical coordinate of particle in 2-D silo

y: horizontal coordinate

$|z|$: normalised vertical coordinate

z_o: initial vertical coordinate of particle

z_{mk}: measured height at position k on top surface

z: vertical coordinate

$z(t)$: function of height distribution on top surface

Greek Characters:

α_k: step size length

α: half angle of hopper

β: angle of the repose

$\Delta t_{i-1,i}$: time taken for particle to move from node i-1 to node i

$\Delta t'_{i-1,i}$: measured time taken for particle to move from node i-1 to node i

$\Delta \mathbf{x}^k$: small change in k^{th} design cycle

δ: parameter of step size

ε_1: convergence standard set for reduced gradients $\mathbf{r}(\mathbf{x}_N)$

ε_2: convergence standard set for equality constraints

ε_3: convergence standard set for design variables

ε_q: convergence standard

ϕ: cone angle of funnel

$\Gamma'(r)$: derivative of FCB equation with respect to radial coordinate

$\Gamma(r)$: equation of flow channel boundary

η: local coordinate

λ_n: coefficients in Eq. (5.7)

$\lambda(t)$: correcting parameter in Eqs. (7.5) and (7.6)

$\bar{\theta}$: constant in Eq. (6.8) dependent on effective angle of friction

θ_i: angle between trajectory path and central axis

ρ_b: bulk density of solid

ρ_{flow}: bulk density of flowing solid

ρ_s: density of particles

ω: reducing parameter for step size

ξ: local coordinate

ψ: dilation of solid

Subscripts:

b: bulk

r: radial

s: solid

z: vertical

opt: optimum

Superscripts:

k: number of iteration during optimisation

p: number of Newton-Rapson iteration

CHAPTER 1

INTRODUCTION

1.1 General

The silo is widely used to store a large quantity of bulk solid. It can be used for long term storage of solids such as agricultural produce, and for short term storage such as at a material receiving station. The handling and storage of bulk solids are important operations in many industries including mining, chemical, electric power generation, agriculture and food processing.

Silos are usually made of steel or reinforced concrete with circular or rectangular plan form. Cylindrical silos are more popular because of their efficiency. Silos may either be built directly on the ground or elevated. An elevated silo generally consists of cylindrical shell and a conical hopper which facilitates the retrieval of the stored solid by gravity.

1.2 Problems in bulk solids storage and handling

It has been estimated that the incidence of silo failures is between 100 and 1000 times that of buildings (Weare, 1989). Many of these failures stem from the unpredictability of the solids flow pattern in silos and the uncertainty of the pressures on the silo walls, which is closely related to the flow pattern.

The relationship between material properties, filling process, flow patterns, wall pressures, structural stresses and structural failure is a complex one (Fig. 1.1). The

mechanical characteristics of the stored solids and the process by which they are filled into the silo determine the distribution of densities and particle orientations in the silo, which strongly affect the flow pattern (Nielsen, 1983; Ooi and Rotter, 1990). The filling process and flow pattern are largely responsible for segregation of the solids. The solids packing and material characteristics also determine whether arching or ratholing will occur (Fig. 1.2). The flow pattern in turn strongly influences the pressures on the silo walls during discharge, so these cannot be predicted with certainty unless the flow pattern itself can be predicted. The pressures on the silo wall are, in general, unsymmetrical and non-uniform. The relationship between these pressures and the stresses which develop in the silo walls depends on shell bending phenomena, which can be very complex, and not easily understood, though they are predictable with finite element analyses (Rotter, 1986, 1987). Finally, the silo wall stresses which will induce structural failure are only currently understood for simple cases, and much work remains to be done.

The flow pattern in a funnel flow silo remains a major topic for research because asymmetries in the flow pattern can increase the unpredictability of the flow, and certainly endanger the silo's structural integrity. Reliable methods of predicting the details of the flow pattern, based on high quality experiments, are the first need.

1.3 Solids flow patterns

The earliest investigation of flow pattern of solids was carried out by Ketchum (1907). However, major progress in terminology and definition does not appear to have occurred until the work of Jenike and his colleagues (Jenike, 1961, 1964). They made a huge number of observations of flow in silo models, and gave the definitions of mass and funnel flow which are widely used today (Fig. 1.3). Mass flow is the flow mode that prevails in a silo/hopper system where every grain of solid is moving. Funnel flow is generally defined as any pattern which is not mass flow, and can be sub-divided into pipe (internal) flow and semi-mass flow. The flow channel

boundary (FCB) is defined as the interface between flowing and stationary solid. The point at which this boundary strikes the silo wall is known as the 'effective transition'. If the FCB stretches from the edge of the orifice right up to the free surface of the solid, the flow is termed pipe or internal flow and there is no effective transition. Semi-mass flow is typified by mass flow in the upper part of the silo whilst converging internal flow takes over nearer the orifice, forming an 'effective hopper' which is surrounded by stationary solid.

It is widely believed that the overpressures principally occur either near where the FCB intersects the silo wall (the effective transition) or where a sloping mass flow hopper meets the vertical bin wall (Jenike *et al*, 1973a, 1973b). In many industrial applications mass flow is highly desirable as this has a 'first-in-first-out' operation and a more predictable discharge rate. However, where the solid is abrasive and non-degradable or where space restrictions constrain the geometry, funnel flow is often used. Funnel flow occurs in flat-bottomed or shallow-hoppered silos. For most solids, the type of funnel flow depends on the aspect ratio of the silo: in very squat silos pipe flow will occur, whereas semi-mass flow is more likely in tall, slender silos. However there is strong evidence that some solids will pipe flow even in slender silos (e.g. Zhong *et al*, 1996). Other factors such as the material properties, filling method and particle shape and size also affect the flow mode (Munch-Andersen and Nielsen, 1990; Carson *et al*, 1991).

Mass flow has been studied extensively and is now well understood. However, funnel flow still remains a problem. So far no reliable method has been developed to predict whether a solid would semi-mass flow or pipe flow ie where the FCB would be. It is therefore important to make experimental observations on funnel flow in silos to further understand the flow behaviour.

Measuring flow pattern is not straightforward. A review of the flow measurement techniques can be found in Chapter 2. The residence time technique which suits model silos as well as full scale silos is widely used. The technique is an indirect

measurement of the flow pattern and only gives the total time each marker takes to move from its initial position to the outlet. Inferring the flow pattern from this limited information is a considerable challenge. An attempt is made in this thesis to infer the flow pattern from the residence time measurement using inverse analysis involving optimisation with minimal assumptions.

1.4 Special terms relating to funnel flow

This thesis focuses on the prediction, deduction and experimental investigations of solids flow in funnel flow silos. Unfortunately many terms have been used by researchers in this field and there has been considerable confusion over the terminology. For clarity, the special terms relating to funnel flow which are frequently used in later chapters are introduced here. Other common terms are briefly mentioned in the literature review in Chapter 2 for completeness.

Figure 1.4 shows the different flow zones during funnel flow. The central zone above the outlet where the solid flows relatively fast is called the *core flow zone*. Surrounding the core flow zone is the *feeding zone* where the solid has little or no movement before it "feeds" into the core flow zone. The flowing layer at the solid surface in which the solid predominantly moves down the sloping surface towards the central axis is named the *top flow layer*. The *dead zone* is a region where the solid is left at the end of discharge.

1.5 Review of topics covered in this thesis

The aim of the research work presented in this thesis is to develop a deeper understanding of the funnel flow of granular solids from silos. The specific objectives are to investigate experimentally the solids flow behaviour, to develop a technique to infer the flow pattern from residence time measurements and to develop a simple kinematic model for predicting the flow pattern.

In Chapter 2, the experimental and theoretical work carried out to date in the field of granular solids flow and flow channel geometries is reviewed. The modelling of granular solids flow can be divided into five fields according to the method of approach: plasticity theory, fluid mechanics theory, kinematic theory, finite element numerical method and discrete element models. A critique of each approach and of the work carried out in each field are presented.

In Chapter 3, an experimental study to investigate the flow of polypropylene pellets in a half cylindrical model silo is described. The flow behaviour including the development of the FCB, the residence times and trajectory paths of particles are measured using residence time measurement and visual observation through a transparent diametrical front wall. Also, an attempt to measure the dilation of bulk density which is believed to have a significant influence on solids flow is reported.

Chapter 4 begins with a brief description of a full scale silo experiment on the flow of iron ore pellets under concentric discharge (Rotter *et al*, 1995). The author was not involved in the conduct of the experiment but did play a small role in the interpretation of the residence time observations from the full scale tests (Chen *et al*, 1995). This chapter only covers one of the many full scale tests conducted at Edinburgh. It describes some of the analyses of flow pattern, including the approximate location of the FCB, in which the author has made some contributions. Further analysis of the full scale test data is presented in Chapter 6.

In Chapter 5, a simple engineering model for describing funnel flow is developed. This model is based on a kinematic theory for steady state flow and simple assumptions on the changing top surface profile, the top flow layer and the particle trajectory. The model is used to predict the flow of iron ore pellets in a full scale silo and polypropylene pellets in a half cylindrical model silo during concentric emptying in Chapter 6. The predicted and measured residence times of the markers for both

silos are compared. The trajectory paths of particles are also predicted and the FCBs are identified according to the different trajectory paths of particles.

In Chapter 7, the development of an inverse analysis technique to infer the solids flow pattern from the residence time measurements is presented. The residence time field in the whole silo arising from measured residence times of markers is treated as the output. That the solid is required to satisfy the continuity equation during flow provides the working mechanism of the system. The unknown velocities and trajectory paths of particles are identified by applying an optimisation algorithm.

The inference technique is applied to the flow of polypropylene pellets in the half cylindrical silo in Chapter 8. The time-depedent FCB, the trajectory paths as well as the velocity distribution are inferred. The good agreement between the deduced and measured data suggests that the deduction technique presented in Chapter 7 is reliable for inferring the flow pattern in a cylindrical silo during concentric emptying.

Finally in Chapter 9, the conclusions of the findings from the previous chapters are presented and recommendations are made for future work in this area.

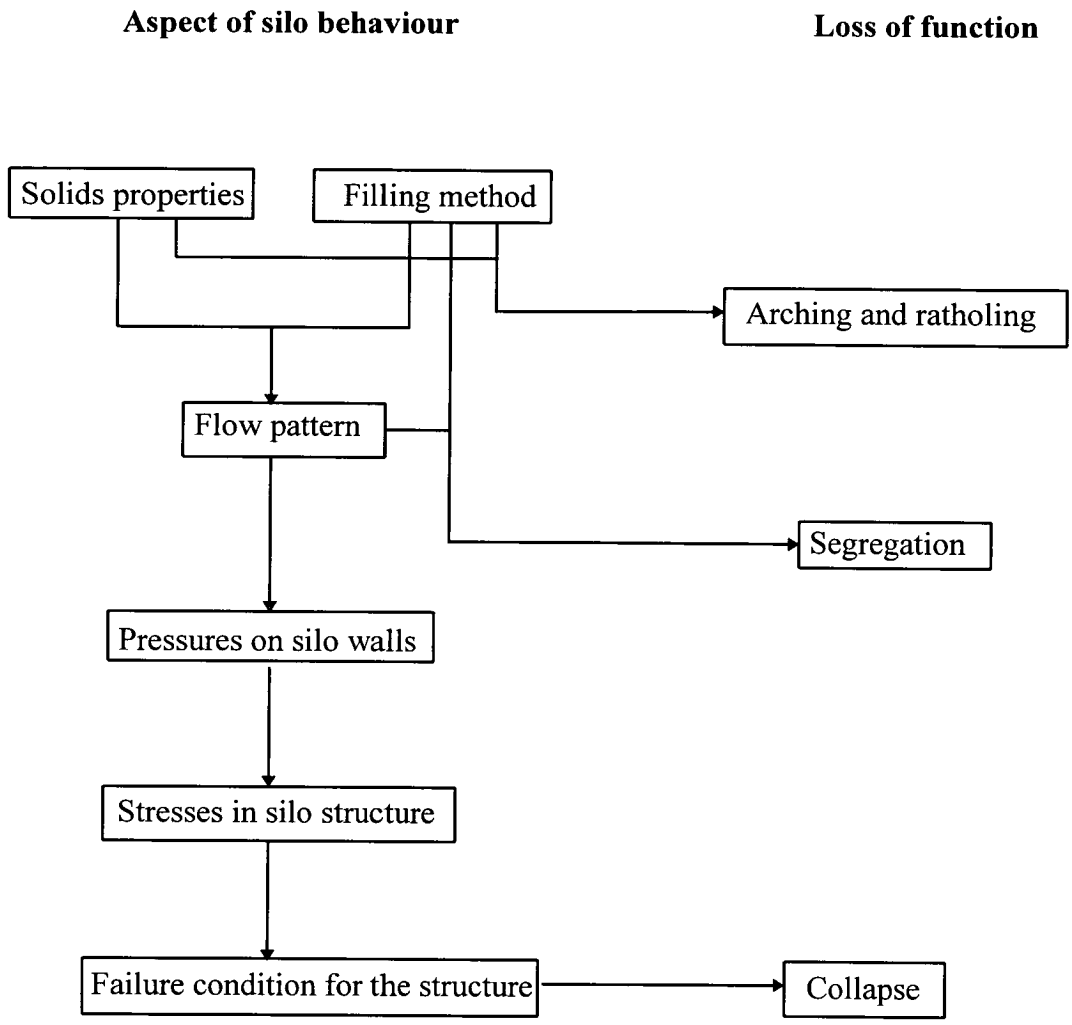

Fig. 1.1: Problems of silos

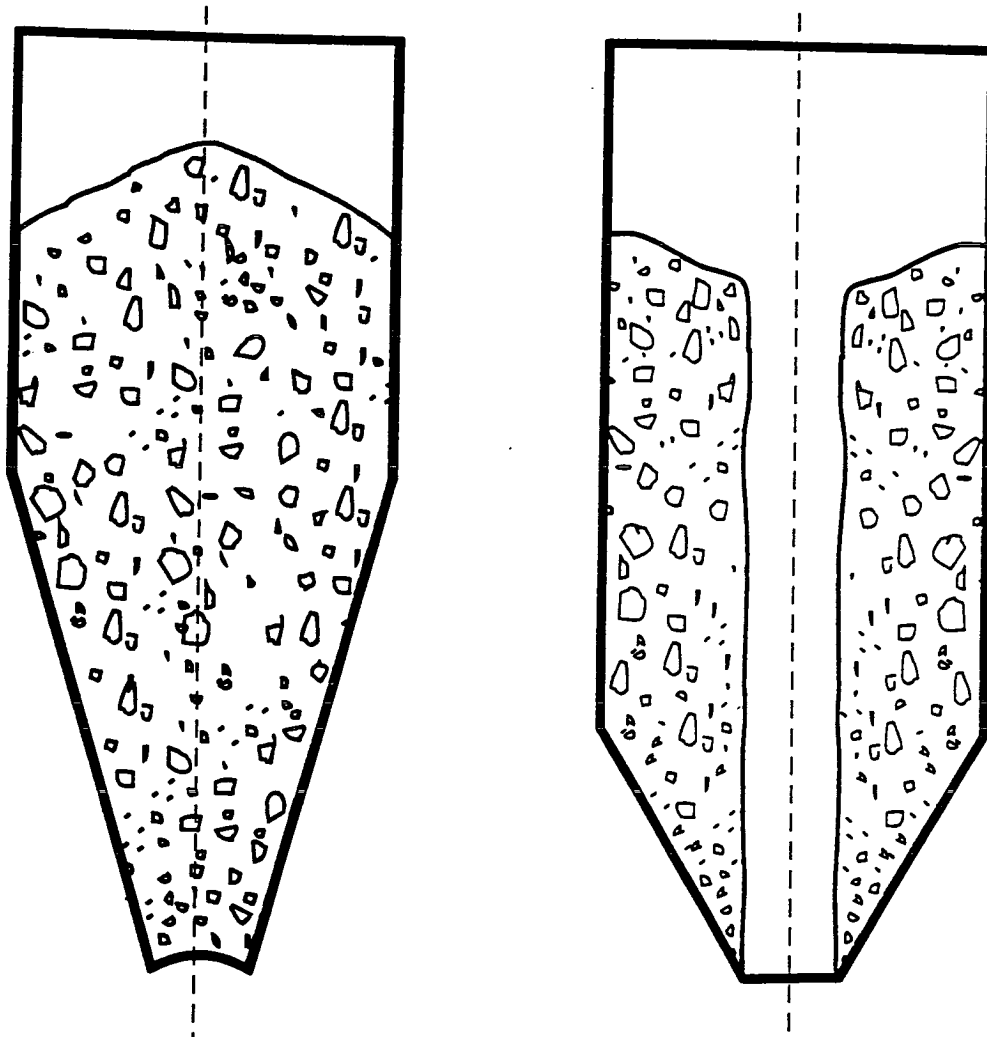

a) Cohesive arch

b) Rathole

Fig. 1.2: Flow obstructions

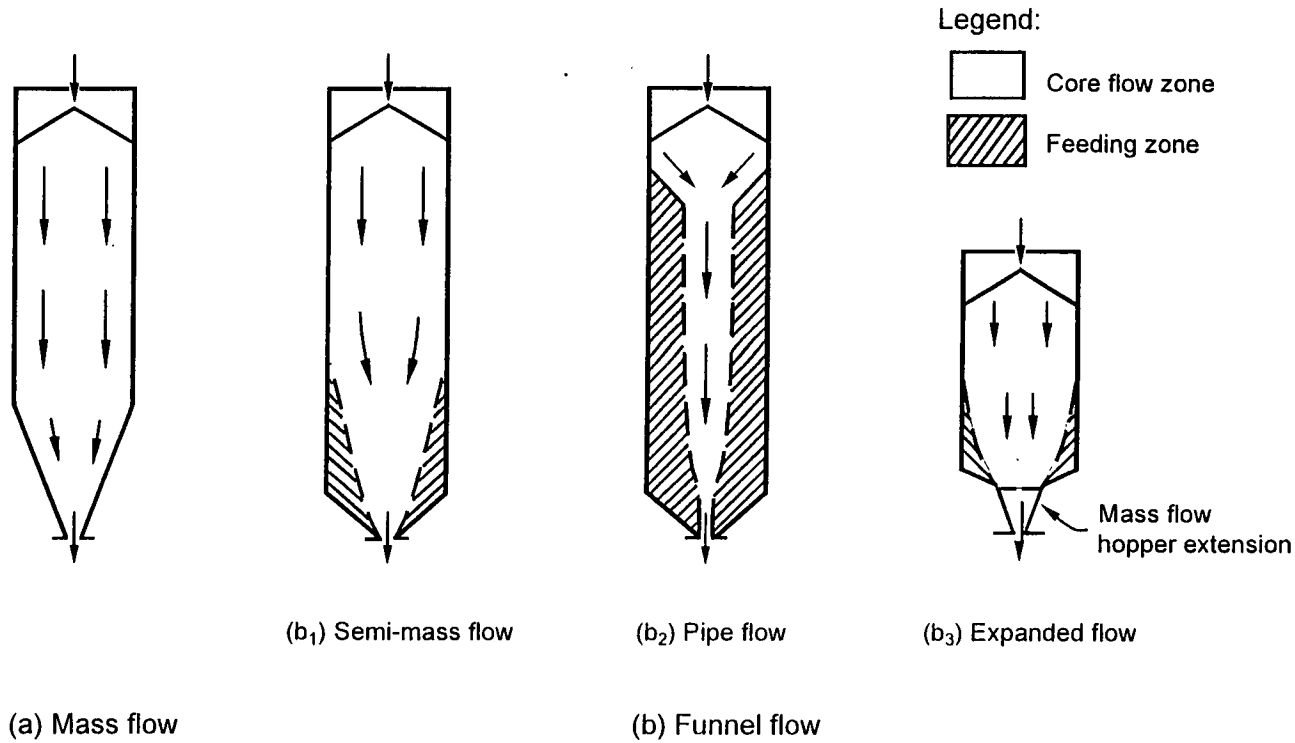

Fig. 1.3: Flow patterns in silos

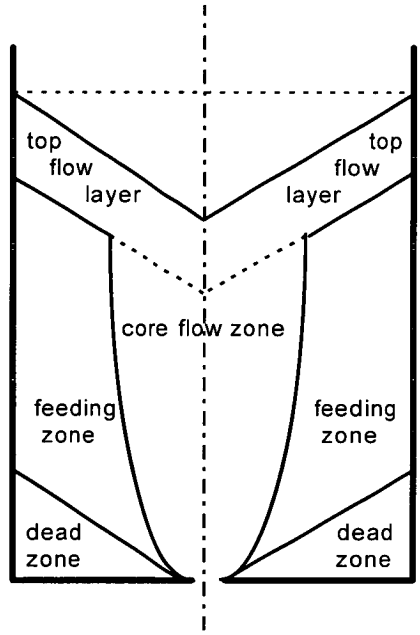

Fig. 1.4: Different zones in internal funnel flow

CHAPTER 2

LITERATURE REVIEW

2.1 Introduction

The review given in this chapter is not intended to be exhaustively comprehensive. Instead, a careful selection of the extensive literature published on granular solids flow is made on the basis of research material that is of direct relevance to the task of measuring and analysing the solids flow in silos.

The review consists of three parts: experimental techniques, experimental observations and theoretical approaches for solids flow. Various experimental methods which have been previously employed including direct observation techniques, bed freezing technique, tracer techniques, residence time technique and probe techniques are reviewed. The recent advances in the theoretical modelling of granular solids flow are outlined according to the method of approach, namely plasticity method, fluid mechanics method, kinematic theory, finite element numerical method and discrete element method. Special attention is paid to the advantages and the limitations of each method in predicting the position of the flow channel boundary (FCB).

Related topics such as the theoretical prediction of the discharge rate from silos, and the measurement and prediction of pressures on silo walls are important but a detailed review of these aspects is beyond the scope of this thesis.

2.2 Techniques for measuring solids flow

A variety of techniques have been used to determine the flow patterns of solids in silos. The experimental techniques reviewed here are grouped into five categories: direct observation techniques, bed freezing technique, tracer techniques, probe techniques and residence time measurement technique.

2.2.1 Direct observation techniques

The observation of displacements of horizontal layers of dyed solid is commonly used in the direct visual observation techniques. In this method, the visually-detectable solid is usually either a sample of the granular solid that has been dyed or a similar granular solid of a different colour so that each layer contains solid which has similar properties to the bulk solid. Brown and Hawksley (1954), Jenike and Johanson (1962), Litwinszyn (1963), Brown and Richards (1965), Gardner (1966), Munch-Anderson and Nielsen (1990) and Cleaver (1991) are amongst those who utilised this technique.

For observing the flow pattern, the silo is usually either a planar flow model (between two glass panels) or a half circular model with a diametrical front wall. It is normally assumed that the flow behaviour observed adjacent to the front wall is representative of the behaviour throughout the bed. However, several researchers (*e.g.* Brown and Richards, 1965; Cleaver, 1991) have reported that the front wall exerts a retarding force on the flow. This should be taken into account somehow when velocities are calculated, as these velocities will be less than those occurring at similar positions within the bed. It is not easy to account fully for the retardation caused by the transparent wall in data processing. Another problem associated with this technique is that the results obtained from visual observations are generally qualitative.

Photography is often used in conjunction with this technique to record the observations. They have been employed by many researchers (*e.g.* Bosley *et al*, 1969; Pariseau, 1970; Levinson *et al* 1977; Tuzun and Nedderman, 1979, 1982) using transparent plane strain silos.

2.2.2 Bed splitting technique

In the bed splitting technique, horizontal layers of dyed granular solid are placed at a number of heights in the silo during filling. After an appropriate period of flow, the discharge is stopped and the bed of granular solid is then immobilised. The commonest immobilisation technique is to pour in a fixing medium which fills the interstices between the granular particles and then solidifies, rendering the particulate solid rigid. Brown and Richards (1965), Novosad and Surapati (1968) and Chatlynne and Resnick (1973) used this technique to investigate the flow behaviour of granular solids.

Although bed splitting technique can capture the actual flow pattern of particles at a certain time, the technique is time consuming, and can be only applied in relatively small models.

2.2.3 Tracer techniques

2.2.3.1 Radiographic techniques

In this technique, lead shot particles are seeded into a silo bed during filling. The flow is halted frequently during discharge and the apparatus exposed to an X-ray source to detect the positions of the tracer particles. Athey *et al* (1966), Cutress and Pulfer (1967), Lee *et al* (1974), Bransby and Blair-Fish (1975) and Drescher *et al* (1978) are amongst those to have used this technique.

The application of this technique is restricted to thin non-metallic plane strain models as X-rays must be able to penetrate the solid and be detected on the far side. The involvement of expensive equipment and trained staff further restricts the application of the technique.

2.2.3.2 Radio pill tracer techniques

The radio pill tracking technique involves following the fate of a radio-transmitter (a radio pill) as it passes through a model silo. Handley and Perry (1965, 1967), Rao and Venkateswarlu (1973, 1975) and Perry *et al* (1976) employed this technique. Usually the radio pills are much larger than the solid particle, so Arteaga and Tuzun (1990) pointed out that the problem of segregation must be addressed when analysing the results. The major drawback of the technique is that the scope is limited and it can only be used in small models.

Other tracers which have been employed include the radio-isotope tracer technique and the magnetic tracer technique (McCabe 1974; Smallwood and Thorpe 1980).

2.2.4 Probe techniques

A number of methods using specially designed probes have been found their applications in silo flow experiments. Hancock (1970), Burkett *et al* (1971), McCabe (1974) and Oki *et al* (1975, 1977) are amongst those who have utilised these techniques to measure the local values of the interstitial voidage in plane strain silos and the velocities and the sizes of individual particles within a field of high flow rate. Further review of the application of the probe techniques can be found in Oki *et al* (1977) and Tuzun *et al* (1982).

2.2.5 Residence time measurement technique

Residence time is the time taken for a particle to travel through the solid from an initial known starting position to the outlet. This technique involves seeding the bulk solid with a large number of markers and measuring the time each marker takes to reach the outlet.

One key issue in this technique is the precise placement of the markers in the solid. Several methods have been developed to realise this purpose. Murfitt (1980), Smallwood and Thorpe (1980), Graham *et al* (1987), Nedderman (1988) and Cleaver (1991) used positioning tubes to place markers into discharging silos. Cleaver (1991) reported that to obtain an accurate result, the tubes should be retracted after positioning a tracer particle as the presence of a positioning tube in the flow field could cause the subsequent movement of the marker to be impeded. Van Zanten *et al* (1977) dropped the tracer particles from marked positions at the top of the silo onto a flattened free surface. This method is simple, but it could lead to inaccuracy in the placement.

Rotter *et al* (1993,1995) constructed a seeding template to introduce radio frequency tags as markers in full scale silo tests. At every selected level, the seeding template was lowered down to rest on the solid surface and then the radio tags were placed into the assigned positions. With care in the process of seeding, it has been proved that the method of employing a seeding template to place the markers is very reliable. This method has been used in a series of full scale silo experiments with different test solids. The same idea was also used by Watson (1993) and Dalaney and Blake (1995) in investigating the flow patterns of sand and polypropylene pellets in a half cylindrical model silo.

The residence time measurement technique is relatively simple and convenient to use, and the resources needed to implement this technique are few and inexpensive.

Thus this approach is commonly used. The information obtained is very limited i.e. the times taken by a limited number of markers to reach the outlet. Whilst it is normally sufficient to deduce whether the flow is mass flow or pipe flow, the inference of the comprehensive picture of the flow pattern from the residence time measurements remains a difficult challenge (see Chapters 3 and 4 in this thesis).

2.3 Experimental observations of solids flow

The main purpose of the experiments on solids flow patterns in silos is primarily to identify the mode of flow and to measure the flow channel boundary (FCB). This section briefly outlines the important findings from several experimental studies which have been reported in the literature.

By observing the flow of cohesionless solid in a model, Brown and Hawksley (1954) reported that there is a finite layer of flowing solid at the solids surface in which the particles move down the slope towards the central axis. They further divided this top flow layer into two parts, as shown in Fig. 2.1(a). The solid in the upper layer A rolls down freely to the fast central zone C while the solid in the lower layer B moves very slowly at first and then with the top surface progressively moving down, it merges and becomes layer A. In a small area D near the outlet, the particles lose contact with neighbouring particles and fall freely.

Kvapil (1959) investigated the cohesionless solids flow and described movements of particles in the direction of gravity as the primary motion and the movements including the rotation and horizontal component as the secondary motion. The zones of motions all have the shape of an ellipse. The ellipse of the primary motion only can be found in the silos with the unlimited height, whilst the ellipse of the secondary motion can be found with the limited or unlimited heights (Fig. 2.1(b)).

The existence of different zones of solids flow was also confirmed by Watson (1993) and Dalaney and Blake (1995) when they investigated the flow of polypropylene pellets in a half cylindrical model silo. Dalaney and Blake (1995) observed that the particles in the top flow layer move predominantly towards central flow zone along the inclined top surface. The particles near the top surface roll rapidly down to somewhere in the central core flow zone and then accelerate and move down towards the outlet. The particles in the feeding zone which surrounds the core flow zone remain stationary until they enter the top flow layer (see Fig. 2.1(c)).

With the aim of determining the FCB, Brown and Richards (1965) and Gardner (1966) took photographs of the flow through the transparent front walls of their plane strain model silos. Careful scrutiny of these photographs reveals a surprising point of contraflexure in the FCB. It seems possible that the stationary zones start to curve into the flow field near the outlet. This phenomenon could, however, be caused by frictional effects against the front wall.

Long time exposures were used by Gardner (1966) and Tuzun and Nedderman (1982) to determine the position of the FCB. Gardner laid horizontal layers of dyed solid in the silo during filling. The FCB was defined as the edge of the stationary solid, and its location was assessed by measuring the extent of the remaining horizontal layers of dyed solid. It has been found that shortly after flow started the flow region was a long ellipsoidal shape located on the axis of symmetry. However, once the top of the flow region reached the solids surface, the flow channel broadened and the FCB well above the outlet became vertical and parallel.

Carson *et al* (1991) used visual observation technique to observe flow pattern in a cylindrical flat-bottomed model silo made of transparent Plexiglas. In their experiments, the boundary between flowing and stationary solid could be visually determined at the cylindrical wall. By assuming a linear flow boundary from the outlet, they plotted the flow channel angle against the circumferential angle. Their experiments were carried out on full, two-thirds full and one third full silos

discharging concentrically and eccentrically. They found that the flow channel closely followed a radial path from the outlet to the cylindrical wall. The FCB as observed through the wall was found to be neither distinct nor stable for most of the solids they tested.

Zhong *et al* (1995, 1996) conducted a series of mylar model experiments to investigate the development and geometry of the FCB during eccentrically emptying silo. Two materials were used: sicila sand and polyethylene pellets. By observing the displacement curves of the coloured layers on the silo walls, the FCB was deduced. They found that the FCB was changing all the times during discharge. The boundaries in the upper part of the silo were vertical at some instants, but curved in the lower part.

In measuring the velocities of particles, Brown and Richards (1965) used molten paraffin wax in their plane strain mass flow hopper experiments with sand. They found that the velocity profiles were unsymmetrical about the vertical centreline and that the flow rate generally increased with distance from the end face. Takahashi and Yanai (1973) took photographs of the plug-flow region in a vertical pipe to measure the flow pattern and the void fraction of 4 mm diameter glass, silica and alumina spheres. They concluded that in the centre region the particle velocities were almost identical but fell abruptly in the shear region near the wall.

In circumstances where mass flow occurs, streamlines and velocity field can be assessed from residence times. With the measured residence times, Cleaver (1991) calculated the streamlines by numerically differentiating these stream functions and found that stream function analysis was very sensitive to errors in the experimental results from his mass-flow silo. Smallwood and Thorpe (1980) used the same method to calculate velocity fields. However, as reported by Watson (1993), with the existence of the stagnant zone during funnel flow, the particles in the stagnant zone would keep still for a considerable long time before they start moving. Thus the

residence times of particles do not represent times in motion. Therefore, the stream function analysis is not totally applicable for funnel flow situations.

For measuring the trajectory paths of particles, Laohakul (1979) and Tuzun and Nedderman (1979) used cine filming. Polynomials describing the position of a tracer particle with time were then fitted to the tracer trajectories. On differentiation, these polynomials yielded the horizontal and vertical velocities at any point at any time on the trajectory. Bransby and Blair-Fish (1975) and Lee *et al* (1974) employed the X-ray method to observe the trajectory paths of particles in sand by embedding regular arrays of lead shots.

Despite the large number of experiments to investigate solids flow pattern, there is still a lack of understanding on the geometry of the changing flow channel boundaries during flow. There is certainly no predictive tool available yet which can predict whether a certain solid will pipe flow or semi-mass flow in a funnel flow situation.

2.4 Theoretical modelling of granular solids flow

The theoretical models for granular solids flow in silos are discussed in this section. The models can be divided into five categories as follows: plasticity theory, fluid mechanics method, kinematic theory, finite element numerical method and discrete element models.

2.4.1 Plasticity theory

In plasticity theory, the material behaviour is assumed to be independent of the strain rate. For the materials consisting of hard, dry and cohensionless particles, the

assumption of stresses independence of the strain rates is generally valid. Therefore, many granular materials have been idealised as plastic materials.

Previous studies undertaken which treated the bulk material as plastic can be split into three categories: mass flow hoppers, funnel flow hoppers with linear stagnant zones and funnel flow hoppers with curved stagnant zones.

2.4.1.1 Mass flow hopper

Johanson (1964) employed the method of characteristics to solve the equations of plasticity, which were adapted to the steady flow of Mohr-Coulomb solids by Jenike and Shield (1959). Johanson showed experimentally that the stress fields in his axisymmetric and plane strain hoppers closely approximated the radial stress fields of Jenike (1964). Based on the assumption of radial flow, Drescher *et al* (1978) analysed the velocity discontinuities that occur across the rupture surfaces using a velocity hodograph. This is a graphical technique which correlates the magnitudes and directions of the different velocities. Drescher *et al* succeeded in producing an analytical solution for the velocity field, although the theoretical results showed a poor correlation with experimental observations. To explain this discrepancy, it was suggested that the flow pattern had been over-simplified.

2.4.1.2 Linear stagnant zones in funnel flow

Stagnant or dead zones of stationary solid are a characteristic of funnel-flow. Flowing solid slides past stationary solid which forms an 'effective hopper'. The boundary between flowing solid and stationary solid is called the flow channel boundary (FCB). A large body of research has been conducted on predicting the wall pressures during funnel flow using the plasticity theory (e.g. Jenike *et al*, 1973a,

1973b; Richards, 1977 and van Zanten *et al*, 1977). It is typical in this work to assume that the FCB takes up a linear geometrical shape.

However, several authors (e.g. Lenczner, 1963; Brown and Richards, 1965 and Gardner, 1966) observed the presence of a curved flow channel boundary taking shape in model tests during discharge. Deutsch and Clyde (1967) demonstrated that the rigid block/rupture surface flow pattern can also occur in funnel flow silos. They believed that it is a fundamental mechanism as it occurs across a wide range of vessel diameter to material diameter ratios. They also proposed, following Johanson (1964), that these flow patterns represent a steady-state phenomenon for much of the period of discharge from the silo. Based on the work of Jenike (e.g. 1964), Arnold *et al* (1980) presented the conditions necessary to prevent flow obstructions from forming. The emphasis was on practical results and proposals that can be directly exploited in the design of bins and silos.

2.4.1.3 Curved stagnant zones in funnel flow

Gardner (1966) assumed that the solid in the flow channel was in a state of plastic equilibrium and used the method of characteristics to solve the equilibrium and plasticity equations for a continuum. His theoretical prediction of the FCB was found to be in good agreement with the experimental. Takahashi and Yanai (1974) developed an analysis for solids flow in flat-bottomed concentrically discharging planar silos. Like Gardner (1966), Takahashi and Yanai used the method of characteristics and assumed a Mohr-Coulomb solid. Tuzun and Nedderman (1982) demonstrated that the FCB predicted by Gardner (1966) give geometrically similar FCBs as the silo width is varied.

2.4.1.4 Concluding remarks on plasticity theory

The plasticity analysis seems a simple appropriate approach to analyse incipient flows of granular solids. However, since the plastic behaviour of dilated, free-flowing granular solids is not yet well defined, there is a considerable mis-match between most theoretical predictions and the experimental observations. This method is now drawing less attention as other numerical techniques (e.g. the finite element method) which can capture a more realistic representation of the solids behaviour emerge.

2.4.2 Fluid mechanics method

In fluid mechanics, fluids can be classed as Newtonian or non-Newtonian. A Newtonian fluid is one in which the shear stress at a point is directly proportional to the velocity gradient at that point and Non-Newtonian fluids generally have non-linear relationships between shear stress and velocity gradient. The behaviour is generally independent of the internal pressure.

During experiments into the shearing of neutrally-buoyant spherical particles, Bagnold (1954) discovered that at low shear rates the granular solid behaved in a Newtonian manner and at higher shear rates the stresses were found to vary with the square of the velocity gradient (*i.e.* as a non-Newtonian fluid). A further example of the fluid nature of granular solids, especially noted in the flow of smooth tiny spheres, was given by Savage (1979). He presented a 3-D constitutive equation which satisfies the Mohr-Coulomb failure criterion for investigating solids flow. He found that the material response was highly sensitive to the volume fraction of solids. By substituting conjectured approximations into the equations, two simple flows are solved analytically: flow down an inclined chute and flow in a vertical channel.

Haff (1983) applied the Navier-Stokes relations and the hydrodynamic equations for conservation of energy to the granular solids flow. By ignoring the variation of properties across a grain diameter, he found an analytical solution and gain a qualitative understanding of simple flows. An important dependent variable in his formulation, in addition to the flow velocity, was the mean random fluctuation velocity of an individual grain (which he termed the 'thermal' velocity). This 'thermal' velocity describes the local state of the medium and facilitates a self-consistent definition of the equations' coefficients. These coefficients were found not to be constants but functions of the local state of the medium. By the very nature of these equations, however, only elementary flows, with strictly-limited contingencies, can be analytically solved. Non-Newtonian flow was postulated (in line with Bagnold, 1954 and Savage, 1979) and the inelastic nature of collisions was found to have a profound effect on the grain system response. Hui and Haff (1986) followed Haff's work (1983) with a numerical treatment of grain flow in a vertical channel. The velocity profiles obtained are encouraging but the complexity of this analysis would increase unreasonably if converging flow were considered, as is the case in a silo. The flow velocity profiles of Haff (1983) and Hui and Haff (1986) show a good qualitative match to those of Savage (1979).

2.4.3 Kinematic theory

In the kinematic approach, it is assumed that the velocity field is completely independent of stress and any effects which interparticle friction or wall friction might have are excluded. The emphasis is on solving for velocities and fluxes (a flux is defined as a flow rate through a unit area normal to the direction of flow) in the granular solid mass rather than for pressures and stresses.

Since the kinematic theory was firstly presented by Litwiniszyn (1958), a number of researchers (Litwiniszyn, 1963, 1971; Mullin, 1972; Tuzun and Nedderman, 1979; Graham *et al*, 1987) have carried out the kinematic modelling of granular solids flow.

All arrived at essentially the same governing differential equation although different assumptions were made in each case.

The equation contains a single unknown parameter which is termed the kinematic constant. In some cases, the governing differential equation, which is similar in form to the equation for two-dimensional diffusion or heat flow, has standard solutions, and in more general cases, numerical solutions have to be explored.

The first known work in this field was by Litwiniszyn (1958, 1963, 1971). In his simple work, the granular particles were considered to be residents in hypothetical cages as shown in Fig 2.2. When cage A becomes empty, it will be occupied by either the particle in cage B or the particle in cage C. In the bulk of the material, the possibilities for the particle in cage B and the particle in cage C to occupy cage A are identical. The probability P that a particle would leave its cage can be evaluated by the governing partial differential equation

$$\frac{\partial P}{\partial z} + B \frac{\partial^2 P}{\partial x^2} = 0 \qquad (2.1)$$

where x is the horizontal co-ordinate and z is the vertical co-ordinate measured vertically upwards, B is a parameter related to the width and the height of cages.

Litwiniszyn (1958) showed that P is proportional to the vertical velocities of particles. He determined the deformed shape on the ground surface when an underground tunnel was excavated and found the displacement profiles for these boundary conditions plausible. However, in his study only planar geometry of unrestricted width was considered.

Mullins (1972) formulated the kinematic theory using similar method of stochastic mechanics from different assumptions. He assumed that the downward flow of particles was equivalent to the upward flow of voids that entered the system through

the orifice. He obtained the following governing differential equation for the steady-state void concentration c.

$$\frac{\partial^2 c}{\partial x^2} + \frac{\partial^2 c}{\partial y^2} = \frac{1}{B}\frac{\partial c}{\partial z} \qquad (2.2)$$

where x and y are horizontal co-ordinates and z is the vertical co-ordinate which is positive upwards.

He hypothesised that the kinematic constant B, which has the dimension of length, should be of the same order of magnitude as the diameter of a particle. The solutions covering a point orifice and a finite orifice at the floor of a semi-infinite bed and a point orifice at the bottom of a pipe were presented. The solution for a point orifice at the bottom of a pipe was later adopted by Graham *et al* (1987) to analyse the flows of epoxy spheres and coke in a cylindrical silo under steady-state flow.

Nedderman and Tuzun (1979) proposed a third variant of this method. They assumed that if the two particles in the lower layer have different velocities (Fig. 2.3), there will be a tendency for the upper particle to move sideway towards the faster falling particle. Tuzun and Nedderman put forward the very simple proposition that the horizontal velocity is a linear function of the horizontal gradient of the vertical velocity.

$$u = -B\frac{\partial v}{\partial x} \qquad (2.3)$$

where u and v are the horizontal and vertical velocities of a particle.

Applying the condition of continuity in incompressible flow to this proposition led to their governing partial differential equation.

$$B\left(\frac{\partial^2 v}{\partial x^2}\right)=\frac{\partial v}{\partial y} \qquad (2.4)$$

Tuzun and Nedderman (1979) exploited a solution valid in the converging flow zone, and a more general product solution in a plane strain, flat-bottomed silo.

Comparing the Eqs. (2.1), (2.2) and (2.4), it has been found that Eq (2.4) is directly analogous to the equation derived by Litwiniszyn (Eq. 2.1) and is slightly simpler than that of Mullins (Eq. 2.2).

Tuzun and Nedderman (1979) investigated the flow of glass ballotini in a 2-D flat bottomed hopper using filming techniques and calculated the horizontal and vertical velocities for the solid using their proposed kinematic model. On the whole, the experimental velocities showed excellent correlation with the analytical predictions. They reported that the kinematic constant, which was independent of silo width and orifice size, may be related to the particle diameter and that it may be possible to deduce its value from a simple material test when an appropriate test is developed. By considering the variation of the vertical velocity down the centreline, Tuzun and Nedderman were able to extrapolate a value for the kinematic constant B for the glass ballotini.

Continuing their research into the discharge of glass ballotini from plain strain silos, Tuzun and Nedderman (1982) directed their work towards an investigation of the flow channel boundary. Long time exposures were used to measure the extent of the flowing region of solid. They found that the FCB as assessed from the experiments corresponded closely with the theoretical velocity contour of 1 particle diameter per second and with the streamline that bounded 99% of the total flow.

The thorough experiments conducted by Tuzun and Nedderman (1982) showed that the silo width, the orifice width and the existence of a fully-rough wedge-shaped hopper had marginal effects on the FCB provided that the hopper was always

covered by 'stationary' solid (i.e. funnel flow situation). However, the particle diameter did affect the size of the fast-flowing core; the core being larger for larger particles. They therefore proposed that, for a given solid, there is a characteristic curve which describes the FCB and that this only depends upon the material properties, such as the particle diameter. However, they also noted that the FCB is affected by a smooth-walled hopper: both the volume of fast-flowing solid and the discharge rate are increased.

The applications of the kinematic theory were restricted to planar or semi-infinite silos until Graham *et al* (1987) exploited a standard series solution to solve the basic kinematic differential equation (Eq 2.2) for discharge through a point orifice of an axisymmetric silo. They obtained a theoretical prediction of the vertical velocity field and developed a graphic method to determine the kinematic constant from experimental residence time data of particles on the centreline. By integrating down a particle trajectory, they calculated the residence time of each particle. They used fixed vertical tubes to introduce marker particles into their discharging axisymmetric silo. The time taken for each marker to exit the silo, the residence time, was measured. Steady state conditions were ensured by recycling two vessel volumes before placing any marker particles into the test silo. The predicted residence times were found to fit their experimental data remarkably well.

Clearly, only in very few special cases can standard solutions be exploited. For more general cases such as the silos with irregular geometry or silos with eccentric or multiple outlets, analytical solution no longer exists. To extend the application scope of the kinematic theory, Watson (1993) implemented the kinematic theory in a finite element program. Starting from the work of Nedderman and Tuzun (1979), he produced the numerical formulations for both planar and axisymmetric geometry. For eccentrically discharging planar silos and for the silos with multiple outlets, Watson's predictions show that the FCB is not symmetrical about the orifice centre and the centre of the crater in the free surface is seen to move towards the wall as the height above the orifice is increased. For the silos with more than one outlet, the

velocity fields above each outlet were predicted to be unaffected by the presence of the other outlet.

Despite the simplicity in the kinematic theory, the outcomes indicate that this approach is viable when applied to the free flow of dilated, smooth granular solids. However it is unable to analyse incipient flows of very frictional and consolidated granular solids.

2.4.4 Finite element method

Finite element method is often used to study the flow behaviour of solids and the pressure exerted on silo walls. In this method, the granular solid is treated as a continuum and follows some prescribed behavioural laws based upon classical mechanics combined with generally quite complex constitutive models.

Many finite element studies of silo discharging have been undertaken. The most notable amongst these include the work by Haussler and Eibl (1984), Ruckenbrod and Eibl (1993), Runesson and Nilsson (1986), Eibl and Rombach (1987a, 1987b and 1988), Schmidt and Wu (1989) and Wu (1990). The work carried out by Haussler and Eibl (1984) was typical among these. In the stimulation of discharge in mass flow silos, Haussler and Eibl employed a viscoplastic constitutive law which covered both fluid-like and solid-like behaviour for a granular solid. The problem was formulated in an Eulerian frame of reference. The whole set of differential equations are solved by finite element spatially and by the finite difference method in the domain of time. A silo with a large outlet (the radio of the outlet width to the channel width is 0.50) was analysed. The improvement of their work can be seen in a number of literature (Runesson and Nilsson 1986; Eibl and Rombach 1987a; 1987b and 1988; Ruchenbrod and Eibl 1993).

To avoid the overwhelming complexity of the formulation proposed by Haussler and Eibl (1984), Link and Elwi (1987) adopted a relatively simple method to analyse the incipient flow of cohesionless material in silos. They used an elastic perfectly plastic constitutive law for the material and a thin layer interface element to consider wall friction. A model silo was analysed and the switch pressures obtained at the outlet were found to be greater than static pressures, but smaller than those obtained by Jenike's and Walker's solution.

Others that have utilised the technique of finite elements to analyse the behaviour of bulk solids in silos include Bishara and Mahmoud (1976), Mahmoud and Abel-Sayed (1981) and Ooi (1990). A comprehensive review of finite element studies of silo filling and discharging can be found in Chen (1996).

Although the finite element method is powerful and has produced many satisfactory predictions, it has some serious shortcomings when modelling silo discharging. It requires vast computing power and has difficulties in stimulating the unsteady-state flow. With the continuum treatment, the finite element method is not capable of predicting rupture zones and flow boundaries.

2.4.5 Discrete element models

The discrete modelling of granular motion is a relatively new development. In the discrete element method, classical Newtonian dynamic equations are employed to deal with the individual particles and their interactions. This method involves keeping track of all the forces and moments acting on each particle at every time step and integrating the equations of motion to determine the new state of the system at the end of each step.

The first and well known work on discrete elements was presented by Cundall and Strack (1979). They formulated the model based on the computation of forces and

the solution of Newtonian dynamic equations for non-spherical particles. The examples of the application of the discrete element method include the study of the flow of granular solids by Walton (1983), vibrationally induced segregation by Haff and Werner (1986) and the plug flow by Tsuji *et al* (1992).

An alternative to compute all the forces and integrate the equations for an entire system is to use a statistical approach. By using a statistical approach, the need for force calculations and integration routines for individual particles are eliminated as the state of the particles is determined according to an assumed statistical distribution. Rosato *et al* (1986) and Barker and Mehta (1992) developed the statistical mechanics approaches by using Monte Carlo ideas of statistical mechanics. Snyder and Ball (1994) applied the Monte Carlo method to settling powders.

Another alternative where the deterministic approach is combined with the statistical approach has also been proposed. Hawkins (1983) stimulated the granular flow of 2-D rigid disks by using stochastic boundaries and binary collisions.

Since the emergence of the discrete models, they have increasingly attracted attention and been extended. More recently, the models have been applied to shear flow of non-cohesive assemblies by many researches (e.g. Bashir and Goddard, 1991; Thompson and Grest, 1991; Campbell and Potapov, 1993; and Turner and Woodcock, 1993). Thornton (1991), Ristow (1992) and Langston *et al* (1995) applied this approach to analyse the solids flow in hoppers. Tanaka and Tsuji (1993) combined the finite element method with the discrete element method to consider the air flow around the particles. A recent international collaboration on numerical modelling of silo phenomena has shown considerable research efforts in discrete element modelling around the world (Rong *et al*, 1996). A good review of the different models by different research groups can be found in Rong *et al* (1996).

In the discrete element models, it is necessary to adopt very small time step during the calculation to achieve a satisfactory simulation. This often requires very

substantial computational efforts. Furthermore, the particle-particle interaction is not yet well defined and idealised circular particle is far away from representing real particles. Therefore, the models are currently restricted to simulate the flow of very limited number of the particles (10^4-10^5) in 2-D silos or hoppers. The discrete element modelling of the discharge in full scale silos with billions of irregularly shaped particles appears to be a very long way off.

2.5 Concluding remarks

A brief review has been given of both the experimental and the theoretical techniques used to study the flow behaviour of discharging silos. From the methods discussed, it can be summarised as follows.

The visual and photographic techniques and the bed splitting techniques have been used in model silo experiments to observe flow patterns. The results obtained are usually qualitative in nature and it is doubtful whether the observed flow behaviour near the transparent wall represent that of the solid away from the wall. The radiographic techniques, the tracer techniques and the probe techniques can be used to show the true flow trajectory of solids, but they are usually high in expense and limited in scope. All these techniques cannot be applied to full scale silos.

On the other hand, the residence time measurement technique can be used in both full scale and model scale silos to investigate the solids flow. The technique is relatively simple and inexpensive, but inferring the flow pattern from the residence time measurements is not a straightforward task.

Amongst the discussed theoretical approaches to analyse the solids flow, the fluid mechanics method is not ideal as the solids flow is very different from the fluid flow. The plasticity theory is able to analyse incipient flows of granular solids, but the plastic behaviour of solids is not easy to capture fully and the predictions often do

not match the experimental observations. The kinematic theory appears to work well for steady state granular flow and is conceptually simple and easy to implement. However the physical meaning of the kinematic constant is not clear and modelling of the unsteady flow of silo emptying has not been attempted before.

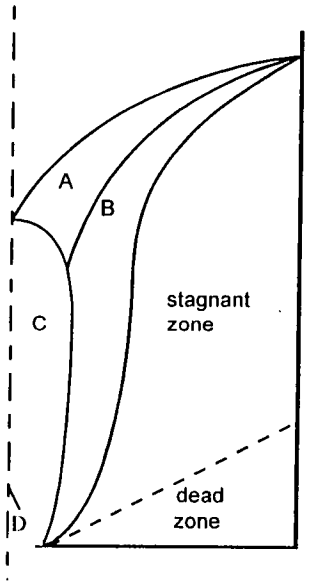

(a) Brown & Hawksley (1954)
A: fast top flow layer, B: slow flow zone,
C: central fast flow zone, D free fall zone

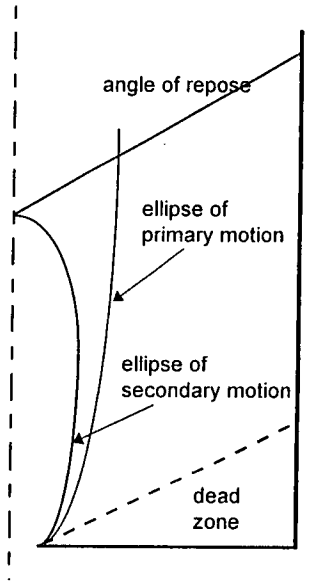

(b) Kvapil (1959)

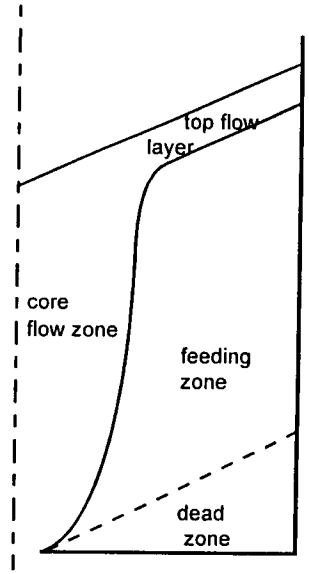

c) Watson (1993);
Delaney and Blake (1995)

Fig. 2.1: Internal funnel flow patterns

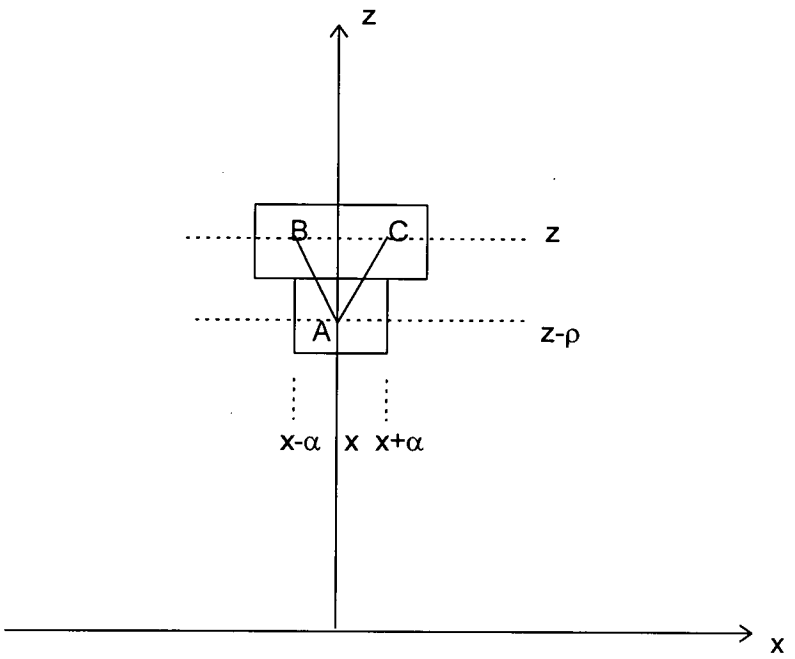

Fig 2.2: Litwinszyn's stochastic model

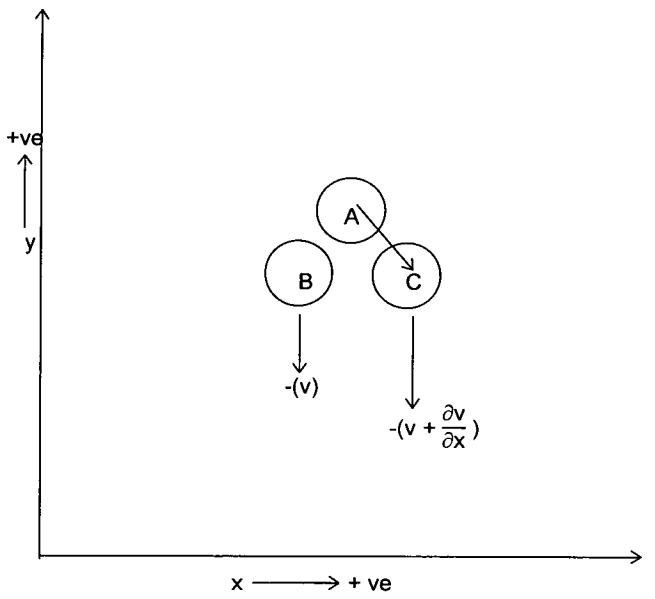

Fig. 2.3: Neddermen and Tuzun's kinematic model

CHAPTER 3

A HALF CYLINDRICAL MODEL SILO EXPERIMENTAL STUDY

3.1 Introduction

It is generally agreed that the unsymmetrical pressure pattern on the silo wall caused by the complex patterns of solids flow is the main cause for many silo failures. There is a strong need to investigate funnel flow in silos and its influence on silo pressures, which should lead to improvement of the standards for structural design of silos.

The principal difficulty in predicting funnel flow patterns is to establish the shape and size of the flow channel boundary (FCB): the interface between flowing and stationary solid. The vertical form of the FCB thus has importance in many studies. Many experimental studies (*e.g.* Lenczner, 1963; Brown and Richards, 1965; Gardner, 1966; Bransby *et al*, 1975; Nguyen *et al*, 1980; Tuzun and Nedderman, 1982) have described the FCB as non-linear, usually becoming steeper away from the outlet. There is a considerable mis-match between most theoretical predictions and experimental observations. The observations recently made by Carson *et al* (1991) on eccentric discharge flow patterns suggest that the FCB may be close to linear in the vertical plane, especially in shallow silos with wide funnel flows.

This chapter describes an experimental study of internal funnel flow in a half cylindrical model silo to further the understanding of the solids flow behaviour in silos. The flow behaviour including the FCB was observed in the model silo using

two different techniques: residence time measurement and visual observation through a transparent diametrical front wall. The experiments were conducted using polypropylene pellets under different discharge conditions. Also, attempts were made at measuring and evaluating the dilation of the solid during flow, which is believed to have a significant influence on solids flow. These experimental observations are used in Chapter 6 for predicting solids flow.

3.2 Experimental set-up

The experimental set-up for the model silo tests is shown in Figs. 3.1 and 3.2. The apparatus consists of a half cylindrical model silo with a transparent front wall, a collector tank, a reservoir tank, and a semi-circular seeding template. The dimensions of the rig are given in Fig. 3.2. The apparatus was originally designed by Watson (1993) for observing concentric flow. Modifications were made to allow experiments of different outlet eccentricities to be conducted. These modifications will be discussed below.

3.2.1 Flat-bottomed half cylindrical model silo

3.2.1.1 Supporting Structure

A tubular steel square scaffolding tower structure of 1.25 m plan dimension and 4.40 m in height was used to support the model silo and the overhead reservoir. It also has to accommodate a collector tank underneath. The scaffolding structure must be strong enough to support the reservoir tank, the silo model and the test solid. No shaking or vibration was observed during the experiments.

A system of wooden templates and runners were used around the silo back in order to frame the silo in place and produce a robust structure. This system also ensured that an accurate semi-circular shape was maintained throughout the experiments.

The silo rested on a wooden base board. The outlet on this base was originally fixed for concentric discharge. This arrangement was modified by first strengthening the base with a sheet of mild steel 3 mm thick, and then freeing the base so that it can move horizontally. This allows the outlet to be positioned at any chosen eccentricity.

3.2.1.2 The Silo Model

The model silo was 1.5 m high, 0.65 m in diameter and had a capacity of 0.25 m^3. However, only 0.15 m^3 of the test material (polypropylene pellets) was available, which gave an effective filling height of around 900 mm. Therefore the silo can be regarded as a squat silo with an aspect ratio of 1.4.

The semi-circular wall was rolled from 1.5 mm mild steel sheets. Flanges were designed to clamp the front diametral wall to the silo wall (Fig. 3.3). Rubber strips were sandwiched in between to cushion the glass wall and also to help seal the silo. The thickness of these rubber strips were taken into account when designing an exact semi-cylindrical shape against the front wall. The outlet was also semi-circular with a diameter of 65 mm, which gave an outlet diameter to silo diameter ratio of 1:10.

Uneven patches of rust were observed on the internal surface of the silo. A sheet of mylar was carefully fixed to the whole surface using a spray photo-mount to produce an even and smooth surface. A pneumatic shutter valve was used to control the material flow. The main advantage of using this system over a hand controlled system was the speed at which the shutter could be opened or closed, thus limiting the effect of the stoppages on test results.

3.2.1.3 The front wall

The diametral front wall to the half cylindrical model consisted of a 10 mm inner glass sheet and a 6 mm outer perspex sheet with a 100 mm by 100 mm square grid marked on the glass using a black tape. Glass was used because of its transparency and lower wall friction. The grid was given the coordinate systems of r in the radial direction for concentric discharge tests and x in the horizontal direction for non-concentric discharge tests, and z in the vertical direction (see Fig. 3.4). The origin was always at the centre of the outlet. This system is especially useful in the analysis of concentric flow.

3.2.2 Material handling system

The collector tank underneath the silo collected the discharged material from the silo during test. The collector tank was then raised using a crane and loaded into the reservoir tank for another test. The collector tank was a 1.2 m square box with a weighted swing door which opened a wedge shaped funnel allowing discharge into the reservoir tank. The reservoir tank contained a series of uniformly spaced 25 mm diameter holes (59 in total) which were drilled through two pieces of wooden base board (Fig. 3.5). Sandwiched in between was a 1.5 mm sliding metal shutter which when moved by a lever arm could offset the holes thus controlling the flow. The hole diameter was chosen to be large enough to prevent arching of the bulk solid. The circumference around this set of holes was the same as that of the silo model which was directly beneath. This arrangement gave a fairly uniform distributed filling which was used in all the tests.

3.2.3 Tracer particles and seeding template

White ceramic tracers 14 mm in diameter were used as tracer particles in the experiments. These were individually labelled using a combination of colour coding and numbering, so that when a tracer was collected from the outlet, its original position could be identified.

The tracers were seeded into the granular mass by means of a tracer seeding template shown in Fig 3.6. The seeding template, which consisted of two sheets of plywood and mounted on a spring system which allowed one to slide relative to the other, had 26 slots cut out which were numbered between 1 to 26 to correspond to the tracers. The seeding template was lowered down onto the solids surface by a string support. The tracers were then released onto the surface at known positions using a spring mechanism which triggered a sliding shutter.

The seeding template was designed to take advantage of the symmetry of concentric discharge and provides 5 such radial lines for comparison (Fig. 3.6). For the convenience of later analysis, the half-circular line of particles 1 to 5 at r = 300.0 mm is referred to as Circle 5 (Fig. 3.6). Four other lines denoted by Circles 4 (r = 240.0 mm), 3 (r = 180.0 mm), 2 (r = 120.0 mm) and 1 (r = 60.0 mm) refer to particles 6 to 10, 11 to 15, 16 to 20 and 21 to 25 respectively.

3.3 Bulk material measurements

The flow behaviour of a granular material is influenced by its mechanical properties. The basic mechanical properties of the blue polypropylene pellets were measured. These include bulk density, particle size distribution, angle of repose, wall friction and angle of internal friction.

3.3.1 Bulk density

Three measurements of bulk density and specific gravity were made simply by filling a cylinder of known volume with the solid. The loose density and tapped density were measured in a container with 203 mm in diameter and 218 mm in height. The loose bulk density was 554.7 kg/m^3 and the tapped bulk density was 598.4 kg/m^3 for polypropylene pellets. The specific gravity was 1.06.

3.3.2 Particle shape, size and size distribution

The pellets are short cylinders in shape. The thickness and diameter of 50 pellets picked randomly were measured using a calliper. The results are tabulated in Table 3.1 and the statistics of the particle dimensions are shown in Table 3.2. The grading of the pellets is uniform with the coefficient of variation of 5.0% and 15.4% for the diameter and the thickness respectively. The pellets are on average 3.3 mm thick and 4.9 mm in diameter.

3.3.3 Angle of repose

The angle of repose is the angle produced by the top free surface of a pile of solid to the horizontal surface on which it rests. Three measurements were made, each producing an angle of repose β of 34°.

3.3.4 Wall friction and internal friction

The wall friction angle and internal friction angle were determined by Jenike shear tests.

For wall friction, six 120 mm x 120 mm sample plates from the same mild steel sheet which was used to construct the original model silo were tested. Three sample were rusty and the others were rust free. All samples had mylar sheets attached to them.

The Jenike test procedure was followed closely (EFChE, 1989) in the conduct of the wall friction and internal friction tests. Typical shear test results with a smooth plate and a rusty plate are shown in Fig. 3.7. The responses were very similar indicating that the mylar sheet was effective in giving a uniformly smooth surface. The least squares fitting of all measured shear strength gave a wall friction angle of 10.6^{o} and a wall adhesion of 0.11 kPa (Fig. 3.8). Forcing the best fit line through the origin gave a wall friction angle of 12.6^{o}. The angle of internal friction for the blue polypropylene pellets was found to be 27.0^{o}.

3.3.5 Moisture content

The effect of moisture on the flowability for some fine-grained materials can be significant. For the polypropylene pellets which consist of relatively large particles (average diameter 3.3 mm), the influence of moisture content is expected to be negligible, and is therefore ignored.

3.4 Experimental techniques

The experiments described in this chapter were carried out in the Structures Laboratory of the University of Edinburgh. Two main observations were made: visual observation through the front wall and the residence time measurement. The transparent front wall allowed direct observations to be made of the FCB, the top surface profile and the particle trajectory. The residence time method allows measurements to be made within the solid mass.

3.4.1 Residence time measurements

Here, the pellets were allowed to fall freely into the silo in a uniformly distributed manner. The filling process was stopped and started many times to seed the solid with tracers using the seeding template. A total of 26 tracers were placed at every 100 mm height interval, giving 8 layers of seeding. The seeding procedure and the careful coding on the tracers ensured that the position of each marker within the silo was accurately known before flow was initiated.

The test was started by simultaneously starting the stop watch and opening the pneumatic shutter valve to begin discharge. As soon as a marker appeared on the 13 mm B.S. sieve placed directly beneath the outlet, the pneumatic shutter valve was closed and the watch was stopped in the same instant. The residence time was recorded for the tracer together with its number and colour on a prepared record sheet. The outlet was then reopened and the procedure repeated until the discharge was complete. After recording the total time of discharge, the silo was completely cleared of any remaining solid, ready for another test.

Seven tests with residence time measurements were carried out: three of concentric discharge, two of full eccentric discharge and two of half eccentric discharge.

3.4.2 Flow channel boundary observations

The flow channel boundary (FCB), an interface between moving solid and stagnant solid, plays an important role in determining the pressures exerted on the silo walls. The half model silo allows one to observe the development of the FCB through the front transparent wall during discharge.

In these tests, no tracers were used and the silo was filled in one continuous process. Some relevelling of the top free surface was occasionally needed. A sheet of mylar

with 100 mm square grid was taped to the front wall for tracing the development of the FCB. The boundary between flowing and stationary solids was distinguished solely by the naked eyes. The discharge was stopped several times in each test. During each stoppage, the FCB and the top solids surface were traced onto the mylar sheet and the cumulative time was recorded. Finally the dead zone at the end of discharge was traced and the total time of discharge was recorded. One test was carried out for each of the three outlet positions.

3.4.3 Particle trajectory observations

The particle trajectory observations give valuable insight into the flow behaviour of a granular solid. The adopted method was to place tracers at specific locations against the front wall and to observe the trajectory paths of these tracers during discharge.

When the silo was filled to a desired level, the tracers were dropped down through a long steel tube onto the surface near the front wall at an interval of around 50 mm horizontally. A total of two layers were placed in each test. Again a sheet of mylar was taped to the front wall to record the trajectory paths of the tracers.

A stop and start process was used for these experiments to capture the movement of the tracer particles especially near the outlet. The trajectory paths of the tracer particles were drawn by marking their positions at every stoppage. At the end of discharge, the surface of the remaining solid in the silo was traced and the total discharge time was recorded.

3.4.4 Dilation of bulk solid

The dilation of the bulk solid during flow may be expected to have a significant influence on the flow pattern development. However, only very limited literature can

be found on the experimental measurement of solids dilation during silo discharge. In this study, an attempt was made to deduce the dilation of the polypropylene pellets in the half cylindrical silo. The average dilation of flowing solid was calculated from the shape and size of the flow zone and the top surface profiles during discharge (see Section 3.5.4).

3.5 Experimental results and analysis for concentric discharge experiments

A total of 7 tests were conducted with concentric discharge. Each test was given a name with 3 characters followed by a number. The three characters describe the bulk material, the filling method and the discharge method, and the number describes the number of test done with such configuration. For example, Test BDC1 is the first test for the **B**lue polypropylene pellets with **D**istributed filling and **C**oncentric discharge.

3.5.1 Residence time measurements

Three similar concentric discharge tests were conducted: BDC1, BDC2 and BDC3. The residence time measurements are given in Table 3.3. Figure 3.9 shows the distributions of residence time at several levels for these tests. The differences between the tests are very small showing that the tests are highly repeatable.

To verify the symmetry of flow for these three concentric discharge tests, the coefficients of variation of the tracers at each semi-circle for all the seeded levels were computed and the results are shown in Table 3.4. The average coefficient of variation was found to be 13.2%, indicating that at any level the tracers at the same semi-circle had similar residence times and the flow pattern was symmetrical with respect to the central axis.

3.5.2 Retarding effect of the front wall

The half cylindrical model technique suffers from the uncertainty of the retarding effect of the diametral front wall. In this section, the retarding effect was investigated by comparing the residence times of the marker adjacent to the front wall with those further away on each semi-circle of markers (Fig. 3.6). Figure 3.10 shows the difference between the average residence time at each semi-circle and the residence time of the marker at the front wall. All markers at the front wall, except those in Circle 2 (r=120 mm) and Circle 3 (r=180 mm), were retarded by less than 10%. The average residence time difference between each marker at the front wall and those on the corresponding semi-circle is 8.8%. At Circle 1 and 2, the much larger residence time differences are caused not just by the wall retarding effect, but also by their positions at or near the flow boundary where large variation in residence time is expected (see Section 3.5.3). The retarding effect of the front wall is ignored in later analysis.

3.5.3 Deduction of flow channel boundary

The chief challenge of the residence time measurements is to identify the flow channel boundary. Several techniques to infer the developed FCB from the residence time measurements are presented here. In Chapter 7, the changing FCB will be inferred more rigorously from the residence time data using an inverse analysis technique.

With the axi-symmetry of the flow, the average residence times of the markers at each radial coordinate can accurately represent the residence times in the silo. Figure 3.11 shows the variation of the mean residence time with the radial coordinate. At lower levels, the residence time increased abruptly from very small values at small radial coordinates to very large values at large radial coordinates.

This pattern clearly indicates the two different flow zones: the fast core flow zone with small residence times and the surrounding feeding zone in which the solid remained stagnant for some time before sloughing off the advancing top surface into the core flow zone. For example, at Level 1 (100 mm from the base), tracers at the central axis and at Circle 1 discharged immediately after the outlet was opened whilst tracers at Circle 2 took about 215 s to discharge (total discharge time is 246 s). Thus the FCB at this level must lie in between Circle 1 and 2. Unfortunately, a more precise location of the FCB can only be determined by using more tracers in this local region. This type of deduction can only be applied to lower levels, as no abrupt change in the residence time of adjacent particles occurs at upper levels. Using an arbitrary definition that the FCB lie between adjacent tracers with a difference in residence time of greater than one third of the total discharge time, the flow channel can be approximately inferred using this radial plot and is shown later in summary Fig. 3.15.

Alternatively, the residence times can be plotted against the initial height of the tracers as shown in Fig. 3.12. The inverted-V shape of the plot is characteristic of the internal funnel flow mode (Rotter *et al*, 1996). The tracers in the core flow zone produced a band of residence times which increased with increasing height. The remaining tracers in the surrounding feeding zone gave a second band of decreasing residence times with increasing height, showing the action of solid sloughing off the top surface. Thus, each tracer can be easily identified to be either in the core flow zone or in the surrounding feeding zone (Fig. 3.12). The tracers associated with each flow zone can then be plotted in the spatial coordinates to reveal the approximate position of the FCB (Fig. 3.13). The approximate FCB inferred from this method is also shown in Fig. 3.15.

The challenge of identifying the FCB may alternatively be approached from another direction. Since the FCB is a discontinuity, particles on different sides of it are expected to have very different residence times. However, the FCB is not perfectly symmetrical or entirely stable. Thus, if the boundary passes through a circle of

markers at a given level, it is likely that some of these markers, all symmetrically placed with respect to the outlet, will emerge at very different times from others. The scatter can be simply measured using the standard deviation of the residence time, or more reliably using the coefficient of variation to indicate scattering in the residence time measurement of symmetrically placed markers.

A plot of the CoV against the radial coordinate at each level is shown in Fig. 3.14. Apart from Level 7 and 8, each level clearly has a peak, which moves steadily to larger radii at higher levels. However the FCB cannot be located accurately because the tracers are too sparsely spaced at the edge of the flow channel. A simple rule is used here whereby the FCB is assumed to lie within a 60 mm band at each level (60 mm is the tracer spacing). The position of the band is linearly weighted using the CoVs of the markers at both sides of the peak CoV.

The FCBs for concentric discharge as inferred from this CoV method and the above two other methods are shown in Fig. 3.15. There is a reasonable agreement in the FCBs inferred from all three methods, thus giving some confidence to the use of these methods to determine FCB. However the precise FCB location cannot be ascertained because the tracers were not closely spaced in the critical area. An improved approach would be to first use equal spacing and analyse the results to locate the approximate position of the FCB, and then to fine tune the seeding pattern for the tracers at each level so that the FCB can be located more accurately.

3.5.4 Development of flow channel boundary

The development of the FCB during discharge was carefully observed through the transparent diametral front wall. This was accomplished by tracing the boundary of moving solid and the corresponding solids surface on a mylar sheet taped to the front wall. The discharge was stopped and restarted several times to record the changing

profiles. Each test ended with a measurement of the final angle of repose and the total time of discharge.

Figure 3.16 shows the FCB and the corresponding top surface profile measured at various stages during concentric discharge. The development of the FCB can be described in three stages (see Fig. 3.17). First, when the orifice was opened, the material directly over the orifice moved rapidly out. As this material exited, the material above moved down along the central axis, then exited itself. As this process continued, the FCB could be observed between the flowing and the stationary material. When the flow was stopped momentarily, the material within the centre flow core was clearly seen to have a less density than the material outwith. The central flow core ascended rapidly upwards and swelled slightly laterally, forming a 'cigar' shape zone until the apex hit the top surface, which remained undeformed up to this stage (Fig. 3.17a).

In the second stage, around 4 s after the start of discharge, the 'cigar' shape flow zone opened out and the material from the top surface funnelled down the central flow zone. Consequently the top surface began to take up an inverted cone. The sides of this funnel quickly adopted a stabilised inclined angle. During this process, a 'top flow layer' was formed in which the material moved essentially parallel to the surface as opposed to the material in the central core which moved essentially downwards. The material in the top flow layer was eventually engulfed into the downward flow stream at some point between the FCB intercept and the centre. Meanwhile, the flow zone continue to widen (Fig. 3.17b).

In the third stage, around 30 s after the start of discharge, the top surface continued to advance downwards and the FCB continued to expand as the discharge progressed. The rate of expansion of the FCB slowed down considerably towards the later stage of discharge. It almost stabilised after 50 s of discharge. At the end of this stage, the inclined top surface reached the outlet leaving the dead zone in the silo (Fig. 3.17c).

The widening of the FCB with time is shown in Fig. 3.18. The flow channel widened rapidly at early stages of discharge. Around 50 s after the start of discharge, the FCB away from the top flow layer became fairly stable and the FCB at that time is taken as the fully developed FCB. The widening of the FCB was much quicker at the upper levels. After 4 s of discharge, the FCB has reached 82% at Level 1 and 54% at Level 6 of the fully developed FCB radius width at the corresponding levels. The fully developed FCB appeared linear from the outlet to about z=200mm. It then began to curve with the FCB becoming nearly vertical from z=300mm upwards (Fig. 3.16).

The measured FCB and the inferred FCBs (Section 3.5.3) are compared in Fig. 3.19. A good agreement can be seen between the inferred FCBs and the measured fully developed FCB.

3.5.5 Trajectory paths of particles

Three experiments were carried out to measure the trajectories of particles at different levels. Figure 3.20 shows the flow trajectories for particles seeded at Levels 3, 5, 6, 7 and 8. All the particles within about 100 mm from the central axis had almost vertical trajectories at the upper levels, followed by smooth curve paths at the lower levels. The remaining particles were each caught by the advancing top flow layer at some stage. Each of these particles had a different inclined trajectory until they entered the core zone, after which they each followed similar smooth path seen for the particles within the 100mm radius. The approximate angles of inclination of these inclined trajectories were plotted in Fig. 3.21. The angle to the horizontal became smaller with increasing radius and decreasing height above the base, tending to approach the angle of repose for the solid.

Figure 3.20 also reveals that in the core flow zone, a particle which passed through a point had very similar flow trajectory to that for the particle which originated from

that point. This observation supports the kinematic theory in which the velocity field propagates from the outlet upwards and is independent of the top boundary condition (e.g. Mullins 1972; Watson and Rotter, 1996; Zhang and Ooi, 1997).

3.6 Experimental results and analysis for fully eccentric discharge experiments

3.6.1 Residence time measurements

Residence time measurements were made in two tests with fully eccentric discharge BDE1 and BDE2). The residence time measurements are given in Table 3.5.

The total discharge times for the two tests were the same at 218 s, which is less than the 246 s for the concentric tests. This is mainly because the 0.035 m^3 remaining volume of solid in the silo after the eccentric discharge is greater than the 0.02 m^3 for the concentric case. In fact the discharge under eccentric discharge was 5.3×10^{-4} m^3/s which is slightly higher than 4.97×10^{-4} m^3/s under concentric discharge.

The same methods for inferring the FCB in the concentric tests were also applied here. The residence times for the tracers closest to the front wall are shown in Fig. 3.22. There is a very good agreement between the two tests, showing that the tests are highly repeatable.

However it was more difficult to infer the FCB from this plot because the tracers were seeded in rings concentric to the central outlet and not optimised for the eccentric flow. To investigate the cross-sectional shape of the flow channel under eccentric discharge, the 3-D residence time distributions from Level 1 to Level 8 for Test BDE1 are plotted in Fig. 3.23 and 2-D contour Fig. 3.24. It reveals that at the

same level the particles having identical distance to the centre line of the outlet have similar residence times, suggesting that the flow channel is close to circular in cross-section.

Figure 3.25 shows the horizontal variation of residence times of markers adjacent to the front wall for Test BDE1. The pattern of the residence time distributions is similar with that under concentric discharge. Using the same arbitrary definition that the FCB lies between adjacent tracers with a difference in residence time greater than one third of the total discharge time, the FCB can be estimated from this method and is shown in Fig. 3.28.

Figure 3.26 shows a plot of the residence times of tracers against their initial vertical coordinate. The inverted-V shape of the plot shows that funnel flow has occurred. The tracers in the core flow zone can be distinguished from the tracers in the surrounding feeding zone. The tracers associated with the two flow zones can be plotted in the spatial coordinates to reveal the approximate position of the FCB (Fig. 3.27).

The FCBs for eccentric discharge as inferred from the above two methods are shown in Fig. 3.28. There is a reasonable agreement in the two inferred FCBs.

3.6.2 Flow channel boundary

Figure 3.29 shows the measured FCB and corresponding top surface profile at different stages of emptying the silo. The three stages involved in the development of the FCB shown in Fig. 3.30 have similar features to those for concentric discharge (c.f. Fig. 3.17). The only difference is that under eccentric discharge the expanding channels were truncated by the wall.

The widening of FCB with time at different levels is shown in Fig. 3.31. After 10 s of discharge, the FCB reached 88% and 65% of the fully developed FCB at Level 1 and Level 6, very close to 86.1% and 58.3% under concentric discharge. The time taken for the FCB to be fully developed is very similar for both eccentric and concentric discharge i.e. 45-50 s. The radii of the fully developed FCB under concentric discharge and the equivalent radii under eccentric discharge at different levels are shown in Table 3.6. It can be seen that at the lower part of the silo the FCB becomes smaller under eccentric discharge.

The measured fully developed FCB is compared with the deduced FCB in Fig. 3.32. The fully developed FCB appeared linear from the outlet and began to curve at about z=150mm, which is similar to the concentric discharge case. However unlike the concentric discharge case, it continued to widen slowly above z=350mm.

3.6.3 Trajectory paths of particles

Figure 3.33 shows the particle trajectories at Level 3 to 8 for eccentric discharge. In general, the trajectories in relation to the central axis of the outlet are quite similar with those under concentric discharge. The particles away from vertical central axis of the outlet had inclined trajectories. The angle of inclination became less steep for particles further away from the vertical axis and eventually approaching the angle of repose observed for the top surface (Fig. 3.34).

3.7 Experimental results and analysis for half eccentric discharge experiments

3.7.1 Residence time measurements

The residence time data for two half eccentric tests (DBH1 and DBH2) are given in Table 3.7. The total discharge times for the two tests were 230 s and 235 s, which are smaller than concentric discharge (245 s) but larger than eccentric discharge (218 s). The remaining volume of the material at the end of discharge was $0.027m^3$. Thus the discharge rate under half eccentric discharge was $5.2x10^{-4}$ m^3/s, which is very similar to that under eccentric discharge.

The residence time distributions of tracers at several levels near the front wall are shown in Fig. 3.35 for both tests. Again, the high repeatability of the experiments under half eccentric discharge is clearly demonstrated.

The shape of the cross-section of the FCB was studied by analysing the 3-D residence time plot and 2-D contour for Level 1 to Level 8 for Test BDH1 (Figs. 3.36 and 3.37). At the same level, the particles with the same distance to the centre-line of the outlet generally have similar residence times, suggesting that the cross-section of the FCB is also close to circular under half eccentric discharge.

Figure 3.38 shows the distributions of residence time near the front wall. The patterns at different levels are similar to those for concentric and eccentric discharge. The only difference is that under half eccentric discharge, the residence times of the particles to the right of the outlet were slightly higher than the corresponding particles to the left. It appears that the wall has some influence on the flow. Again, using the same arbitrary definition that the FCB lies between adjacent tracers with a difference in residence time greater than one third of the total discharge time, the FCB estimated from the radial plot is shown in Fig. 3.41.

The inverted V shape plot of residence time with height for half eccentric discharge is shown in Fig. 3.39. The tracers associated with the two flow zones is plotted in the spatial coordinates in Fig. 3.40, revealing the approximate position of the FCB.

The FCBs for half eccentric discharge as inferred from the above two methods are compared in Fig. 3.41. Again, they are in good agreement.

3.7.2 Flow channel boundary

The measured FCB and the top surface profile at various stages during the process of half eccentric discharge are shown in Fig. 3.42. The development of FCB during half eccentric discharge can be similarly divided into three stages (Fig. 3.43). In the first stage (Fig. 3.43a), the 'cigar-shaped' flow zone developed, similar to the concentric case. In the second stage, due to the half eccentricity, the sloping top surface hit the silo wall at the right earlier. Soon afterwards, the centre of the 'sink hole' moved towards the right until it reached the wall (Fig. 3.43c). During the last stage, the FCB continued to widen. The centre of the 'sink hole' started to shift away from the wall towards the central axis of the outlet and descend towards the outlet. Finally, a dead zone at the angle of repose remained.

It took around 55 s to reach the fully developed FCB. To the left of the outlet, the development and the shape of the FCBs are very similar with those under concentric discharge. However, the FCBs to the right were affected by the wall. It intercepted the wall of about 11 s of discharge and thereafter having a pipe flow against the wall.

Figure 3.44 shows the deduced and the measured fully developed FCB under half eccentric discharge. They are also in good agreement.

3.7.3 Trajectory paths of particles

The trajectories of particles from different levels are shown in Fig. 3.45 for the half eccentric case. Comparing with the concentric discharge, the main difference is that at higher levels, the particles to the right of the outlet had vertical trajectory paths. This is because for a significant part of discharge, the solid displayed pipe flow against the right wall. However, the solids to the left had internal funnel flow characteristic, so their trajectories are similar to those under concentric discharge.

3.8 Comparison between predicted and measured discharge rate

The rate of discharge from a silo outlet has been investigated by many researchers e.g. Deming and Mehring, 1929; Fowler and Glastonbury, 1959; Brown and Richards, 1960; Beverloo *et al*, 1961; Harmens, 1963; Al-Din and Gunn, 1984; and Memon and Foster, 1985 and Nedderman, 1985). Several empirical equations for evaluating discharge rate have been proposed. In this section, these equations are compared with the measured discharge rate for the model silo.

Deming and Mehring (1929) proposed a formula for the mass discharge through funnels with a hopper half angle of α

$$W = \frac{52.7D^{2.5}\rho_b}{\{34.6 + [67.4 + 444\sin(\alpha/2)][\bar{x}/D + 0.130 - 0.161\tan\beta]\}\tan\beta} \qquad (3.1)$$

where $\bar{x}$ and D are the mean particle diameter and the diameter of the outlet, ρ_b is the bulk density of solid.

For flat-bottomed silos, Eq. (3.1) can be used if α is replaced by (Rose and Tanaka, 1959)

$$\alpha = 180^{o} - 2\beta \tag{3.2}$$

Based on dimensional analysis, Fowler and Glastonbury (1959) proposed an equation to estimate the mass flow from a circular outlet

$$W = 0.059\pi D^{2}\sqrt{2gD}\rho_{b}\left(\frac{D}{\bar{x}}\right)^{0.185} \tag{3.3}$$

Beverloo *et al* (1961) developed an empirical correlation for solids discharge from central conical outlet

$$W = 0.58\rho_{b}\sqrt{g}(D - k\bar{x})^{2.5} \tag{3.4}$$

Experimental data of Beverloo *et al* show that the value of the particle shape constant k lies within the range of 1.3 to 2.9. An average value of 1.4 was recommended.

Some researchers (Brown and Richards 1960; Harmens, 1963; Memon and Foster, 1985; and Nedderman, 1985) found that the choice of bulk density ρ_b in the above equations is questionable since bulk density decreases appreciably as solids approach the outlet. Harmens (1963) suggested that the particle density is a more appropriate parameter, whilst Nedderman (1985) argued that a bulk density defined as the ratio of mass flow to volumetric flow rate gives the least scatter in data when used in the Beverloo correlation.

Using dimensional analysis, Brown and Richards (1960) proposed an equation for mass discharge rate using particle density instead of bulk density

$$W = \frac{\sqrt{2}}{15}\pi\rho_{s}\sqrt{g}(D - k\bar{x})^{2.5} \tag{3.5}$$

Harmens' (1963) equation involving the particle density ρ_s and the angle of repose β for discharge through a circular outlet is given by

$$W = \frac{1}{4}\pi D^2 \rho_s \sqrt{gD}[0.505 - 0.160\tan\beta - \frac{0.38(\bar{x}/D)^{1.5}}{0.045 + (\bar{x}/D)^{1.5}}] \qquad (3.6)$$

In 1984, Al-Din and Gunn presented the following formula for design calculations

$$W = 0.406 F_p \rho_b \sqrt{g}\frac{D}{4}(D - \bar{x})^{2.5}(\frac{D}{\bar{x}})^{0.154} \qquad (3.7)$$

where F_p is a particle constant. The value of F_p is unity for round particle and is 0.32 for particle with irregular shape.

So far, there has been no equation specially formulated to estimate discharge rate from a semi-circular outlet. Investigations have shown that the shape of outlet has a significant influence on the discharge rate (Brown and Richards, 1960; Beverloo *et al*, 1961; and Kotchanova, 1970). Beverloo *et al* (1961) found that mass discharge rate decreases in the order of circle, square, rectangle and triangle outlet cross-section, while Kotchanova (1970) reported that a semi-circular outlet has smaller mass discharge rate than that from a circular or square outlet. Brown and Richards (1960) found that mass discharge rate from a slit is about 20 % lower than that from a circular opening. Harmens (1963) recommended that for non-circular or regular polygonal outlet, the mass discharge rate is between 80 to 100% of a circular one.

The above equations were used for estimating the discharge rate for the half cylindrical model silo. In the calculations, the bulk density of the polypropylene pellets ρ_b is taken to be 0.52 ρ_s and the volumetric discharge rate from the semi-circular outlet is taken as 80% of half the discharge rate from a circular outlet of the same diameter. Figure 3.46 shows the comparison between the volumetric discharge rates predicted by the different equations and the measured discharge rate. The

agreement between the predictions and the experimental observation is reasonable. The difference is in the range of 2.7% to 31.0%. The equations proposed by Deming and Mehring (1929), Brown and Richards (1960) and Harmens (1963) gave closer predictions. However, the Beverloo equation which is widely used overpredicted the discharge rate by some 30.0% for this case.

3.9 Dilation of bulk solid

Most granular solids are expected to dilate (increase in porosity) during flow. The dilation of the bulk solid is thought to have a key influence on the flow pattern which develops during discharge. The dilation properties of different solids have been measured under static and small strain conditions in triaxial or plane strain samples (e.g. Ooi and Rotter, 1988; Hartlen *et al* 1984), but serious doubts remain on whether such measured static dilation is representative of the volumetric changes which occur during the dynamic silo discharging process. The solids dilation during flow is difficult to measure, so this aspect has often been ignored and no measurement of flow dilation appears to have been reported before. In this study, the average dilation of flowing solid was evaluated from the FCB geometry and the top surface profile during flow in this half cylindrical model silo.

Visual observation of looser material in the flow zone has clearly demonstrated that the solid has dilated during the discharge. The solid appeared to be in its loosest state in a very small area near the outlet and no noticeable difference in packing was observed in the feeding zone. As a first approximation, the dilation of the solid is assumed to be uniform within the FCB.

At time t during discharge, the volume of solid Q_{flow} in the core flow zone can be evaluated from

$$Q_{flow} = \frac{1}{2}\sum_{i=1}^{n} \pi\left(\frac{r_{i-1} + r_i}{2}\right)^2 \Delta h_i \qquad (3.8)$$

where n is the number of increments used to evaluate the volume, r is the radius of the FCB and Δh is the height for each increment.

Since discharge rate is independent of the head of solid in a silo and remains relatively constant throughout the discharge (Fowler and Glastonbury, 1959; Brown and Richards, 1960; Beverloo *et al*, 1961; Harmens, 1963; Al-Din and Gunn, 1984), the volume of discharged solid Q_{exit} at time t can be evaluated from

$$Q_{exit} = \bar{q}\, t \qquad (3.9)$$

where $\bar{q}$ is the average volumetric discharge rate for the whole discharge, which is given by

$$\bar{q} = \frac{\pi R^2}{2 T_{tot}}\left(H - \frac{2}{3} R \tan\beta\right) \qquad (3.10)$$

where R is the radius of the silo, H is the height of fill, β is the angle of the repose at the end of filling and T_{tot} is the total discharge time.

Assuming a uniform bulk density in the flow zone, the solids dilation can be expressed as the expansive volume strain as

$$\psi = (Q_{exit} - Q_{cone})/Q_{flow} \qquad (3.11)$$

in which Q_{cone} is the displaced volume at the top solid boundary which was evaluated from the changing surface profiles.

Alternatively, the bulk density in the core flow zone can be evaluated as

$$\rho_{flow} = \rho_b (1-\psi) \tag{3.12}$$

in which ρ_b is the initial bulk density of the pellets at the end of filling.

Applying Eq. (3.8) to the measured FCBs shown in Fig. 3.16, the volume of flowing solid Q_{flow} within the FCB at each stage can be obtained. The solids dilation ψ was evaluated at different times during discharge and are shown in Table 3.8 and Fig. 3.47. As the flow was initiated, the solids within the FCB dilated immediately and by merely 4 s into discharge, the solids have dilated by 17.1%. Further widening of the flow channel only caused slight increase in dilation which stabilised at 17.7%. Since the bulk density at rest was found to be 554.7 kg/m^3 from control tests, the dilated flowing bulk density was 456.5 kg/m^3. More careful tests which include weighing the discharged solid are being conducted at Edinburgh to give a more precise description of the dilation and to study the effect on flow channel geometry.

3.10 Concluding remarks

In this chapter, the experiments to investigate the flow behaviour of polypropylene pellets in a half cylindrical model silo under concentric, eccentric and half eccentric discharge conditions have been reported. The experimental techniques used were boundary observations and residence time measurements. All the experiments were found to be highly repeatable. The following conclusions can be reached

1. The retarding effect of the front glass wall has been shown to be small and was ignored in this study.

2. The discharge rate under eccentric discharge and half eccentric discharge is 5% higher than that under concentric discharge. For concentric discharge, the discharge rate was found to be $4.97 \times 10^{-4} m^3/s$, while $5.32 \times 10^{-4} m^3/s$ and $5.24 \times 10^{-4} m^3/s$ for eccentric and half eccentric discharge.

3. The FCB had a curved convex form in all three cases. However, under concentric discharge, the upper part of the FCB is close to vertical.

4. The residence time measurements have been used to infer the fully developed FCB. The proposed methods of analysing the residence time measurements have been shown to be reliable, giving inferred FCBs which are in good agreement with the measured FCB.

5. In spite of the different discharge conditions, the times for the FCB to develop fully in all three cases were almost identical. The FCB widened rapidly in the early stages of discharge and the expansion rate decreased considerably at the later stages.

6. The particles in the core flow zone generally had vertical trajectories at the upper levels and smooth curved trajectories converging towards the outlet at the lower levels. The particles caught up by the top flow layer had inclined trajectories until they were drawn into the fast core flow zone. The angle of inclination with the horizontal was found to be approximately inversely proportional to the distance between the initial position of the particle and the vertical axis of the outlet.

7. The dilation of solid was found to be fairly uniform except for a small area above the outlet. The loosening of the bulk density only increased very slightly with discharge and had an average value of around 17.7% for these experiments.

Table 3.1: Measurements of size distribution of polypropylene pellets

Pellet No.	Diameter (mm)	Thickness (mm)	Pellet No.	Diameter (mm)	Thickness (mm)
1	4.9	2.9	26	4.7	3.0
2	5.0	3.6	27	4.7	3.1
3	4.7	3.6	28	4.8	3.6
4	4.9	3.6	29	4.7	3.2
5	4.7	3.1	30	5.1	3.8
6	4.6	3.5	31	4.2	2.1
7	4.8	2.8	32	5.0	3.6
8	4.8	4.0	33	5.1	3.9
9	4.7	3.3	34	4.9	2.8
10	4.7	3.9	35	5.2	3.5
11	4.8	3.9	36	5.1	2.8
12	5.0	4.0	37	5.0	3.8
13	4.7	3.3	38	5.0	3.7
14	5.0	2.9	39	4.8	3.1
15	4.7	4.0	40	5.2	3.8
16	4.9	3.1	41	5.0	3.1
17	4.5	2.1	42	5.4	3.8
18	4.8	3.4	43	5.0	3.9
19	4.1	2.6	44	5.1	3.6
20	4.6	2.2	45	5.1	3.8
21	5.0	2.9	46	5.1	3.9
22	4.9	2.9	47	5.1	3.6
23	4.7	3.8	48	5.1	3.6
24	5.0	2.9	49	5.3	3.6
25	4.7	3.9	50	4.9	3.8

Table 3.2: Properties of polypropylene pellets

Bulk density (kg/m^3)		Specific gravity	Size distribution								Angle of repose	Internal friction angle	Wall friction angle
			Diameter				Thickness						
Loose	Tapped		Max. (mm)	Min. (mm)	Mean (mm)	CoV (%)	Max. (mm)	Min. (mm)	Mean (mm)	CoV (%)			
554.7	598.4	1.06	5.4	4.1	4.9	5.0	3.9	2.2	3.3	15.4	34.0°	27.0°	10.6°

Table 3.3: Residence time data for the three concentric tests (Total discharge time: 244 s (Test BDC1), 249 s (Test BDC2), 243 s (Test BDC3))

Test No.	Level No.	Residence times for each tracer no.																									
		Circle 5					Circle 4					Circle 3					Circle 2					Circle 1					Ctr.
		1	2	3	4	5	6	7	8	9	10	11	12	13	14	15	16	17	18	19	20	21	22	23	24	25	26
BDC1	1												137	233	233	138	220	174	157	214	220	2	3	2	3	2	1.2
BDC2												242	238	235	235	237	226	220	127	86	220	4.4	3	3	1.4	3	1.4
BDC3														223		226	216		63		209	3.7		1.6		1.6	1.6
BDC1	2	238	230	222	226	228	222	216	212	214	216	208	203	200	198	203	39	21	18	15	21	4.1	4.1	3	3	3	2.1
BDC2		238	237	239	237	240	226	222	220	220	226	211	204	202	206	209	33	37	22	23	42	4.4	3	3	3	4.4	3
BDC3		235		220		223	217		207		211	204		168		197	48		16		24	4.1		3.7		3.7	1.6
BDC1	3	209	204	203	203	204	196	192	185	187	190	198	108	46	92	215	24	18	16	16	22	6.5	5.3	5.3	5.3	5.3	4.1
BDC2		208	206	204	208	211	198	191	190	195	202	179	102	98	138	184	24	20	20	23	30	6.3	6.3	6.3	8.7	9.2	4.4
BDC1	4	185	182	177	182	185	172	168	168	168	168	133	85	64	78	115	34	21	18	19	25	9.5	8.5	8.5	8.5	8.5	7.8
BDC2		184	182	176	181	187	174	166	165	168	170	156	103	74	82	166	38	24	20	20	35	11	11	9.2	11	11	9.2
BDC3		182		178		180	168		162		167	171		71		157	30		21		29	11		11		11	9.5
BDC1	5	165	157	156	157	163	152	150	153	153	150	125	85	64	78	119	39	25	22	22	33	14	13	13	13	14	12
BDC2		166	158	155	156	160	152	147	145	145	149	145	104	67	90	127	59	38	27	26	33	17	16	16	16	16	14
BDC3		159		153		160	150		146		151	135		68		129	35		21		37	16		15		15	14
BDC1	6	148	141	136	136	138	137	138	129	132	127	129	135	156	137	111	46	33	39	25	37	19	19	19	18	19	16
BDC2		141	136	131	135	138	131	125	123	121	128	117	92	87	73	111	50	42	37	37	48	23	22	20	20	22	20
BDC3		135		123		148	121		114		127	113		70		108	43		29		41			20		21	20
BDC1	7	120	120	113	120	120	112	108	104	106	112	99	77	68	77	102	46	37	35	35	46	26	25	25	24	26	24
BDC2		117	98	110	113	118	103	115	94	98	106	82	74	70	71	87	55	48	45	43	52	30	30	30	30	33	27
BDC3		110		110		114	97		97		99	82		70		82	45		38		42	28		25		27	25
BDC1	8	92.2	99	96	102	97	89	84	80	87	91	69	61	59	65	73	48	48	43	41	48	35	34	33	33	34	33
BDC2		87	82	80	86	84	74	69	69	66	72	59	52	52	52	55	46	43	42	42	46	40	40	39	39	39	38
BDC3		80		79		87	71		62		70	54		48		52	41		37		38	35		32		33	32

Table 3.4: Calculations of coefficients of deviation of residence times under concentric discharge

Level	Statistical items	Circle 5	Circle 4	Circle 3	Circle2	Circle 1
1	Stdev			39.17	55.00	0.90
	Average			216.00	180.87	2.59
	CoV			18.14	30.95	34.81
2	Stdev	7.22	5.77	10.72	10.69	0.89
	Average	215.10	217.59	200.92	27.52	3.72
	CoV	3.36	2.65	5.34	38.83	23.93
3	Stdev	2.83	5.17	55.60	4.16	1.41
	Average	205.95	192.6	135.85	21.31	6.45
	CoV	1.38	2.68	40.93	19.50	21.92
4	Stdev	3.30	2.96	39.93	6.69	1.01
	Average	181.54	167.9	111.78	25.66	9.78
	CoV	1.82	1.77	35.72	26.08	10.30
5	Stdev	3.95	2.78	28.83	6.79	1.33
	Average	158.84	149.321	102.55	30.37	14.77
	CoV	2.49	1.86	28.11	22.34	9.00
6	Stdev	6.54	6.53	25.28	7.18	1.53
	Average	137.35	127.03	110.44	38.81	20.13
	CoV	4.76	5.14	22.89	18.49	7.60
7	Stdev	6.34	6.66	10.64	6.16	2.79
	Average	114.08	103.85	79.89	43.46	27.62
	CoV	5.56	6.42	13.32	14.18	10.09
8	Stdev	7.71	9.42	7.56	3.04	3.04
	Average	88.38	75.45	57.63	43.03	35.58
	CoV	8.72	12.49	13.11	7.06	8.54

Table 3.5: Residence time data for the two full eccentric tests (Total discharge time: 218 s (Test BDE1), 218 s (Test BDE2))

Test No.	Layer No.	Residence times for each tracer no.																									
		Circle 5					Circle 4					Circle 3					Circle 2					Circle 1					Ctr.
		1	2	3	4	5	6	7	8	9	10	11	12	13	14	15	16	17	18	19	20	21	22	23	24	25	26
BDE1	1					1					1.8				216	69					203						
BDE2						2				218	2				218	173			216		211						
BDE1	2				183	1.8				180	3.1			216	183	14			216	187	175		217	204	194	193	204
BDE2					189	2				182	3.5			218	180	16			214	189	180	218	218	208	201	199	210
BDE1	3			194	108	3.9		217	189	80	3.9	217	200	181	119	12	200	194	179	154	67	189	185	179	165	162	179
BDE2				207	155	4.7			194	138	4.7	218	211	187	131	18	211	191	184	163	70	191	191	180	169	144	180
BDE1	4	218	198	174	97	6.1	198	187	166	65	6.1	187	180	158	65	12	176	168	152	117	54	165	159	152	140	129	153
BDE2		217	208	180	106	7	208	194	172	81	8.5	193	184	165	88	20	180	176	159	148		169	167	155	144	144	157
BDE1	5	187	180	155	86	12	174	167	146	64	13	162	157	141	64	22	157	148	134	95	60	148	144	132	116	115	134
BDE2		178	163	140	81	8.8	165	156	129	63	8.8	154	146	125	65	13	143	135	121	88	53	132	126	119	104	101	117
BDE1	6	161	155	140	69	14	152	143	117	58	14	144	131	112	65	23	129	125	106	73	52	119	115	103	92	92	105
BDE2		162	154	129	73	7.5	152	146	118	64	18	146	134	116	63	27	131	125	110	81	61	121	115	106	91	88	106
BDE1	7	140	128	104	58	19	133	117	96	52	19	119	108	92	56	25	108	99	87	63	49	96	93	87	73	71	84
BDE2		144	131	104	63	22	129	123	101	57	22	123	111		60	31	111	106	90	64	57	102	99	86	77	73	88
BDE1	8	112	104	78	46	25	103	93	71	43	24	99		66	43	30	92	77	63	49	43	75	71	63	56	54	65
BDE2		121	108	81	47	27	108	102	73	44	27	96		70	46	35	91	77	68	50	44	87	70	64	60	57	64

Table 3.6: Equivalent radius of FCB at different levels under concentric and eccentric discharge

z (mm)	Radius of FCB (mm)	
	Concentric discharge	Eccentric discharge
100	88.2	70.3
200	141.2	116.2
300	167.6	148.6
400	176.5	164.8
500	179.4	170.2

Table 3.7: Residence time data for the two half eccentric tests (Total discharge time: 230 s (Test BDH1), 235 s (Test BDH2))

Test No.	Layer No.	Residence times for each tracer no.																									
		Circle 5					Circle 4					Circle 3					Circle 2					Circle 1					Ctr.
		1	2	3	4	5	6	7	8	9	10	11	12	13	14	15	16	17	18	19	20	21	22	23	24	25	26
BDH1	1										6				181	1				63	2			187	59		206
BDH2						215				221	5				209	2			233	105	2			221	207	220	220
BDH1	2				181	45			196	97	4			185	28	2		192	176	17	3	187	183	172	43	17	174
BDH2					202	43			215	131	5		223	209	26	3	216	213	196	15	3	207	204	188	35	24	190
BDH1	3		196	181	161	30	196	187	174	54	7	185	181	166	23	4	178	172	154	19	4	166	161	131	34	18	118
BDH2			223	202	134	29	216	207	191	57	8	206	200	182	22	5	196	188	167	19	6	188	180	153	32	21	135
BDH1	4	183	176	159	110	36	174	170	152		11	166	159	138	28	8	154	150	131	20	8	140	137	91	34	23	95
BDH2		207	195	180	140	33	195	190	171	49	10	188	178	159	27	8	178	167	149	26	8	162	155	118	37	24	112
BDH1	5	167	161	147	103	43	161	152	138	56	15	151	143	123	28	11	140	135	103	22	12	127	118	85	30	22	79
BDH2		182	176	155	108	41	175	169	144	60	15	167	157	131	35	11	153	146	112	26	13	136	126	100	41	27	96
BDH1	6	151	143	130	87	55	143	135	118	56	20	137	127	107	34	17	124	118	91	29	18	108	101	86	43	30	84
BDH2		166	155	135	104	53	153	146	128	55	19	147	136	114	39	17	136	128	99	30	17	114	110	88	44	33	88
BDH1	7	135	127	113	84	59	125	118	101	65	28	118	116	93	45	23	108	101	85	36	25	93	89	76	49	38	77
BDH2		144	135	120	80	60	138	126	105	65	26	128	118	97	43	22	114	108	85	39	24	97	94	79	50	39	80
BDH1	8	114		89	75	58	107	99	83	56	32	103	93	77	48	29	89	85	69	40	30	79	76	63	48	40	65
BDH2		120	114	94	71	57	105	99	83	55	33	108	90	74	47	30	94	85	68	41	32	79	74	62	49	41	62

Table 3.8: Calculation of dilation of bulk density

Time (sec)	Q_{exit} (cm^3)	Q_{cone} (cm^3)	Q_{flow} (cm^3)	$Q_{exit} - Q_{cone}$ (cm^3)	Dilation (%)
4	1988.0	0.0	11596.9	1988.0	17.1
10	4970.0	2538.7	14220.9	2431.3	17.1
20	9940.0	5660.4	24373.0	4279.6	17.6
30	14910.0	9555.5	287204.4	5354.5	18.5
50	24850.0	18794.2	32832.6	6055.8	18.4

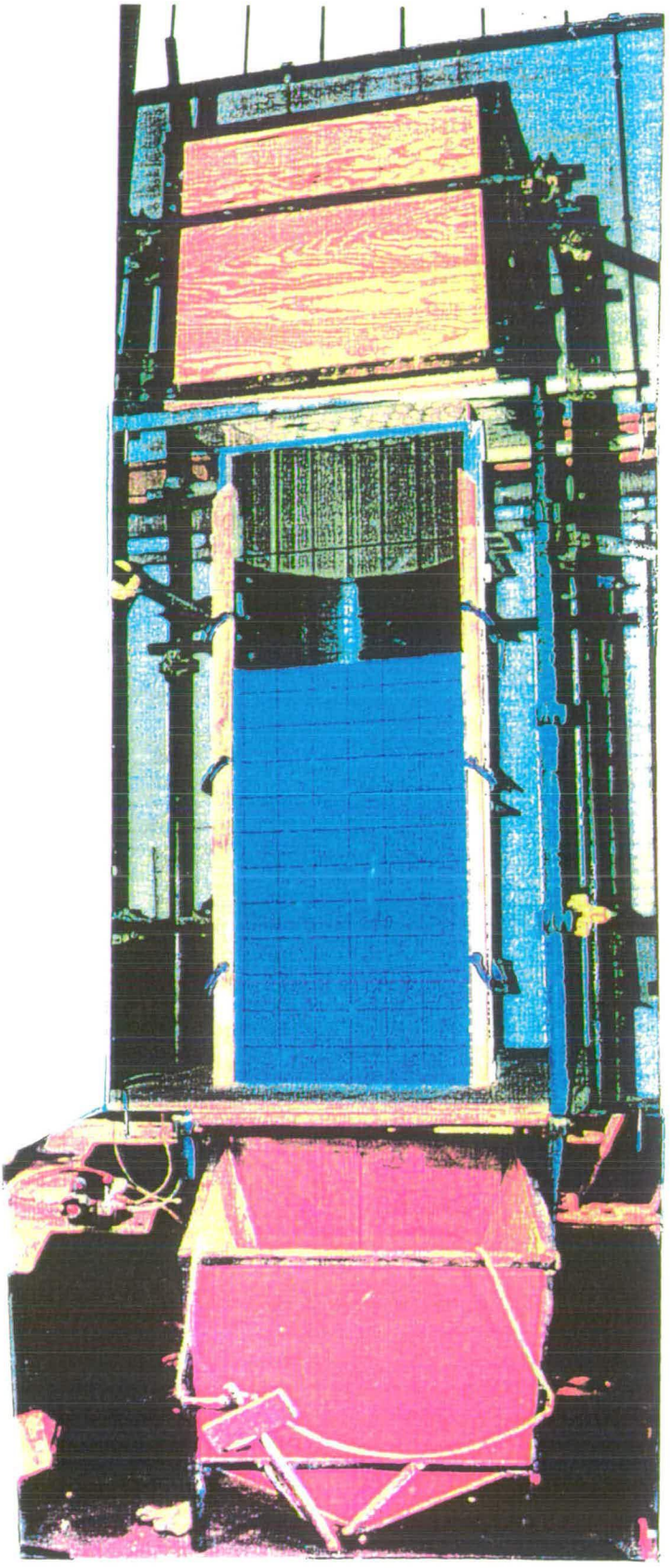

Fig.3.1 Half cylindrical model silo

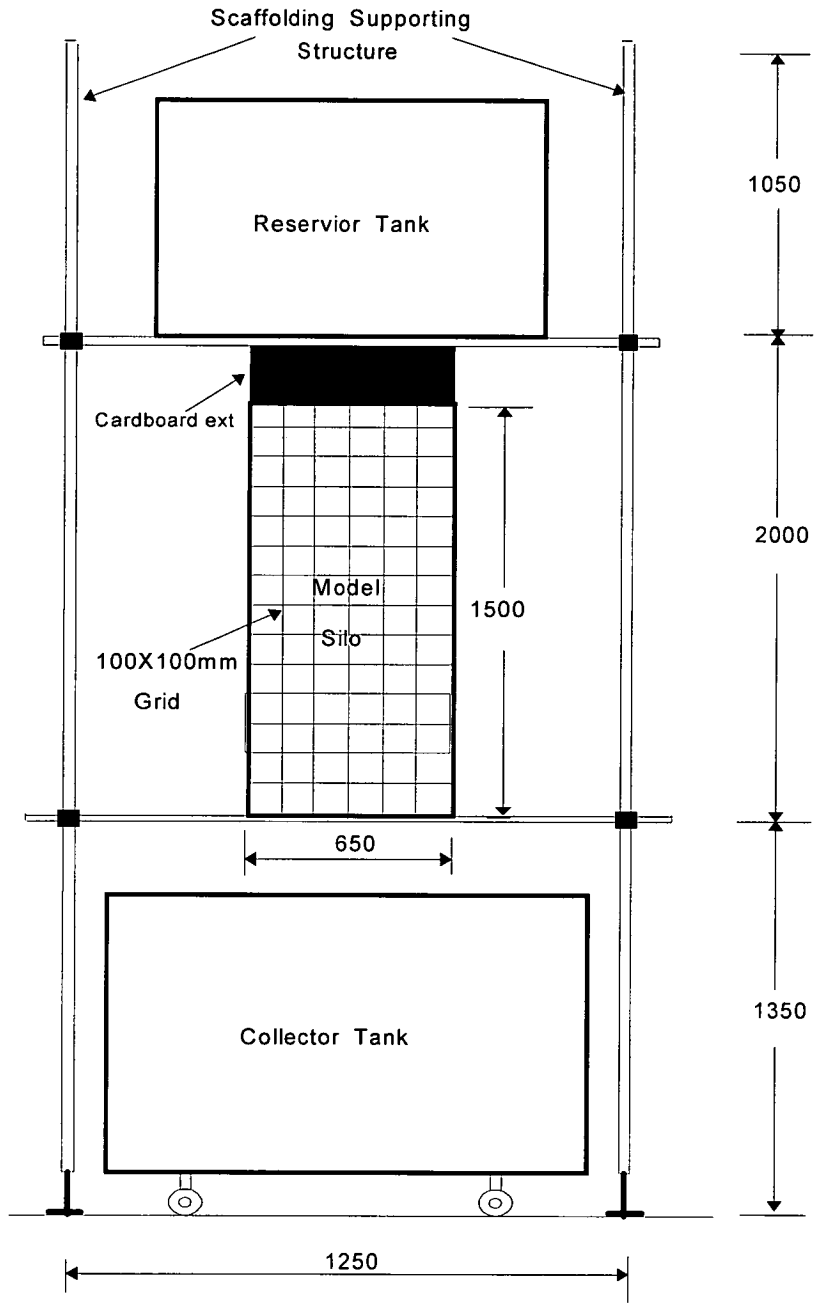

Fig. 3.2: Dimensions of model silo

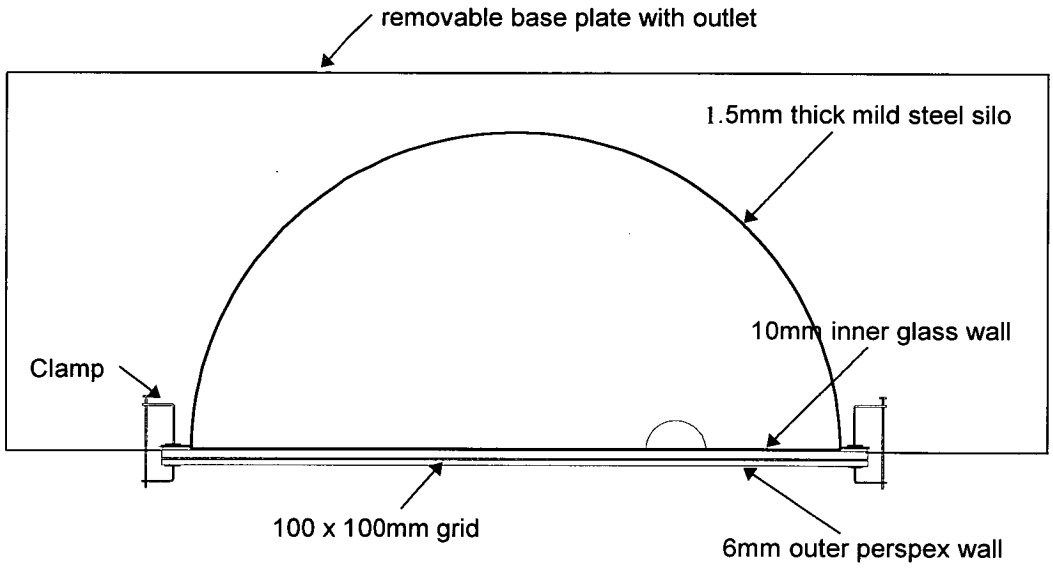

Fig. 3.3: Plan view of model silo

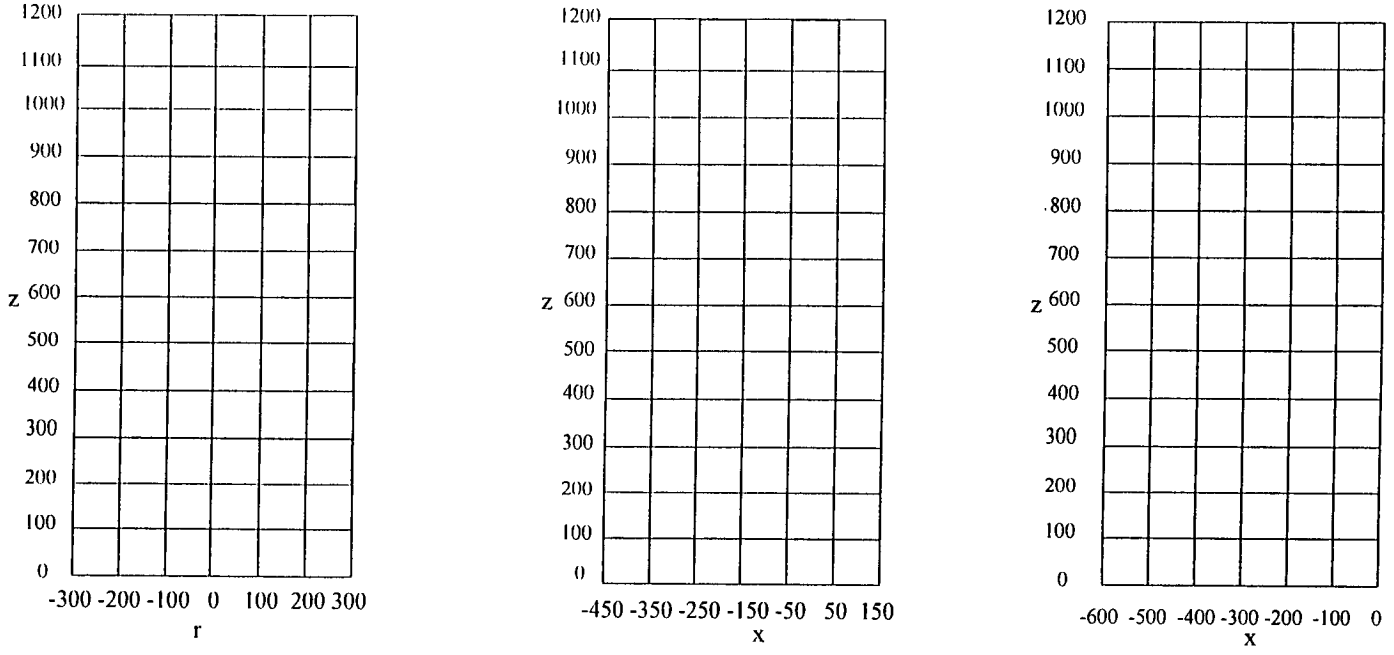

a) concentric discharge

b) half eccentric discharge

c) full eccentric discharge

Fig. 3.4: Coordinate systems for different discharge conditions

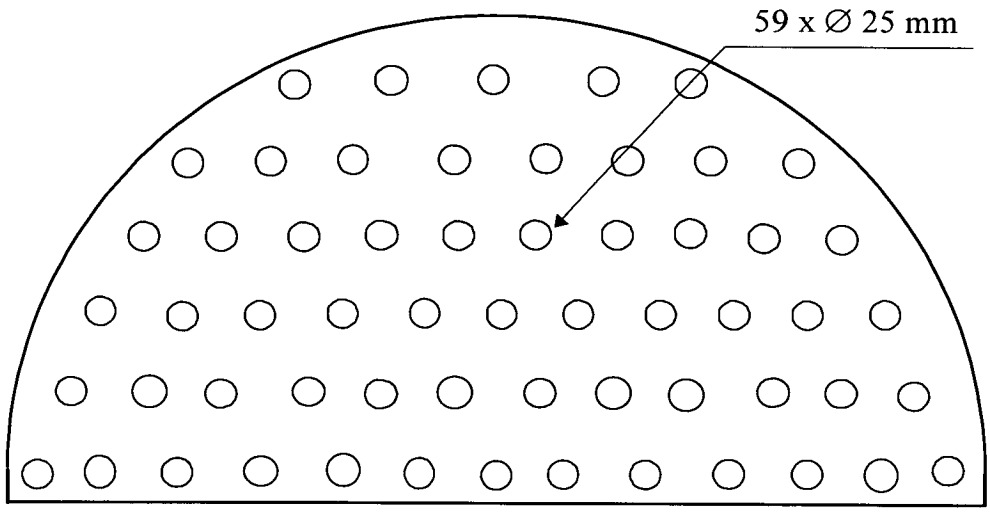

Fig. 3.5: Board for distributed filling

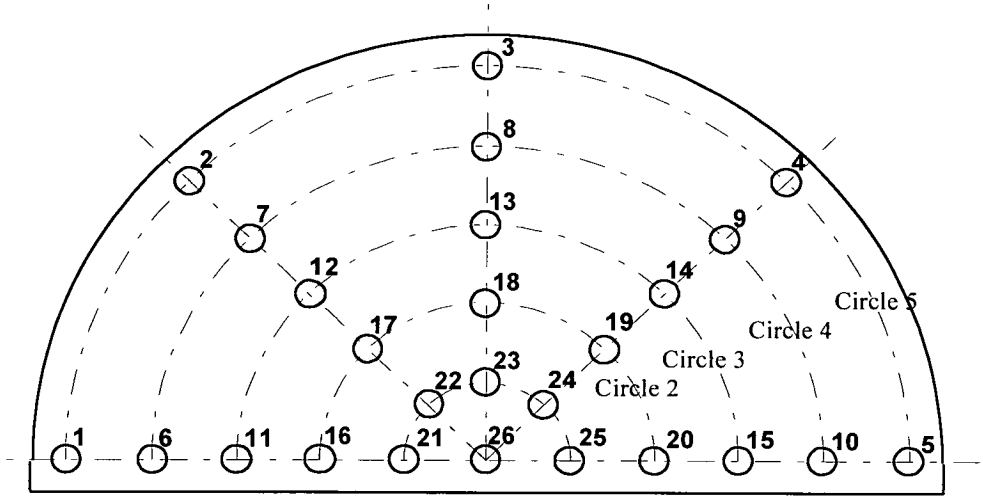

Fig. 3.6: Tracer seeding template

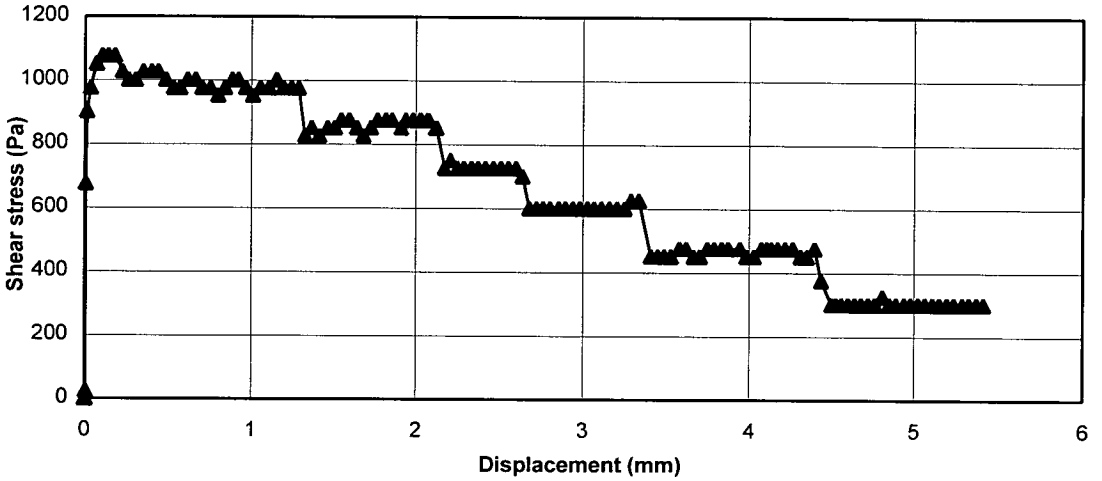

(a) smooth plate with mylar

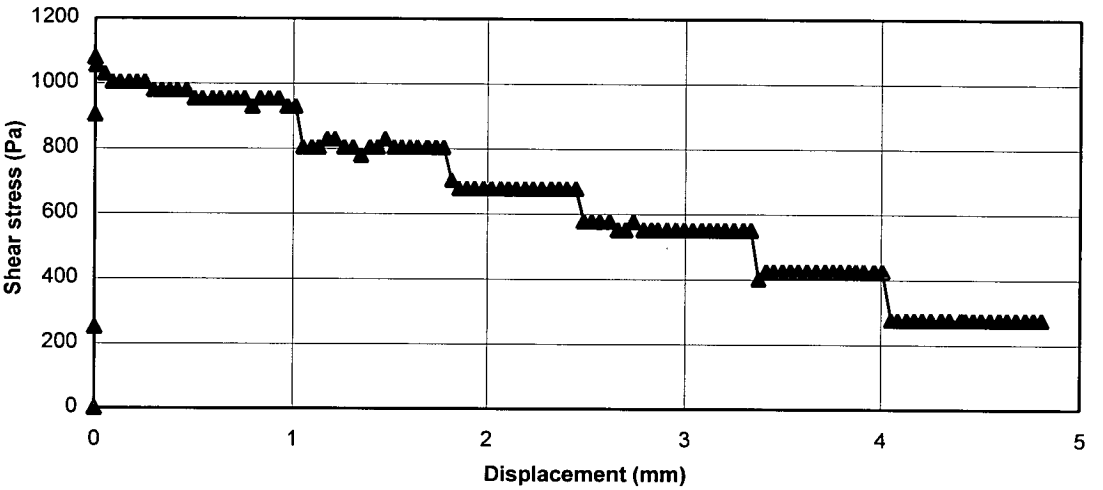

(b) rusty plate with mylar

Fig. 3.7: Jenike shear test for wall friction

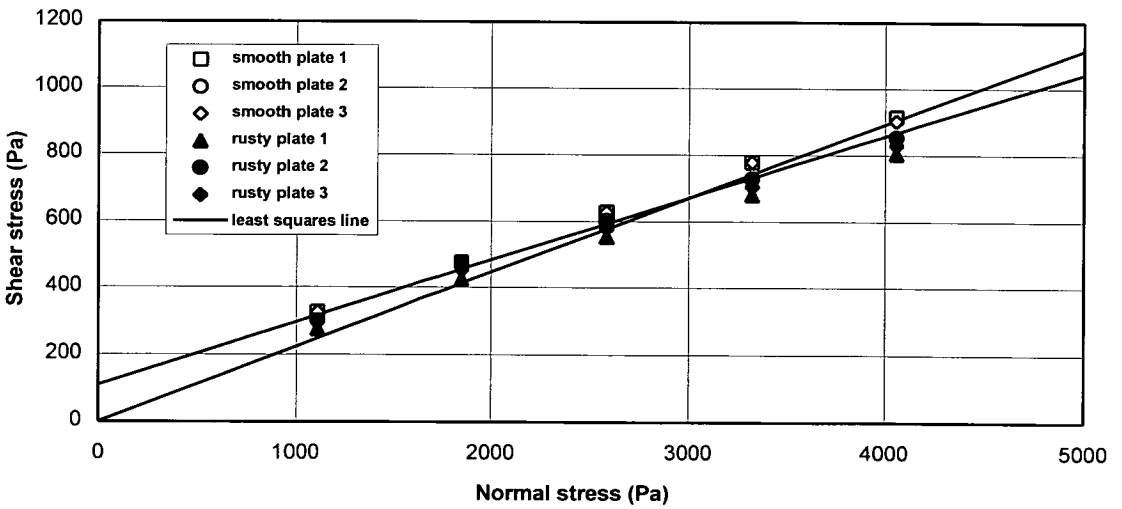

Fig.3.8: Wall friction tests for polypropylene pellets

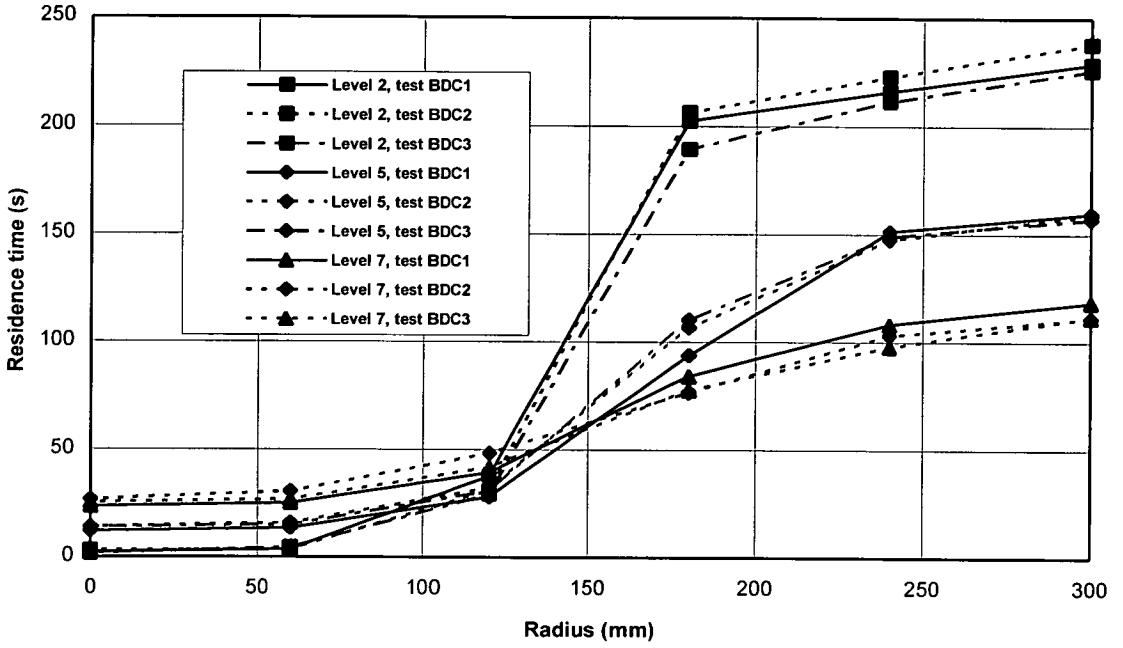

Fig. 3.9: Comparisons of residence time distributions under concentric discharge

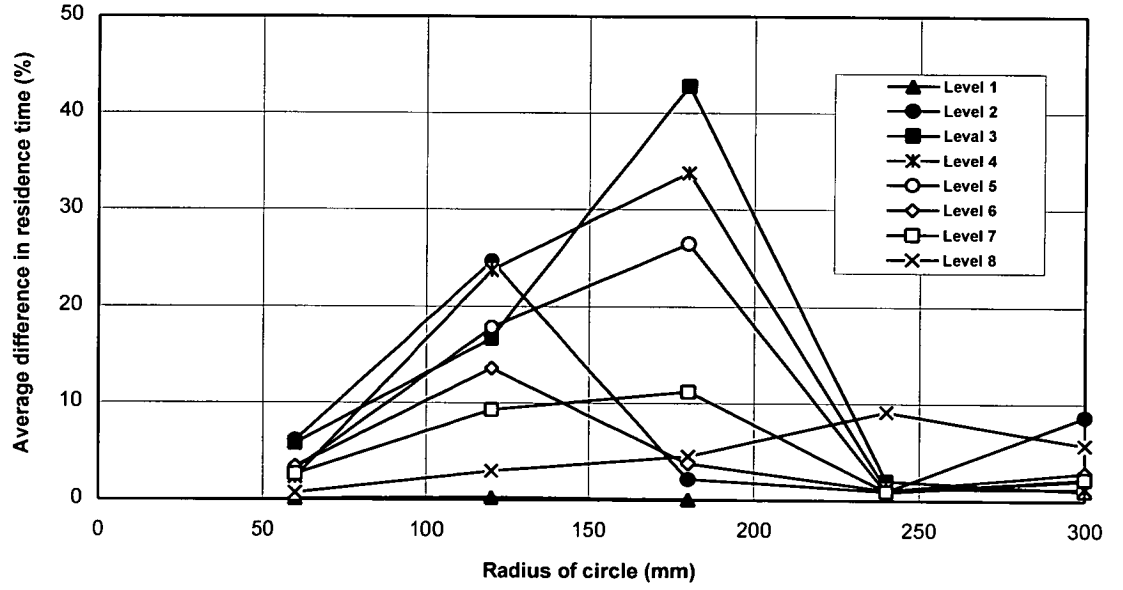

Fig. 3.10: Anaysis of retarding effect of front wall

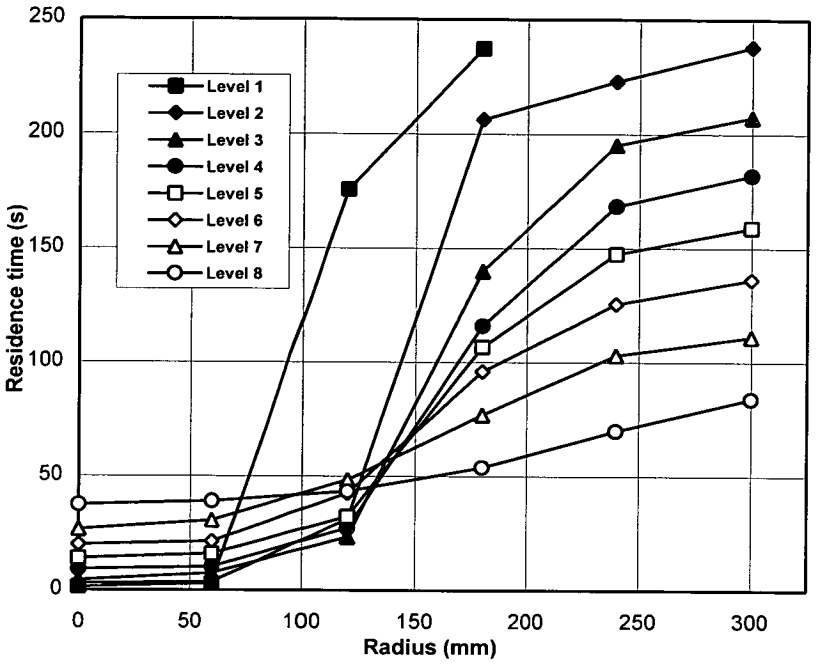

Fig. 3.11: Mean residence time distributions under concentric discharge

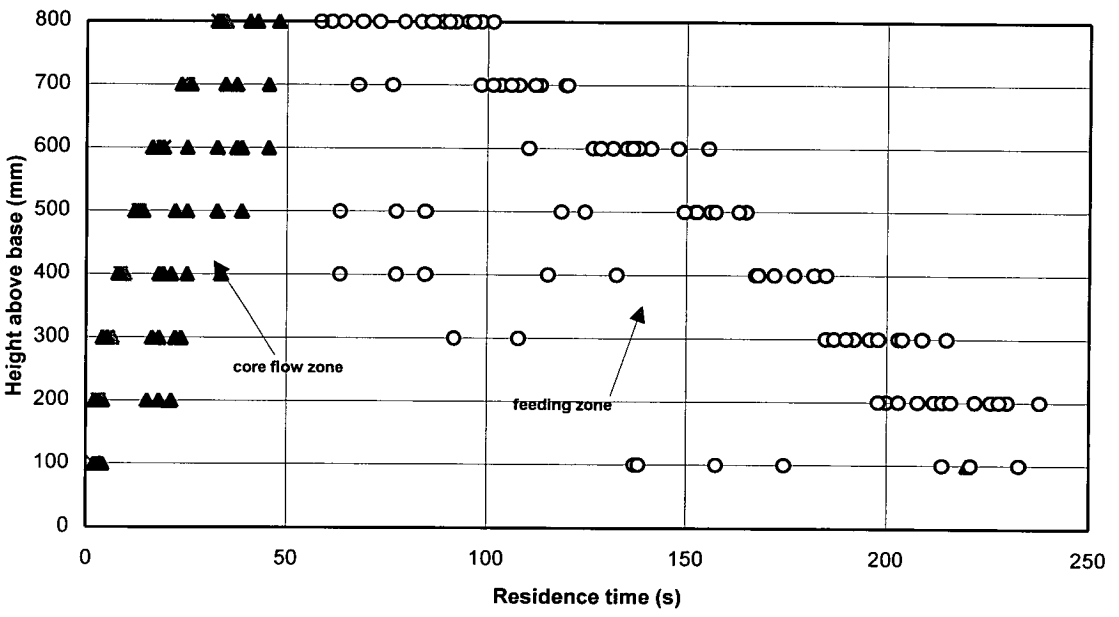

Fig. 3.12: Variation of residence time with vertical coordinate under concentric discharge

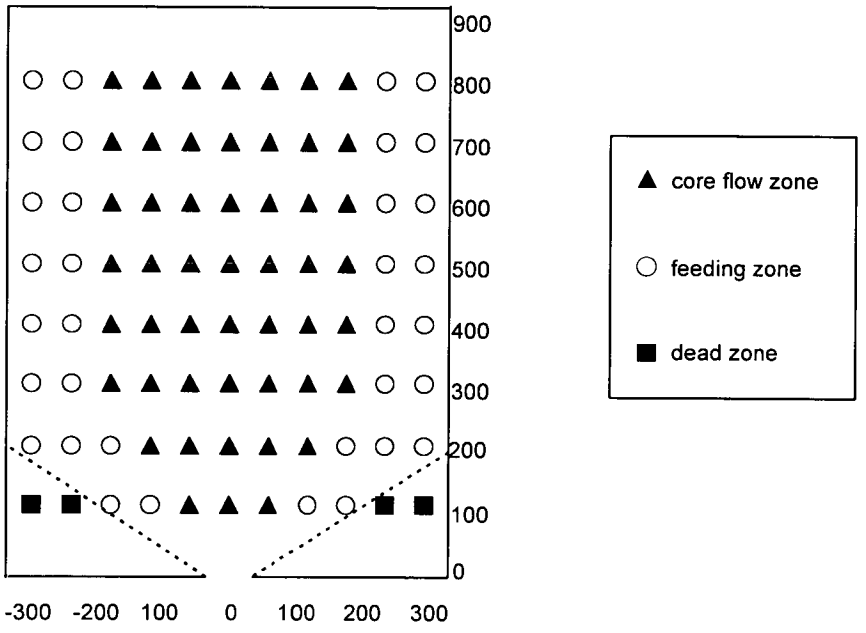

Fig. 3.13: Tracers in different flow zones under concentric discharge

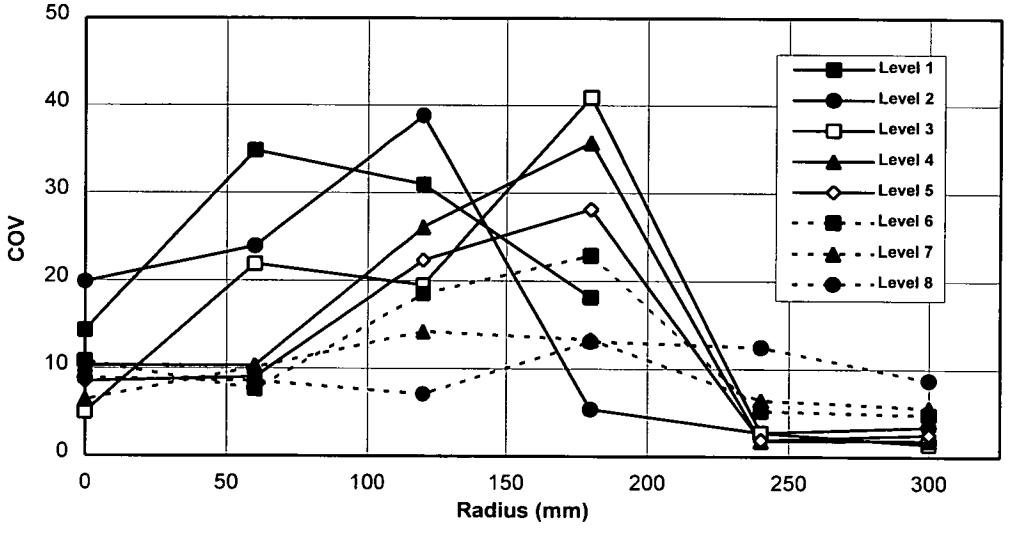

Fig.3.14: Statistical analysis of measured residence time data

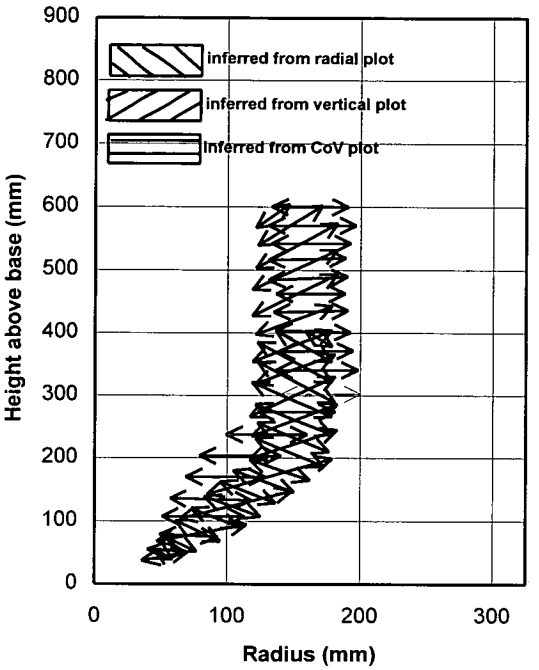

Fig.3.15: Inferred FCBs from different analysis methods under concentric discharge

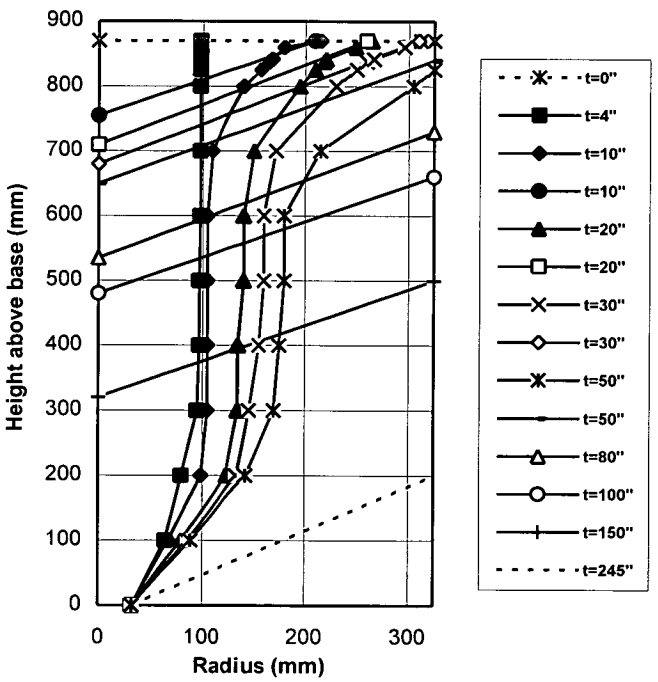

Fig. 3.16: Measured FCBs and top surface profiles during concentrical discharge

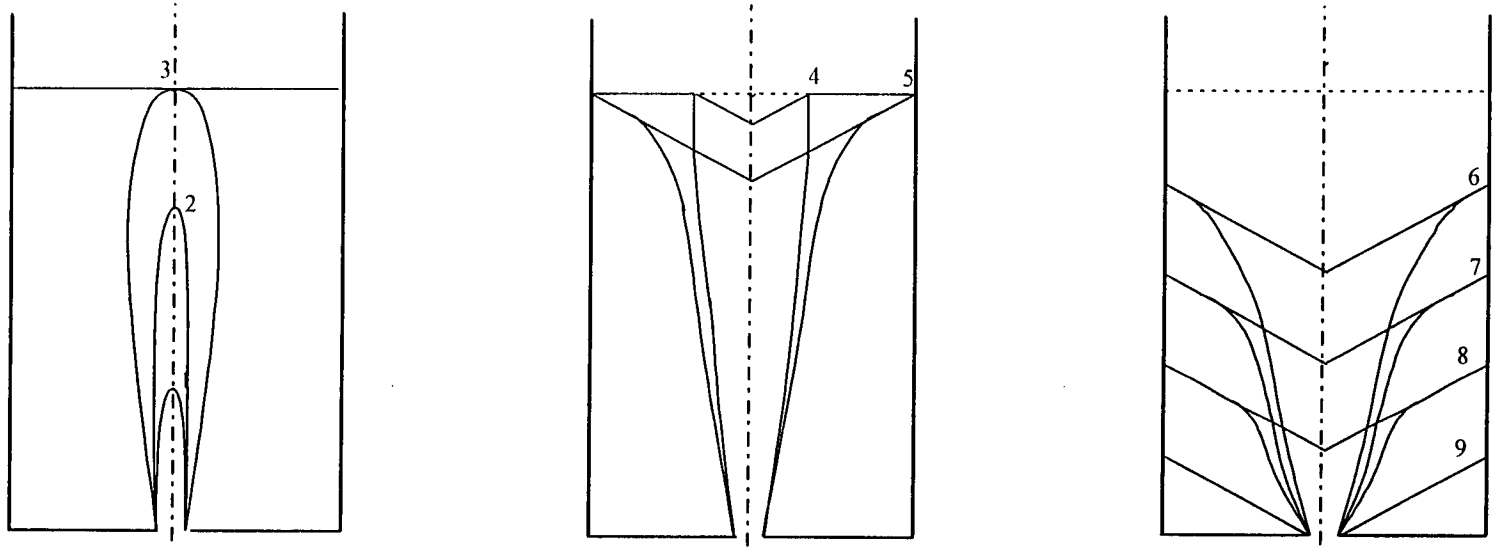

a) stage 1 b) stage 2 c) stage 3

Fig. 3.17: Typical stages involved in development of FCB under concentric discharge

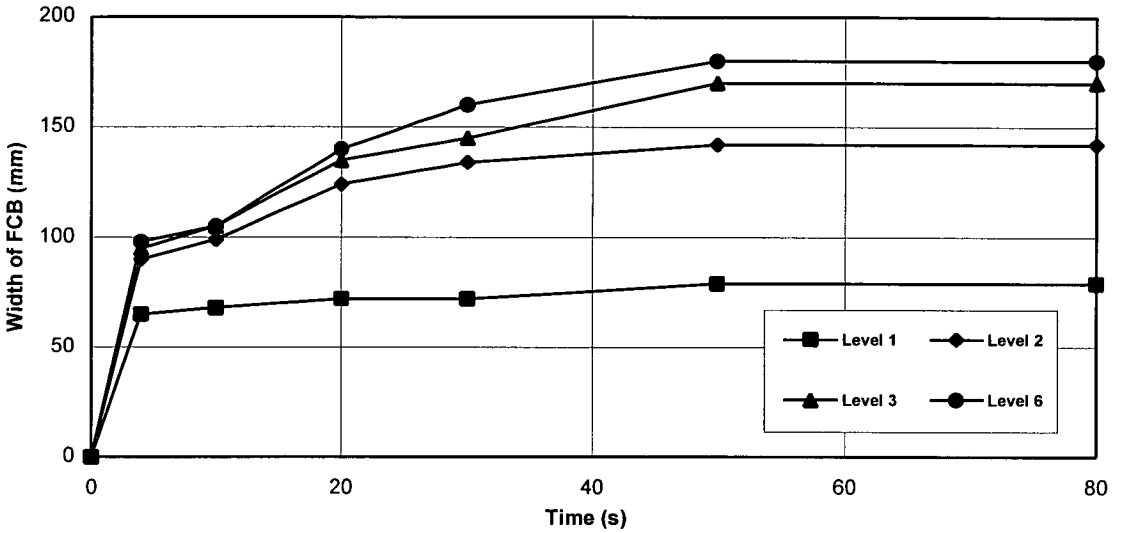

Fig.3.18: Developemnt of FCB with time under concentric discharge

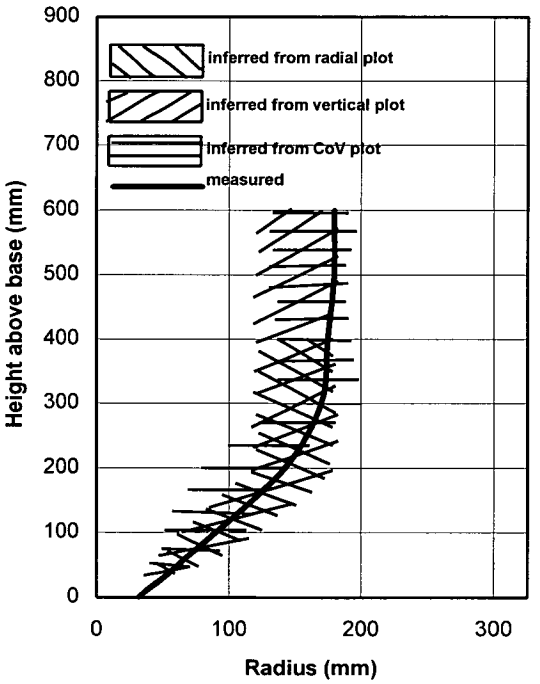

Fig. 3.19: Comparisons between deduced and measured fully developed FCB under concentric discharge

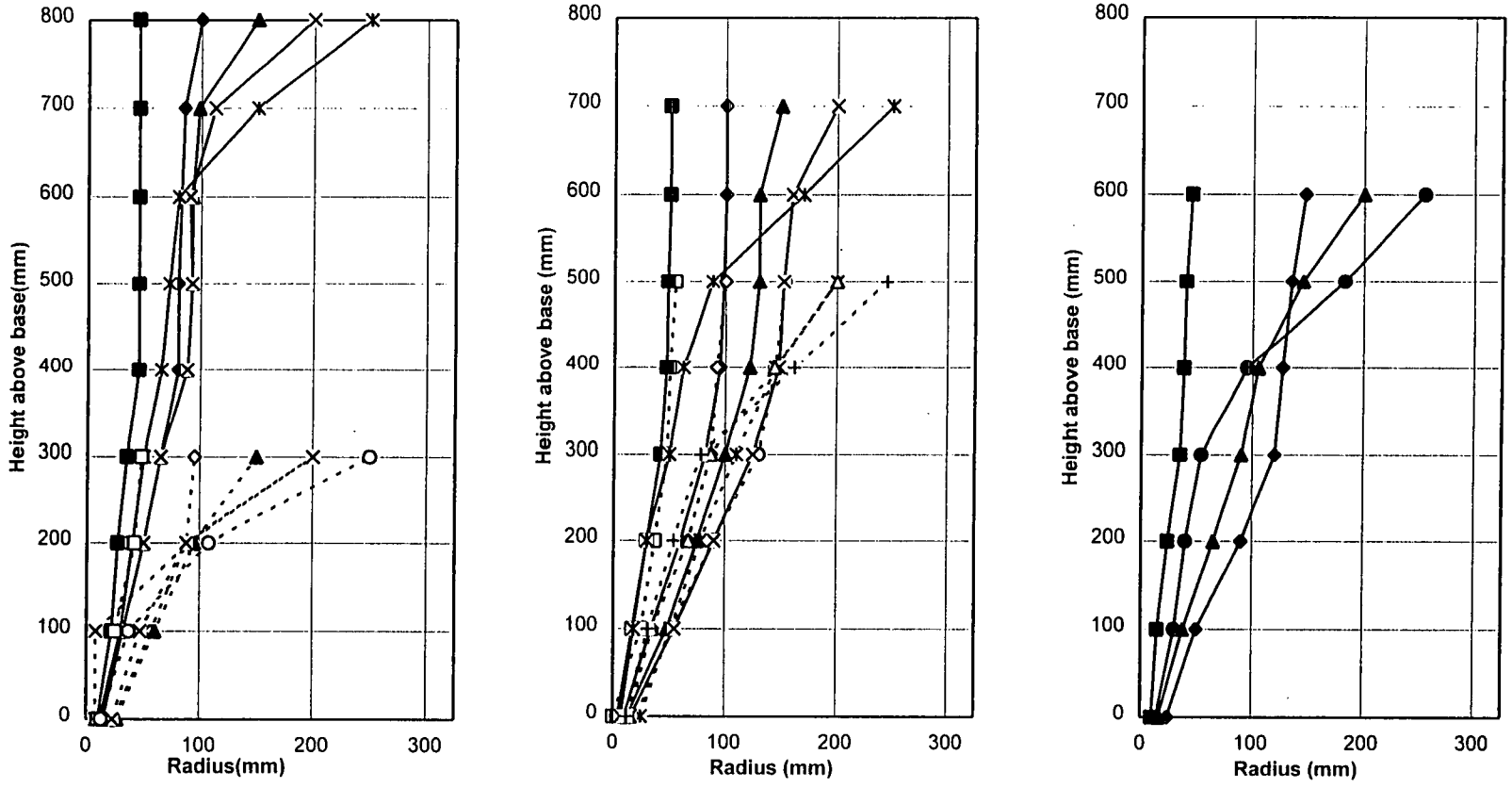

a) markers seeded at levels 3,8 b) markers seeded at levels 5.7 c) markers seeded at level 6

Fig.3.20: Trajectory paths of particles under concentric discharge

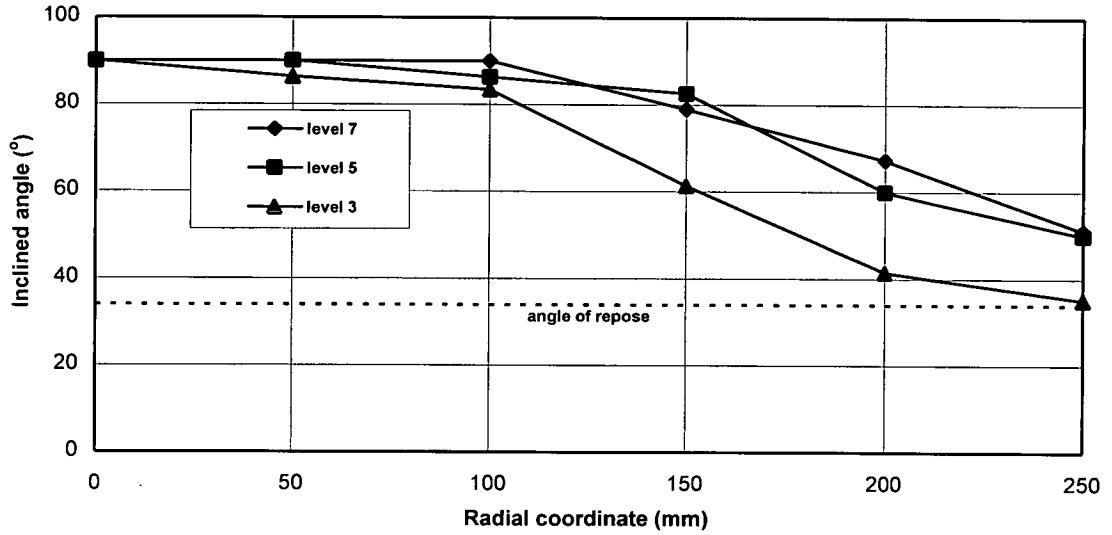

Fig. 3.21: Variation of inclined angle of trajectory path with radial coordinate under concentric discharge

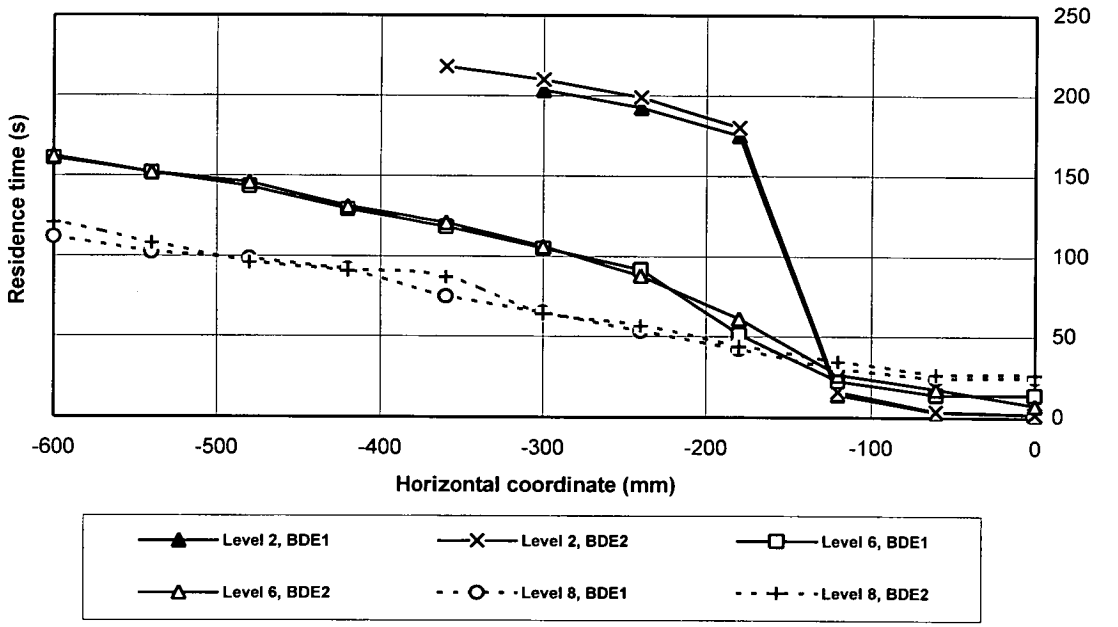

Fig. 3.22: Comparisons of residence time distributions under eccentric discharge

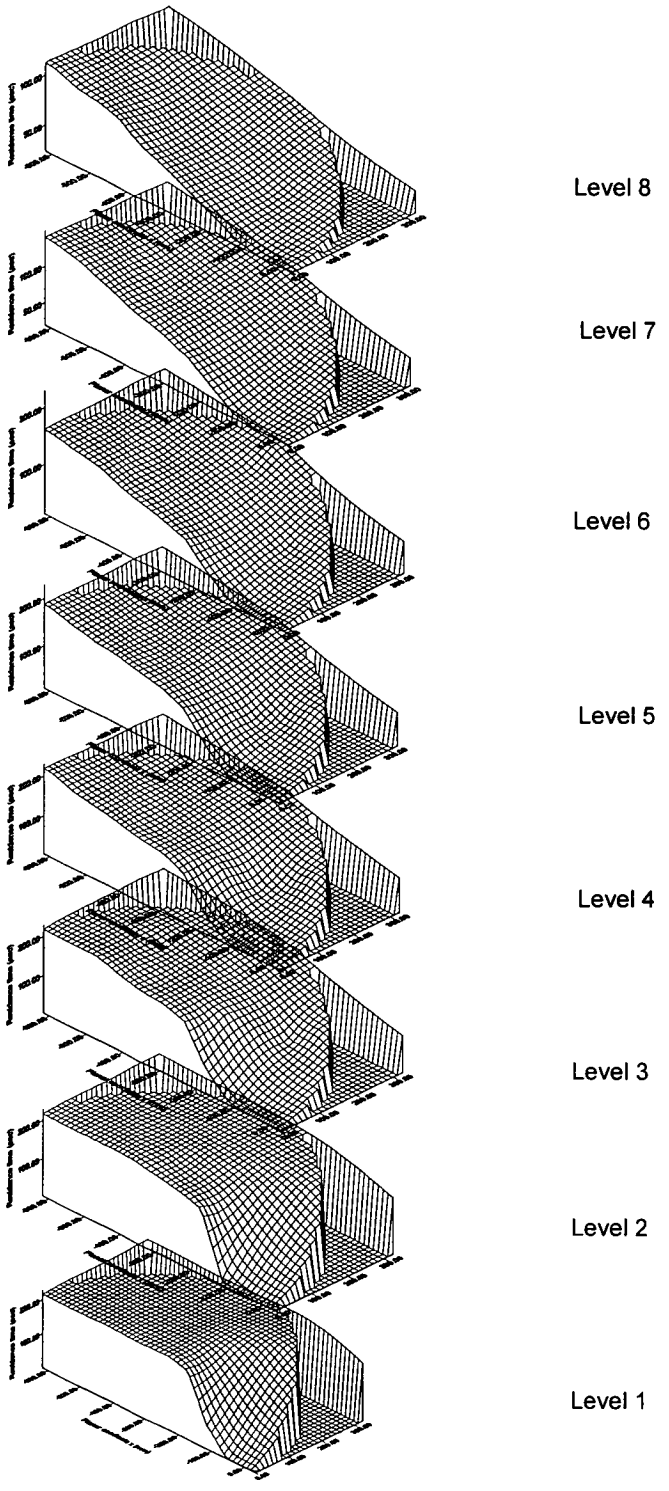

Fig. 3.23: Residence time distributions at different levels under eccentric discharge

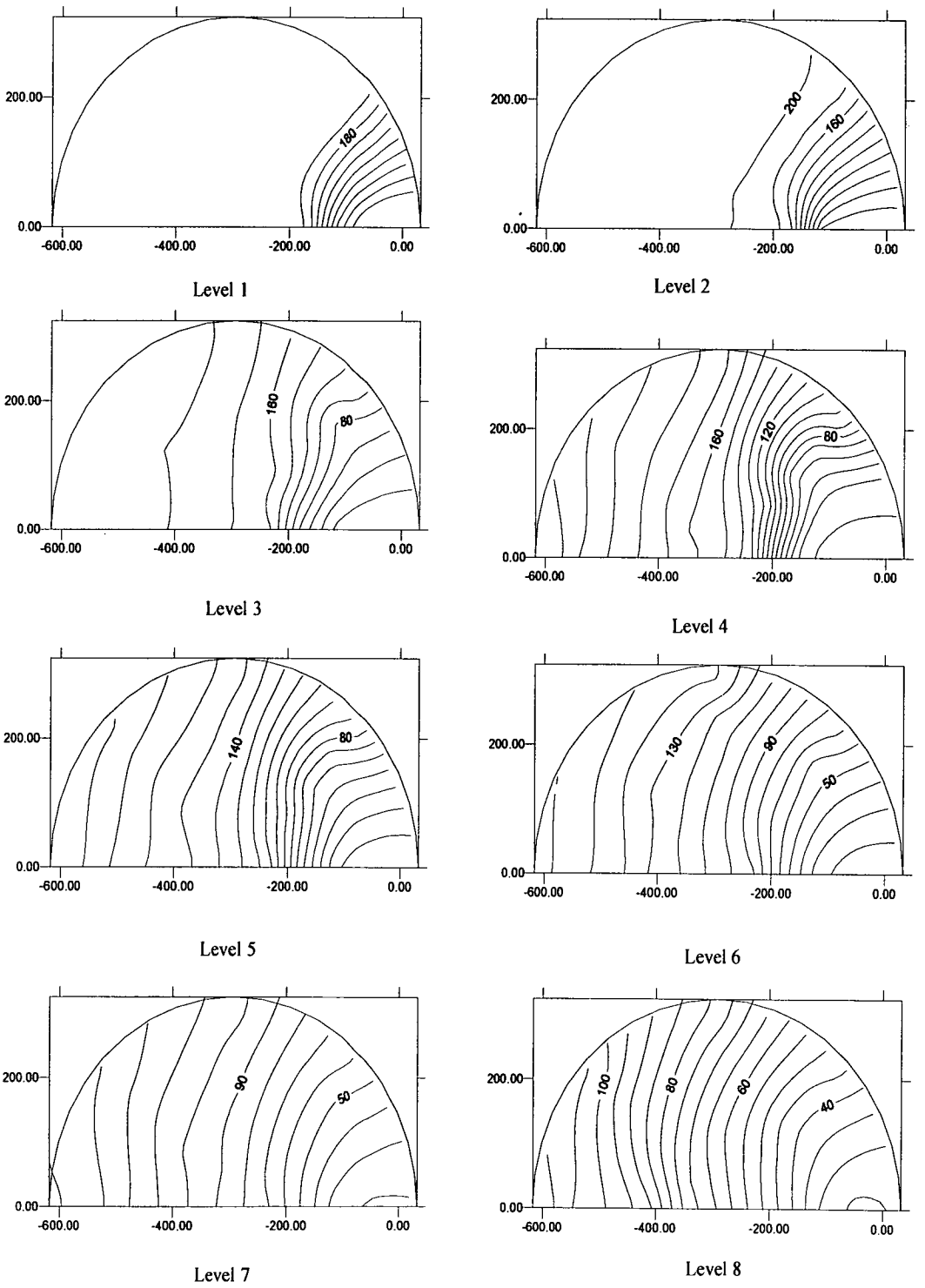

Fig 3.24: Residence times at different levels under eccentric discharge

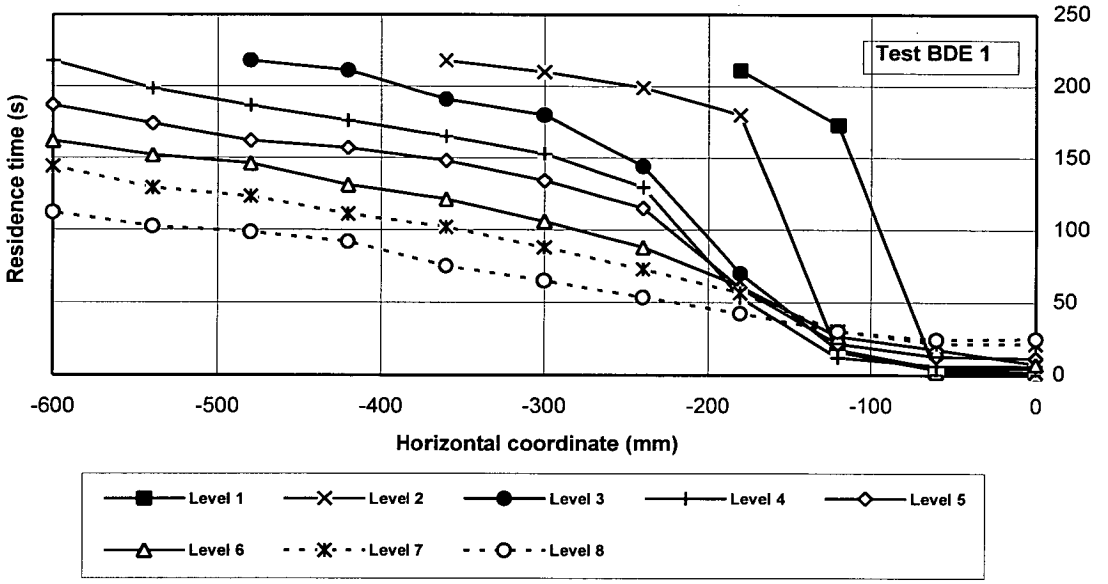

Fig. 3.25: Residence time distributions at the front wall under eccentric discharge

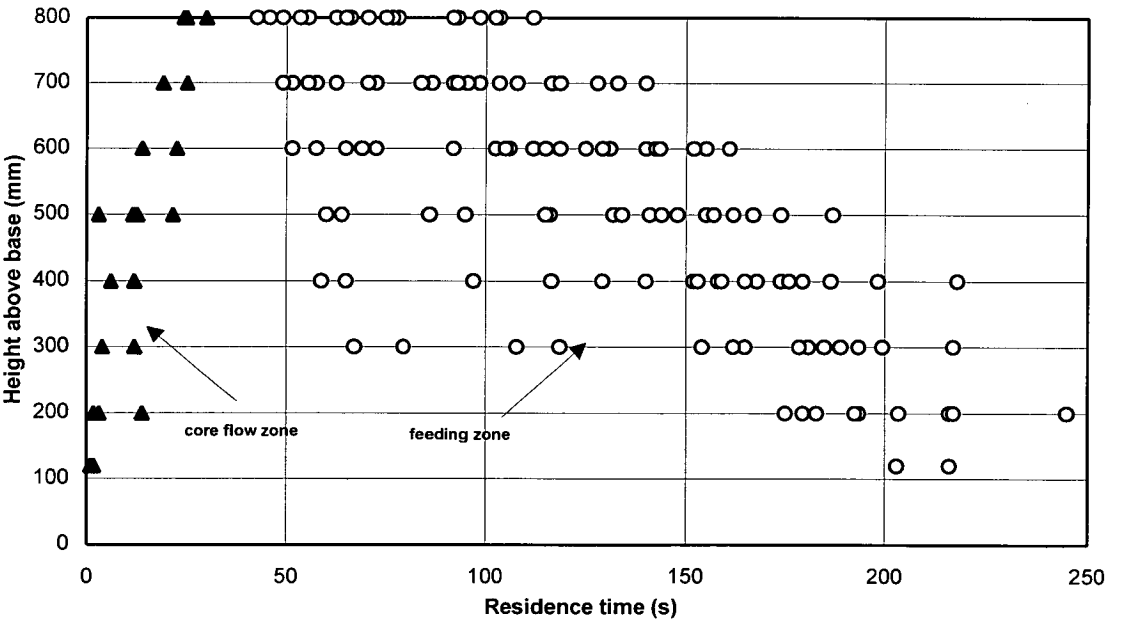

Fig. 3.26: Variation of residence time with vertical coordinate under eccentric discharge

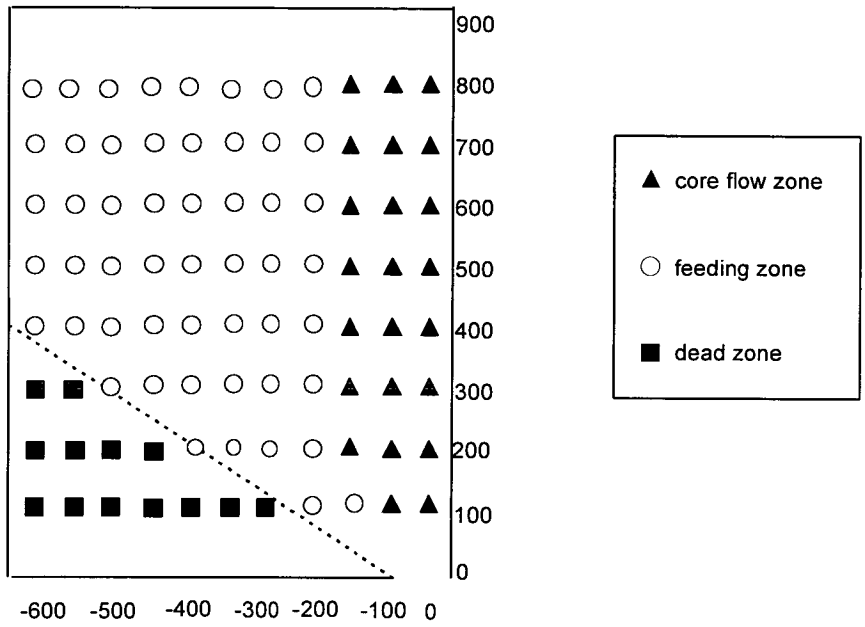

Fig. 3.27: Tracers in different flow zones under eccentric discharge

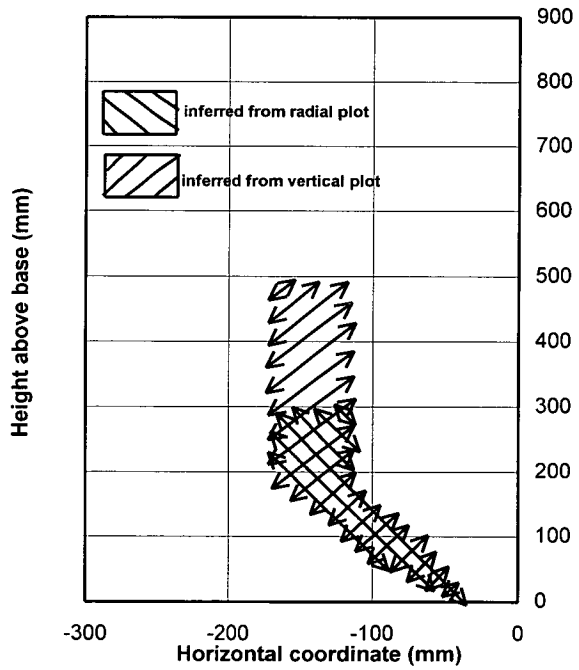

Fig. 3.28: Inferred FCBs from different analysis methods under eccentric discharge

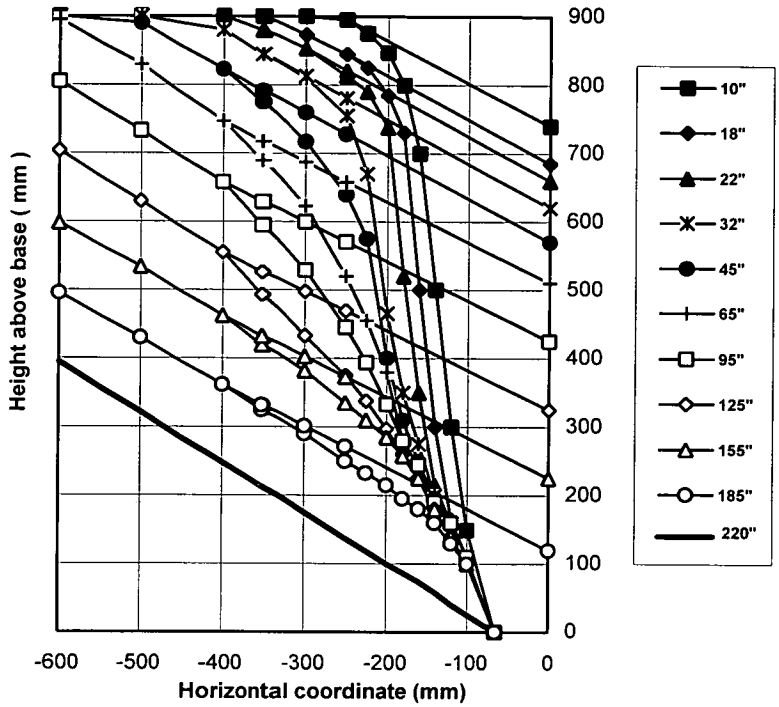

Fig.3.29: Measured FCBs and top surface profiles at front wall during eccentric discharge

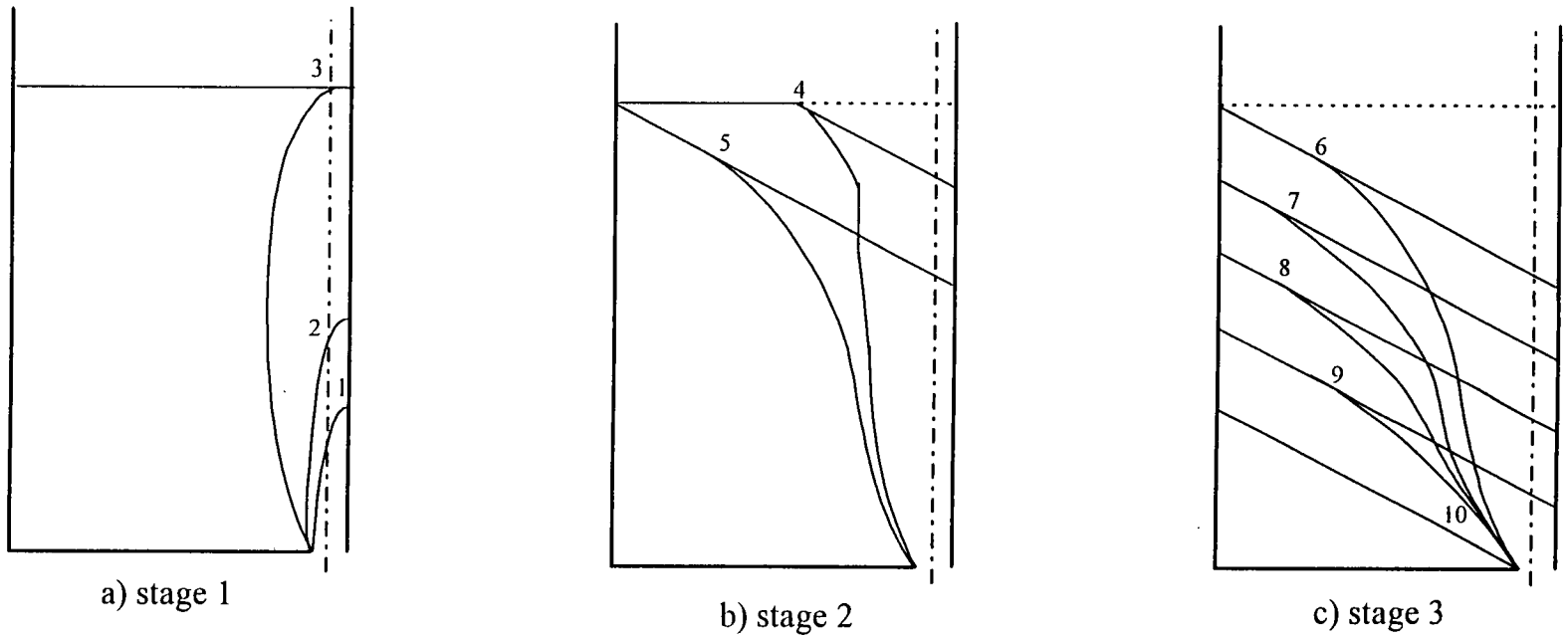

Fig. 3.30: Typical stages involved in development of FCB under eccentric discharge

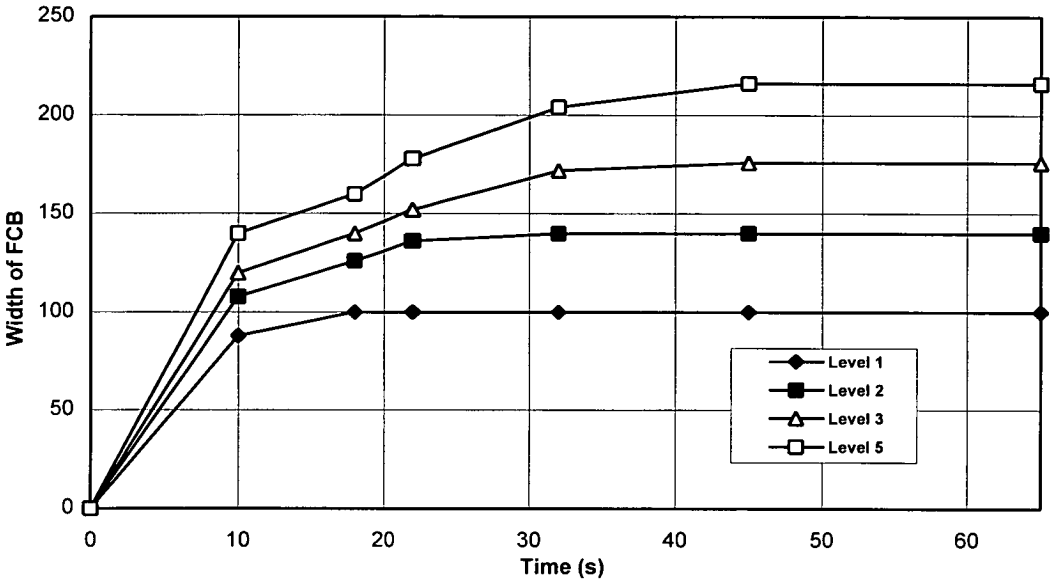

Fig. 3.31: Development of FCB at front wall with time under eccentric discharge

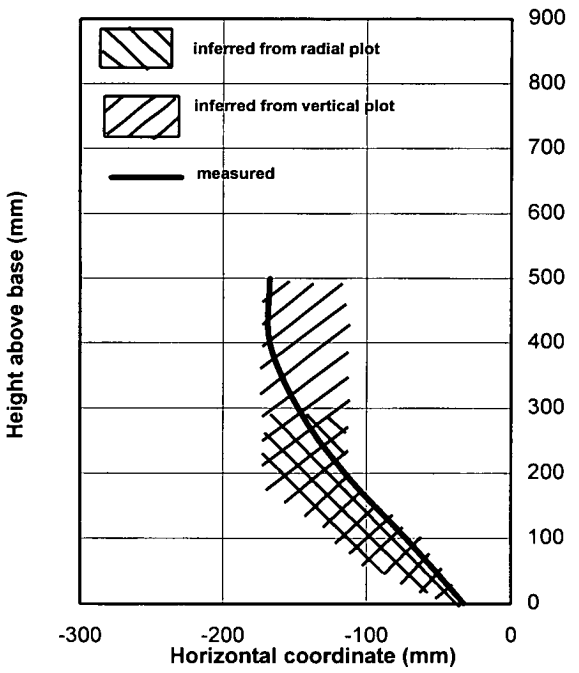

Fig. 3.32: Comparisons between deduced and measured fully developed FCB under eccentric discharge

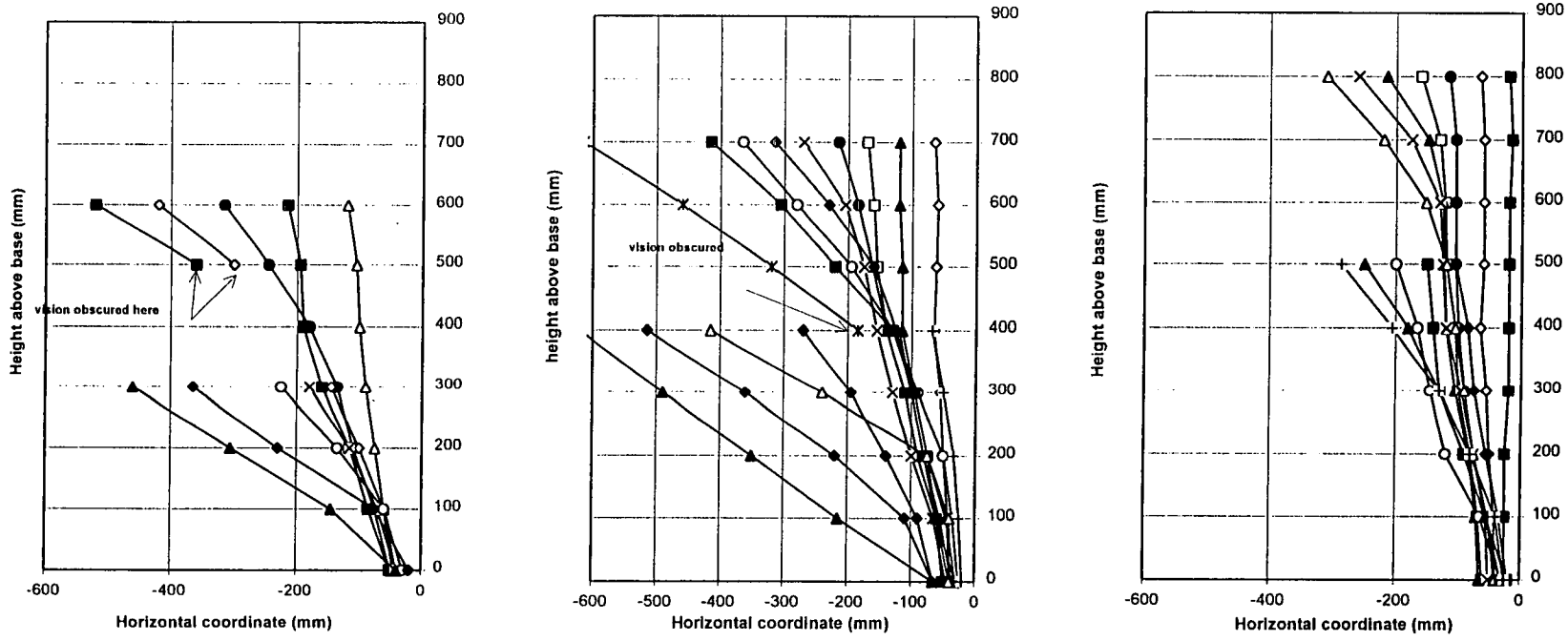

a) markers seeded at levels 3,6 b) markers seeded at levels 4, 7 c) markers seeded at levels 5, 8

Fig. 3.33: Trajectory paths of particles under eccentric discharge

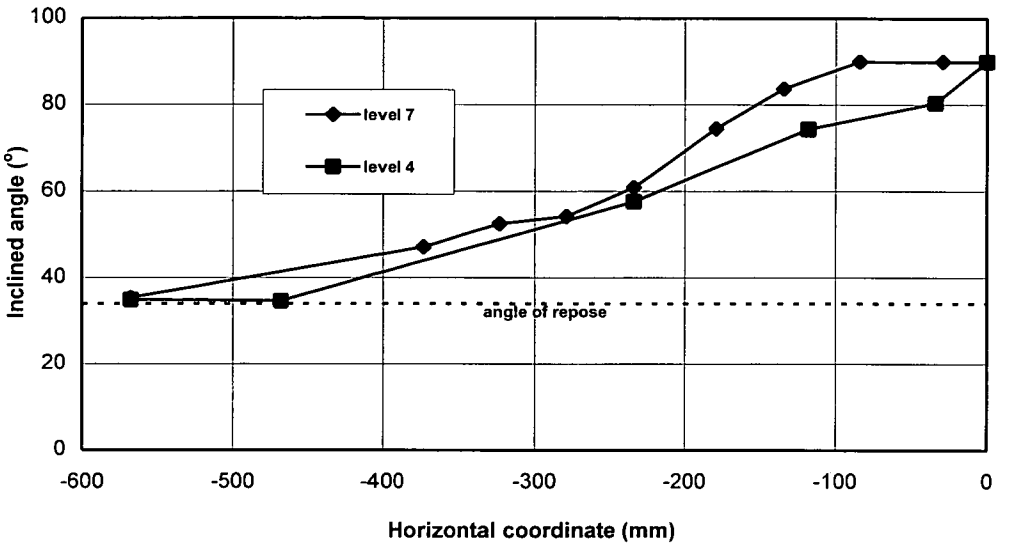

Fig. 34: Variation of inclined angle of trajectory path with horizontal coordinate under eccentric discharge

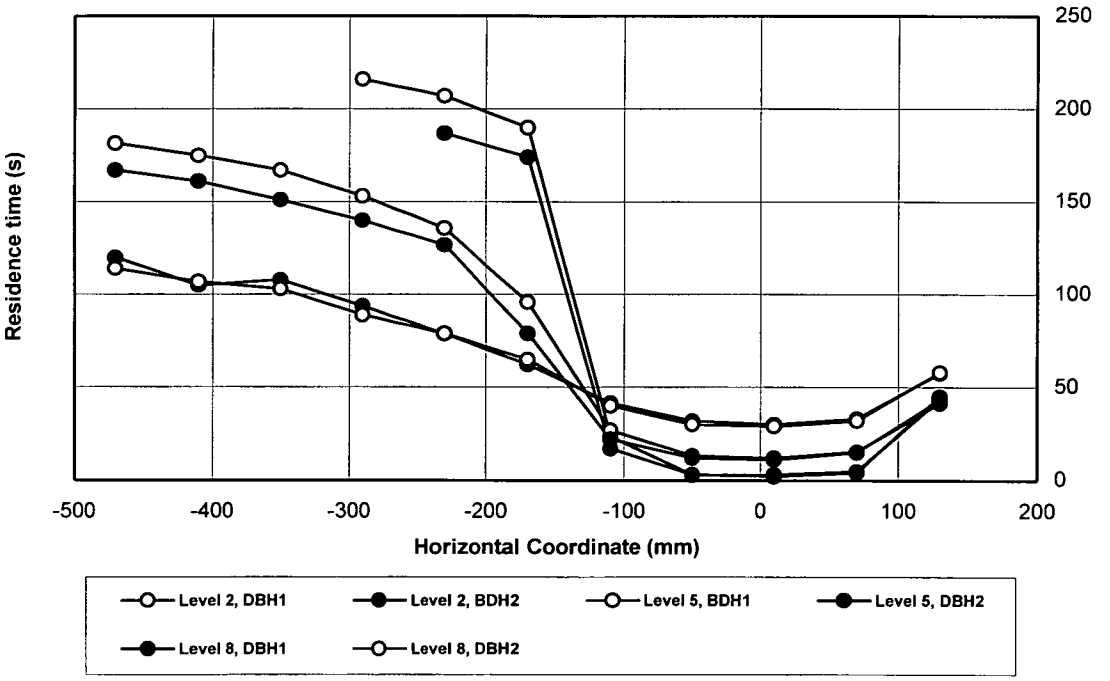

Fig. 3.35: Comparisons of residence time distributions at front wall under half eccentric discharge

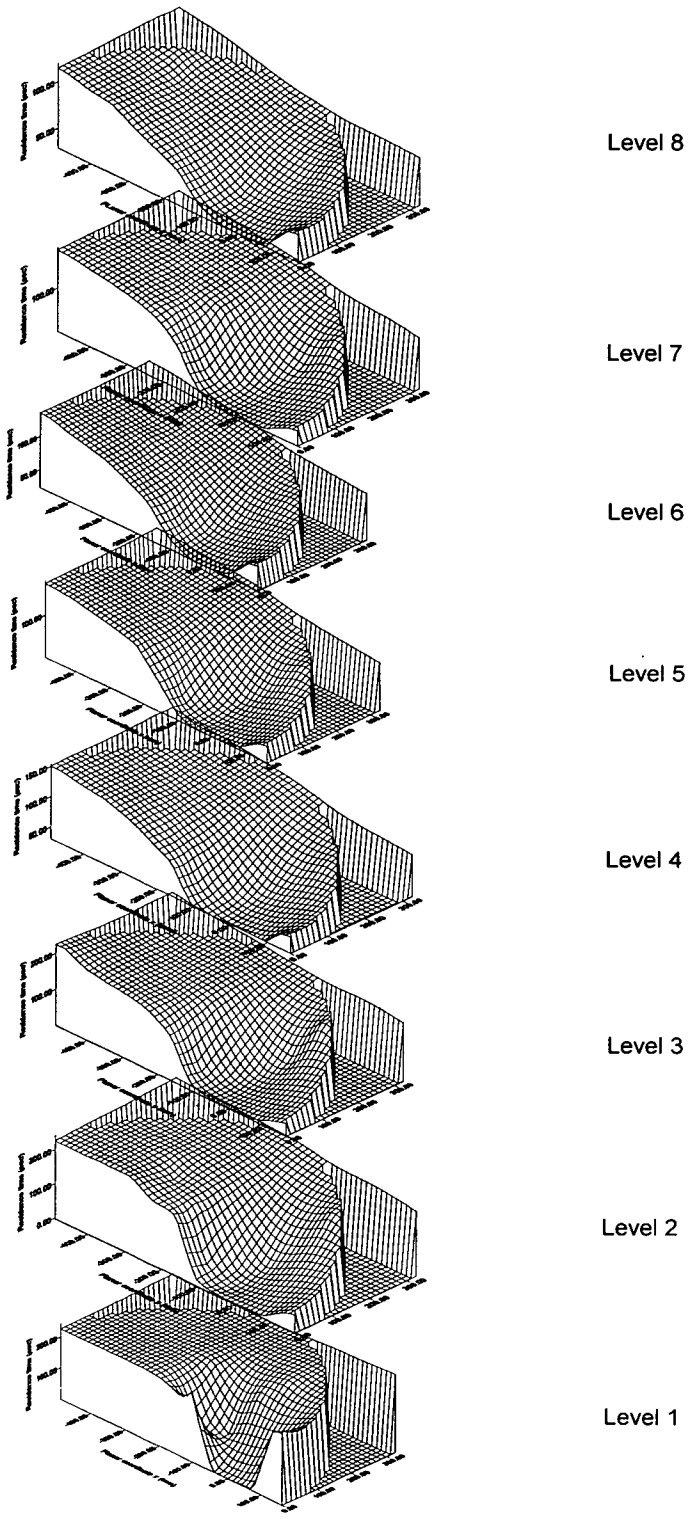

Fig. 3.36: Residence time distributions at different levels under half eccentric discharge

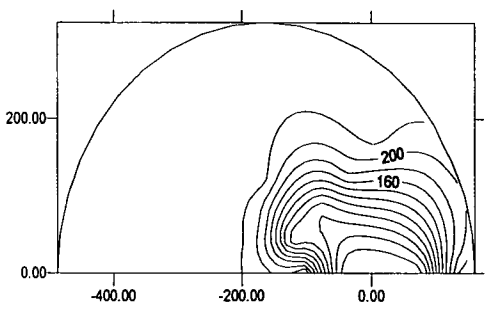

Level 1

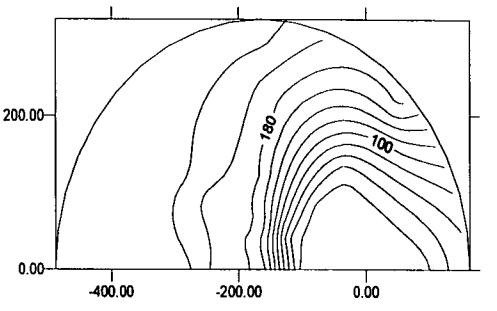

Level 2

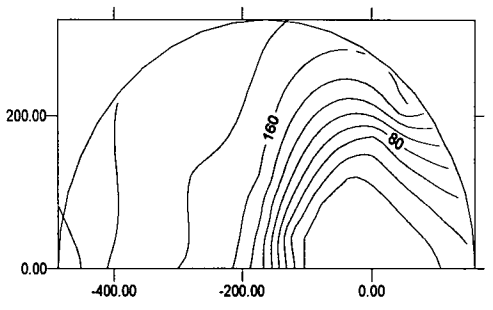

Level 3

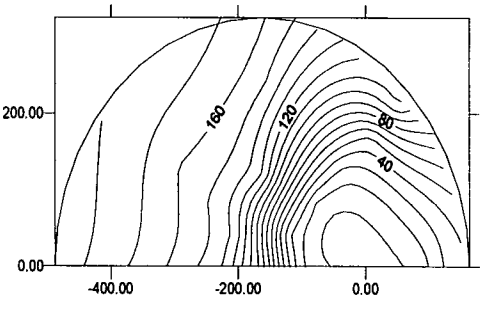

Level 4

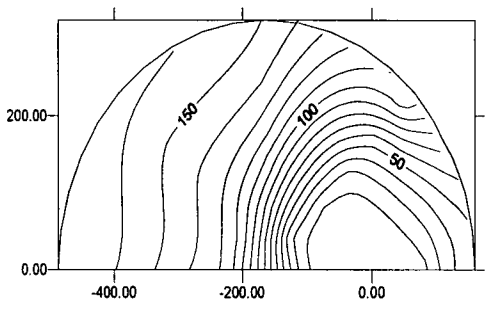

Level 5

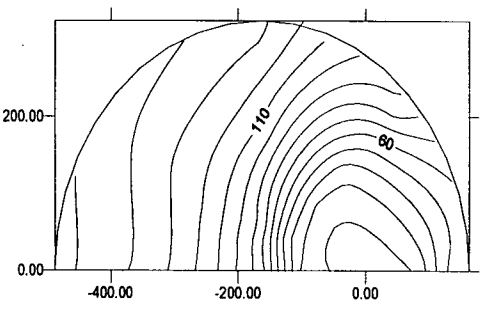

Level 6

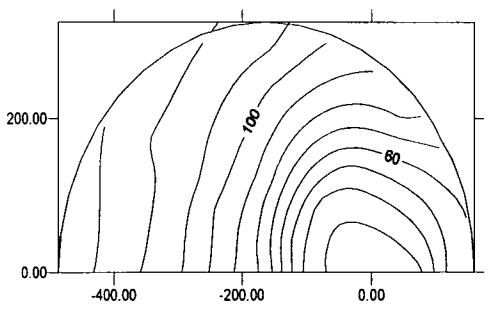

Level 7

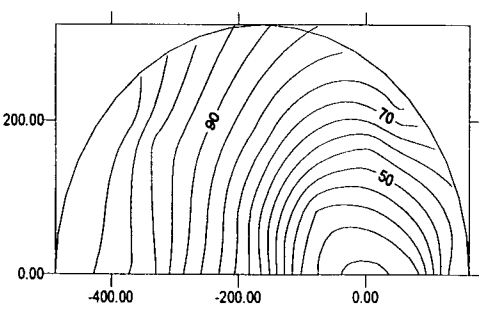

Level 8

Fig 3.37: Residence times at different levels under half eccentric discharge

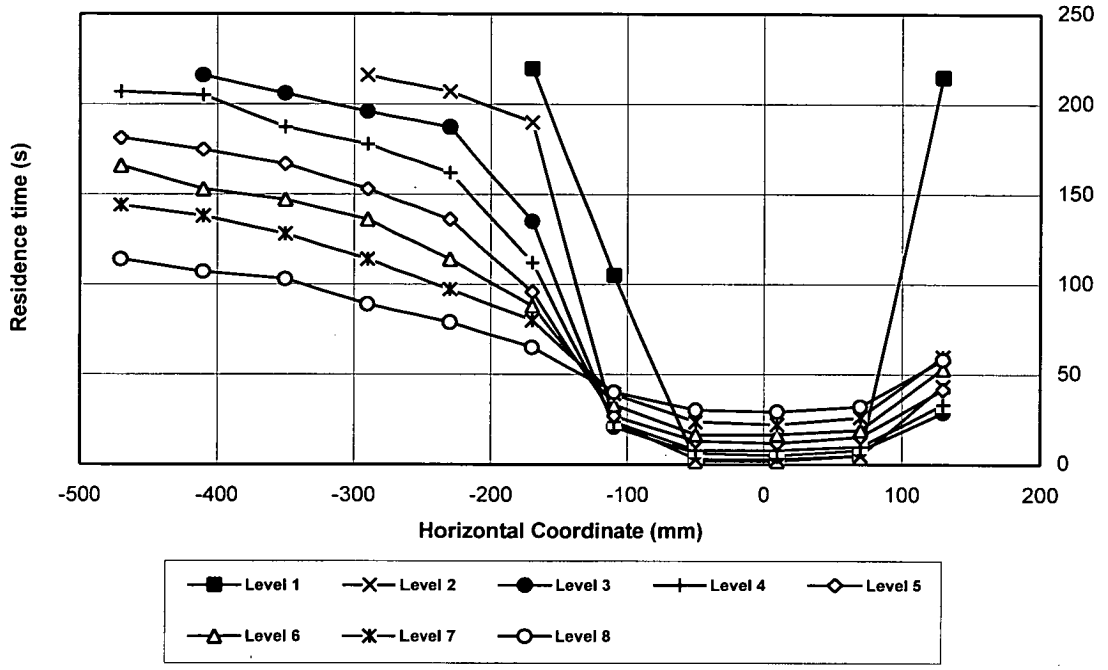

Fig. 3.38: Residence time distributions at the front wall under half eccentric discharge

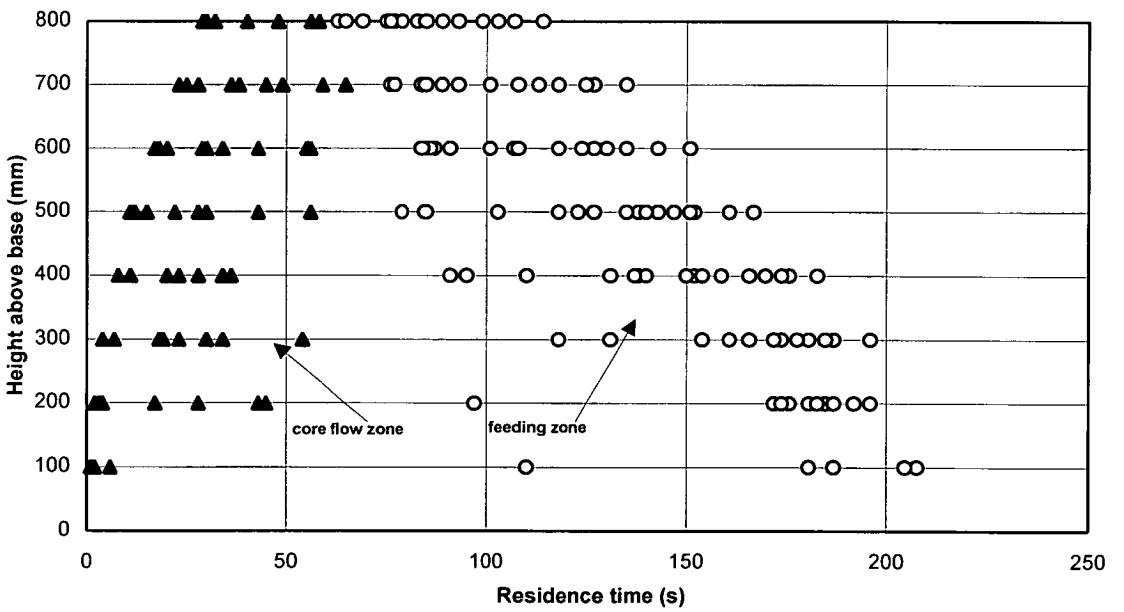

Fig. 3.39: Variation of residence time with vertical coordinate under half eccentric discharge

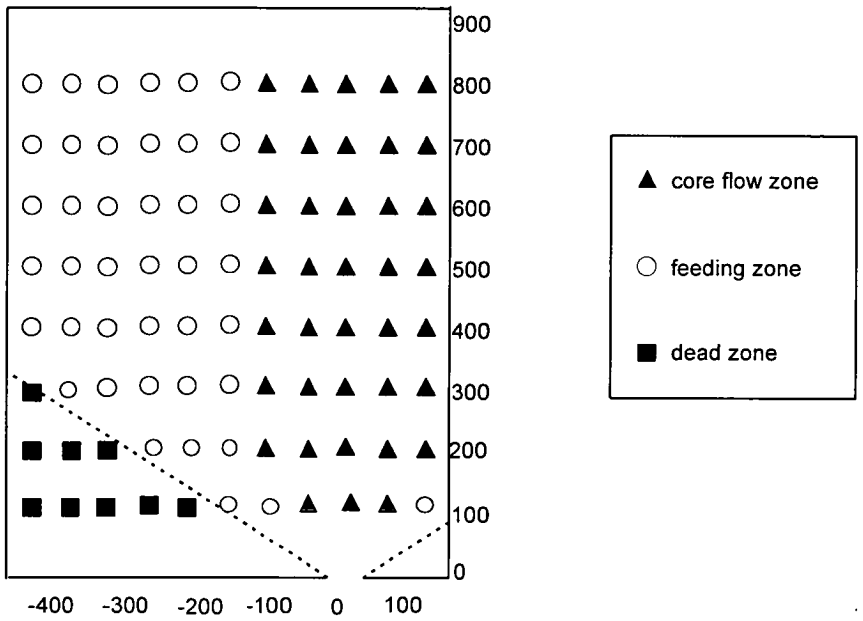

Fig. 3.40: Tracers in different flow zones under half eccentric discharge

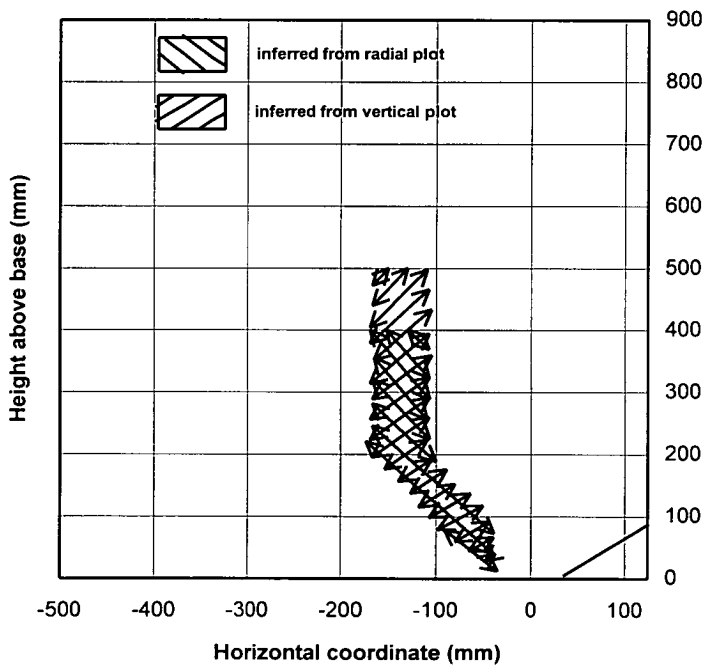

Fig. 3.41: Inferred FCBs from different analysis methods under half eccentric discharge

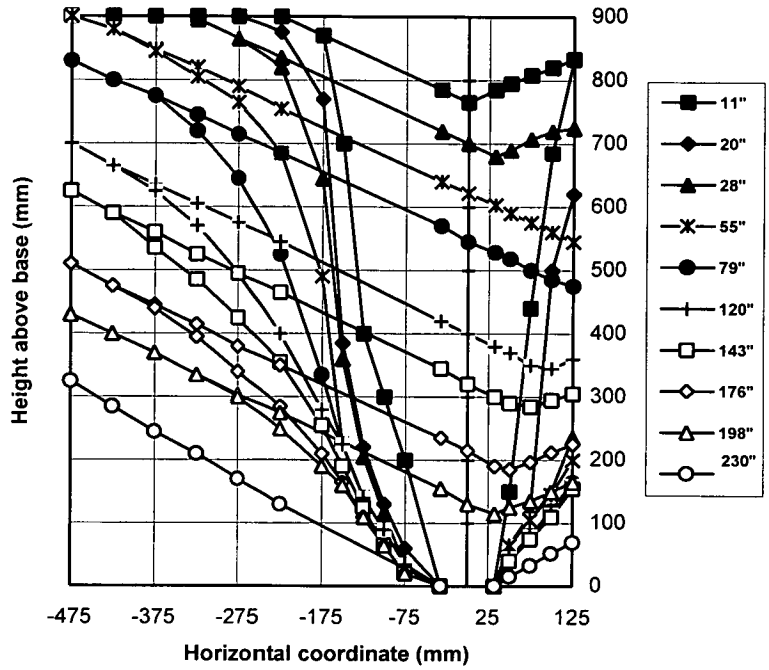

Fig. 3.42: Measured FCBs and top surface profiles at front wall during half eccentric discharge

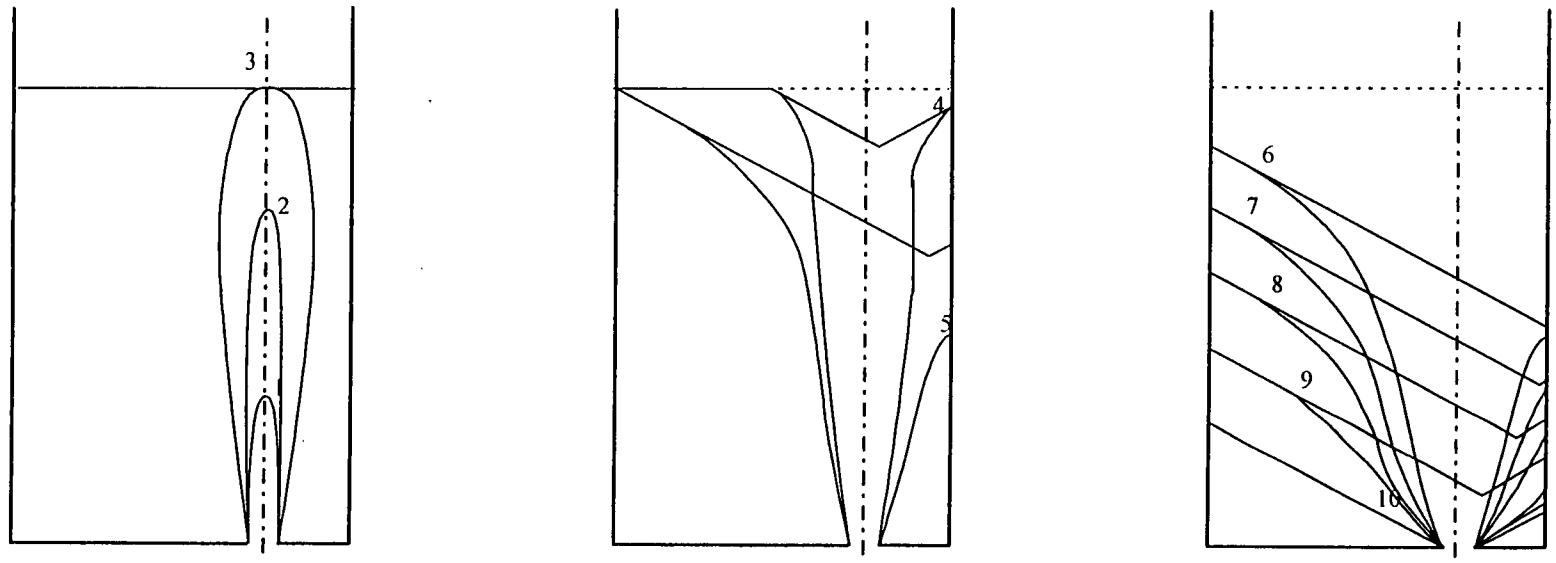

Fig. 3.43: Typical stages involved in development of FCB under half eccentric discharge

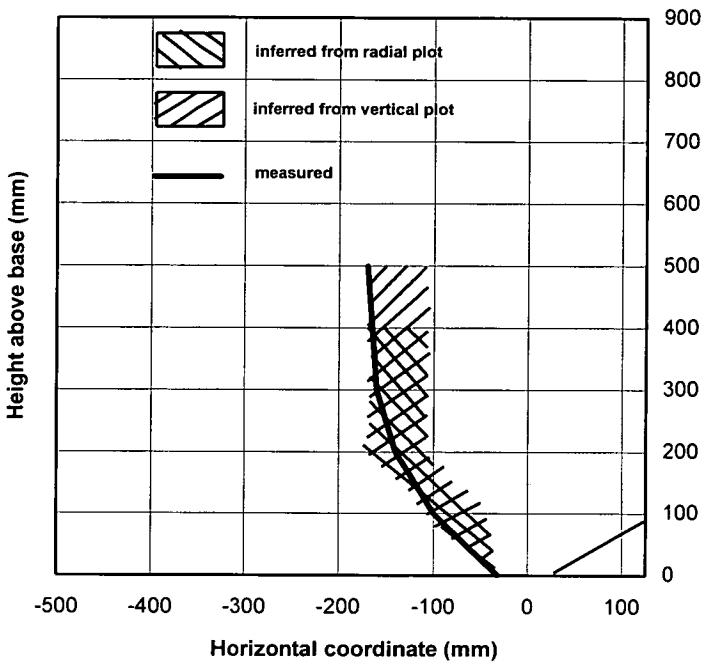

Fig. 3.44: Comparisons between deduced and measured fully developed FCB under half eccentric discharge

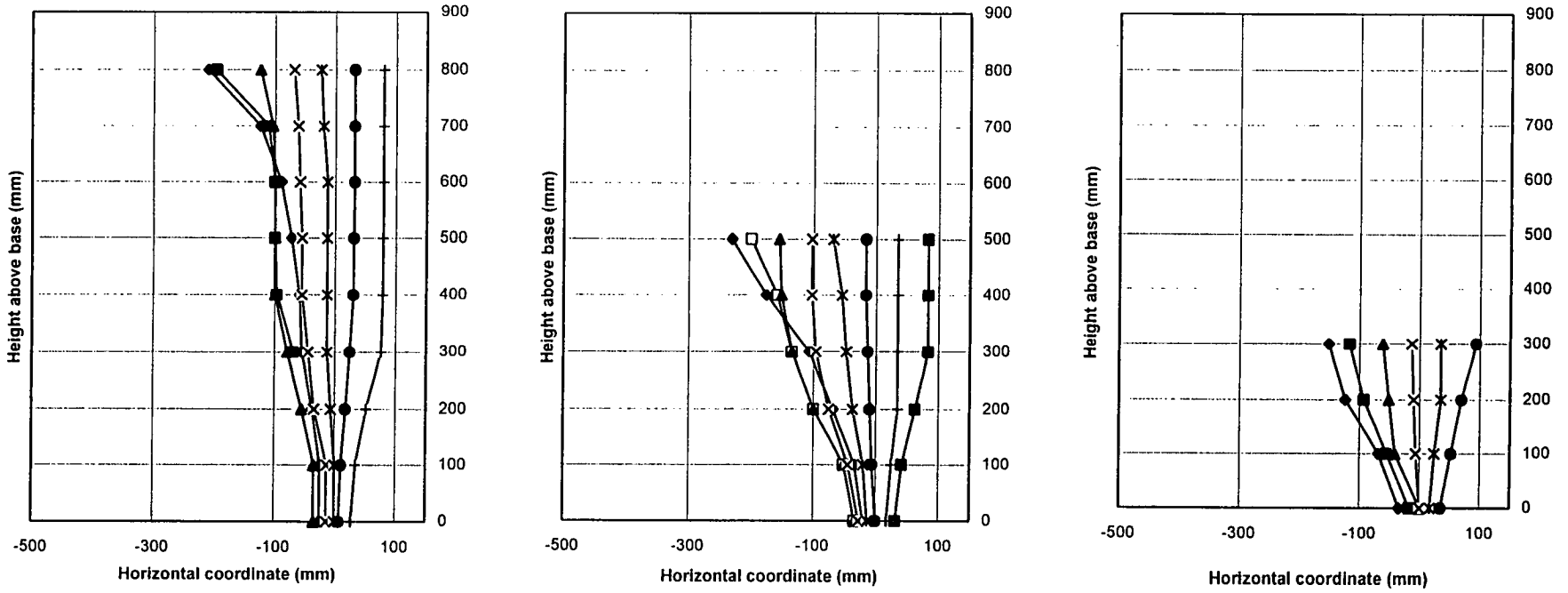

a) markers seeded at level 8

b) markers seeded at level 5

c) markers seeded at level 3

Fig. 3.45: Trajectory paths of particles under half eccentric discharge

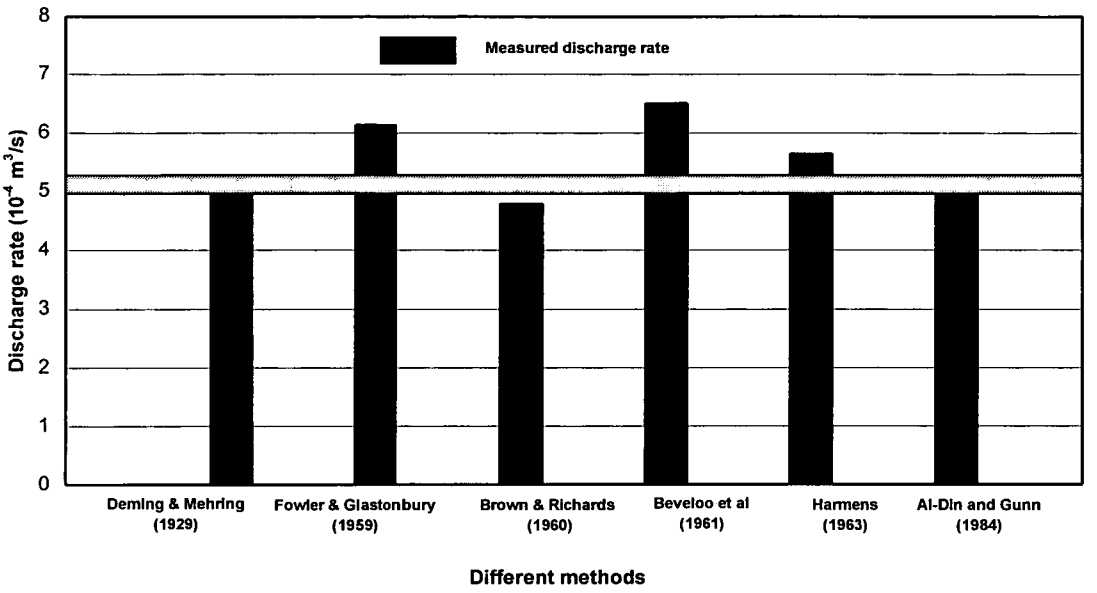

Fig. 3.46: Comparison between measured and predicted discharge rate

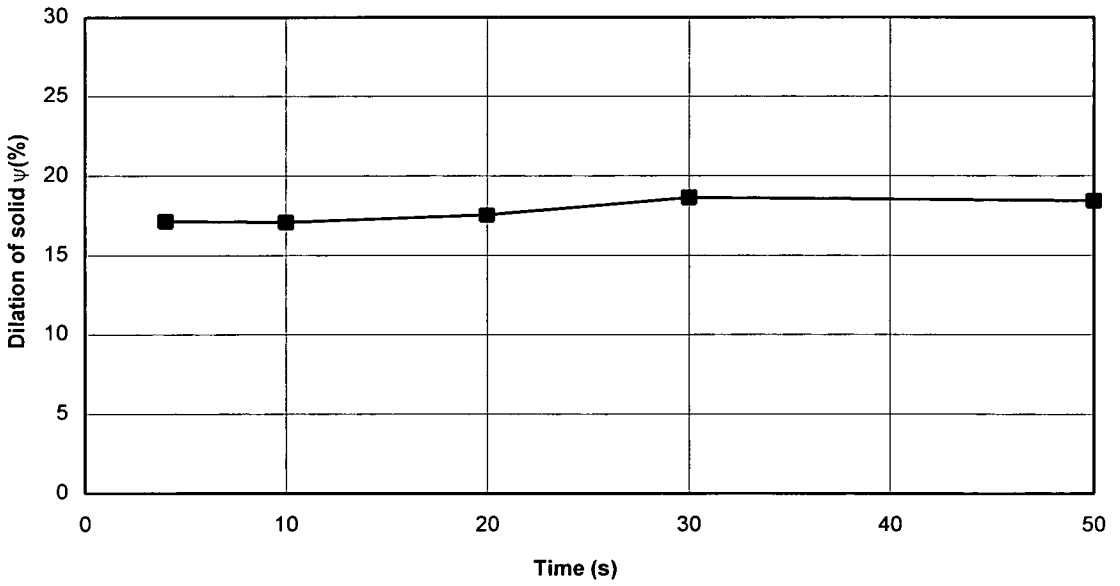

Fig. 3.47: Variation of solid dilation with time

CHAPTER 4

A FULL SCALE SILO EXPERIMENT AND INITIAL ANALYSIS

4.1 Introduction

It is widely recognised that the flow pattern of a bulk solid can have a considerable influence on the silo wall loads. Many experiments have been undertaken to measure the complex pattern of solids flow during silo discharge (e.g. Nielsen and Askegaard, 1977; Nedderman and Tuzun, 1979; Hartlen *et al*, 1984; Nielsen, 1984; Runesson and Nilsson, 1986; Watson, 1993; Rotter *et al*, 1995). Some of these studies have shown that flow patterns observed in model silos are not fully representative of those in full scale silos (e.g. Nielsen and Askegaard, 1977; Nielsen, 1984). It is therefore very important to conduct full scale silo experiments to measure the flow patterns and the resulting wall pressures.

Due to the complications and high expenses, silo experiments conducted at full scale are very rare. The experiment described in this chapter is one from a series of experiments conducted in a well instrumented full scale silo which was utilised to measure the solids flow patterns and silo wall loads for different materials under different discharge conditions. The technique of residence time measurement was used in these experiments to investigate the flow behaviour of solids.

In this chapter, a very brief description of the test silo is given, and the measurements of solids flow from one experiment (Test PCB) under concentric discharge are processed and presented. Full details of the experiments can be found elsewhere

(Rotter *et al*, 1993, 1995). The flow pattern and the approximate location of the flow channel boundary (FCB) are identified from the analysis of the residence time data. The residence time data will also be used in Chapter 6 for the comparison with those predicted by a simple engineering model for solid flow presented in Chapter 5.

4.2 Experimental set-up

The full scale experiments were conducted by the Silos Research Group at the University of Edinburgh. Measurements were made of both the silo wall pressures and the solids flow pattern for different bulk solids under different discharge conditions (Rotter *et al*, 1993, 1995). Only a brief description is given here.

4.2.1 Test silo

The test silo is a cylindrical flat-bottomed steel structure of 4.2 m diameter with a 9.5 m high by 3 mm thick barrel section. The silo floor was 2.4 m above ground level. Five ring stiffeners were positioned on the barrel. The aspect ratio, which is an important factor in the study of flow patterns, is 2.26. Figure 4.1 shows the test silo on site.

The silo floor was 12 mm thick and accommodated three outlets, two of which were eccentrically positioned and the third outlet was concentric. All the outlets were circular with a diameter of 480 mm, and they were positioned at 850 mm centres with the fully eccentric outlet centred at 400 mm from the silo wall. The arrangement of three outlets in the silo floor is shown in Fig. 4.2. With these outlets, the experiments can be conducted under concentric, half eccentric and fully eccentric discharge conditions.

4.2.2 Filling and discharging

Many investigators (e.g. Sudgen, 1980; Moriyama *et al*, 1983; Hartlen *et al*, 1984; Munch-Anderson and Nielsen, 1990; Zhong *et al*, 1996) have reported that the filling manner has a strong influence on the packing of the bulk solid which in turn produces different flow patterns. Two filling methods are commonly used: distributed filling (uniform raining down on the entire area of the silo cross-section) and concentric filling (filling through a concentric chute which produces denser material in the centre).

In this experiment, the silo was filled via a small concentric tun-dish on the silo roof, so the filling was close to concentric filling. The chosen outlet was kept open during filling and the discharge rate was controlled by the feeder beneath the outlets.

4.2.3 Seeding template and markers

The measurements of residence time were made using radio tags as markers. Every radio tag consists of a miniature radio receiver and transmitter with a unique code so that the detection system can identify it. These radio tags were encapsulated in tennis balls which were filled with a mixture of iron fines and sand to achieve the same overall bulk density as that of the test material. During discharge the tags passed through the outlet and were detected by the aerial detector located there.

Great care was taken to ensure that each marker was placed precisely at the intended location using a specially designed wooden seeding template (Fig. 4.3). The template had eight spokes, each with four seeding holes in it. There was also a central insert with four holes. The holes were colour coded to correspond to their radii from the central axis of the silo.

4.2.4 Top surface measurement

During discharge, the top surface profile was measured by taking depth measurements at eight positions from the roof of the silo. The locations of these positions are shown in Fig. 4.4. These measurements were used to determine the shape of the top surface profile and the remaining volume of solid at each instant. The readings were made at about ten minute intervals during silo emptying.

4.3 Physical properties of test material

In Test PCB analysed here, iron ore pellets were used as the bulk solid. Many characterisation tests were performed on the iron ore pellets. Those relevant to the work presented in this thesis are given below. Further details can be found in Rotter *et al* (1995).

4.3.1 Particle size and grading

To determine the particle size of the pellets, 50 virgin iron ore pellets were measured. The pellets had a fairly uniform size with a mean of 12.9 mm and a coefficient of variation of 13.0%. The statistical measures on the particle diameter are given in Table 4.1.

4.3.2 Bulk density

The virgin samples were found to have a mean loose bulk density of 2320 kg/m^3 and a mean maximum vibrated bulk density of 2510 kg/m^3. The specific gravity was around 4.28.

4.3.3 Internal friction and wall friction

Standard Jenike shear tests were performed on a sample of fines. The effective angle of internal friction was found to be 52^{o}. The wall friction between the iron ore pellets and mild steel plate is 26.2^{o}.

4.4 Experiment

The placement of markers was a key issue in the experiment for solids flow investigation. This process was implemented as follows: once the silo was filled to a certain height, the conical pile of solid at the top was raked flat. The seeding template was then lowered down to rest on the surface of the solid. The markers, previously labelled with the level of the seeding layer, a spoke letter and a colour, were placed through the holes in the template. This procedure ensured that each marker was placed precisely at the intended location on the surface. After the seeding at one level, the template was raised and filling re-commenced. The seeding procedure was repeated at several levels until the silo was full.

In this concentric discharge experiment (Test PCB), the silo was filled to the depth of 6.35 m with the iron ore pellets. A total of 7 levels were seeded with 252 radio markers (Fig. 4.5). During the experiment, 163 out of the 252 markers were detected. Some markers were not detected on exit due to the consequence of two markers exiting simultaneously, and some still remained in the silo at the end of discharge.

4.5 Results and analysis

The main observations gathered from the experiment concerning the flow pattern of solids are: the top surface measurements at different stages and the residence times of

markers. The initial analyses of the results are presented in this chapter. Further analyses will be presented in Chapter 6.

4.5.1 Top surface observations

Figure 4.6 shows the variation of the mean height of the solids surface with time at the different radii during the whole discharge process. In the first half an hour or so, the readings at outer edges (r = 1.3 m and r = 1.9 m) remained fairly constant while towards the centre of the silo, the readings changed considerably. This indicates the gradual formation of an inverted cone at the top surface emanating from the centre. After this stage, all the readings changed at nearly the same rate until the discharge was complete, which indicates that the shape of the inverted cone did not change significantly once it was fully developed.

The development of the top surface profile can be seen more clearly in Fig. 4.7 which shows the mean cross-section of the advancing top surface profile during discharge. The angle of inclination at the top surface became fairly constant less than an hour into discharge. This angle is sometimes termed the angle of repose although the angle of repose is normally defined as the slope angle of a conical pile on a horizontal surface. For Test PCB, the stabilised angle of inclination at the top surface was around 32^{o} which is slightly less than the inclined angle of 34.7^{o} at the end of discharge.

The remaining volume of solid was computed from the depth measurements. The variation of the remaining volume with time is shown in Fig. 4.8. It can be seen that the volumetric discharge rate was not kept constant during discharge. In the first 2.5 hrs, the discharge took place at a constant rate of about 12.0 m^3/hr, and in the last hour, the discharge rate was increased rapidly to around 40.0 m^3/hr.

4.5.2 Residence time observations

The residence time observations for Test PCB are given in Table 4.2. These observations were made to study the flow pattern of the pellets. This section describes simple interpretations of the residence time observations to deduce the symmetry of the flow and the approximate location of the FCB.

4.5.2.1 Axisymmetry of flow

If the flow pattern is exactly axisymmetric, the residence times of the markers at the same height and radius should be identical. To test the precision of this axisymmetry, the residence time observations at each ring of markers (Fig. 4.3) at each level are assumed to be a stochastic distribution. The mean value and the coefficient of variation (CoV) of these residence times were calculated and the results are given in Table 4.3.

Apart from a few exceptions which have a special significance and will be explained in Section 4.5.2.3, the coefficient of variation of the residence times is less than 5%. showing that the above proposition of a predominantly axisymmetric flow is basically valid in Test PCB.

4.5.2.2 Flow mode of pellets

Since the flow is fairly axisymmetric, the residence time distributions in the silo can be reasonably well represented by the mean residence time at each ring location. Figure 4.9 shows the variations of the mean residence times with the radius at different levels. The markers within small radii had relatively small residence times indicating that these markers were the first to exit the silo and were thus in the core flow zone. Along the central axis of the silo, the residence time progressively

increased with the vertical coordinate. The situation was reversed for the markers near the silo walls: the markers at higher levels have lower residence times. This pattern of residence time distribution reveals that the flow was an internal funnel flow.

The mode of the solid flow can be identified by the above simple interpretation, but the chief challenge is to identify the flow channel boundary (FCB). The approximate location of the FCB will be identified in the following section by analysing the residence time distributions and using the statistical measures of the residence time. A more careful and accurate analysis of the residence time data together with the top surface measurements will be given in Chapter 6.

4.5.2.3 Flow channel boundary

The techniques which are utilised to infer the fully developed FCB from residence times have been fully described in Chapter 3. In this chapter these techniques are directly employed to detect the FCB in the full scale silo experiment.

Figure 4.9 shows the mean residence time distributions at different levels. At lower levels in a pipe flow, the solids in the core flow zone have much smaller residence times than those in the feeding zone, so a large difference in residence time between two adjacent markers exists in the region of the FCB. The largest difference in residence time between two adjacent markers at Level 1 occurred between Ring 2 and Ring 3 (3.28 hr, 93.7% of total discharge time). At Level 2 and 3, the largest difference occurred between Ring 3 and Ring 4 at 2.22 hr and 1.93 hr respectively. These huge differences in residence time indicate that the FCB lies between Ring 2 and Ring 3 at Level 1 and between Ring 3 and Ring 4 at Levels 2 and 3. At higher levels, there are no clear sudden changes between adjacent markers, so this deduction does not work.

The coefficient of variation (CoV) for each ring of markers at each level is plotted in Fig. 4.10. It can be seen that the peaks of CoV are located at r = 0.921 m for Levels 4, 5 and 6 and there is no obvious peak at Level 7. These peaks of CoV show the approximate location of the FCB at these levels. Considering the fact that in general the width of the FCB at its upper part should not be less than that at its lower part, the FCB at Levels 5 and 6 is therefore thought to locate beyond the radius of the markers with the maximum CoV. Based on the above analysis, the FCB is deduced and shown in Fig. 4.11.

Over the last two years, considerable efforts have been spent in improving the interpretation of the residence time observations in the full scale tests. Further details can be found in Chen *et al* (1997).

4.6 Concluding remarks

The analyses presented above shows that during discharge, the top surface profile gradually took the shape of an inverted cone. The inverted cone form expanded and moved progressively towards the bottom of the silo with a stabilised angle of inclination of 32°. This process is well supported by the visual observations during the experiment.

The statistical analysis shows that the flow was highly axisymmetric in Test PCB (CoV=5%), with the exception of markers which were close to the FCB.

The simple interpretations of the residence time observations are quite useful in determining the flow pattern and the approximate location of the FCB. For Test PCB, an internal funnel flow with a wide channel occurred during the concentric discharge.

Table 4.1: Iron ore pellets diameters

Diameter	Largest	Smallest	Random	Mean	D_{max}/D_{min}
Mean (mm)	14.2	11.5	12.9	12.9	1.3
Standard Deviation (mm)	2.2	1.9	1.7	1.8	0.2
CoV (%)	16.0	17.0	13.0	14.0	19.0

Table 4.2: Residence times of markers (hr)

Radius (m)	Level 1	Level 2	Level 3	Level 4	Level 5	Level 6	Level 7
0.092	0.16		0.29	0.49	0.77	1.10	1.18
	0.16		0.30		0.77	1.11	1.18
			0.30		0.77		1.19
			0.30				1.19
0.466	0.20	0.19	0.29	0.50	0.84	1.12	1.20
	0.20	0.24	0.31	0.51	0.84	1.12	1.20
	0.20	0.25	0.39	0.53	0.90	1.13	1.21
		0.29	0.47	0.56	0.97	1.14	
		0.32	0.49	0.66		1.18	
			0.53	0.71		1.18	
				0.78			
				0.81			
0.921	3.46	0.97	0.92	0.91	1.51	1.39	
	3.46	1.04	1.00	1.01	1.94	1.48	
	3.47	1.16	1.16	1.35	2.04	1.60	
	3.48	1.21	1.30	1.67	2.18	1.61	
	3.48	1.21	1.39	1.81	2.19	1.67	
	3.48		1.45	1.86		1.69	
	3.50		1.47	1.90			
1.381		3.33	3.13	2.96	2.12	1.68	1.36
		3.34	3.15	2.99	2.24	1.70	1.38
		3.34	3.15	3.00	2.54	1.77	1.40
		3.35	3.17	3.03	2.55	1.77	1.41
		3.35	3.18	3.14	2.56	1.79	1.47
			3.21		2.56	1.87	1.47
					2.57	1.88	1.51
					2.59		1.51
1.84		3.42	3.21	2.95	2.60	1.94	1.52
		3.42	3.21	2.95	2.61	1.95	1.55
		3.44	3.22	2.95	2.61	1.96	1.58
		3.46	3.23	2.96	2.64	2.02	1.66
			3.23	2.96	2.64	2.03	1.67
			3.24		2.66	2.04	1.67
					2.67		1.67

Table 4.3: Axisymmetry of residence time observations

Level No.	Ring No.	Mean time (hr)	CoV (%)	Level No.	Ring No.	Mean time (hr)	CoV (%)
2	1			5	1	0.767	0.22
	2	0.256	19.03		2	0.888	6.91
	3	1.118	9.57		3	1.973	14.04
	4	3.339	0.22		4	2.467	7.25
	5	3.432	0.45		5	2.638	1.08
3	1	0.298	1.22	6	1	1.103	0.57
	2	0.413	25.31		2	1.147	2.54
	3	1.241	17.61		3	1.573	7.26
	4	3.166	0.96		4	1.781	4.41
	5	3.222	0.37		5	1.992	2.34
4	1	0.485		7	1	1.186	0.53
	2	0.614	20.45		2	1.2	0.59
	3	1.501	27.37		3		
	4	3.023	2.21		4	1.439	4.09
	5	2.954	0.21		5	1.619	4.03

Fig 4.1: Full scale silo

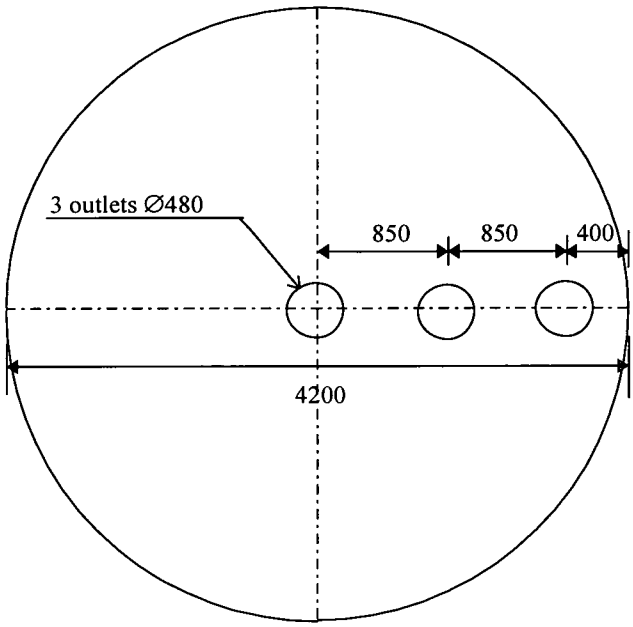

Fig 4.2: Silo outlets in floor

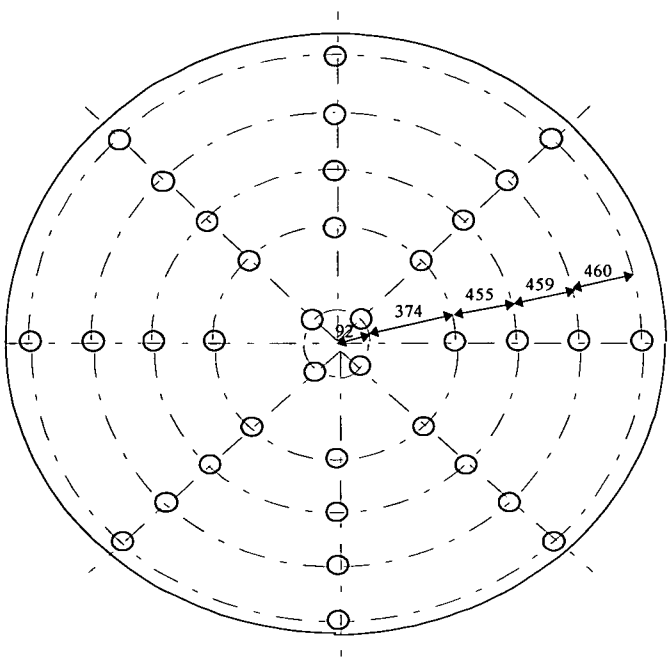

Fig. 4.3: Radio tags seeding template

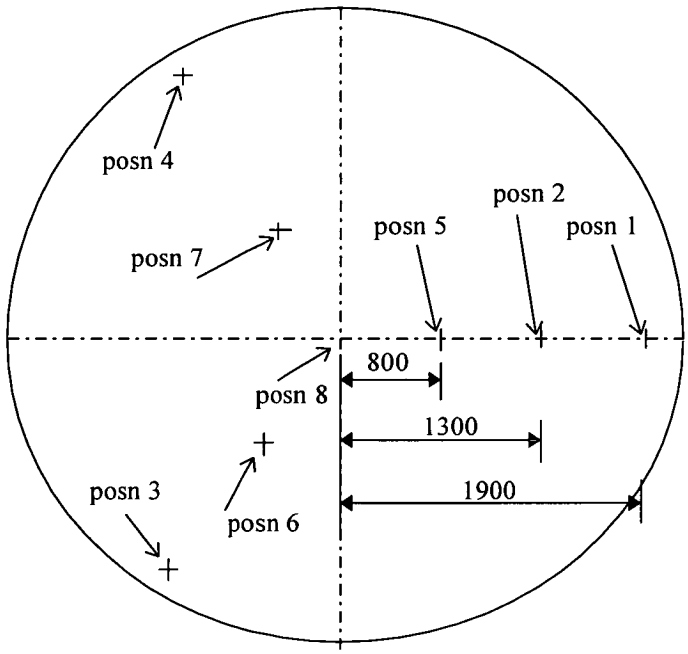

Fig. 4.4: Positions of depth measurement on the solid surface

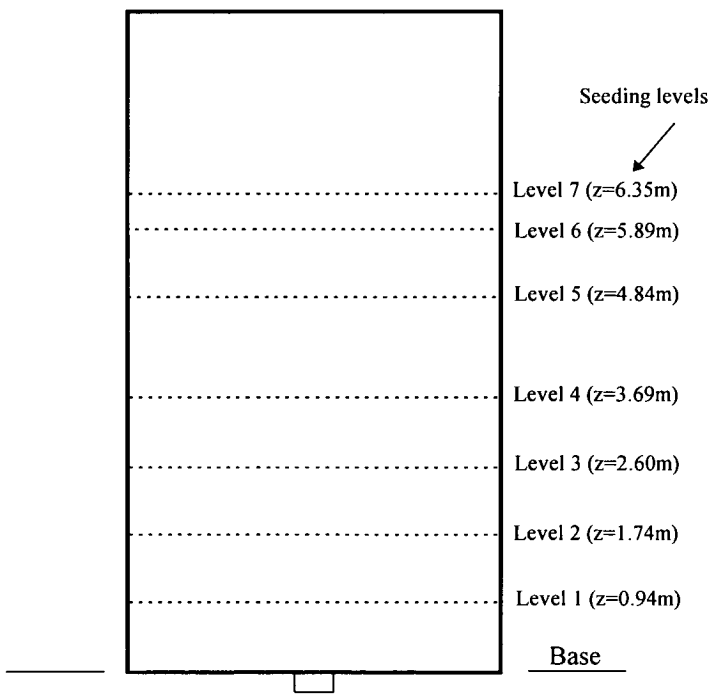

Fig. 4.5: Seeding levels for Test PCB

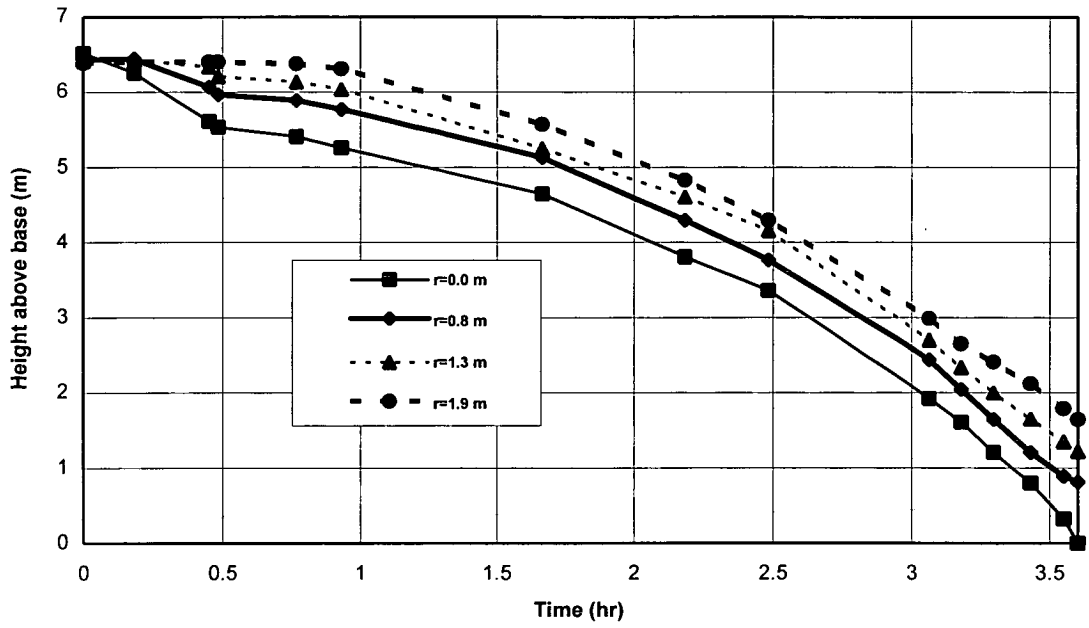

Fig 4.6: Heights of measuring points on top surface during discharge

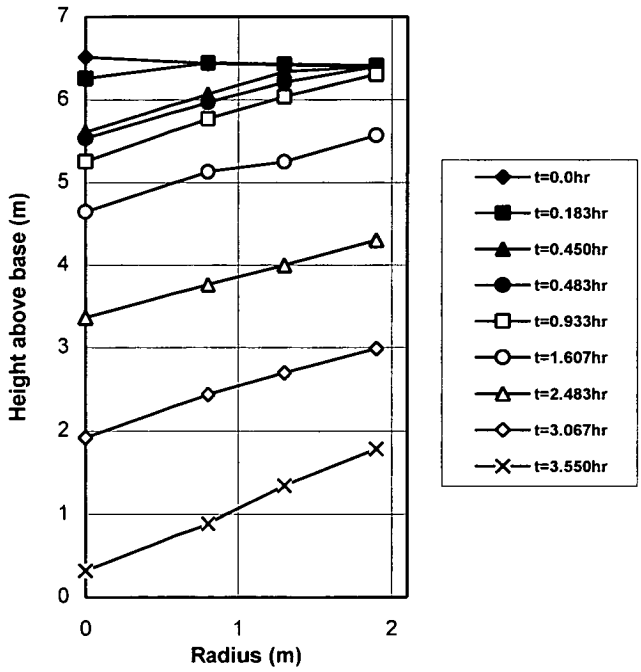

Fig 4.7: Top surface profile during discharge

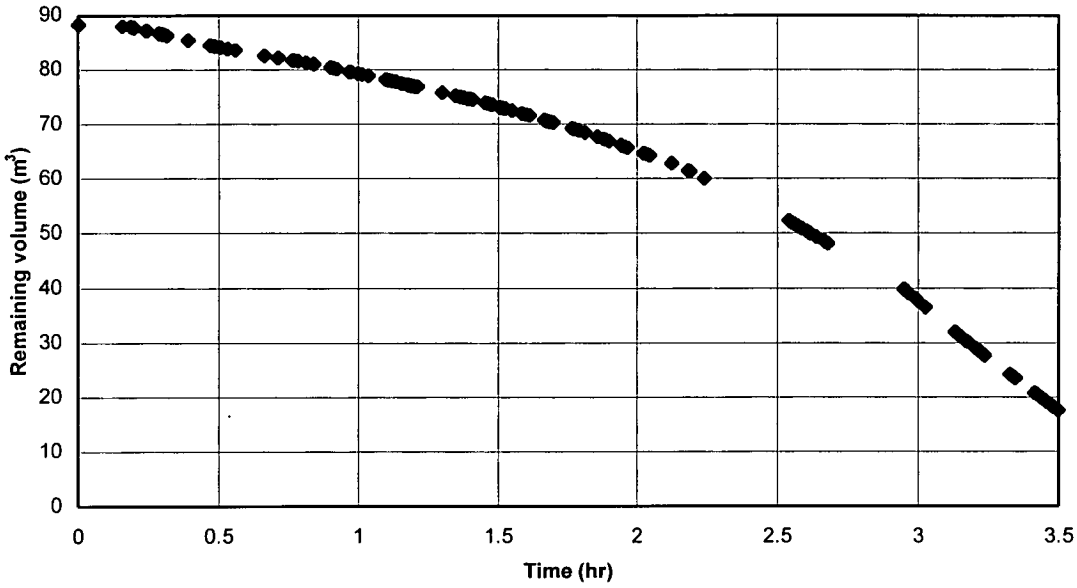

Fig.4.8: Remaining volume of solids during discharge

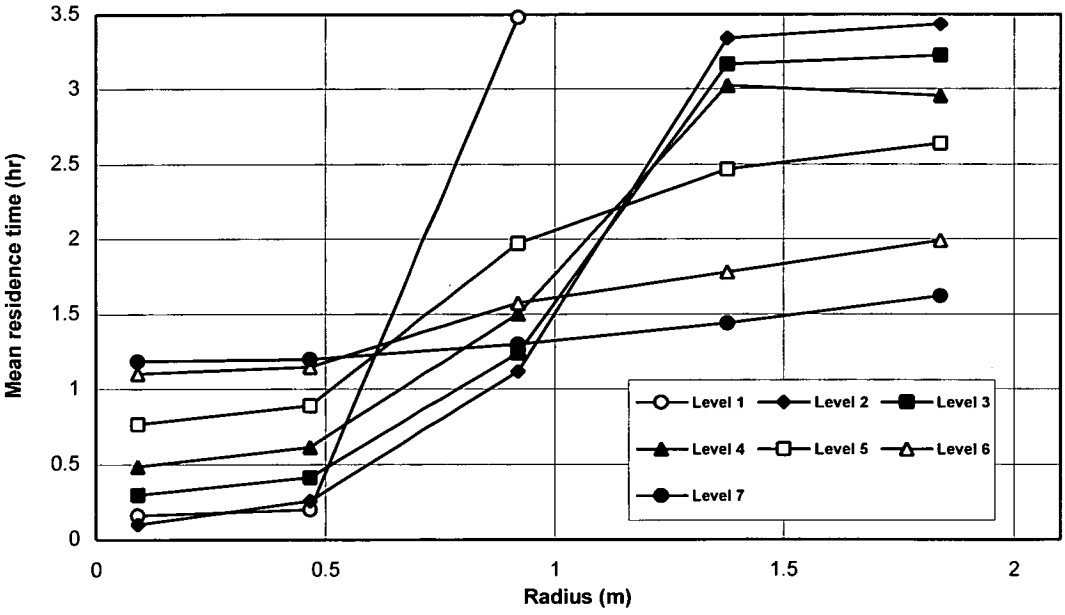

Fig 4.9: Mean residence time distributions at different levels

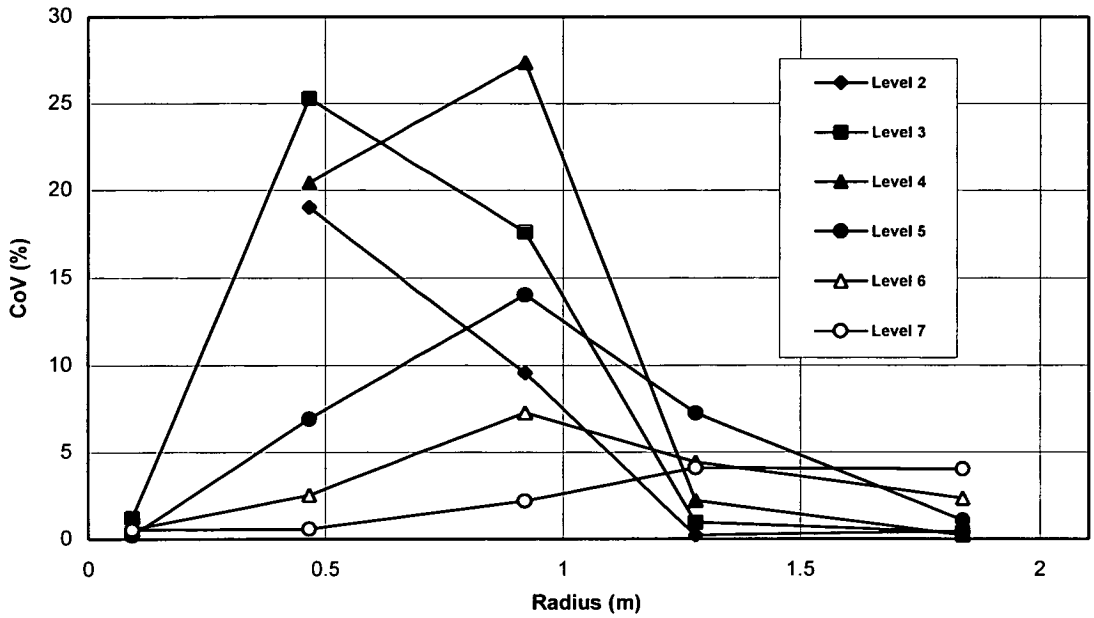

Fig 4.10: CoV distributions of residence timeds of markers

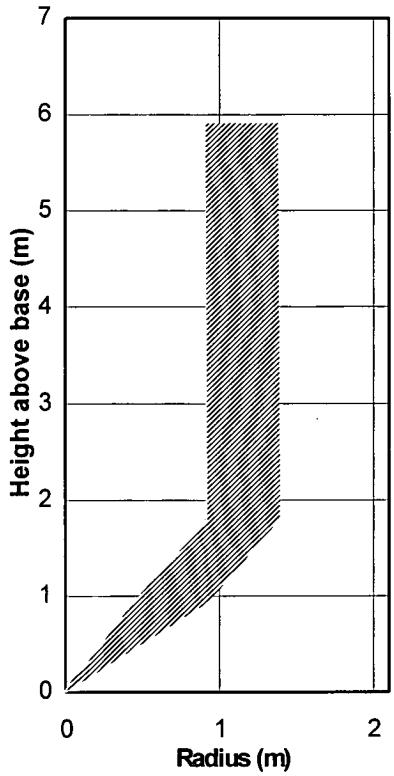

Fig. 4.11: Inferred position of flow channel boundary

CHAPTER 5

AN ENGINEERING MODEL FOR SOLIDS FLOW IN CONCENTRIC DISCHARGE SILOS

5.1 Introduction

Many industrial silo problems can be attributed either to the unpredictability of solids flow or to uncertainties about silo wall loads, which are closely related to the flow pattern. In recent years, numerous attempts at measuring and predicting the pattern of solids flow during silo discharging have been undertaken (e.g. Nedderman and Tuzun, 1979; Hartlen *et al*, 1984; Haussler and Eibl, 1984; Runesson and Nilsson, 1986; Watson, 1993; Rotter *et al*, 1995). Significant progress still has to be made before the flow behaviour of a granular solid is sufficiently understood.

Several analytical and numerical models have been used to predict the flow patterns of solids in silos. These methods are primarily based on either particulate solids continuum mechanics (e.g. Haussler and Eibl, 1984), discrete particle dynamics (e.g. Cundall and Strack, 1979), fluid mechanics (e.g. Haff, 1983) or kinematic theories (e.g. Nedderman and Tuzun, 1979). Each of these methods has its own shortcomings and at present, none of them appear to be capable of producing realistic predictions of complex funnel flow patterns seen in silos during emptying.

In this chapter a simple engineering model for describing funnel flow is presented. This model is based on a combination of kinematic theory for steady state flow and

assumptions of top surface profile, top flow layer and particle trajectory which are made according to previous observations. The kinematic theory is used to represent the velocity field in the solid during discharge.

5.2 Engineering model for flow

5.2.1 Assumptions

5.2.1.1 Top surface profile during discharge

There have been many experiments undertaken to investigate the internal funnel flow of granular solids during the emptying process (e.g. Brown and Hawksley, 1954; Kvapil, 1959; Jenike, 1961; Hartlen *et al*, 1984; Watson, 1993; Rotter *et al*, 1995). It has been observed that after an initial period, the top surface profile adopts an inverted cone form and the angle of inclination of the top surface (i.e. angle of repose) remains relatively constant during discharge.

In the present model, it is therefore assumed that during discharge, an inverted conical surface at the angle of repose exists at the top such that the volume displaced is equal to the volume of solid discharged. Figure 5.1 illustrates the assumed conical surface profiles during discharge when the solids surface is horizontal initially. The distance h_c from the inverted conical apex to the initial top surface can be determined using the following equations.

$$h_c = \frac{q_{exit}t + 2/3\ \pi R^3 tg\beta}{\pi R^2} \qquad \text{if } q_{exit}t \geq 1/3\ \pi R^3 tg\beta \qquad (5.1)$$

$$h_c = \sqrt[3]{\frac{3q_{exit}t}{\pi ctg^2\beta}} \qquad \text{otherwise} \qquad (5.2)$$

where q_{exit} is the volumetric discharge flow rate, t is the time from the beginning of discharge, β is the angle of repose and R is the radius of the silo.

5.2.1.2 Particle trajectory path

It is known that during internal funnel flow, the solid flows relatively fast in the central flow zone, with little or no movement in the stagnant zone beyond (Brown and Hawksley, 1954; Kvapil, 1959; Jenike, 1961; Tuzun and Nedderman, 1979; Hartlen *et al*, 1984; Watson, 1993; Rotter *et al*, 1995). Some of these observations (Brown and Hawksley, 1954; Kvapil, 1959; Watson, 1993; Dalaney and Blake, 1995) further revealed that at the solids surface, there is a finite layer of flowing solid in which the particles predominantly move down the slope towards the central axis (sloughing off the surface).

Whilst the existence of the top flow layer is recognised, little is known about its shape and size and how it changes with time. The top flow layer can be expected to be influenced by the geometry and size of silo and the bulk solid properties. Further investigations are needed in this area before the flow behaviour of solids are better understood. In this chapter, the following simple assumptions are made

- The top flow layer is inclined at the angle of repose and the thickness of the top flow layer h_t is uniform; and

- Once a particle enters the top flow layer, it moves instantaneously down the slope at the angle of repose to the central axis. It will then accelerate and move vertically down towards the outlet, adopting the velocity field given by the kinematic theory.

The assumptions are simple and are the first attempt at defining the top boundary to allow the steady state kinematic solution to be used to model silo emptying. In

reality, particles emerging on the solids surface will not all roll to the central axis but close to it, giving an array of different trajectories within the central fast flow zone. Improving the assumptions should lead to a better model and are being investigated.

5.2.2 Kinematic theory

Kinematic models for steady state flow were proposed by Litwiniszyn (1963), Mullins (1972; 1974 and 1979) and Nedderman and Tuzun (1979). Based on different assumptions, they each arrived at essentially the same differential equation. Since then, some contributions have been made either in verifying the model or extending the application field. The applications of kinematic models were restricted to predicting the velocity fields in planar and semi-infinite silos until Graham *et al* (1987) applied the model to predict the flow pattern of granular solid in a cylindrical model silo. Watson and Rotter (1996) extended the model to the prediction of the flow pattern in irregular silos using the finite element method instead of analytical solutions.

5.2.2.1 Solution to kinematic theory for axisymmetric flow

Under axisymmetric conditions, it is assumed (Mullins, 1972) that the radial velocity v_r of a particle at any point is related to the vertical component of its velocity v_z by

$$v_r = - B \frac{\partial v_z}{\partial r} \tag{5.3}$$

The parameter B has the dimension of length and is often termed the kinematic constant.

If the solids flow is treated as incompressible i.e. no void changes, the velocity components are related by the continuity equation

$$\frac{\partial v_z}{\partial z} + \frac{\partial v_r}{\partial r} + \frac{v_r}{r} = 0 \tag{5.4}$$

Combining Eqs. (5.3) and (5.4) leads to

$$\frac{\partial v_z}{\partial z} = B\left(\frac{\partial^2 v_z}{\partial r^2} + \frac{\partial v_z}{r\partial r}\right) \tag{5.5}$$

If the diameter d of the outlet is much smaller than the diameter D of the cylindrical silo, say d/D<5, the outlet can be approximated as a point orifice. For a cylindrical silo with a point orifice, Eq. (5.5) has an approximate series solution (Mullins, 1972; Graham *et al*, 1987)) given by

$$v_z(r, z) = \frac{q_{exit}}{\pi R^2} \sum_{n=1}^{\infty} \frac{J_o(\lambda_n r)}{J_o^2(\lambda_n R)} e^{-\lambda_n^2 Bz} \tag{5.6}$$

where R is the radius of the silo.

Substituting Eq. (5.6) into Eq. (5.3) the radial velocity is then obtained

$$v_r(r, z) = \frac{Bq_{exit}}{\pi R^2} \sum_{n=1}^{\infty} \frac{J_1(\lambda_n r)}{J_o^2(\lambda_n R)} e^{-\lambda_n^2 Bz} \tag{5.7}$$

in which λ_n are coefficients to be determined from the boundary condition.

J_o is a Bessel function of the first kind

$$J_o(\lambda) = \frac{1}{\pi} \int_o^{\pi} \cos(\lambda \sin x) dx \tag{5.8}$$

and J_1 is the first derivative of the Bessel function J_o

$$J_1(\lambda) = \frac{1}{\pi} \int_o^{\pi} \sin(\lambda \sin x) \sin x dx \tag{5.9}$$

Usually, the volumetric discharge rate keeps constant during the whole discharge process either under steady flow (continuously filling) or unsteady flow (no filling) as the discharge rate only has close relation to the size of the outlet (Fowler and Glastonburg, 1959; Beverloo *et al*, 1961). However, in some cases, the volumetric discharge rate is controlled for other reasons. If so, the volumetric discharge rate is a function of time.

$$q_{exit} = q_{exit}(t) \tag{5.10}$$

Therefore, for more general cases, the vertical and radial velocities are the functions of the coordinates and time.

$$v_z(r, z, t) = \frac{q_{exit}(t)}{\pi R^2} \sum_{n=1}^{\infty} \frac{J_o(\lambda_n r)}{J_o^2(\lambda_n R)} e^{-\lambda_n^2 Bz} \tag{5.11}$$

$$v_r(r, z, t) = \frac{Bq_{exit}(t)}{\pi R^2} \sum_{n=1}^{\infty} \frac{J_1(\lambda_n r)}{J_o^2(\lambda_n R)} e^{-\lambda_n^2 Bz} \tag{5.12}$$

To satisfy the wall boundary condition that the radial velocity of a particle vanishes on the wall, it is demanded that

$$J_1(\lambda_n R) = 0 \tag{5.13}$$

Thus, the coefficients λ_n used in Eqs. (5.11) and (5.12) can be obtained by solving the above equation. They are

$$\lambda_n = 0, \frac{3.83}{R}, \frac{7.02}{R}, \frac{10.17}{R} \qquad (n=1, 2, 3, 4,...) \qquad (5.14)$$

5.2.2.2 Convergence of the solution

Since the analytical solutions to the vertical and the radial velocities of a particle are series solutions, it is necessary to investigate the convergence of these solutions. To simplify the analysis, the vertical velocity v_z is normalised

$$|v_z| = \frac{v_z \pi R^2}{q_{exit}} = \sum_{n=1}^{\infty} \frac{J_o(\lambda_n r)}{J_o^2(\lambda_n R)} e^{-\lambda_n^2 Bz} \qquad (5.15)$$

The terms of 5 and 6 for the Bessel function of the first kind J_0 were tried to study the convergence for the solution shown in Eq. (5.15). Figure 5.2 shows the variations of the normalised vertical velocity $|v_z|$ with the radial coordinate r at the normalised heights (H/R) of 1, 2 and 3 for the cases B = 0.015R and B = 0.025R. It is clear from the figure that normalised vertical velocities obtained using 5 and 6 terms are extremely close at different heights. It therefore can be considered that 5 terms are adequate to represent the solution.

5.2.2.3 Calculation of residence time

From the series solution for the vertical velocity and the radial velocity shown in Eqs. (5.11) and (5.12), the residence time T for each particle to move from its starting position (r_o, z_o) to the outlet (0,0) can be obtained from

$$T = \int_0^{z_o} \frac{1}{v_z} dz \tag{5.16}$$

Since the vertical velocity depends on the coordinates r and z, the integrating equation Eq. (5.16) can not be solved individually. Another equation that is trajectory equation needs to be introduced. Therefore the problem is transferred into solving the following set of differential equations.

$$\begin{cases} \dfrac{dz}{dr} = \dfrac{v_z(r, z, t)}{v_r(r, z, t)} & (5.17) \\ \dfrac{dt}{dz} = \dfrac{1}{v_z(r, z, t)} & (5.18) \end{cases}$$

with the initial conditions

$$\begin{cases} r = r_o \\ z = z_o \end{cases} \quad \text{when } t = 0 \tag{5.19}$$

Thus the residence time and the trajectory can be calculated for any particular particle with known starting position by solving the differential equations Eqs (5.17) and (5.18) with initial conditions Eq. (5.19).

To solve the above ordinary differential equations, the Runge - Kutta numerical method is employed. This is a common method extensively adopted to numerically deal with ordinary differential equations. The main principles and the detailed calculation procedures of the method can be seen in Kreyszig (1993).

5.2.3 Engineering model for solids flow

The present model for funnel flow is based on the kinematic theory and the assumptions above. In short, every particle moves according to the kinematic velocity field and when a particle emerges on the inclined solids surface, it is assumed to move rapidly to the central axis along the inclined surface and attain the velocity there. The instantaneous top surface is defined by the volume of solid discharge at the time.

In this model, there are four distinct zones in which the flow patterns are very different. First there is a top flow zone with a finite thickness and all the particles in this zone move towards a central flow zone rapidly along the angle of repose. Secondly there is a central flow zone in which the particles are moving relatively fast towards the outlet. This central zone is surrounded by a feeding zone with very slow moving solid which does not move directly to the outlet, but follows the trajectory stipulated above and feeds into the central zone. Finally, there is a dead zone at the bottom which remains in the silo at the end of discharge. These proposed flow zones are in accordance with the conventional view of a funnel flow condition.

5.3 Determination of parameters

Before the proposed simple engineering prediction model for solids flow in flat-bottomed silo during concentric discharge is used, two important parameters that are the kinematic constant B and the thickness of top flow layer h_t have to be determined.

5.3.1 Kinematic constant

Since the kinematic theory was proposed, experiments have been carried out to investigate the kinematic constant B for different materials.

Nedderman and Tuzun (1979) proposed a kinematic theory and conducted tests in a planar silo to observe and photograph the flow of 1.5 - 2.0 mm glass ballotini at various widths of the silo and orifice sizes under steady-state flow conditions. They discovered that the kinematic constant B is not proportional to the filling height, the width of the silo, the width of the converging flow zone and the orifice size, but is probably proportional to some length scale of the system. The best fitted value of B was found to be 4.5 mm within the converging flow zone.

Mullins (1974) verified his stochastic theory of particle flow under gravity proposed in 1972 with Gunita's experimental evidence. In this experiment (Gunita, 1969), the iron ore pellets (size range: 0.041-0.318 mm, approximate median particle size: 0.127 mm) were used to investigate the flow behaviour in a model concentrically discharging silo with the diameter of 45.7 mm and the height of 61.0 mm. The best value B of 0.280 mm were estimated by using the solution to a semi-infinite bed.

Graham *et al* (1987) used the residence time technique to investigate the flow patterns of Epoxy spheres (size range 1.6 - 6.4 mm) and Coke (size range 0.1 - 12.5 mm with the distribution of the particle size shown in Fig. 5.3(a)) in a cylindrical vessel with the diameter of 560 mm. A kinematic model was employed to calculate the steady-state velocity profiles and residence time distributions . A simple graphic technique was developed to determine the kinematic constant using the residence times of markers on the centre line. The best fitted kinematic constants were found to be 15.0 mm and 26.0 mm for Coke and Epoxy spheres respectively.

Watson (1993) developed five different methods of finding a value of the kinematic constant B using a finite element kinematic analysis. The kinematic constant B was determined from the flow channel boundary as traced through the front wall, measured residence times, measurements of velocity, Mullins' and Graham's methods. Apart from the Graham's method with which the deduced kinematic constant was apparently much higher, all other methods could give a fairly close value of B. For the test material sand (size range: 0.43-1.7 mm with the distribution of the particle size shown in Fig. 5.3(b)) and polypropylene pellets (size range: diameter of pellets 5.0 mm, length 3.3 mm), the constant values of 3.5 mm and 7.0 mm could provide a good description of the behaviour of the granular solids sand and polypropylene pellets.

All the research work stated above is summarised in Table 5.1.

It has been suggested that the kinematic constant is closely relative to the sizes of the particles rather than other parameters (Mullins, 1972; Tuzun and Nedderman, 1979). The influence of the particle size on the kinematic constant B is explored in this study. The best way is to establish the all relationships between the kinematic constant and the various characteristic sizes of particles, and then the most representative characteristic size can be decided. Unfortunately, most of the published literature lacked the detailed information about the particle size. Here only the mean particle size $\bar{x}$ is considered as the characteristic size of the particles. If the kinematic constant B is expressed as proportional to the mean particle size, the constant of proportionality k can be determined with the following equation

$$B = k\,\bar{x} \tag{5.20}$$

where the mean particle size $\bar{x}$ can be determined by

$$\bar{x} = \frac{1}{\sum_{i=1}^{n} \frac{w_i}{\bar{x}_i}} \tag{5.21}$$

in which w_i and $\bar{x}_i$ are the weight percentage and average diameter of particles in the size interval i.

The mean particle size $\bar{x}$ and the constant of proportionality k for all six different materials appear in Table 5.2. From this Table, clearly, the k values obtained by Graham's method are much higher than those by other methods. The most fitted kinematic constant B for Epoxy spheres with Graham *et al*'s proposed graphical method reaches up to 8.13 times the mean diameter of the particles. Such a phenomenon was also confirmed by Watson (1993). Watson adopted Graham *et al*'s method to estimate the B values for sand and polypropylene pellets and obtained the best fitted B values of 19.8 mm and 28.6 mm which were much higher than 3.5 mm and 7.0 mm obtained by other methods. This casts doubt on Graham *et al*'s method for estimating a value for B. Apart from the Graham *et al*'s results, the kinematic constants were within the range of 2.1 to 3.58 times the mean diameter of the particles. This suggests that the kinematic constant in the range of 2 to 4 times the mean diameter of the particles could give a good prediction.

5.3.2 Thickness of top flow layer

Although many researchers (Brown and Hawksley, 1954; Kvapil, 1959; Jenike, 1961; Watson, 1993) have discovered that there exist the top flow layer in internal funnel flow during emptying silo discharge, the precise descriptions of the shape and size of the top flow layer and their changes with time are still unavailable. The top flow layer, perhaps mainly relative to the material properties such as angle of repose, size distribution of particles, and the geometry of the silo needs to be further investigated.

5.4 Calculation procedures

According to the engineering model of solids flow stated above, the detailed calculation procedures to predict the residence time and the trajectory path for each particle can be summarised as follows.

Step 1 input initial data including kinematic constant B, thickness of top flow layer h_t, silo radius R, filling height H, angle of repose β and volumetric discharge rate q_{exit};

Step 2 for the particle with starting position (r_o, z_o), determine the size length step Δz, set $n = z_o/\Delta z$, $r = r_o$, $z = z_o$ and $T = 0$;

Step 3 do loop for i=1,n;

Step 4 calculate vertical and radial velocities v_z and v_r at (r, z);

Step 5 compute ΔT and Δr for the particle to move from z to z - Δz via solving the differential equations (Eqs. (5.17) and (5.18)) using Runge - Kutta method;

Step 6 calculate $T = T + \Delta T$, $z = z - \Delta z$ and $r = r - \Delta r$, and determine the location of the top surface;

Step 7 check the position of the particle, if it locates in the top flow layer, then go to Step 8, otherwise go to Step 3 if $i < n$, or go to Step 11 if $i = n$;

Step 8 roll down instantaneously to the central axis along the top surface when the particle exposes on the top;

Step 9 insert z and r based on instantaneous movement to the centre line;

*Step 10*move down to the outlet along the central axis and evaluate the time taken to the outlet ΔT; calculate $T = T + \Delta T$;

Step 11 print out total residence time T and the trajectory path of the particle, stop.

5.5 Concluding remarks

An engineering model for solids flow in concentrically discharging silos is proposed based on the simple kinematic model for steady state flow coupled with reasonable assumptions about top surface profile and top flow layer during the whole process of emptying silos. Only three parameters the angle of repose β, the kinematic constant B and the thickness of top flow layer h_t are involved.

Amongst these parameters, the angle of repose β can be easily and precisely determined. The kinematic constant B can be measured by placing several markers along the central axis and recording their residence times in control tests which can be carried out in labs. However, due to the lack of the detailed investigations on the thickness of the top flow layer h_t, it is difficult to choose the correct value at present. Fortunately, the calculations in the next chapter will show that this parameter does not have significant influence on the location of the flow channel boundary which is most concerned in funnel flow silos.

Table 5.1: Summary information relating to the kinematic constant

Workers	Materials	Size (mm)	Internal friction angle (deg)	Fitted kinematic constant B (mm)
Nedderman and Tuzun	Glass ballotini	1.5-2.0	26	4.5
Mullins	Iron ore	0.041-0.318	30	0.28
Graham *et al*	Coke	0.1-12.5 (D_{10}=0.25, D_{90}=10.2, C_u=29.6, C_z=8.22)	42	15
	Epoxy spheres	1.6-6.4	26	26
Watson	Sand	0.43-1.7 (D_{10}=0.63, D_{90}=1.60, C_u=1.59, C_z=0.94)	43	3.5
	Polypropylene pellets	4.9 diameter 3.3 height	25	7

Table 5.2: The value of k for different materials ($B = k \bar{x}$)

Materials	Glass ballotini	Iron ore	Coke	Epoxy spheres	Sand	Polypropylene pellets
Mean size $\bar{x}$ (mm)	1.8	0.13	6.0	3.2	0.9	2.5
k value	2.5	2.2	2.3	8.1	3.9	2.8

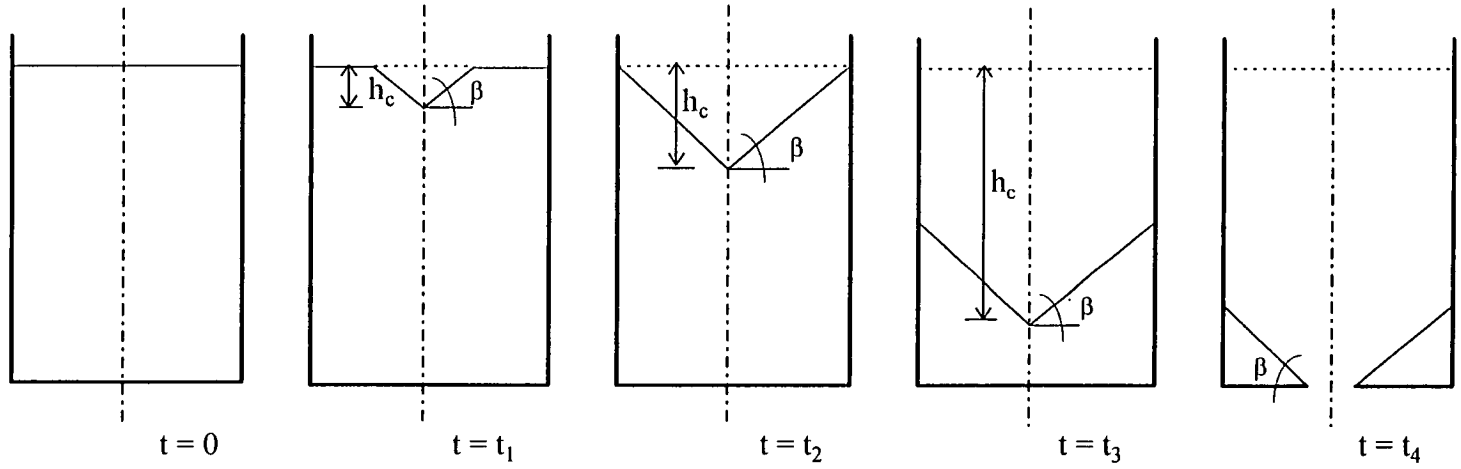

Fig. 5.1: Assumed top surface profile during discharge

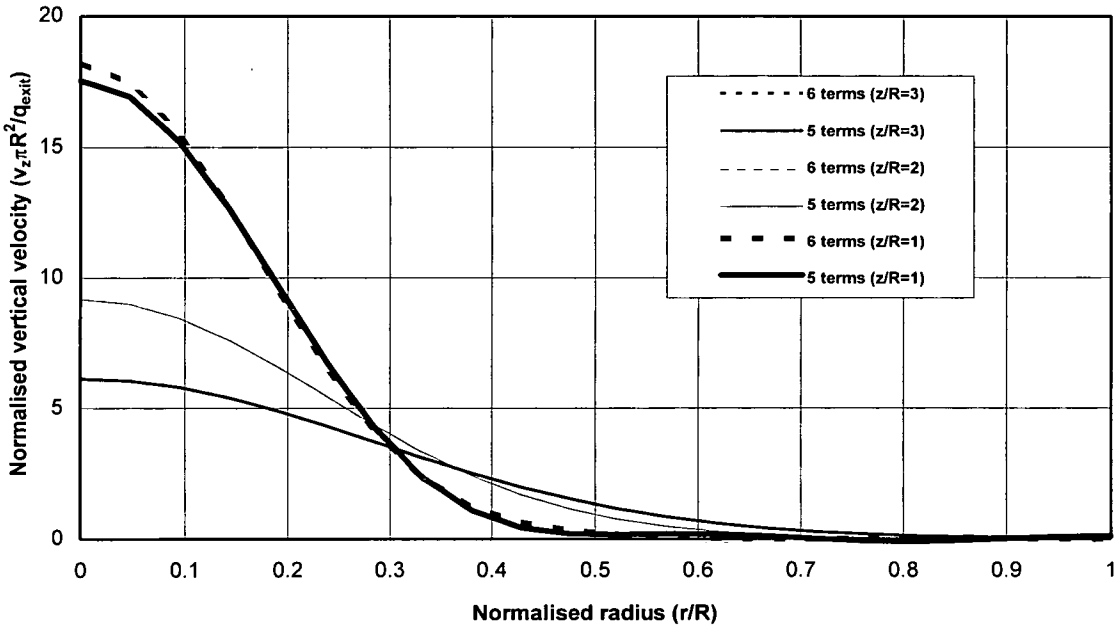

a) B=0.015R

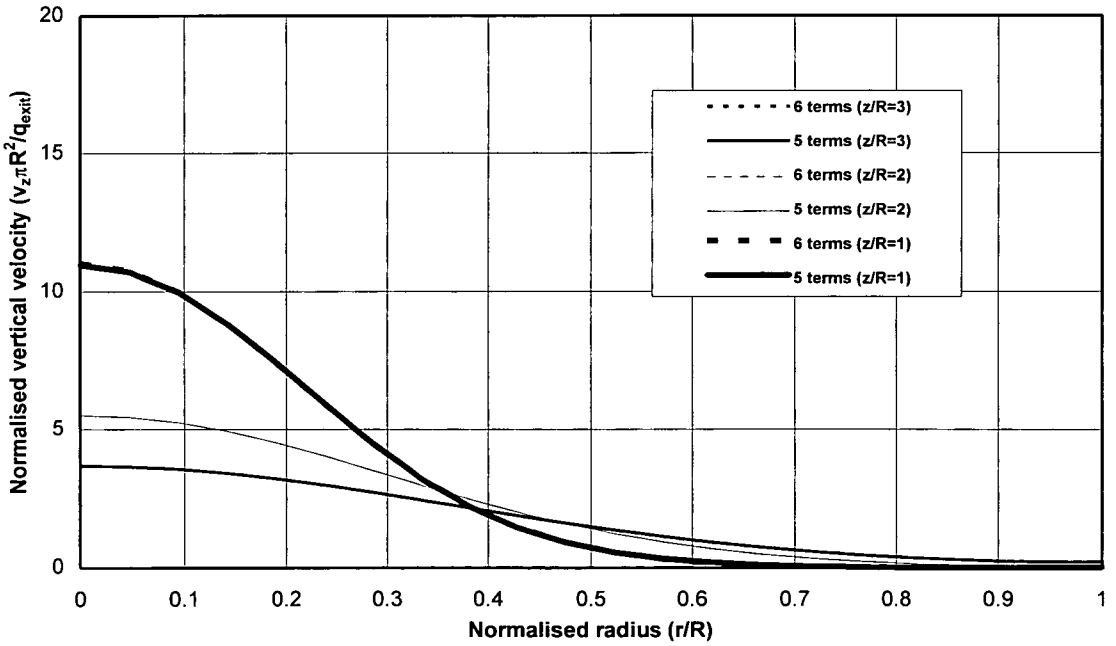

b) B=0.025R

Fig 5.2: Variation of normalised vertical velocity with different number of terms

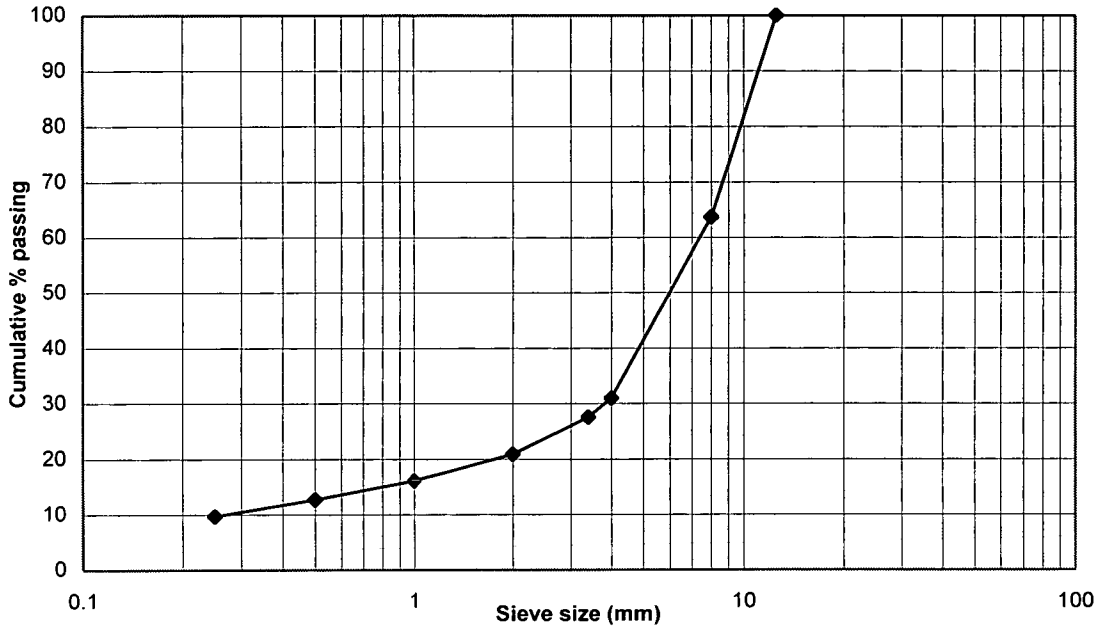

a) Coke

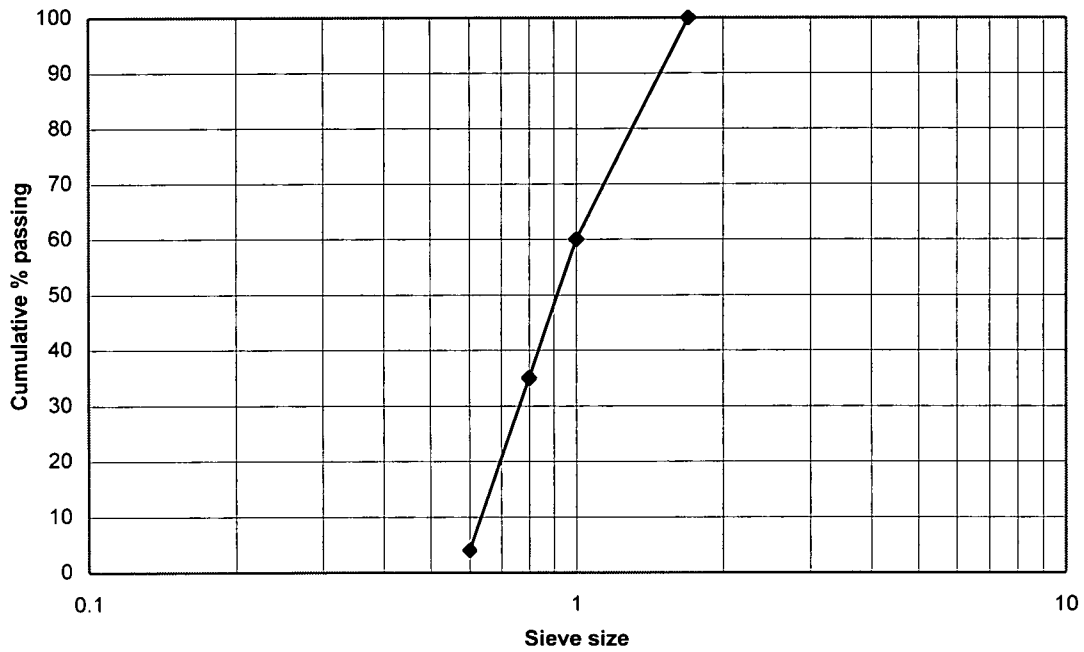

b) Sand

Fig. 5.3: Particle size distribution for materials coke and sand

CHAPTER 6

APPLICATIONS OF ENGINEERING MODEL FOR PREDICTING SOLIDS FLOW IN SILOS

6.1 Introduction

In this chapter, the flow of iron ore pellets in a full scale silo and polypropylene pellets in a half cylindrical model silo during concentrically emptying silo will be predicted using the simple engineering model proposed in Chapter 5. The predicted and measured residence times of the markers for both silos are compared. The trajectory paths of particles are also predicted. Furthermore, the flow channel boundaries (FCBs) are identified according to the different trajectory paths of particles. The good agreements between the experimental observations and the predictions suggest that this new engineering model can represent solids flow in funnel flow silos quite well.

6.2 Determinations of parameters

As mentioned in Chapter 5, the proposed engineering model for solids flow involves three parameters which should be determined in advance. They are: kinematic constant B, the thickness of the top flow layer h_t and the angle of repose β. Besides, the volumetric discharge rate which is used to determine the location of the top surface during discharge is also a parameter to be known.

6.2.1 Volumetric discharge rate

6.2.1.1 Full scale silo

The calculation of the volume of solid remaining in the silo at any instance is based on the depth measurements from 8 positions on the roof of the silo (see Chapter 4). There are several possible methods to evaluate the remaining volume of solid from the depth measurements. Here the following mapping relationship is employed to determine the height at any position on the top surface from the measured depths at 8 positions during discharge.

$$z = \sum_{k=1}^{8} \frac{z_{mk}}{d_k} \Big/ \sum_{k=1}^{8} \frac{1}{d_k} \tag{6.1}$$

where z_{mk} is the measured height at position k, and d_k is the horizontal distance from the position k to where the height needs to be determined.

With the help of the height distribution on the top surface, the volume of remaining solid can be calculated by using the following equation

$$Q_r(t) = \int_0^{2\pi} \int_0^R z(t) r dr d\theta \tag{6.2}$$

where $Q_r(t)$ is the remaining volume of solid at time t, z(t) is a function of height distribution on the top surface shown in Eq. (6.1).

Figure 6.1 shows the measured remaining volume of solid obtained by using Eq. (6.2) throughout the emptying process. To be convenient for the calculation, the remaining volume of solids $Q_r(t)$ during the discharge has been fitted into polynomial

series with various orders, and it was found that a best fitting quartic equation could give a high quality approximation.

$$Q_r(t) = 88.2 - 10.97t + 2.5864t^2 - 1.734t^3 + 0.056t^4 \ (m^3) \qquad (6.3)$$

The plot of Eq. (6.3) is also showed in Fig. 6.1 and it can be found that the remaining volume of solid between the measured and calculated is in excellent agreement, indicating that the fitting equation Eq. (6.3) well represents the variation of the remaining volume in the silo during the whole process and therefore it will be utilised in the subsequent analysis.

The whole discharge was lasting for 3.5 hr. At the end of discharge, 17.6 m^3 (20.0% of initial content) of solid still remained in the silo.

The volumetric discharge rate $q_{exit}(t)$ can be gained by differentiating Eq. (6.3) with respect to time t.

$$q_{exit}(t) = \frac{dQ_r(t)}{dt} = 10.97 - 5.1728t + 5.202t^2 - 0.224t^3 \ (m^3/hr) \qquad (6.4)$$

The variation of the volumetric discharge rate with time is shown in Fig 6.2. It is noticed that the volumetric discharge rate varies in a non-linear manner with time. The flat pattern of the curve at the beginning of the discharge reveals that the discharge rate was almost identical at early stages and the nearly inclined straight lines means that the volumetric discharge rate increased sharply with time at later stages.

6.2.1.2 Half cylindrical model silo

The volumetric discharge rate from a semi-circular outlet for the model silo was investigated in Chapter 3, and it has been found that under concentric discharge the average discharge rate was 4.97×10^{-4} m^3/s.

6.2.2 Kinematic constant

A careful study of limited experimental observations (Tuzun and Nedderman, 1979; Graham *et al*, 1987; Graham, 1993) has been done in Chapter 5, which shows that the kinematic constant B can be expressed to be proportional to the mean particle size $\bar{x}$ and the value of the proportionality coefficient k is around 2 for most materials, but under some circumstances it can reach up to more than 3. It is difficult to determine B value theoretically in advance. The best way to determine the kinematic constant is conducting a simple control test by placing several markers along the central axis at different heights. The best fitted B value can be easily obtained by using Mullin's method (Mullin, 1974). Such a simple control test is feasible for most granular solids.

However, the control test for measuring B of iron ore pellets was not undertaken due to the heavy density of the material. The determination of B value for iron ore pellets and polypropylene pellets is based on the analysis of the available experimental observations shown in Chapter 5. The constants of proportionality k of 2 and 4 are tried to predict the flow of iron ore pellets in the full scale silo and polypropylene pellets in the half model silo.

6.2.3 Thickness of top flow layer

As previously mentioned, the information about the top flow layer is so limited that it is impossible at this stage to estimate exactly the thickness of the top flow layer. Further investigation into this topic is worth carrying out. In this chapter, the thickness of 0.5 m and 1.0 m for iron ore pellets and 50 mm and 100 mm for polypropylene pellets during emptying silos are assumed in the subsequent predictions.

6.2.4 Angle of repose

According to the physical property measurements for the test materials, the angles of repose of 35^{o} for iron ore pellets and 34^{o} for polypropylene pellets are adopted in the following calculation for predicting solids flow.

6.3 Comparisons between measured and predicted residence times

After the determinations of all the parameters involved in the simple engineering prediction model proposed in Chapter 5, the residence times of the markers can then be computed.

Figure 6.3(a) -6.3(f) show the predictions of residence time distributions at different heights for iron ore pellets in the full scale silo using different values of parameters B and h_t. Clearly, the B value of 2 times the mean particle size is not correct for this material as the discrepancies of the residence times of solid in the central core flow zone in which the kinematic model is supposed to be the most suitable are quite large. However, the B value of 4 times the mean particle size can make an excellent prediction in the central core flow zone, and it also can be found that the measured residence times and residence time distributions obtained with such value B coupled

with the thickness of 1.0 m of the top surface are in good agreement in the whole silo. It is therefore considered that kinematic constant for iron ore pellets is 51.6 mm and the thickness of top surface flow layer is 1.0 m.

Similar phenomena can also be found for polypropylene pellets in the half model silo shown in Fig. 6.4(a)-6.4(f). The difference between these two materials is that the kinematic constant B is 2 times the mean particle size for polypropylene pellets, while 4 times that for iron ore pellets. The fairly good agreement between the measured and predicted residence times (Fig. 6.4e) indicates that B value is 6.6 mm and the thickness the top surface is 100 mm for polypropylene pellets.

The present model also predicts that at certain levels, the residence time increases from the central axis to a 'peak' at a certain radius before dropping off again towards the silo wall. From the central axis up to the 'peak', the present model predicts continuous particle trajectories from the initial positions to the outlet. Beyond the 'peak' right up to the wall, the particles are predicted to be caught up in the top flow layer and cascaded to the central axis. Since the velocity at the centre is high, it is possible that the particles which cascaded may exit the silo sooner than the particles at some smaller radii which are moving at moderate velocities but are not caught up in the advancing top flow layer. These different particle trajectories have caused the 'peak' residence time pattern, which seems strange at first and is not borne out by the experimental observations presented so far. However, a more extensive seeding at some intermediate height (500 mm above base) in two different experiments revealed that such a pattern can happen (Fig. 6.5), although the present simple model has somewhat exaggerated the 'peak' in the residence time pattern.

6.4.1 Vertical velocity distributions

Since the volumetric discharge rate varied significantly for iron ore pellets during the discharge, the vertical velocity of a particle changed accordingly. To be convenient for the comparisons, the vertical velocity is normalised

$$|v_z| = \frac{v_z \pi R^2}{q_{exit}} \tag{6.5}$$

Correspondingly, the vertical coordinate z is also normalised

$$|z| = \frac{z}{R} \tag{6.6}$$

Figure 6.6 show the predicted normalised vertical velocity profiles for all seeded levels and how the vertical velocity varies down the central axis for iron ore pellets in the full scale silo. The results for polypropylene pellets in the half model silo are shown in Fig. 6.7.

The vertical velocity is negative since it is in the opposite direction to the vertical coordinate z. In general the vertical velocity decreases rapidly with increasing radial coordinate at each level, with the rate of decrease becoming smaller towards the top of the silo. Along the central axis, the vertical velocity is predicted to increase rapidly towards the outlet.

The vertical velocity profiles along the central axis for the full scale silo storing iron ore pellets and for the half model silo storing polypropylene pellets are shown in Fig. 6.8. The vertical velocity in the model scale silo is slightly larger than that in

the full scale silo at the same normalised height. From the semi-infinite solution to the continuity equation, it can be shown that the vertical velocity at the centre can be expressed as (Neddermen and Tuzun, 1979)

$$\frac{v_z \pi R^2}{q_{exit}} = \left(\frac{R}{4B}\right)\frac{R}{z} \tag{6.7}$$

Since the ratio R/B is 40.7 for the full scale silo and 49.2 for the model scale silo, the two velocity profiles appear to be quite similar, with the velocity in the model scale silo some 20% larger than that in the full scale silo.

6.4.2 Flow channel boundary

Kinematic models give a continuous velocity field and cannot predict the stagnant zones which are frequently encountered in silo discharge. To approximately predict the FCB, many authors have put forward their definitions though these definitions are somewhat arbitrarily. Tuzun and Nedderman (1979) defined the boundary as the streamline within which 99% of the total flow rate takes place, while Watson and Rotter (1996) defined it as the surface where the velocity at each height is a fixed proportion (usually 1%) of the centre-line velocity at that height. These two criteria produce very similar flow boundaries.

Another definition based on the solid's different trajectory paths is adopted in this study. The particles which follow the paths predicted by the kinematic model are considered in the core flow zone, and the particles which follow the short paths predicted by the kinematic model and then roll down towards the central axis along the inclined top surface and finally move down to the outlet belong to the feeding zone. Figure 6.9 outlines the FCB for the full scale silo and the half cylindrical model silo in accordance with above definition. The boundary predictions using Giunta's method (Giunta, 1969) are also shown in Fig. 6.9. In Giunta's prediction,

the half maximum radius of the boundary which depends on the effective angle of internal friction and the height of fill is determined by

$$\bar{r} = \frac{1}{2}[D + 2\tan\bar{\theta}(\frac{H - A\frac{D}{2}}{1 + A\tan\bar{\theta}})] \qquad (6.8)$$

where H is the head of material, $\bar{\theta}$ and A are the parameters dependent on the effective angle of friction.

It is clear that the predicted boundaries with Giunta's method appear too narrow for both silos. The present simple prediction agrees reasonably well with the other analyses of the flow pattern on the experiment for the full scale silo (Rotter *et al*, 1995) and with the observed flow boundary for the half model silo which is also shown in Fig. 6.9.

6.4.3 Trajectories of particles in different zones

The particle trajectories of iron ore pellets at the heights of 4.84 m (Level 5) and 2.60 m (Level 3) are shown in Fig. 6.10a, and the particle trajectories of polypropylene pellets at the heights of 600 mm (Level 6) and 300 mm (Level 3) are shown Fig. 6.10b. Theoretically, all particles should reach the same point at the outlet as in the derivation of the solution for the kinematic model the outlet is treated as a point orifice. However it is not the case according to Fig. 6.10. The reason for this is due to the approximate nature of the series solutions to the vertical and radial velocities.

The trajectories for the particles in the core flow zone are distinctly different from those beyond this zone. In the core zone, the trajectories are smooth from the starting position to the outlet as predicted by the kinematic model. In the surrounding

feeding zone, the trajectories consist of a short path as predicted by the kinematic model, followed by a path inclined at the angle of repose and finally a vertical path down the central axis as predicted by the kinematic model. The time taken to roll down the inclined surface to the central axis is very small compared with the total residence time and was ignored in this study.

6.5 Parameteric study

The ultimate purpose of the solids flow prediction is to make a good estimation of the FCB. For the funnel flow, the lower part of the FCB is the most important as in this part, there is a transition of the FCB where the overpressure principally occurs. In this section, the influence of the parameters B and h_t to the lower part of the FCB is studied.

6.5.1 Kinematic constant

In the investigation of the influence of the B value to the position of the FCB, two different B values (B = 25.8 mm and 51.6 mm for full scale silo, and B = 6.6 mm and 13.2 mm for model silo) for both the full scale silo and the half model silo were chosen and the produced FCBs are shown in Fig. 6.11. It can be found that the FCB is sensitive to the kinematic constant B The width of the FCB increases with B value. The reason for this is that the B value has a close relationship with the velocities of particles in the silo. Near the central axis, the vertical velocity of a particle is inversely proportional to the radial position of the particle, and the situation is inverse when the radius reaches a certain value. Generally, the FCB is fairly away from the central axis, and for the particles near the FCB the vertical velocities have a proportional relationship with the B value. The larger the B value, the greater the velocities of particles and the more the particles which move to the outlet with the trajectory paths governed by the kinematic theory without being

caught by the top flow layer. According to the definition of the FCB stated in Section 6.4.2, the width of the FCB then increases.

6.5.2 Thickness of top flow layer

Figure 6.12 shows the FCBs predicted by different values of the thickness of the top flow layer h_t (0.5 m and 1.0 m for the full scale silo, and 50 mm and 100 mm for the half model silo) for the full scale silo and the half model silo. It is clear that the influence of the h_t value to the FCB for both silos is much less than that of the kinematic constant B to the FCB. The value of h_t only has a very slight effect on the upper part of the FCB and almost has no influence on the lower part of the FCB. This is because the velocities of particles decrease sharply with the radius at the lower part of the FCB, which leads to the significant time difference for the particles near the FCB with small different radial positions to move out according to the prediction of the kinematic model. The limited change in the thickness of the top flow layer, therefore, almost has no influence on the location of the lower part of the FCB.

6.6 Concluding remarks

By applying the simple engineering model proposed in Chapter 5 to the flow of iron ore pellets in a full scale silo and polypropylene pellets in a half cylindrical model silo, the following conclusions can be drawn.

1. The simple engineering model for predicting flow behaviour has the ability to make a good prediction of solids flow as long as the kinematic constant and the thickness of the top flow layer can be properly chosen.

2. For the iron ore pellets, the kinematic constant B of 51.6 mm (4 times the mean particle size) and the thickness of 1.0 m of the top flow layer can make a good prediction for the flow occurred in the full scale silo, whilst the kinematic constant B of 6.6 mm (2 times the mean particle size) and the thickness of 100 mm of the top flow layer are suitable for predicting the polypropylene pellets flow in the half model silo.

3. The agreement between the predicted and the measured FCB for polypropylene pellets in the model silo is remarkable, proving that the definition of the FCB using different trajectory paths of particles is reasonable.

4. The kinematic constant plays a key role in determining the FCB and the thickness of the top flow layer has negligible influence on the FCB.

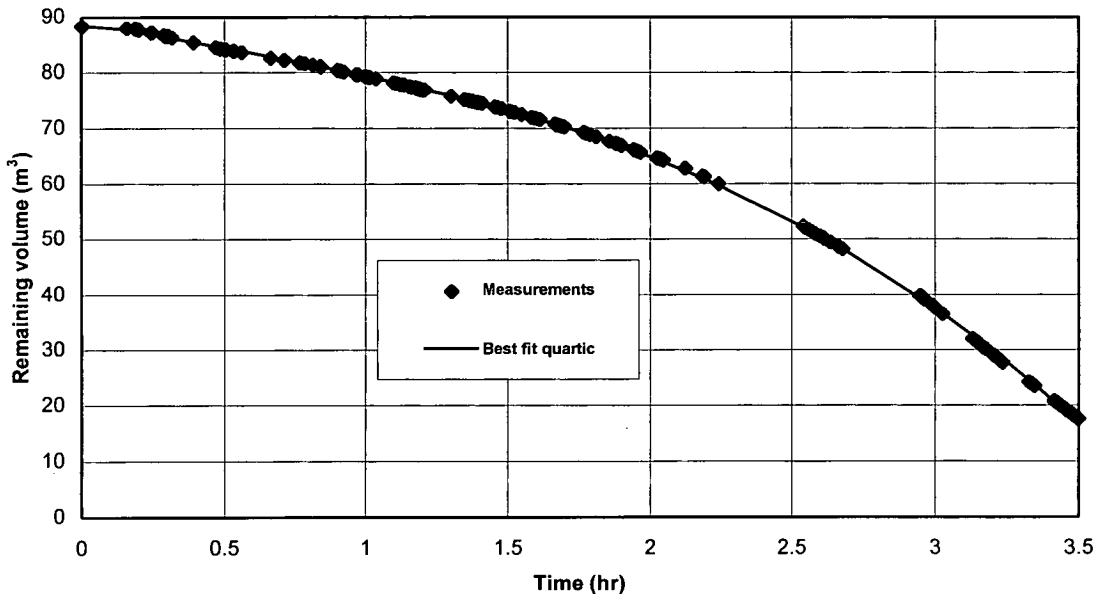

Fig. 6.1: Remaining volume of solid in full scale silo during discharge

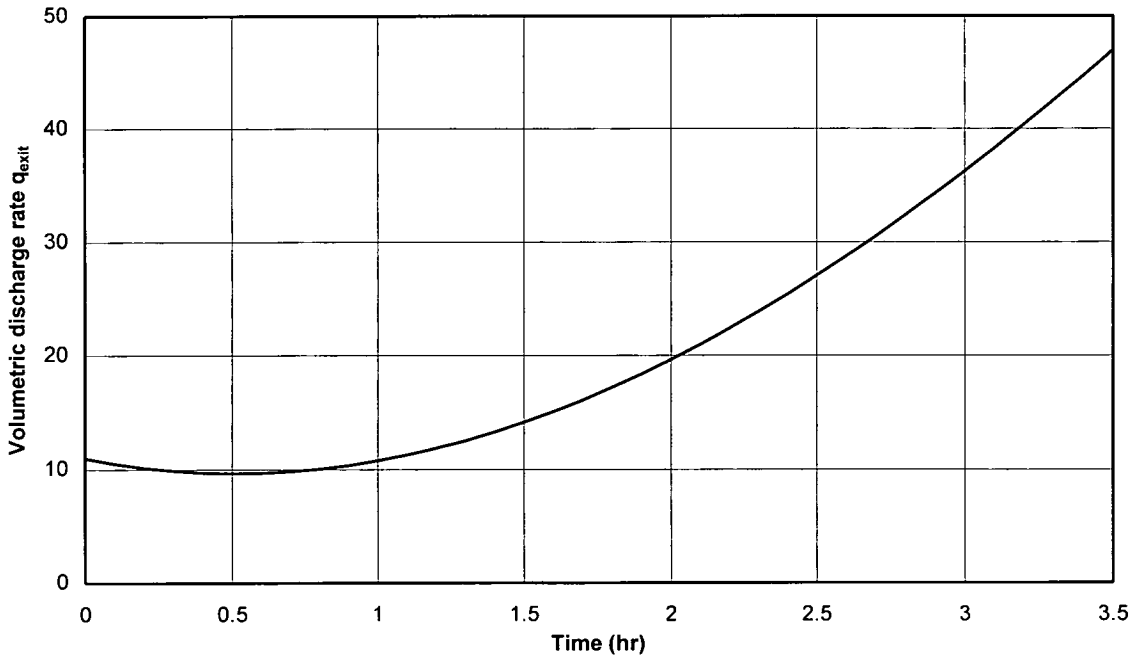

Fig 6.2: Variation of volumetric discharge rate with time in full scale silo

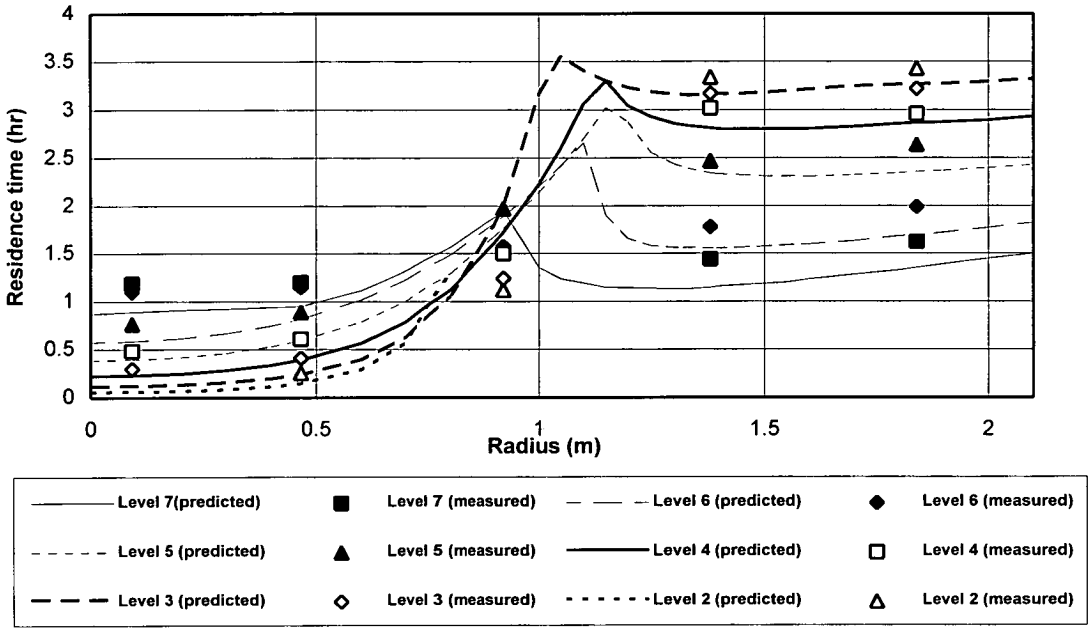

(a) B=25.8mm, h_t=0.0m

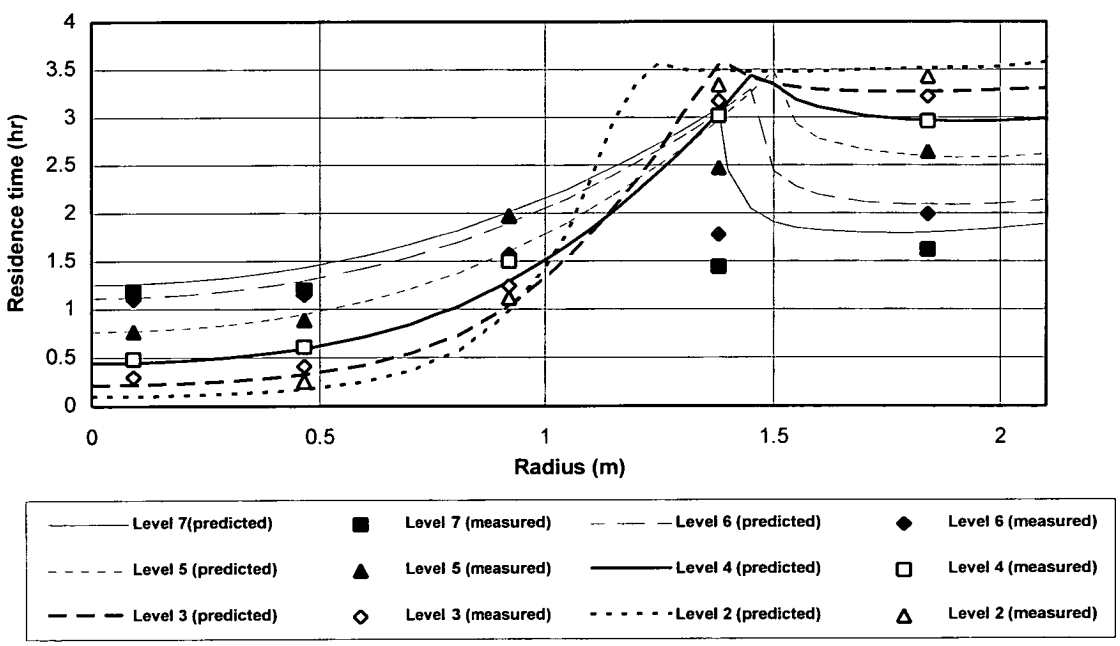

(b) B=51.6mm, h_t=0.00m

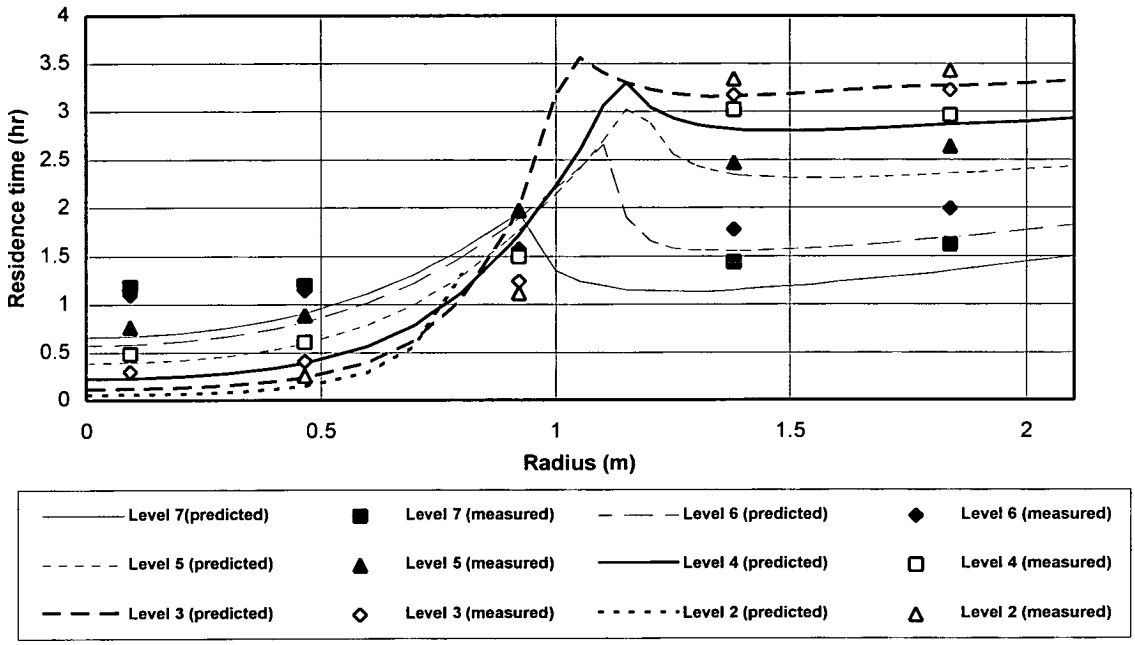

(c) B=25.8mm, h_t=0.5m

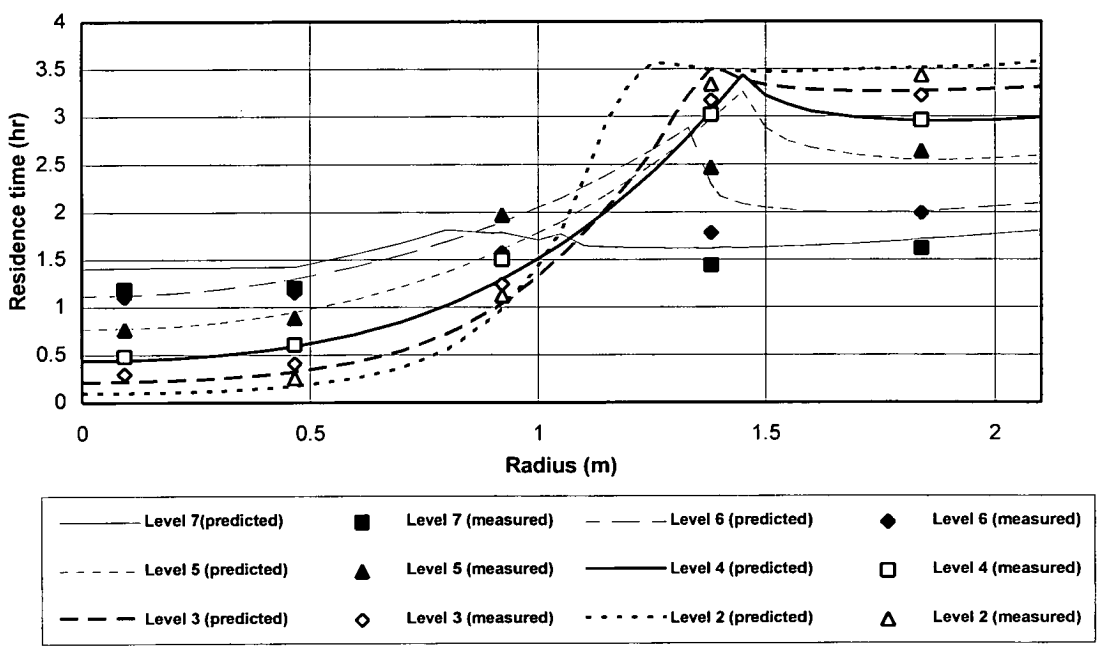

(d) B=51.6mm, h_t=0.5m

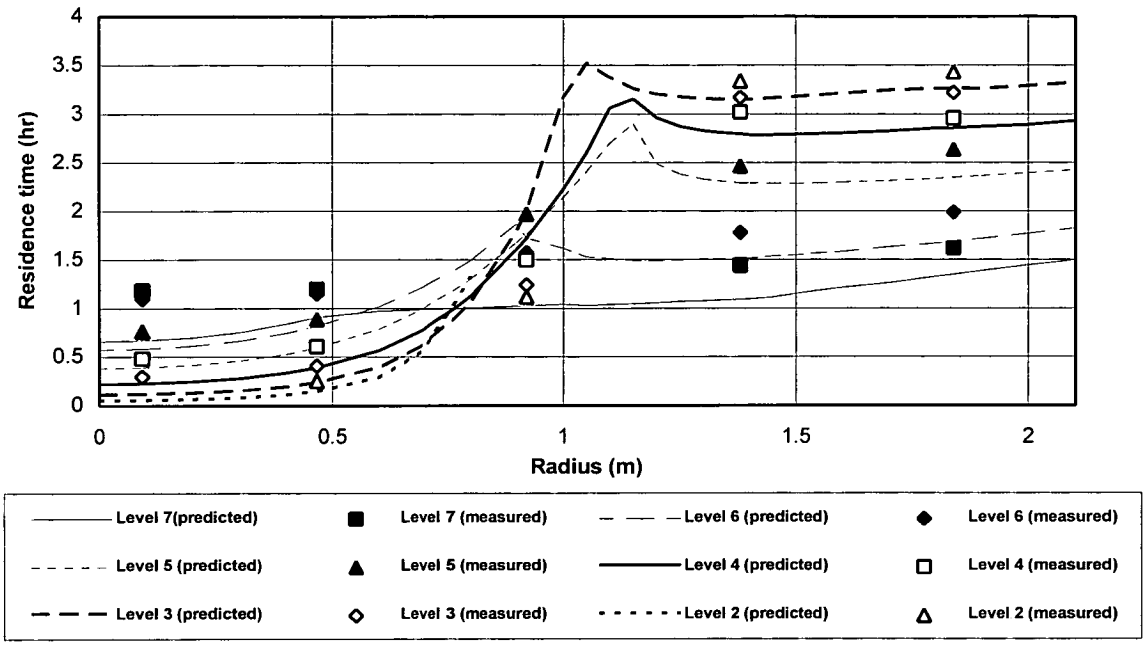

(e) B=25.8mm, h_t=1.0m

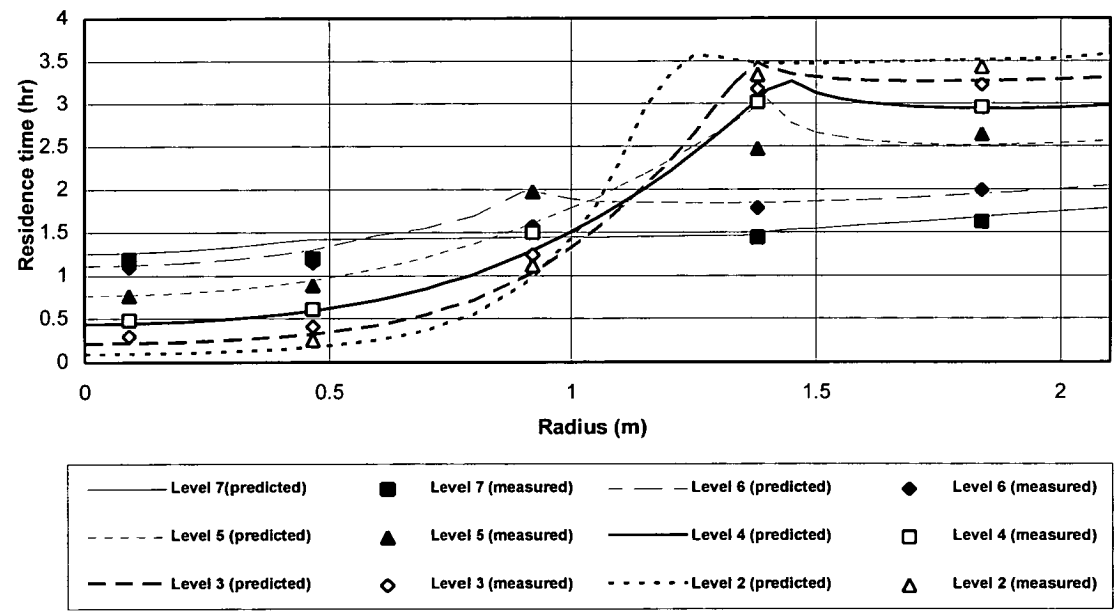

(f) B=51.6mm, h_t=1.0m

Fig. 6.3: Comparison between predicted and measured residence times in full scale silo

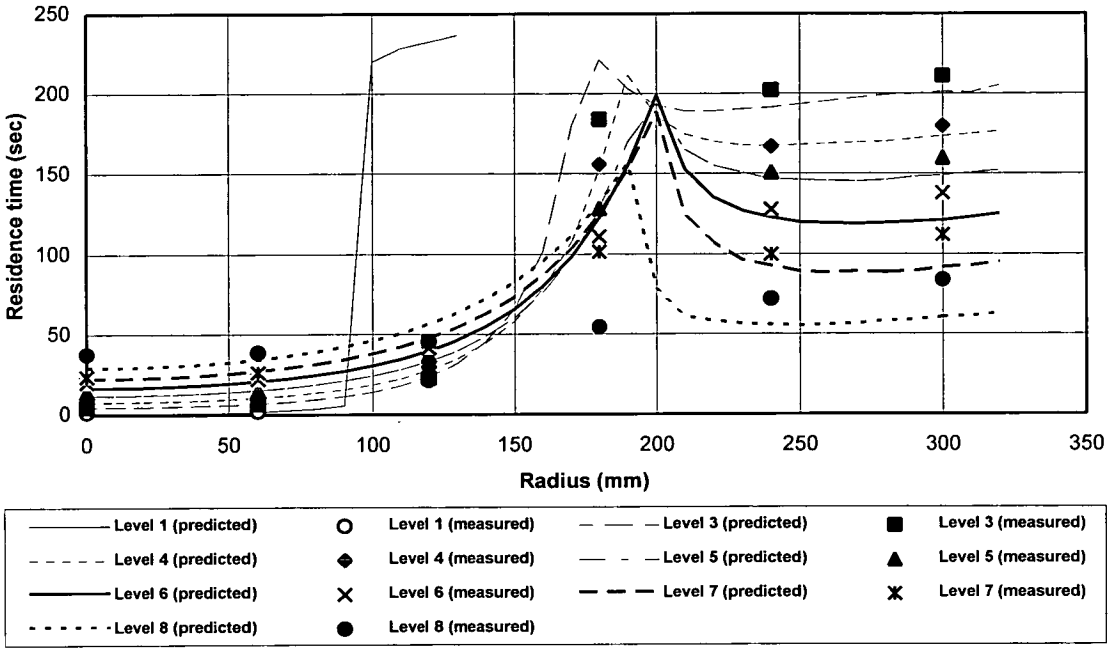

(a) B=6.6mm, h_t=0.0m

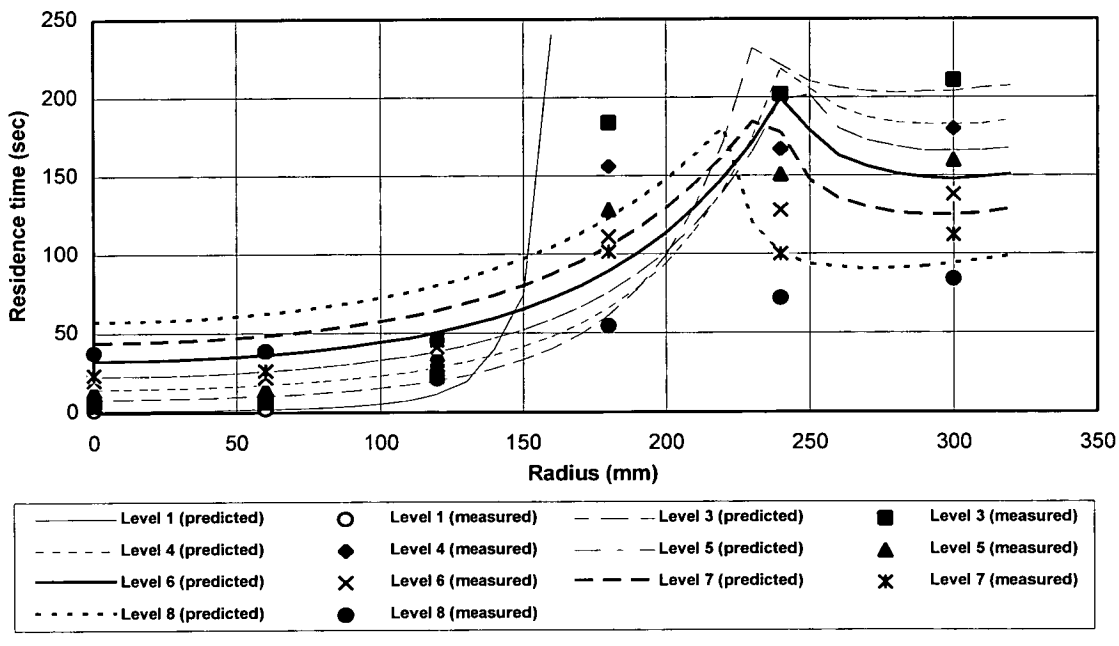

(b) B=13.4mm, h_t=0.0m

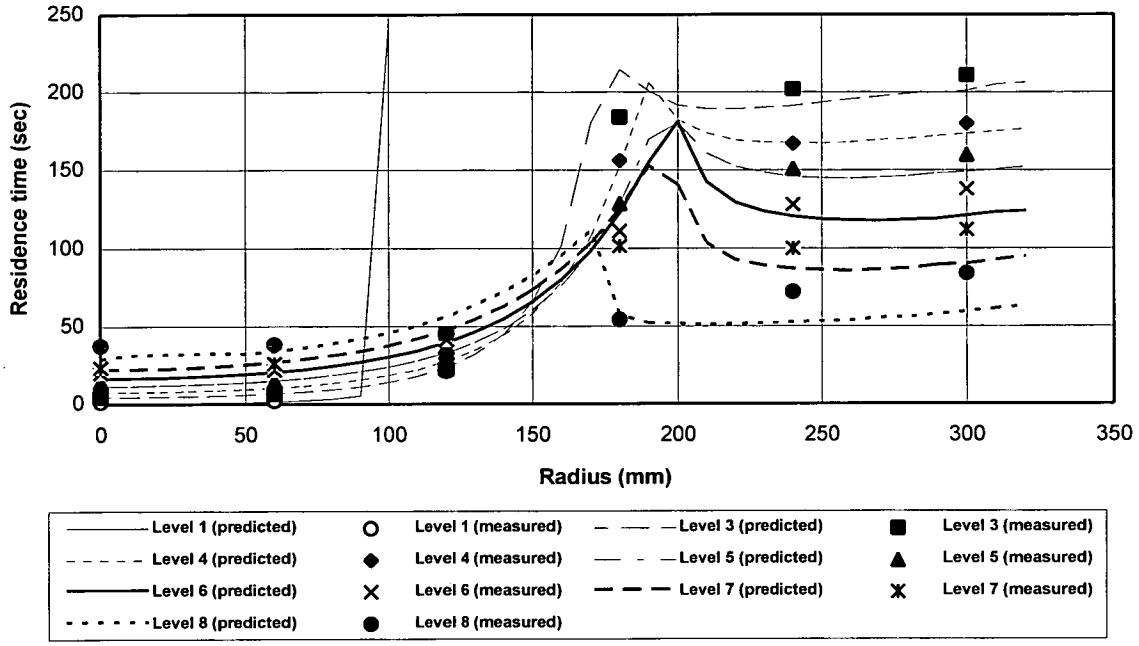

(c) B=6.6mm, h_t=0.05m

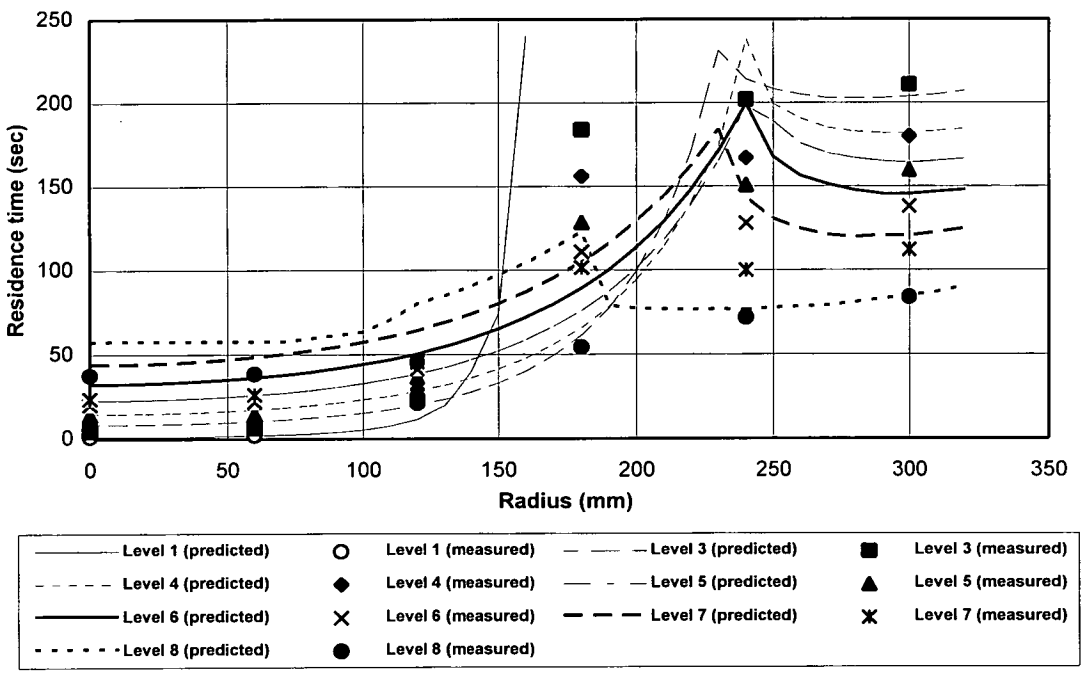

(d) B=13.4mm, h_t=0.05m

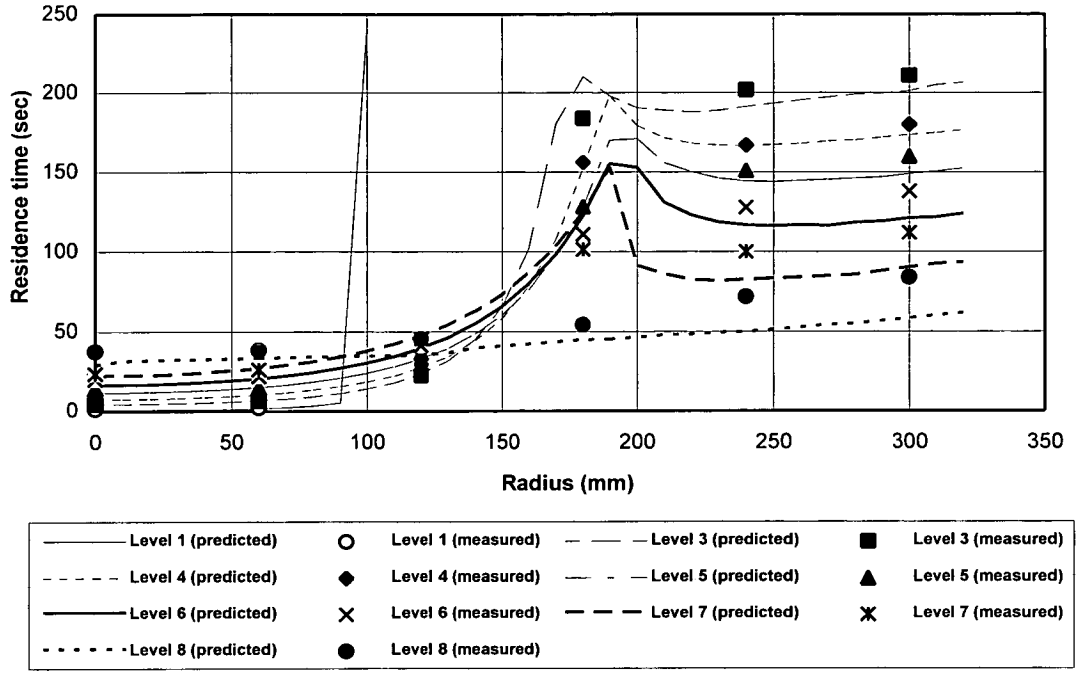

(e) B=6.6mm, h_t=0.10m

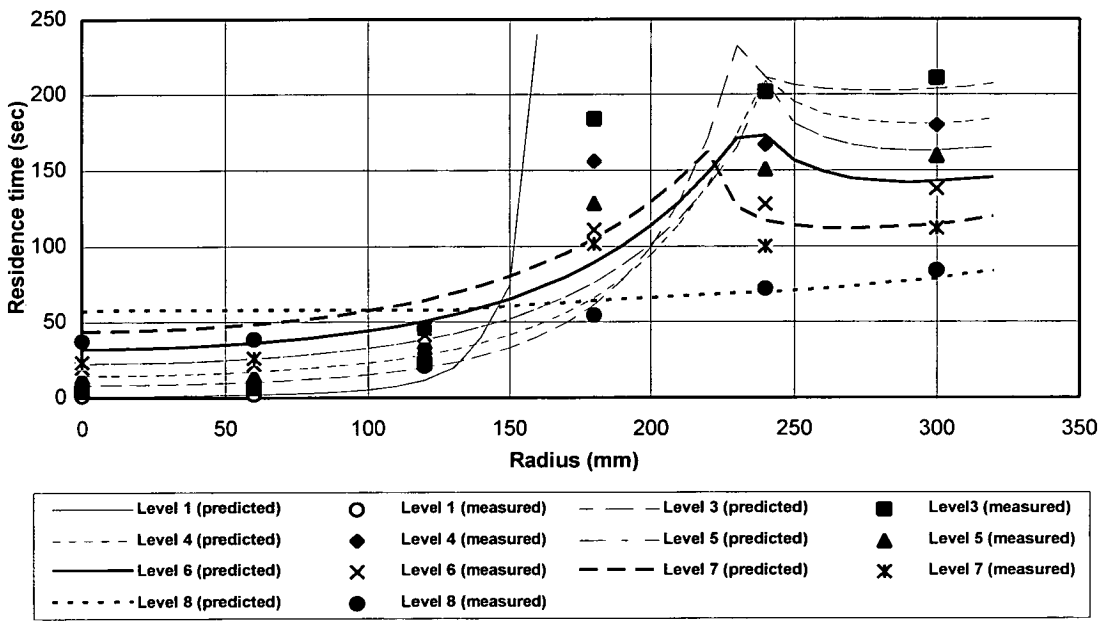

(f) B=13.4mm, h_t=0.10m

Fig. 6.4: Comparison between predicted and measured residence times in half model silo

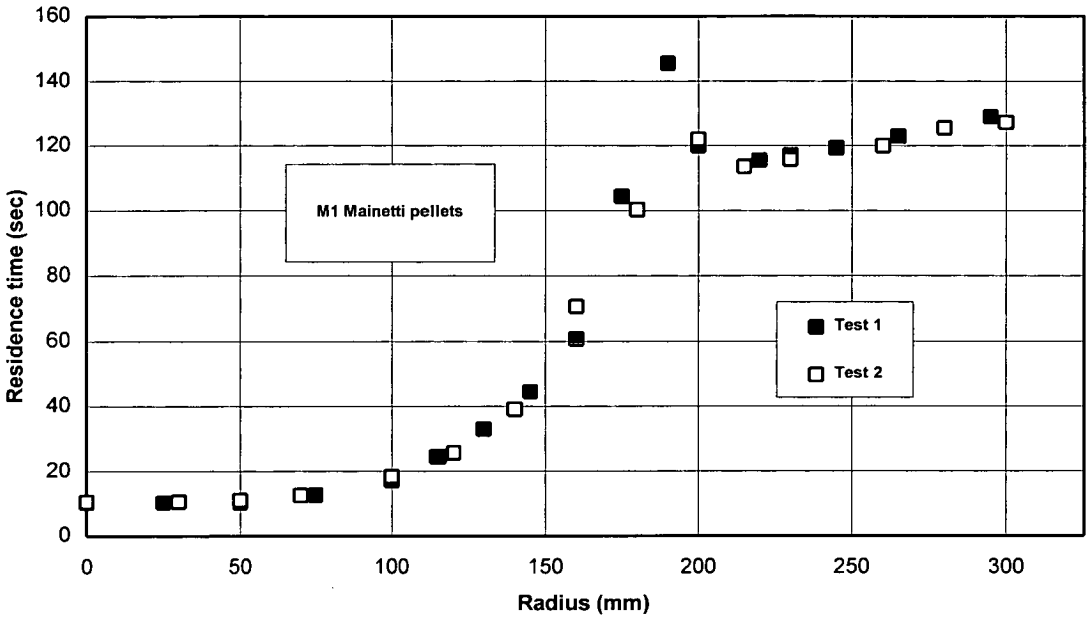

Fig. 6.5: Residence time observations at z=500mm with extensive seeding

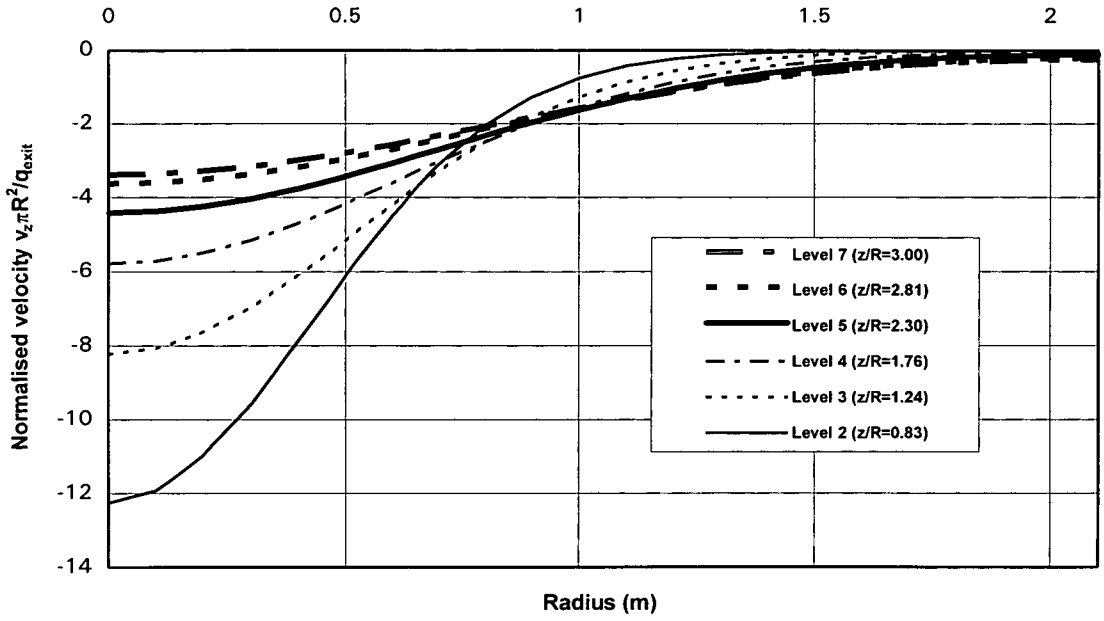

(a) at different heights

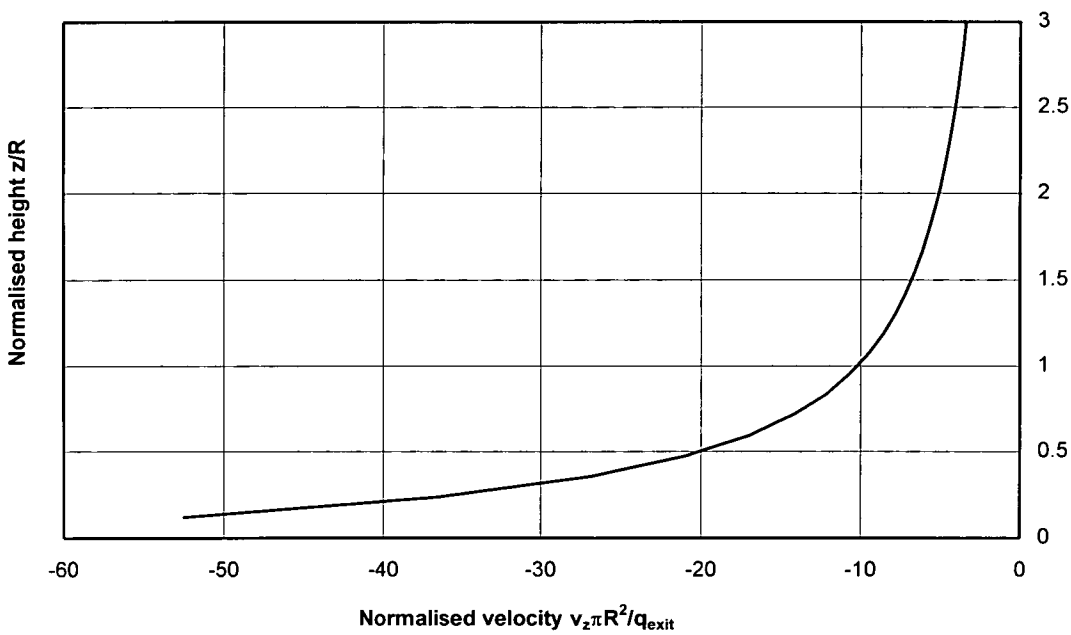

(b) along the central axis

Fig. 6.6: Vertical velocity distribution in full scale silo

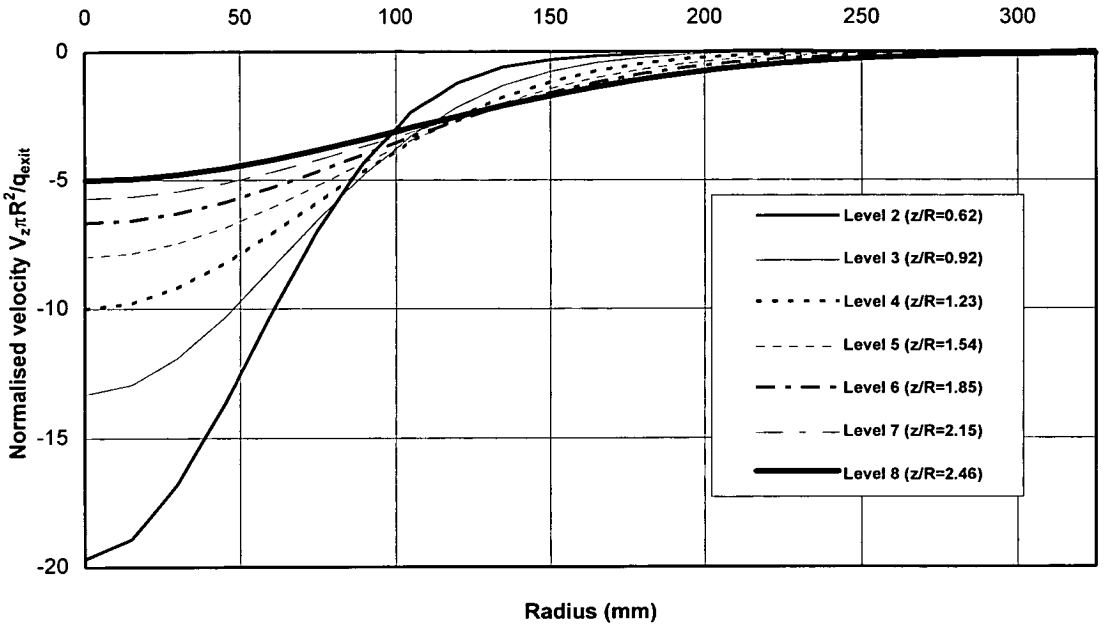

(a) at different heights

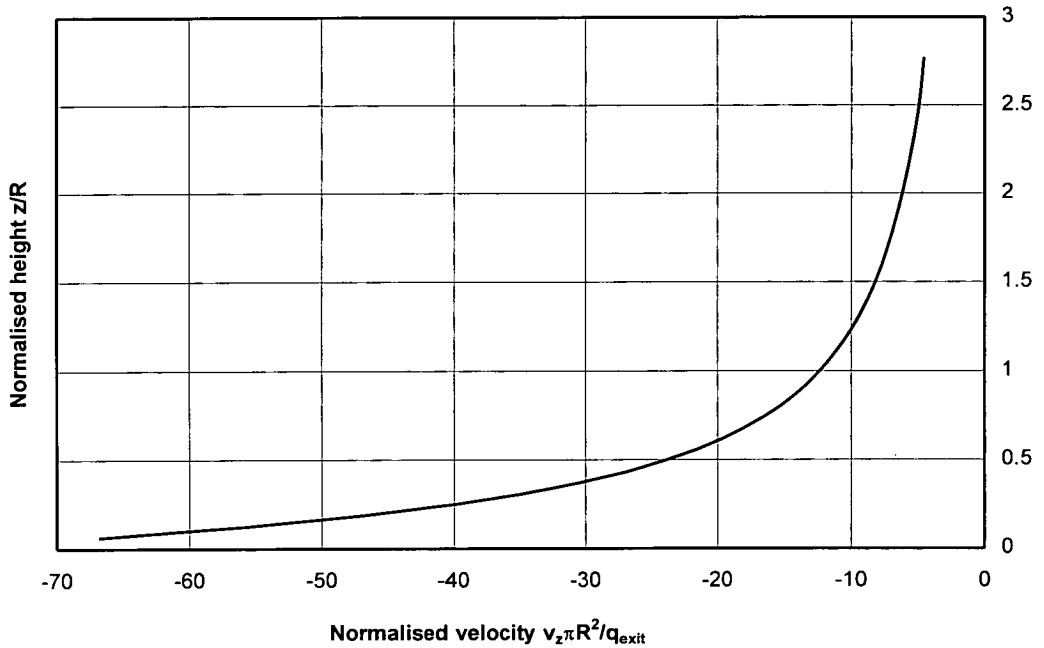

(b) along the central axis

Fig 6.7: Vertical velocity distribution in half model silo

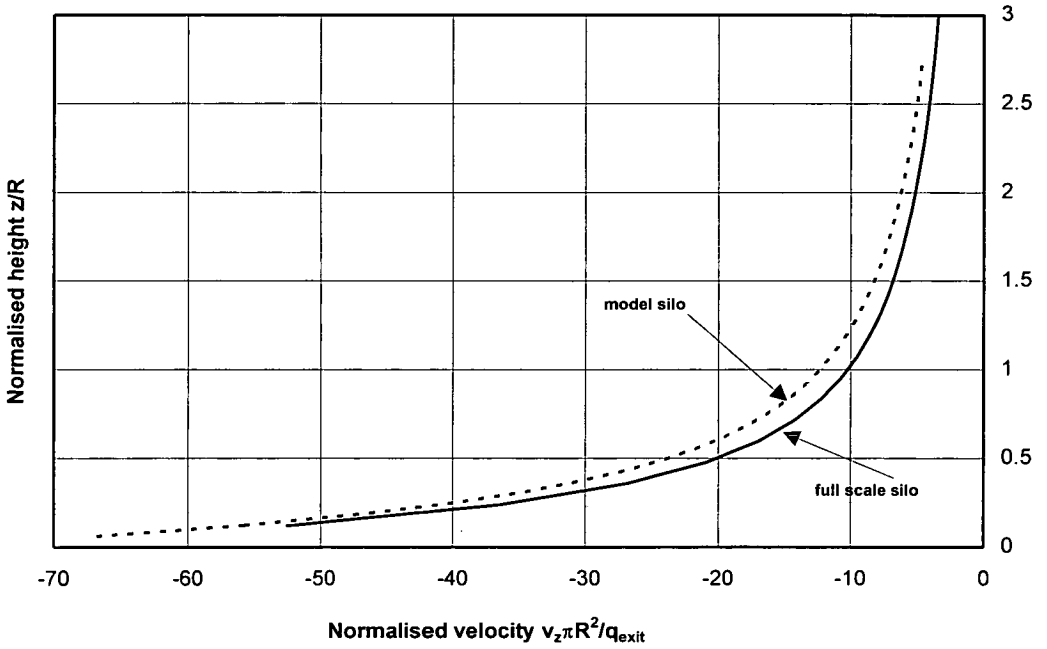

Fig 6.8: Comparison of vertical velocity along the central axis in full scale silo and half model silo

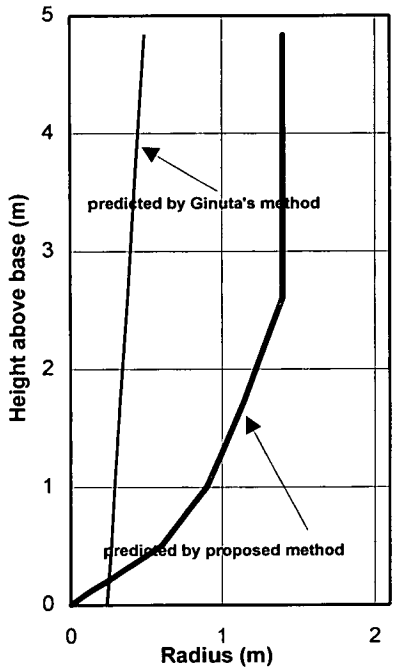

(a) full scale silo

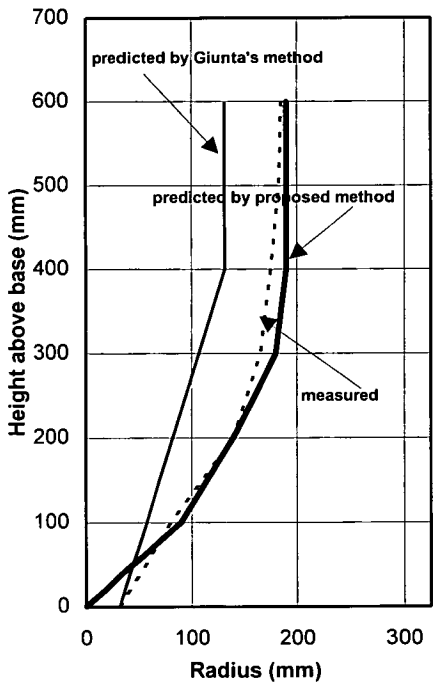

(b) half model silo

Fig. 6.9: Comparison of flow channel boundaries (FCB)

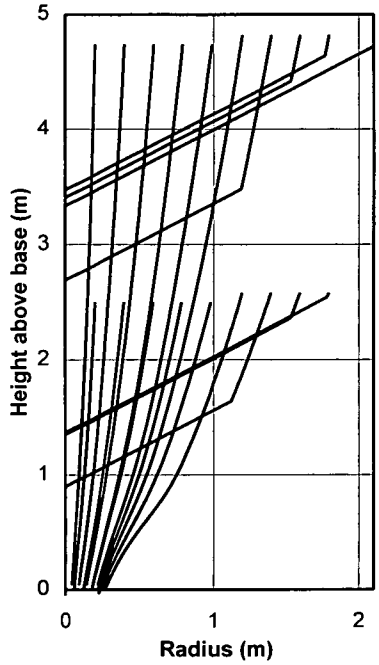

(a) full scale silo

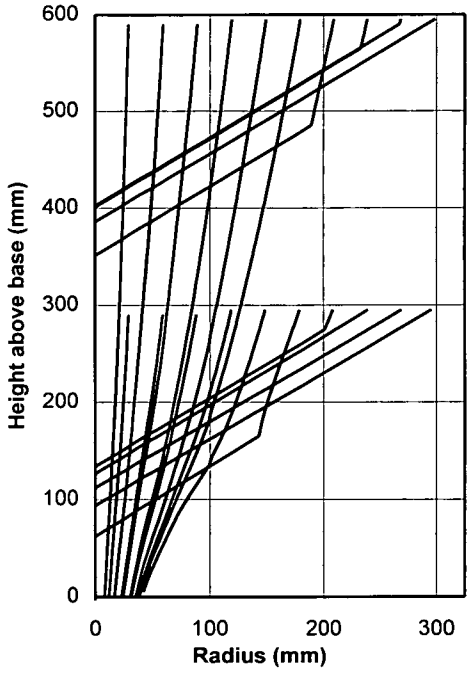

(b) half model silo

Fig. 6.10: Particle trajectories in different zones

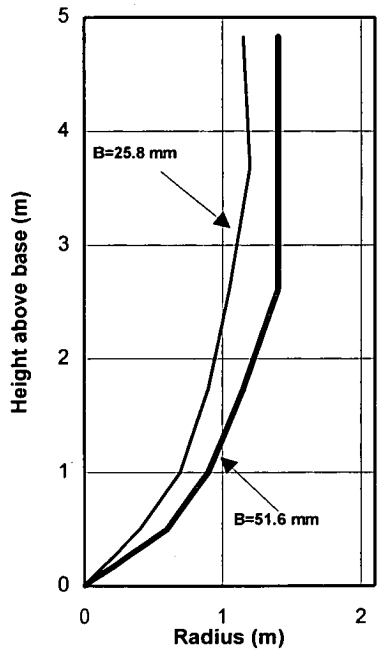

(a) full scale silo (h_t = 1.0m)

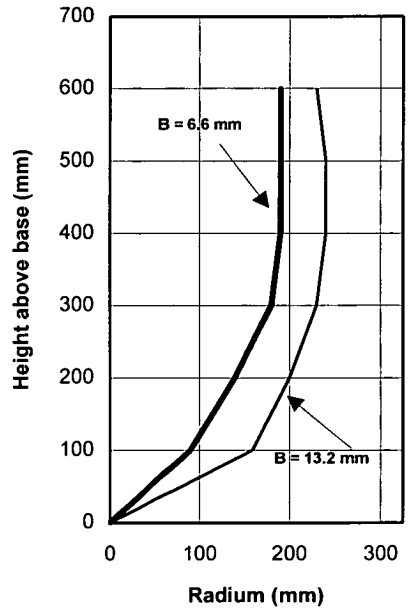

(b) half model silo (h_t = 0.1m)

Fig 6.11: Comparisons of FCBs predicted by different kinematic constants

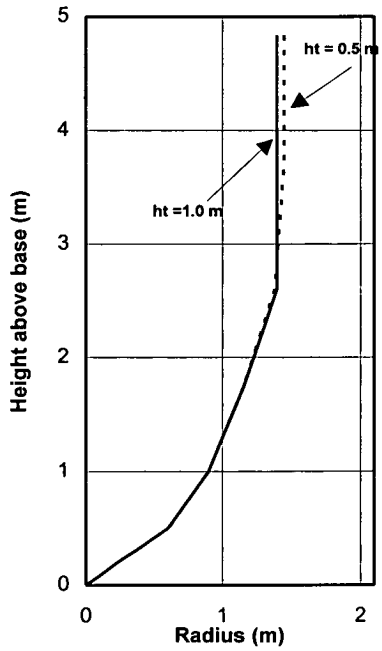

(a) full scale silo (B = 51.6 mm)

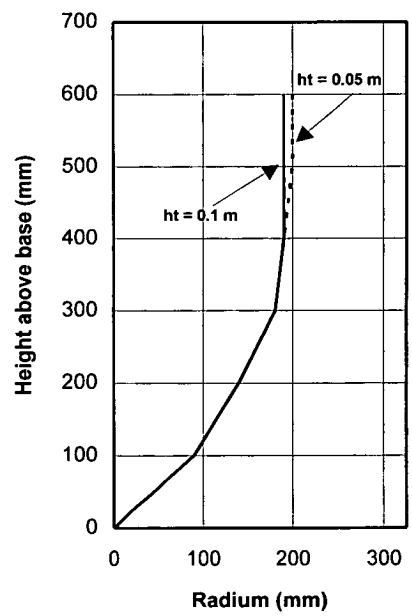

(b) half model silo (B = 6.6 mm)

Fig 6.12: Comparisons of FCBs predicted by different thicknesses of top flow layer

CHAPTER 7

INVERSE ANALYSIS OF RESIDENCE TIME OBSERVATIONS

7.1 Introduction

To fully understand the complicated flow behaviour of granular solids in silos during discharge, considerable efforts have been spent in both theoretical and experimental studies. Although many models based on continuous or discrete solid mechanics, fluid mechanics and stochastic theory etc. have been put forward, none of them can accurately predict the solids flow patterns during emptying.

In this chapter, an attempt is made to develop a technique to infer the flow patterns including the time-dependent FCB from measured residence times of the markers by employing an inverse analysis method. In this deduction technique, the residence time field is treated as the output, and the solids flow is required to satisfy the continuity equation to provide the working mechanism of the system. The unknown velocities and trajectory paths of particles are identified by applying an optimisation algorithm. In the next chapter, the deduction technique is applied to the model silo under concentric discharge.

7.2 Setting out of the inverse analysis

Inverse analysis is a process to infer the system working mechanism based on the known input and output, or infer the input of the system based on the known output

and the system working mechanism. This section outlines the procedure to infer the time-dependent FCB, the particle velocity field and the particle trajectories using the inverse analysis technique.

- First, the shape of the FCB is assumed to be given by the trajectory path of the outermost particle in the core flow zone.

- With the shape defined, the FCB at any instant is then determined by finding the least squares of the differences between the computed and measured times of particles in motion subject to satisfying the mass continuity equation.

- At every instant when the FCB is inferred, the influx of solid through a level is calculated. If the calculated influx of solid is found to be equal to the volumetric discharge rate, the FCB at that time is taken to have reached the fully developed stage.

- Once the FCBs at different instants are identified, at a selected level the time for each particle to start moving is then determined according to its location, and the velocity distribution is finally deduced.

7.3 Formulation of the inverse analysis

7.3.1 Assumptions

The technique to infer the solids flow in silos during concentric emptying is based on the following assumptions.

- Once the FCB hits the undeformed top surface, it expands gradually as shown in Fig. 7.1. The particle trajectory of the outermost particle in the central core flow zone at a particular time is considered as the shape of the FCB at that time.

- The top surface profile and the top flow layer vary as shown in Fig. 7.2 during discharge.

7.3.2 Generation of residence time field in silo

In this deduction technique, the only known results are the measured residence times of the markers. The first task is to generate the residence time field in the whole silo from these measured residence times. As the deduction procedure is directly based on the residence time field, it is desirable to obtain a residence time field as precisely as possible.

There are several possible approaches to generate the residence time field in the whole silo from measured residence times. Here the residence time of a particle is interpolated from four measured residence times T_1, T_2, T_3 and T_4 at the four nodes 1, 2, 3 and 4 which are closest to the particle (Fig. 7.3). The mapping relationship is expressed as follows

$$T = \sum_{i=1}^{4} N_i T_i \tag{7.1}$$

where T_i is the measured residence time at node i, and N_i is the mapping function.

A linear mapping function is employed

$$N_i = \frac{1}{4}(1 + \xi_i\xi)(1 + \eta_i\eta) \tag{7.2}$$

in which ξ_i, η_i are the values of the local coordinates at node i.

7.3.3 Equations for computing time of movement of a particle

7.3.3.1 Derivation of the velocity equations

The curved trajectory path of a particle in the core flow zone is approximated by a number of linear segments as shown in Fig. 7.4. For a trajectory path from node i-1 to node i as shown in Fig. 7.5, the radial and vertical velocities of a particle have the relationship

$$v_r = \tan\theta_i \, v_z \tag{7.3}$$

in which v_r and v_z are the radial and vertical components of the velocity of a particle along the line, and θ_i is an angle between the trajectory path and the vertical axis.

Considering a cylindrical silo under concentric discharge, the continuity equation has the form

$$\frac{\partial v_z}{\partial z} + \frac{\partial v_r}{\partial r} + \frac{v_r}{r} = 0 \tag{7.4}$$

Substituting Eq. (7.3) into Eq. (7.4) yields

$$v_z = c\, e^{r - \ln r - \tan\theta_i z} \tag{7.5}$$

$$v_r = c\, e^{r - \ln r - \tan\theta_i z} \tan\theta_i \tag{7.6}$$

where c is a parameter which can be determined in accordance with the time of movement of a particle from node i-1 to i.

The magnitude of the velocity along the line is

$$v = \sqrt{v_z^2 + v_r^2} = c\, e^{r - \ln r - \tan\theta_i z} \sqrt{1 + \tan^2\theta_i} \qquad (7.7)$$

7.3.3.2 Calculation of the moving time of a particle

After obtaining Eqs. (7.5) and (7.6) for computing the radial and vertical velocities of a particle, the time taken for a particle to move from node i-1 to node i can be calculated as

$$\Delta t_{i-1,i} = f_i(c_i, r_{i-1}, r_i, z_{i-1}, z_i) = \int_{z_i}^{z_{i-1}} \frac{1}{v_z} dz$$

$$= \int_{z_i}^{z_{i-1}} \frac{1}{c_i} e^{-\{r_{i-1} + \frac{r_i - r_{i-1}}{z_i - z_{i-1}}(z - z_{i-1}) - \ln[r_{i-1} + \frac{r_i - r_{i-1}}{z_i - z_{i-1}}(z - z_{i-1})] - \tan\theta_i z\}} dz \qquad (7.8)$$

The total moving time of a particle from its original position to the outlet is therefore

$$t_{tot} = \sum_{i=1}^{n} \Delta t_{i-1,i} \qquad (7.9)$$

where n is the total number of linear segments of the trajectory path.

7.3.3.3 Determination of the trajectory path of a particle

As the initial position (z_o, r_o) and the final position (0, 0) of a particle are known, the radial coordinates at other levels (r_1, r_2, ...,r_{n-1}) where the particle goes through can be determined by solving the following set of n non-linear equations

$$\begin{aligned} \Delta t'_{0,1} &= f_1(c_1, r_o, r_1, z_o, z_1) \\ \Delta t'_{0,1} + \Delta t'_{1,2} &= f_2(c_2, r_1, r_2, z_1, z_2) + f_1(c_1, r_o, r_1, z_o, z_1) \\ &\cdots\cdots \\ \sum_{i=1}^{n} \Delta t'_{i-1,i} &= \sum_{i=1}^{n} f_i(c_i, r_{i-1}, r_i, z_{i-1}, z_i) \end{aligned} \qquad (7.10)$$

where f_i is a function for calculating the time taken for a particle to move from node i-1 to node i, given in Eq. (7.8).

The term $\Delta t'_{i-1,i}$ in Eq. (7.10) denotes the "measured" time taken for a particle to move from node i-1 to node i. For particles which start to move as soon as the outlet is open, the time in motion can be obtained from the residence time field in the silo as

$$\Delta t'_{i-1,i} = T_{i-1} - T_i \qquad (7.11)$$

where T_{i-1} and T_i are the interpolated residence times at the nodes i-1 and i respectively.

Equation (7.10) is a set of n equations with 2n-1 unknowns (r_1,...,r_{n-1}) and (c_1,...,c_n). To solve the problem, another n-1 equations need to be found. These are given by the equations which establish the continuity of velocities at the nodes

$$c_i = c_{i+1} e^{(-\tan\theta_{i+1} + \tan\theta_i) z_i} \sqrt{\frac{1+\tan^2\theta_{i+1}}{1+\tan^2\theta_i}} \qquad i = 1,...,n-1 \qquad (7.12)$$

Thus, the 2n-1 unknowns in Eq. (7.10) can theoretically be solved.

The goal of the analysis is to find the particle trajectory which gives minimum errors in predicting the residence time observations. This is achieved by finding the least squares of the difference between the computed and measured moving times. It is expressed as: to find a vector $\mathbf{x} = [v_{zo}, r_1, r_2, ..., r_{n-1}]^T$

$$\text{min.} \quad F(v_{zo}, r_1, ..., r_{n-1}) = \sum_{i=1}^{n} (\Delta t_{o,i} - \Delta t'_{o,i})^2 \qquad (7.13)$$

in which

$$v_{zo} = c_o e^{r_o - \ln r_o - \tan\theta_i z_o} \qquad (7.14)$$

This is an unconstrained non-linear optimisation problem with n design variables, in which F is termed the objective function, and the vector of the unknowns $\mathbf{x} = [v_{zo}, r_1, r_2,..., r_{n-1}]^T$ is termed the design variables.

In funnel flow, not all the particles move from the beginning of discharge. A significant portion of solid remains stationary for some time before starting to move towards the outlet. Under such circumstances, the term $\Delta t'_{i-1,i}$ in Eq. (7.11) should be modified by the following equation

$$\Delta t'_{i-1,i} = (T_{i-1} - T_s) - (T_i - T_s) \qquad (7.15)$$

where T_s is the time in which the particle remains stationary.

7.3.4 Mathematical formulation for deducing FCB

7.3.4.1 Deduction of the time dependent FCB

According to the assumptions in Section 7.2.1, the trajectory path of the outermost particle in the core flow zone is considered to be the shape of the FCB at the instant. It follows that the instantaneous FCB can be deduced (Fig. 7.6) by finding the trajectory path of the outermost particle at the instant which satisfies the condition that the volume of the discharged solid is the sum of the displaced volume in the top solids surface and the volume resulting from the dilation of solid in the core flow zone. Mathematically, it can be stated as: to find a vector $\mathbf{x} = [v_{zo}, r_o, r_1, ..., r_{n-1}]^T$

$$\text{min.} \quad F(v_{zo}, r_o, r_1, ..., r_{n-1}) = \sum_{i=1}^{n} (\Delta t_{o,i} - \Delta t'_{o,i})^2 \tag{7.16}$$

subject to the condition

$$Q_{exit} = Q_{cone} + \psi Q_{flow} \tag{7.17}$$

where ψ is the dilation of solid, Q_{exit}, Q_{cone} and Q_{flow} are respectively the discharged volume of solid, the volume of the inverted cone at the top solid surface and the volume of solid in the core flow zone.

This is a constrained optimisation problem with n+1 design variables. Equation (7.16) is similar to Eq. (7.13) for solving the particle trajectory field, with the exception that the number of design variables in Eq. (7.16) is one more than that in Eq. (7.13). A two-stage strategy is therefore proposed so that the program is

capable of solving both the unconstrained and constrained problems. These are outlined as follows

Stage 1

- Choose a level where the FCB and the top flow layer meet and pick a set of trial values of r. The selection of the level may be seen somewhat arbitrary at first. However, as can be seen in Fig. 7.7, the optimum FCB is very much controlled by the optimisation procedures.

- Solve the unconstrained optimisation problem of Eq. (7.16) for the set of the trial values of r to locate the optimum FCB.

Stage 2

- Determine the FCB from the above set of the optimum results by finding an optimum point which satisfies the constraint condition Eq. (7.17).

To solve the unconstrained and constrained optimisation problems, many techniques such as the sequential linear programming method, the sequential quadratic programming method, the feasible direction method, gradient project method and the generalised reduced gradient method have been developed (Kirsch 1981; Morris 1982; Arora 1989; Wang *et al* 1991). In this thesis the generalised reduced gradient method (GRG method) is employed. A description of this method is given in the appendix of this chapter.

7.3.4.2 Deduction of fully developed FCB

It has been observed by many that after some time in silo emptying, the FCB tends to stabilise away from the top solid boundary which progressively moves downwards. Once the FCB away from the top flow layer has stabilised, it is considered to be fully developed and the influx of solids flowing through any horizontal section at the

lower part of the FCB will be constant. The fully developed FCB can therefore be deduced by finding the instantaneous FCB for which the influx of solid through a horizontal section is equal to the volumetric discharge rate.

Once the expansion of the FCB with time is evaluated, the time before each particle starts to move can be determined according to its initial position. The vertical velocity distribution v_z of the particles at a selected level i can be deduced. The influx of solids flowing through this level is given by

$$q = \int_0^{r_i} \pi r v_z dr \tag{7.18}$$

where r_i is the radial coordinate of the FCB at the selected level and v_z is the vertical velocity.

As the material in the core flow zone possesses a looser density, the influx of solids flowing through the level has to be converted to the influx of solids at the initial packed state for comparison with the volumetric discharge rate, thus

$$q_1 = (1 - \psi)q \tag{7.19}$$

where q_1 is the flow influx through the level at the packed state.

If the relationship between the influx of solids through the level and the volumetric discharge rate satisfies the following equation, the FCB at the specific time can be treated as the fully developed FCB.

$$\frac{|q_1 - q_{exit}|}{q_{exit}} \leq \varepsilon_q \tag{7.20}$$

where ε_q is a convergence standard.

7.3.5 Extension of technique to account for varying volumetric flow rate

The volumetric flow rate does not appear in any of the above equations as the flow has been treated as a constant so far. However, in some cases the volumetric flow rate is controlled for other purposes. It is therefore necessary to extend the model to deal with the varying volumetric flow rate.

If the volumetric flow rate varies during discharge, the moving time for a particle depends on not only its initial position, but also on the volumetric flow rate. To take the effect of the changing flow rate into consideration, the radial and vertical velocities in Eqs. (7.5) and (7.6) are multiplied by the following normalising factor

$$\lambda(t) = \frac{q_{exit}(t)}{q_{exito}} \tag{7.21}$$

where $q_{exit}(t)$ is a function representing the volumetric flow rate, and q_{exito} is the volumetric flow rate at the beginning of discharge.

7.4 Calculation procedure

The deduction technique to infer from the measured residence times, the time-dependent FCB, the particle trajectory field and the velocity field in the core flow zone has been fully described above. The algorithm for implementing the calculations can be summarised as follows.

7.4.1 Inference of the time-dependent FCB

Stage 1

Step 1 input parameters including the positions and the residence times of the marker, the volumetric flow rate, the dilation of solid, the top surface profile and the filling height;

Step 2 select a level where the top flow layer and the FCB meet;

Step 3 choose m trial positions at the selected level, do loop for j = 1,...,m;

Step 4 assign initial values **x** for the trial position;

Step 5 if the volumetric flow rate is constant, go to Step 6, otherwise, evaluate the normalising factor $\lambda(t)$;

Step 6 determine the optimum **x** using GRG algorithm.

Step 7 if j<m, j=j+1, go to 4, otherwise, print out the results, stop.

Stage 2

Step 1 do loop for j=1,...,m for the optimum design variables;

Step 2 calculate Q_{flow}, Q_{exit} and Q_{cone};

Step 3 If $[Q_{exit} - (Q_{cone}+\psi Q_{flow})]/Q_{exit} \leq \varepsilon_Q$ go to Step 4, otherwise, j=j+1 go to Step 2;

Step 4 print out the optimum parameters **x** and F, stop.

7.4.2 Inference of fully developed FCB

Step 1 do loop for i=1,...,k for the FCBs at different instants;

Step 2 select a level where the vertical velocity distribution is deduced;

Step 3 determine the times of particles to start moving according to their locations;

Step 4 infer the velocities of particles and calculate the influx of solid flowing through this level;

Step 5 if Eq. (7.20) is satisfied, go to Step 7, otherwise go to Step 6;

Step 6 i = i + 1, if i < k, go to Step 2;

Step 7 print the location of the final FCB, stop.

7.5 FORTRAN program

A FORTRAN program to infer the time-dependent FCB has been developed for the procedure outlined in Section 7.4. The input parameters are the positions and the residence times of the marker, the initial positions of particles and the time for which the solution is sought, the volumetric flow rate, the dilation of solid, the top surface profile and the filling height.

7.6 Concluding remarks

In this chapter, the inverse analysis theory is employed to infer the solids flow pattern in a silo. By using the measured residence times of markers as the output and continuity equation as the system working mechanism, a deduction technique to infer the expansion of the FCB, the trajectory paths and the velocities of particles in a concentrically discharging silo has been developed. The gradient-based GRG method is adopted to solve the optimisation problem. The technique is applied to the model silo tests in the next chapter.

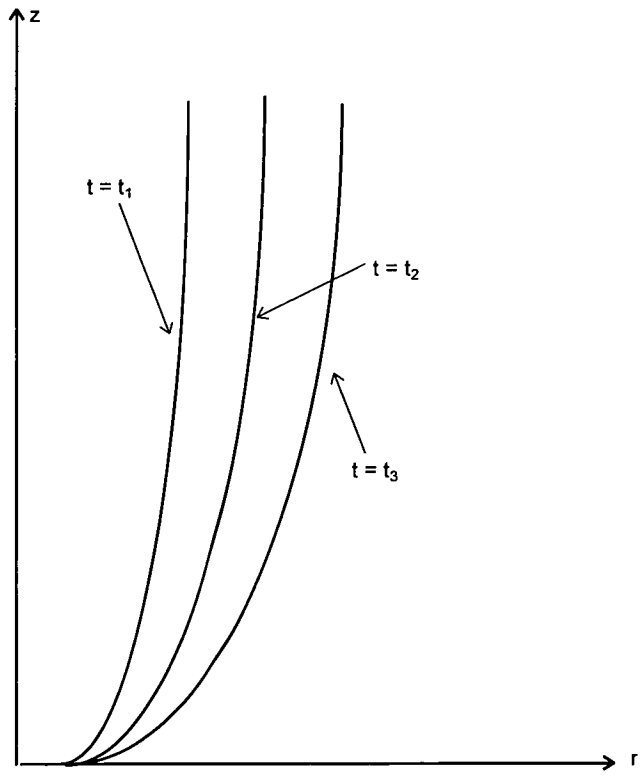

Fig. 7.1: The expansion of FCB during discharge

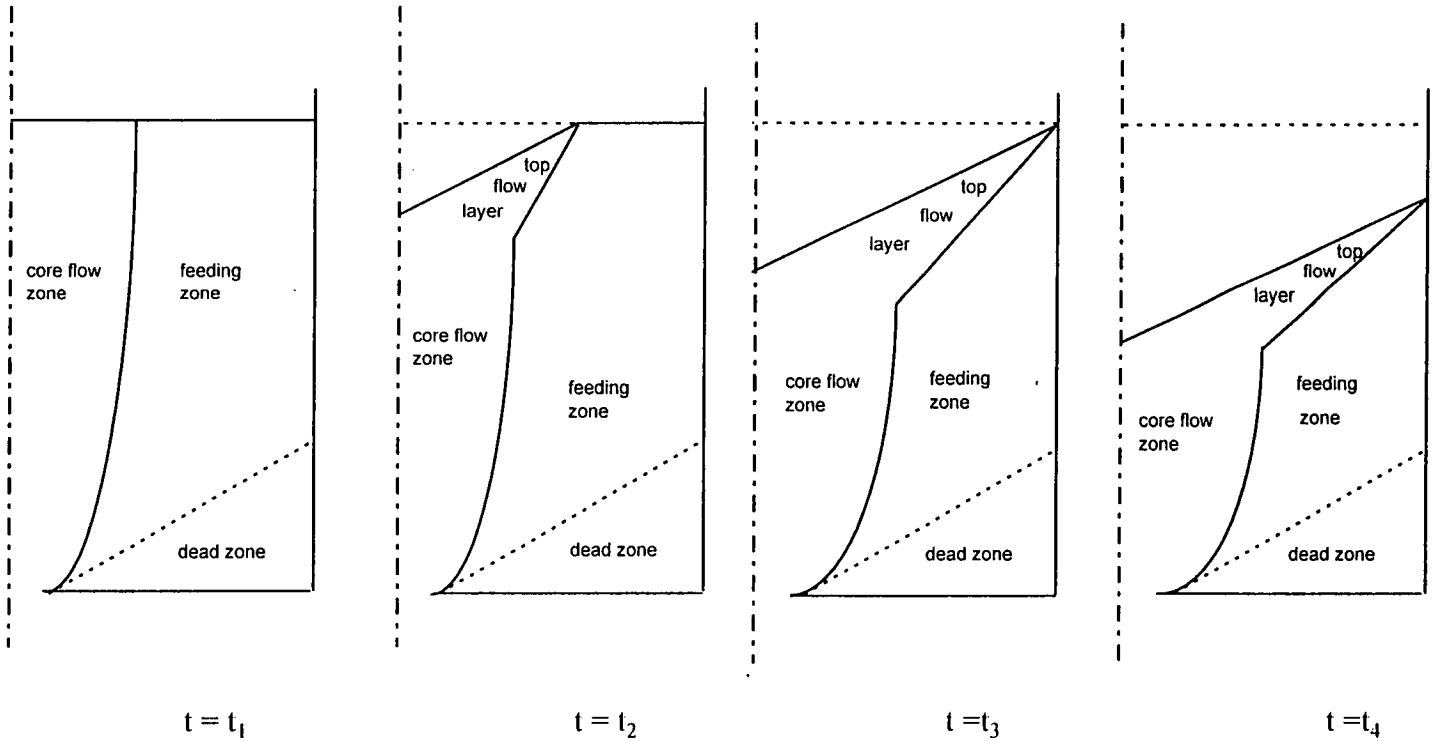

Fig.7.2: Assumed top flow layer during discharge

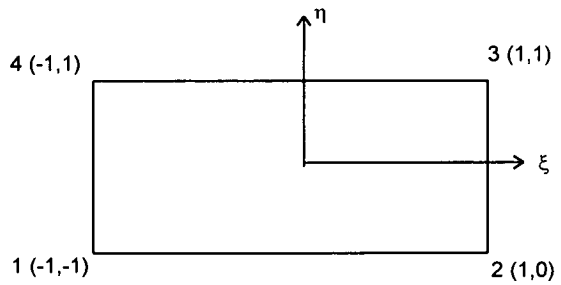

Fig.7.3: ξ,η coordinate system for interpolating residence time

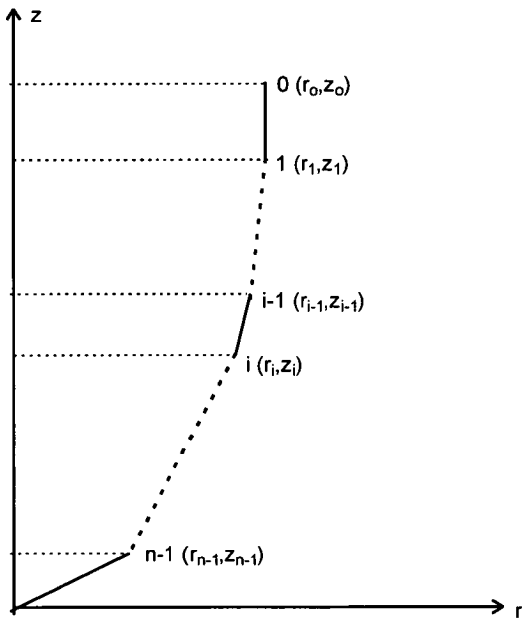

Fig. 7.4: Trajectory path of particle in core flow zone

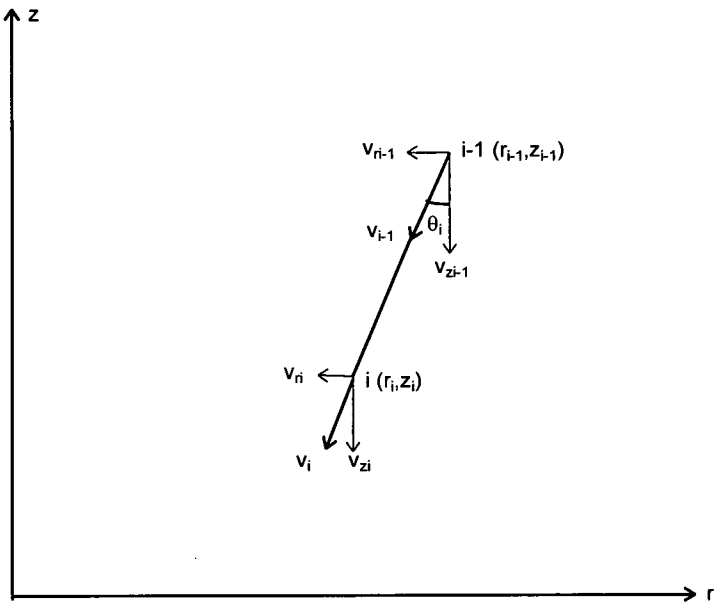

Fig. 7.5: Vertical and radial velocities of particle

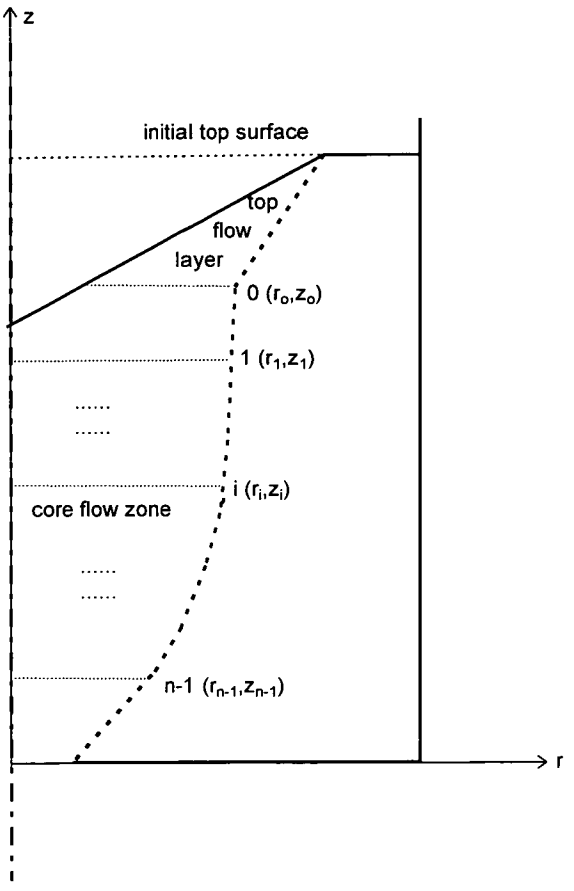

Fig. 7.6: Design variables describing FCB during discharge

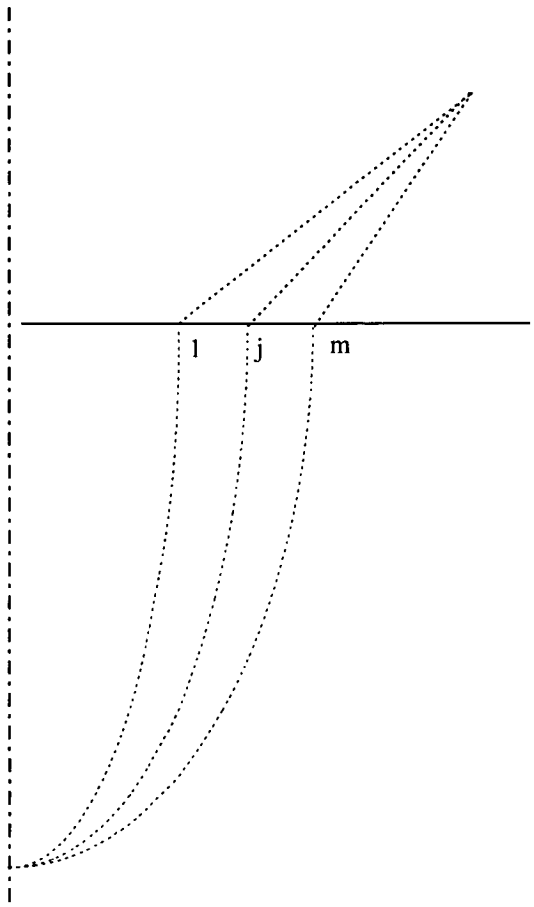

Fig. 7.7: A set of trial points for FCB deduction

APPENDIX

GENERALISED REDUCED GRADIENT (GRG) METHOD

A7.1 Introduction

So far, many techniques including the sequential linear programming method, the sequential quadratic programming method, the feasible direction method, gradient project method and the generalised reduced gradient method have been developed for solving the general constrained optimisation problems (Kirsch 1981; Morris 1982; Arora 1989). Of all these methods, the latter three techniques are believed to have the ability to handle complex engineering design problems. In this thesis the generalised reduced gradient (GRG) method is employed. As many textbooks in optimisation (Morris 1982; Arora 1989, Wang *et al* 1991) have detailed descriptions of the reduced gradient method, only the formulation of the GRG method is reviewed below.

A7.2 Mathematical statement of general optimisation problem

The constrained optimisation problem can generally be described as: find $\mathbf{x} = [x_1, x_2, \ldots, x_n]^T$, a design variable vector of dimension n, to minimise an objective function

$$F = F(\mathbf{x}) \tag{A7.1}$$

subject to the equality constraints

$$h_i(\mathbf{x}) = 0 \qquad i = 1,2,...,l \tag{A7.2}$$

and the inequality constraints

$$g_j(\mathbf{x}) \geq 0 \qquad i = 1,2,..., m \tag{A7.3}$$

and explicit bound on design variables

$$x_{il} \leq x_i \leq x_{iu} \qquad i = 1,2,...,n \tag{A7.4}$$

where x_{il} and x_{iu} are respectively the smallest and largest allowed values for the *i*th design variable x_i. Generally speaking, the equality constraints Eq. (A7.2) and inequality constraints Eq. (A7.3) are implicit functions of the design variables **x** and are complicated and difficult to treat in actual numerical implementation, while the explicit bound constraints of Eq. (A7.4) are quite simple and easy to deal with.

A7.3 Generalised reduced gradient method

A7.3.1 Principles of GRG method

The GRG optimisation algorithm, which is an extension of the reduced gradient method to accommodate non-linear inequality constraints, is one of the most efficient methods used to solve non-linear programming problems.

Consider the optimisation problem with equality constraints as follows

$$\text{min.} \quad F(\mathbf{x}) \qquad \mathbf{x} \in E^n \tag{A7.5}$$

$$\text{s.t.} \quad h_r(\mathbf{x}) = 0 \qquad r=1,2,...,l \tag{A7.6}$$

$$\mathbf{x} \geq 0 \tag{A7.7}$$

The general inequality constraints shown in Eq. (A7.3) can be converted to equality constraints by adding slack variables

$$h_{l+j}(\mathbf{x}) = g_j(\mathbf{x}) - x_{n+j} = 0 \qquad j=1,2,...,m \tag{A7.8}$$

in which x_{n+j} is termed slack variables.

A7.3.2 Determination of search direction

If $\mathbf{x}^k$ is a feasible point for the model described in Eqs (A7.5) to (A7.7), the equality constraints Eq. (A7.6) are linearly approximated at the point $\mathbf{x}^k$

$$h_r(\mathbf{x}) \approx h_r(\mathbf{x}^k) + \nabla h_r(\mathbf{x}^k)^T(\mathbf{x} - \mathbf{x}^k) \qquad r = 1,2,...,l \tag{A7.9}$$

Obviously, the first term on the right side hand in Eq. (A7.9) is zero as the feasible point $\mathbf{x}^k$ satisfies the equality constraint Eq. (A7.6). To utilise the above equation to predict the next feasible position, it is necessary that

$$\nabla h_r(\mathbf{x}^k)^T(\mathbf{x} - \mathbf{x}^k) = 0 \qquad r = 1,2,...,l \tag{A7.10}$$

This produces a set of l linear equations with n unknowns as the derivatives of the constraints $\nabla h_r(\mathbf{x}^k)$ are known. To get l variables from Eq. (A7.10), let

$$\mathbf{x}_B = [x_1, x_2,..., x_l]^T \tag{A7.11}$$

Thus the rest of the variables are defined as

$$\mathbf{x}_N = [x_{l+1}, x_{l+2}, \ldots, x_n]^T \tag{A7.12}$$

where $\mathbf{x}_B$ and $\mathbf{x}_N$ are vectors of independent and dependent design variables respectively.

According to the above classification of the variables, the gradient vector $\nabla h_r(\mathbf{x}^k)$ with l constraints is also separated as

$$\mathbf{J}(\mathbf{x}^k) = \begin{pmatrix} \frac{\partial h_1}{\partial x_1} & \frac{\partial h_1}{\partial x_2} & \cdots & \frac{\partial h_1}{\partial x_l} \\ \frac{\partial h_2}{\partial x_1} & \frac{\partial h_2}{\partial x_2} & \cdots & \frac{\partial h_2}{\partial x_l} \\ \cdots & \cdots & \cdots & \cdots \\ \frac{\partial h_l}{\partial x_1} & \frac{\partial h_l}{\partial x_2} & \cdots & \frac{\partial h_l}{\partial x_l} \end{pmatrix} \tag{A7.13}$$

and

$$\mathbf{C}(\mathbf{x}^k) = \begin{pmatrix} \frac{\partial h_1}{\partial x_{l+1}} & \frac{\partial h_1}{\partial x_{l+2}} & \cdots & \frac{\partial h_1}{\partial x_n} \\ \frac{\partial h_2}{\partial x_{l+1}} & \frac{\partial h_2}{\partial x_{l+2}} & \cdots & \frac{\partial h_2}{\partial x_n} \\ \cdots & \cdots & \cdots & \cdots \\ \frac{\partial h_l}{\partial x_{l+1}} & \frac{\partial h_l}{\partial x_{l+2}} & \cdots & \frac{\partial h_l}{\partial x_n} \end{pmatrix} \tag{A7.14}$$

For simplicity, Eq. (A7.10) is rewritten as

$$\mathbf{J}(\mathbf{x}_B - \mathbf{x}_B^k) + \mathbf{C}(\mathbf{x}_N - \mathbf{x}_N^k) = \mathbf{0} \tag{A7.15}$$

If $\mathbf{J}$ is not a irregular matrix, the independent variable vector $\mathbf{x}_B$ can be obtained by solving the linear equation (Eq. (A7.15))

$$\mathbf{x}_B = \mathbf{x}_B^k - \mathbf{J}^{-1}\mathbf{C}(\mathbf{x}_N - \mathbf{x}_N^k) \tag{A7.16}$$

Correspondingly, the objective function can be expressed as

$$F(\mathbf{x}) = F(\mathbf{x}_B^k - \mathbf{J}^{-1}\mathbf{C}(\mathbf{x}_N - \mathbf{x}_N^k), \mathbf{x}_N) \tag{A7.17}$$

The reduced gradient of function F with respect to $\mathbf{x}_N$ is

$$\mathbf{r}(\mathbf{x}_N) = \frac{\mathbf{dF}}{\mathbf{dx}_N} = \nabla_N F - (\mathbf{J}^{-1}\mathbf{C})\nabla_B F \tag{A7.18}$$

Thus, the search direction can be found

$$\mathbf{d}^k = \begin{pmatrix} \mathbf{d}_B^k \\ \mathbf{d}_N^k \end{pmatrix} \tag{A7.19}$$

in which

$$d_{Ni}^k = \begin{cases} -r_i(\mathbf{x}_N^k) & \text{if } r_i(\mathbf{x}_N^k) \le 0 \text{ or } r_i(\mathbf{x}_N^k) > 0 \text{ and } x_{Ni} > 0 \\ 0 & \text{Otherwise} \end{cases} \tag{A7.20}$$

$$\mathbf{d}_B^k = -(\mathbf{J}^{-1}\mathbf{C})\mathbf{d}_N^k \tag{A7.21}$$

A7.3.3 Solution to basic variables

Although the search direction Eq. (A7.19) produces a descent direction, it is not guaranteed that such direction is a feasible direction as the iterative point along $\mathbf{d}^k$ only satisfies the approximated linear function Eq. (A7.15). The common approach to enhance the approximation accuracy is to use limited step size, but producing non-

feasible points is unavoidable, especially when the constraint functions are highly non-linear. Another technique has been developed to deal with this problem.

After finding the search direction $\mathbf{d}_N^k$, the vector of the independent design variables $\mathbf{x}_B$ will be determined in the actual constraint space instead of determining the step size δ along $\mathbf{d}^k$. That is

$$h_r(\mathbf{x}_B, \mathbf{x}_N^k + \delta \mathbf{d}_N^k) = 0 \qquad r = 1,2,...,l \tag{A7.22}$$

where δ is parameter of step size.

The vector of independent design variables $\mathbf{x}_B$, which can be obtained by solving Eq. (A7.22), precisely satisfies all the constraint functions. Thus the new point obtained not only reduces the value of the objective function, but also is feasible. Due to more than l unknowns involved in the set of l equations, the parameter δ has to be identified with a trial method. For a trial value of δ, the vector of independent design variables $\mathbf{x}_B$ is solved, and then the objective function is evaluated. If the value of the objective function at this point is smaller, this point can be treated as a new starting point; otherwise, the previous trial δ value is discarded and the procedure is repeated with another value.

The non-linear Eq. (A7.22) is solved by applying the Newton-Raphson (NR) method. The superscript p in the following equations denotes the iteration cycle at the point $\mathbf{x}_N^k$ during NR iterations.

$$\mathbf{y}^p = \begin{pmatrix} \mathbf{x}_B^p \\ \mathbf{x}_N^k + \delta \mathbf{d}_N^k \end{pmatrix} = \begin{pmatrix} \mathbf{y}^p \\ \mathbf{y}_N^p \end{pmatrix} \tag{A7.23}$$

where $\mathbf{y}^p$ is the solution to Eq. (A7.22).

Correspondingly the NR iteration formulation is

$$\mathbf{x}_B^{p+1} = \mathbf{x}_B^p - [\mathbf{J}(\mathbf{y}_p)]^{-1}\{\mathbf{h}(\mathbf{y}_p)\} \tag{A7.24}$$

in which

$$\mathbf{h}(\mathbf{y}_p) = [h_1(\mathbf{x}_B^p, \mathbf{x}_N^k + \delta\mathbf{d}_N^k), \ldots, h_l(\mathbf{x}_B^p, \mathbf{x}_N^k + \delta\mathbf{d}_N^k)]^T \tag{A7.25}$$

$$\mathbf{J}(\mathbf{y}_p) = \nabla_B \mathbf{h}(\mathbf{y}_p) \tag{A7.26}$$

During the iterations, if the following convergence criteria is satisfied

$$\| \mathbf{x}_B^{p+1} - \mathbf{x}_B^p \| \leq \varepsilon_3 \tag{A7.27}$$

where ε_3 is the convergence standard, it indicates that the result has converged and Eq.(A7.21) has the solution.

$$\mathbf{x}^{k+1} = \begin{pmatrix} \mathbf{x}_B^{p+1} \\ \mathbf{x}_N^k + \delta\mathbf{d}_N^k \end{pmatrix} \tag{A7.28}$$

If $f(\mathbf{x}^{k+1}) < f(\mathbf{x}^k)$, NR method is applied again with an increased value of δ. This procedure is repeated until the value of the objective function becomes constant. Otherwise, NR method is repeated with a reduced value of δ to find the vector of independent design variables $\mathbf{x}_B$.

The search direction and the revision of the basic variables $\mathbf{x}_B$ of the method is shown in Fig. A7.1.

A7.3.4 Iteration procedure of GRG method

The basic procedure of the GRG method is to start with an initial feasible solution. Then the calculations in determining the search direction and seeking a feasible point are repeated until the optimum is reached. The steps of the procedure are summarised as follows. Here the parameters ε_1, ε_2 and ε_3 are convergence standards, δ is the initial step size parameter and ω is the reducing parameter for step size, $0 < \omega < 1$.

Step 1 choose an initial feasible point $\mathbf{x}^o$, set k = 0;

Step 2 divide $\mathbf{x}^k$ into the vector of independent design variables $\mathbf{x}_B^k$ and the vector of dependent design variables $\mathbf{x}_N^k$, calculate constraint gradients **J** and **C**. If $|\mathbf{J}(\mathbf{x}^k)| = 0$, divide the independent and dependent design variables again until the matrix **J** is not irregular.

Step 3 calculate the reduced gradients $\mathbf{r}(\mathbf{x}_N) = \dfrac{\mathbf{dF}}{\mathbf{dx}_N} = \nabla_N F - (\mathbf{J}^{-1}\mathbf{C})\nabla_B F$, if $\|\mathbf{r}(\mathbf{x}_N)\| \le \varepsilon_1$, the optimum point is found to be $\mathbf{x}^k$ and the calculation is terminated. otherwise, decide the search direction according to Eqs.(A7.20) and (A7.21)

$$\mathbf{d}^k = \begin{pmatrix} \mathbf{d}_B^k \\ \mathbf{d}_N^k \end{pmatrix}$$

let $\delta = \delta_o$;

Step 4 set p = 1, calculate $\mathbf{y}^p = \begin{pmatrix} \mathbf{y}_B^p \\ \mathbf{y}_N^p \end{pmatrix} = \mathbf{x}^k + \delta\mathbf{d}^k$, check all the constraints, if $|h_r(\mathbf{y}^p)| \le \varepsilon_2$, r = 1,2,...,*l*, go to Step 7, otherwise go to Step 5;

Step 5 seek a feasible point with the Newton-Raphson iterations, that is

$$\mathbf{y}_B^{p+1} = \mathbf{y}_B^p - [\mathbf{J}(\mathbf{y}^p)]^{-1}\mathbf{h}(\mathbf{y}^p)$$

$$\mathbf{y}_N^{p+1} = \mathbf{y}_N^p$$

Step 6 if $||\mathbf{y}^{p+1} - \mathbf{y}^{p}| \geq \varepsilon_3$, go to Step 5 to continue the iteration, set p = p+1; otherwise, check all the constraints, If $|h_r(\mathbf{y}^{p})| \leq \varepsilon_2$, r = 1,2,...,*l*, go to Step 7; otherwise, reduce the step size, $\delta = \omega\delta$, go to Step 4;

Step 7 calculate the objective function, if $f(\mathbf{x}^{k}) \leq f(\mathbf{y}^{p})$, let $\delta = \omega\delta$, go to Step 4; otherwise, $\mathbf{x}^{k+1} = \mathbf{y}^{p}$, set k = k+1, go to Step 2.

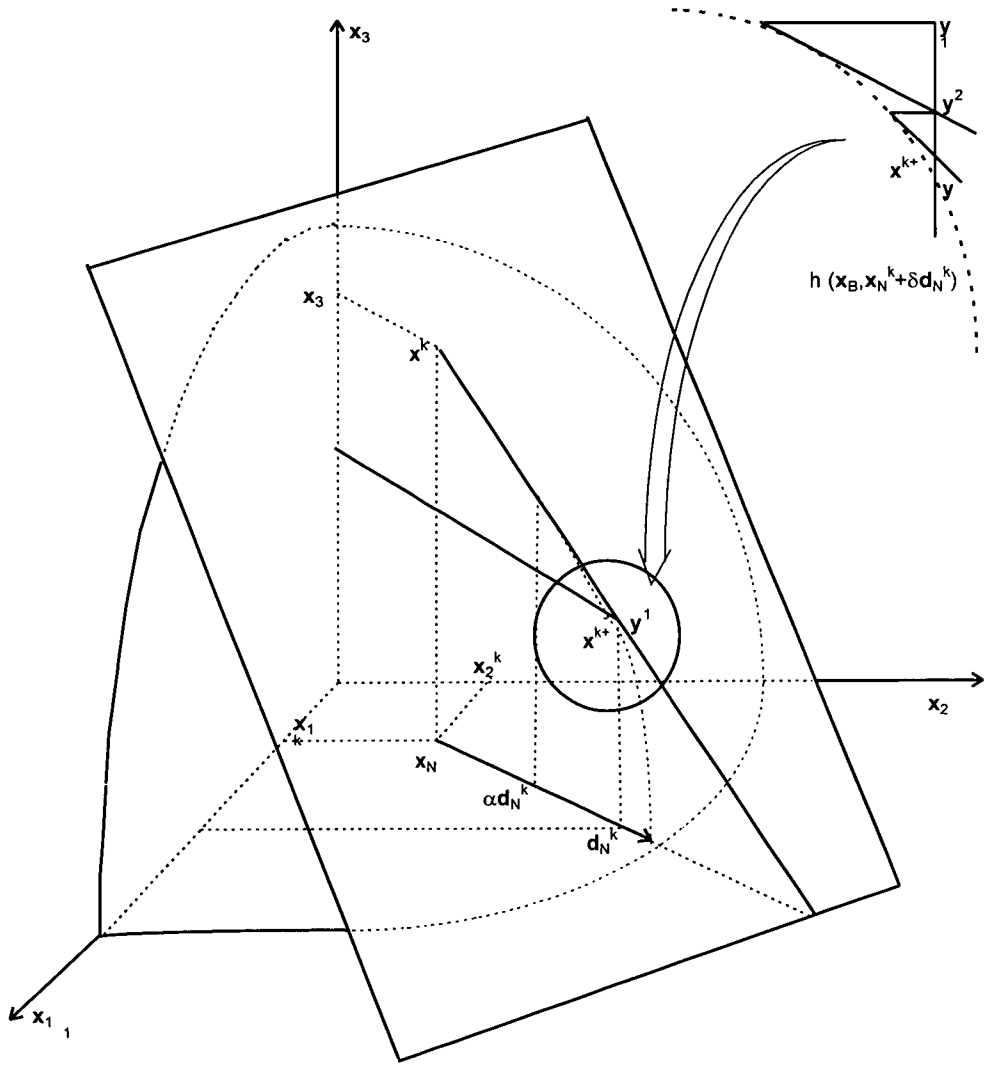

Fig. A7.1: The search direction and the revision of basic variables $\mathbf{x}_B$ of GRG method

CHAPTER 8

INFERENCE OF THE TIME DEPENDENT FLOW PATTERN IN A MODEL SILO

8.1 Introduction

In Chapter 7, a technique to infer the time dependent flow channel boundary (FCB) in a cylindrical silo from the measured residence times was developed. The technique is here applied to deduce the flow pattern in the concentric discharge model experiments presented in Chapter 3.

The deduced FCBs at several stages of discharge are compared with the corresponding FCBs measured through the diametral front wall of the half model. Further comparisons on the particle trajectory paths and particle velocities are also made.

8.2 The experiments and input parameters

The experiments analysed here were conducted in a half cylindrical model silo. The half silo, with an outlet diameter of 65 mm, is 650 mm in diameter and 1.5 m in height. The test material was polypropylene pellets, whose physical properties are listed in Table 4.1.

The residence times of the markers are taken from the average of the measured residence times of three highly repeatable concentric discharge tests. The average residence times of markers in every semi-circle from Level 1 to Level 8 are shown in Table 8.1. In these experiments, the silo was filled up to the height of 870 mm in a distributed manner. The average total discharge time for emptying the silo was found to be 246 s and the average volumetric discharge rate was 4.97 x 10^5 mm^3/s. The measured top surface profile and FCB at different times, and the trajectory paths of selected particles from different levels, can be found in Chapter 3.

8.3 Outline of the optimisation problem

8.3.1 Deduction of time dependent FCB

As previously mentioned, the optimisation problem for deducing the FCB at any specific time T' can be described as follows

$$\text{min.} \quad F(\mathbf{x}) = \sum_{i=1}^{n} (\Delta t_{o,i} - \Delta t'_{o,i})^2 \tag{8.1}$$

$$\text{s.t.} \quad Q_{exit} = Q_{cone} + \psi Q_{flow} \tag{8.2}$$

where the vector of design variables is

$$\mathbf{x} = [v_{zo}, r_o, r_1, \ldots, r_{n-1}]^T \tag{8.3}$$

and the discharged volume of solid is

$$Q_{exit} = q_{exit} T' \tag{8.4}$$

For the half model silo with a typical top surface profile shown in Fig. 8.1, the volume of the top inverted cone is given by

$$Q_{cone} = \begin{cases} \frac{1}{2}\pi R^2 (h_c - \frac{2}{3} R\tan\beta) & \text{when } h_c > R\tan\beta \\ \frac{1}{6}\pi \frac{h_c^{\ 3}}{\tan^2\beta} & \text{Otherwise} \end{cases} \qquad (8.5)$$

and the volume of the material in the core flow zone is given by

$$Q_{flow} = \begin{cases} \int_0^R \frac{\pi r^2}{2} \Gamma'(r)dr - \frac{1}{6}\pi R^3 \tan\beta & \text{when } h_c > R\tan\beta \\ \int_0^{\frac{h_c}{\tan\beta}} \frac{\pi r^2}{2} \Gamma'(r)dr - \frac{1}{6}\pi \frac{h_c^{\ 3}}{\tan^2\beta} & \text{Otherwise} \end{cases} \qquad (8.6)$$

where h_c is the distance from the apex of the inverted cone to the initial horizontal top solid boundary, and $\Gamma'(r)$ is the derivative of the equation $z = \Gamma(r)$ describing the geometry of the FCB.

8.3.1.1 FCB at time of 10 s

The FCB and the top flow layer at the time of 10 s is shown in Fig. 8.2. Level 7 is chosen as the level where the FCB of the central core flow zone and the top flow layer meet. As mentioned in Chapter 7, the selection of the level is somewhat arbitrary. However the deduced FCB is still very much influenced by the optimisation calculations.

The optimisation problem for deducing the FCB at the time of 10 s is summarised as:

to find $\mathbf{x} = [v_{zo}, r_o, r_1, r_2, r_3, r_4, r_5, r_6]^T$

min. $F(\mathbf{x}) = F(v_{zo}, r_o, r_1, r_2, r_3, r_4, r_5, r_6)$

$$= \sum_{j=1}^{6} \left(- \sum_{i=j-1}^{6} \int_{z_{i-1}}^{z_i} \frac{1}{c_i} e^{-\{r_{i-1} + \frac{r_i - r_{i-1}}{z_i - z_{i-1}} - \ln[r_{i-1} + \frac{r_i - r_{i-1}}{z_i - z_{i-1}}(z - z_{i-1})] - \tan q_i z\}} dz - \Delta t'_{j-1,6} \right)^2 \tag{8.7}$$

s.t. $10q_{exit} - \frac{1}{2}\pi R^2 (h_c - \frac{2}{3} R\tan\beta) - \psi \left[\int_0^R \frac{\pi r^2}{2} \Gamma'(r) dr - \frac{1}{6}\pi R^3 \tan\beta \right] = 0$

when $h_c > R\tan\beta$

$$10q_{exit} - \frac{1}{6}\pi \frac{h_c^3}{\tan^2\beta} - \psi \left[\int_0^{\frac{h_c}{\tan\beta}} \frac{\pi r^2}{2} \Gamma'(r) dr - \frac{1}{6}\pi \frac{h_c^3}{\tan^2\beta} \right] = 0$$

Otherwise

(8.8)

8.3.1.2 FCB at time of 20 s

The optimisation equations for the deduction of the FCB at the time of 20 s are similar with those of Eqs (8.7) and (8.8). The only difference is that at this time Level 6 is chosen as the level where the FCB is deduced. The number of design variables reduces from 8 to 7.

8.3.2 Deduction of fully developed FCB

As mentioned previously, the fully developed FCB is inferred by ensuring that the volumetric discharge rate is equal to the influx of solid through each level of the FCB.

After the time dependent FCB has been determined, the time taken for each particle in the core flow zone to start moving can be evaluated in accordance with its initial position. The velocity of each particle at each selected level can then be deduced, which makes it possible to evaluate the influx of solid flowing through the level.

8.4 Initial values of design variables and convergence criteria

8.4.1 Initial values of design variables

The initial values assigned to the design variables can have a significant effect on the process of the optimisation and the optimum results. Appropriate initial values can lead to fast convergence and good optimum results. Otherwise, the convergence could be very slow and even cause oscillation. It is very important to choose appropriate initial values of design variables to accelerate the process of the optimisation and achieve stable convergence.

It has been shown in Chapter 6 that the kinematic model can produce a reasonable prediction of the flow pattern. The initial values of the design variables are therefore taken from the trajectory path predicted by the kinematic model. The trajectory path of a particle in a planar flow infinite silo predicted by the kinematic theory is

$$x = x_o \sqrt{\frac{y}{y_o}} \tag{8.9}$$

where x_o and y_o are the initial coordinates of the particle.

The remaining design variable to be assigned an initial value is the particle velocity at the starting position v_{zo}. For the particle at the central line at Level 7, the average velocity, given by the shortest path divided by the residence time, was 27.7 mm/s. At the same level, the average shortest path velocity for the particle at r=120 mm was only 16.4 mm/s. In the optimisation, an initial vertical velocity of 20 mm/s is assigned to all particles

$$v_{zo} = 20 \text{ mm/s} \tag{8.10}$$

8.4.2 Convergence criteria

In the following calculations, the allowable error tolerances for terminating the optimisation iterations are set at

$$\| F_i - F_{i-1} \| \leq \varepsilon_1 = 10^{-3} \tag{8.11}$$

$$\| \mathbf{x}_i - \mathbf{x}_{i-1} \| \leq \varepsilon_2 = 10^{-4} \tag{8.12}$$

where F_i, F_{i-1} and $\mathbf{x}_i$, $\mathbf{x}_{i-1}$ are values of the objective functions and the design variables in two adjacent iterations. It is thought to be of the right order to give a good engineering solution. Setting too small tolerances as convergence criteria can result in considerably more computational effort which is unnecessary.

8.5 Inference and comparison of FCB

A two-stage strategy as proposed in Chapter 7 is implemented for solving the optimisation problem given in Eqs. (8.7) and (8.8). Firstly, the constrained optimisation problem is converted to an unconstrained problem by ignoring the constraint, and solved using the GRG method with several trial sets of the design variables. Secondly, Eq. (8.8) is utilised to check all these optimum solutions and find one which satisfies this constraint condition. The optimum design variables which minimise the objective function of Eq. (8.7) and satisfy the constraint condition of Eq. (8.8) give the inferred FCB.

8.5.1 FCB at time of 10 s

The FCB at Level 7 is expected to lie in the range of r=90–140 mm at the time of 10 s after discharge. Solutions are sought for 6 trial positions at Level 7 i.e. at r_o=90, 100, 110, 120, 130, 140 mm. The remaining initial values of the design variables $\bar{\mathbf{x}}= [r_1, r_2, ..., r_6]^T$ are then evaluated using Eq. (8.9). For instance, the initial values of $\bar{\mathbf{x}}$ for r_o = 90 mm is given by

$$\bar{\mathbf{x}} = [83.3, 76.1, 68.0, 58.9, 48.1, 34.0]^T \tag{8.13}$$

The 6 trial sets of the initial values of $\bar{\mathbf{x}}$ can be assembled in one single matrix as follows

$$\mathbf{X} = \begin{pmatrix} 20.0 & 20.0 & 20.0 & 20.0 & 20.0 & 20.0 \\ 83.3 & 92.6 & 101.8 & 111.1 & 120.4 & 130.0 \\ 76.1 & 84.5 & 93.0 & 101.5 & 109.9 & 118.3 \\ 68.0 & 75.6 & 83.2 & 90.7 & 98.3 & 105.6 \\ 58.9 & 65.5 & 72.0 & 78.6 & 85.1 & 91.7 \\ 48.1 & 53.4 & 58.9 & 64.1 & 69.5 & 74.8 \\ 34.0 & 37.8 & 41.6 & 45.4 & 49.1 & 52.9 \end{pmatrix} \tag{8.14}$$

where the value 20 is the assigned initial value for velocity v_{zo}.

The optimisation procedure produced the following solutions

$$\mathbf{X}_{opt} = \begin{pmatrix} 22.5 & 18.8 & 16.3 & 14.3 & 11.9 & 9.9 \\ 90.0 & 100.0 & 105.3 & 108.1 & 121.5 & 123.8 \\ 90.0 & 100.0 & 105.3 & 106.8 & 115.1 & 120.1 \\ 90.0 & 99.9 & 105.3 & 106.8 & 115.1 & 110.8 \\ 90.0 & 99.9 & 105.3 & 102.8 & 109.1 & 97.6 \\ 80.0 & 81.1 & 81.0 & 80.8 & 83.4 & 75.7 \\ 62.0 & 62.0 & 62.0 & 61.9 & 62.0 & 62.0 \end{pmatrix} \tag{8.15}$$

Further detail of the optimisation calculations is given in Table 8.2. It is noted that all the optimum solutions are reached within 50 iterations. The minimum value of the objective function for each set is very small, indicating that the calculated and the measured moving times of particles are close.

An optimum solution which satisfies the constraint condition of Eq. (8.8) can now be found from these 6 sets of solution by evaluating

$$\frac{\Delta Q}{Q_{exit}} = 1 - \frac{Q_{cone} + \psi\, Q_{flow}}{Q_{exit}} \tag{8.16}$$

The constraint given by Eq. (8.8) is satisfied when $\Delta Q/Q_{exit}$ has a very small value. The experimental results show that at 10 s after discharge, the volume of discharged solid was $Q_{exit}=4.97 \times 10^6$ mm^3 and the volume of the inverted cone was $Q_{cone}=2.65 \times 10^6$ mm^3.

The volume of solid in the core flow zone Q_{flow} can be evaluated for each set of solution. Figure 8.3 shows the plot of $\Delta Q/Q_{exit}$ against the initial values assigned to Level 7. The magnitude of $\Delta Q/Q_{exit}$ decreases to a minimum from $r_o=90$ mm to $r_o=100$ mm. It then increases again with larger r values. An optimum solution which satisfies the constraint almost exactly ($\Delta Q/Q_{exit}=0.01$) is therefore given by the set of solution with an initial value of $r_o=100$ mm. The final optimum design variables given by

$$\mathbf{x}_{opt} = [18.8, 100.0, 100.0, 99.9, 99.9, 81.1, 62.0]^T \qquad (8.17)$$

is considered the FCB at time of 10 s after discharge.

The efficiency of the GRG method is clearly illustrated in the optimisation history for the case of $r_o=100$ mm (Fig. 8.4). The value of the objective function F decreased rapidly in the first iteration and thereafter decreased gradually towards $F=2.5$ s^2 after 40 iterations when the convergence criteria were reached. The initial and optimum FCB are compared in Fig. 8.5.

Figure 8.6 compares the deduced FCB at time of 10 s with the measured FCB at the same time. The deduced FCB matches the measured FCB remarkably well, which shows the proposed inference technique is very reliable.

8.5.2 FCB at time of 20 s

The FCB at time of 20 s after the starting of discharge is deduced in a similar way. This time, the starting position of the FCB at Level 6 is expected to lie in the range of r_0=130–170 mm. The matrix of 5 sets of initial values of the design variables for r_0=130, 140, 150, 160 and 170 is given by

$$\mathbf{X} = \begin{pmatrix} 20.0 & 20.0 & 20.0 & 20.0 & 20.0 \\ 118.7 & 127.8 & 136.9 & 146.1 & 155.2 \\ 106.1 & 114.3 & 122.4 & 130.6 & 138.8 \\ 91.9 & 99.0 & 106.1 & 113.1 & 120.2 \\ 75.1 & 80.8 & 86.6 & 92.4 & 98.1 \\ 53.1 & 57.1 & 61.2 & 65.3 & 69.4 \end{pmatrix} \tag{8.18}$$

The corresponding optimum solutions are

$$\mathbf{X}_{opt} = \begin{pmatrix} 14.2 & 9.9 & 7.7 & 6.1 & 5.2 \\ 127.7 & 132.1 & 138.2 & 144.3 & 148.3 \\ 125.5 & 127.9 & 131.6 & 133.7 & 134.0 \\ 124.4 & 125.2 & 127.0 & 128.0 & 129.9 \\ 112.7 & 103.3 & 104.7 & 101.7 & 103.0 \\ 65.3 & 64.9 & 65.0 & 64.9 & 65.0 \end{pmatrix} \tag{8.19}$$

Further details of the optimisation are given in Table 8.3. Next, an optimum solution which satisfies the constraint equation of Eq. (8.8) is evaluated using Eq. (8.16). This time, the volume of discharged solid is Q_{exit}=9.94 x 10^6 mm^3 and the volume of the top inverted cone is Q_{cone}=5.90 x 10^6 mm^3. The plot of $\Delta Q/Q_{exit}$ for the 5 sets of solutions is shown in Fig. 8.7. The minimum value of $\Delta Q/Q_{exit}$ is easily identified at r_0=150 mm (minimum $\Delta Q/Q_{exit}$=0.003). Therefore the final optimum design variables defining the FCB at the time of 20 s is given by

$$\mathbf{x}_{opt} = [7.7, 138.2, 131.6, 127.0, 104.7, 64.9]^T \tag{8.20}$$

The optimisation history is illustrated in Fig. 8.8. Again there is good convergence. The optimum solution was achieved after 40 cycles of iteration, and the value of the objective function decreased from 5267.2 s^2 to 1.35 s^2. The initial and optimum FCB are shown in Fig. 8.9. Figure 8.10 compares the deduced and the measured FCB at the time of 20 s. Again an excellent agreement is found between the two.

8.5.3 Fully developed FCB and velocity distribution

The vertical velocity distribution at Level 6 can be found by inferring the velocities at several points at 10 mm intervals starting from the central axis. Following the procedure used in inferring FCB, the design variables $\bar{\mathbf{x}} = [z_{ro}, r_1, r_2, \ldots, r_5]^T$ for particles starting from the initial positions of r_o=10, 20, ..., 150 mm are then assigned initial values as follows

$$\mathbf{X}=\begin{pmatrix} 20.0 & 20.0 & 20.0 & 20.0 & 20.0 & 20.0 & 20.0 & 20.0 & 20.0 & 20.0 & 20.0 & 20.0 & 20.0 & 20.0 & 20.0 \\ 9.1 & 18.2 & 27.3 & 36.5 & 45.6 & 54.8 & 63.9 & 73.0 & 82.2 & 91.3 & 100.4 & 109.5 & 118.6 & 127.8 & 136.9 \\ 8.2 & 16.3 & 24.5 & 32.7 & 40.8 & 49.0 & 27.2 & 65.3 & 73.5 & 81.6 & 89.8 & 98.0 & 106.1 & 114.3 & 122.5 \\ 7.1 & 14.4 & 21.2 & 28.3 & 35.4 & 42.4 & 49.5 & 56.6 & 63.6 & 70.7 & 77.8 & 84.9 & 91.9 & 99.0 & 106.1 \\ 5.8 & 11.5 & 17.3 & 23.1 & 28.9 & 34.6 & 40.4 & 46.2 & 52.0 & 57.7 & 63.5 & 69.3 & 75.0 & 80.8 & 86.6 \\ 4.1 & 8.2 & 12.2 & 16.3 & 20.4 & 24.5 & 28.6 & 32.7 & 36.7 & 40.8 & 44.9 & 49.0 & 53.1 & 57.2 & 61.2 \end{pmatrix} \tag{8.21}$$

The times when these particles were in motion can be expressed as

$$\mathbf{T'}_m = \mathbf{T}_m - \mathbf{T}_s \tag{8.22}$$

where $\mathbf{T'}_m$, $\mathbf{T}_m$, $\mathbf{T}_s$ are matrices indicating the particles moving times, total residence times, and the times when the particles remained stationary. The times when the particles remained stationary can be evaluated from the inferred FCB as follows.

Since the FCB propagated upwards very fast at the early stages (reached the top surface at 4 s after discharge), the times taken for particles within the first circle of markers (r=60 mm) to start moving were ignored. The stationary times for the particles beyond r=60 mm were estimated from the observation that at Level 6, the FCB expanded from r=60 mm to r=100 mm at the time of 10 s, and further expanded from r=100 mm to r=150 mm at the time of 20 s. Therefore, the FCB took 6 s to develop from a radius of 60 mm to 100 mm and 10 s to develop from a radius of 100 mm to 150 mm. The stationary times for the particles in the positions of r=10 mm to 150 mm at an interval of 10 mm can therefore be estimated at

$$\mathbf{T}_s = [0.0, 0.0, 0.0, 0.0, 0.0, 0.0, 4.0, 6.0, 8.0, 10.0, 12.0, 14.0, 16.0, 18.0, 20.0]^T \tag{8.23}$$

Once the initial values of the design variables and the times for the particles at the different initial positions to start moving are decided, the optimum values of the design variables can be determined by solving a series of unconstrained optimisation problems. Table 8.4 lists the optimisation results. The very small values of optimum objective functions indicate that the inferred residence times of particles from any position are in excellent agreement with the measured residence times, and also prove that the current algorithm to solve the optimisation problem is successful.

The first element in the vector of design variables is the inferred vertical velocity of the particle at the starting position, so the inferred vertical velocity distribution at Level 6 is given by the first element in each of the optimised design variables vectors. The vector of the vertical velocity distribution at Level 6 is therefore given by

$$\mathbf{V} = [21.4, 21.4, 21.3, 21.3, 20.8, 20.1, 20.1, 19.6, 19.2, 18.8, 17.5, 15.8, 12.0, 9.4, 7.7]^T \tag{8.24}$$

The influx of solid flowing through this level within the radius of 150 mm can then be numerically computed as

$$q = \int_0^{150} \pi r v_z(r) dr = 5.83 \times 10^5 \text{ mm}^3/\text{s} \tag{8.25}$$

Converting the influx of solid to the initial solid packing according to Eq. (7.19) using the measured dilation coefficient of ψ=17.7% gives

$$q_1 = (1-\psi)q = 4.80 \times 10^5 \text{ mm}^3/\text{s} \tag{8.26}$$

The difference between the converted flow rate and the volumetric discharge rate q_{exit} of 4.97×10^5 mm^3/s is

$$\frac{|q_1 - q_{exit}|}{q_{exit}} = 0.034 \tag{8.27}$$

Thus the volumetric discharge rate is close to the flow rate of solid through Level 6. The FCB at the time of 20 s is therefore taken as the fully developed FCB. Figure 8.11 compares the deduced and the measured fully developed FCB which shows that the deduced FCB is narrower than the measured one.

One explanation is the limited number of residence time measurements. The residence times of particles in other positions were interpolated from these limited number of measurements. In this study, a linear interpolation of residence time between markers was used. It is a good assumption where a gradual change of residence time occurs, such as in the central core flow zone. However, where the fully developed FCB lies between two adjacent markers, the real residence time distribution is probably closer to a bilinear distribution as shown in Fig. 8.12, rather than the assumed linear distribution. This inherent approximation can be expected to affect the outcome of the deduction significantly.

Another reason for the smaller deduced FCB is the considerably reduced velocities for the solids near the FCB. These solids did not contribute much to the discharge rate given by Eq. (8.25), but had a significant influence on the position of the flow boundary.

8.6 Inference and comparison of particle trajectory path

The trajectory paths of particles at Level 6 evaluated above and listed in Table 8.4 are here compared with the measured paths in the experiment. Figure 8.13(a) shows the comparison for three particles at the radius of 50, 100 and 150 mm at Level 6. Another comparison is made for Level 5 in Fig. 8.13(b). The agreement between the measured and the deduced trajectory paths are generally very good.

The trajectory paths for particles at any level can be deduced accordingly. Generally speaking, the deduced trajectory paths are in better agreement with the measurements in the upper part of the silo, say above 300mm height, but less so in the lower part. This is thought to be caused by the existence of the outlet and the very loose packing near the outlet where the particles were almost under free fall. The continuity equation no longer holds in this region.

8.7 Inference and comparison of vertical velocity distribution

8.7.1 Comparison between deduced and measured vertical velocity distribution

The inferred vertical velocity distribution at Level 6 is shown in Fig. 8.14(a). The inferred vertical velocity decreases towards the flow boundary as expected. Within the radius of 100 mm, the vertical velocity decreases only slightly, with an average of

about 20 mm/s. Beyond this, the vertical velocity decreases sharply with increasing radius. At the radius of 150 mm, the vertical velocity has dropped to 7.7 mm/s.

Experimental validation of the inferred velocity distribution is not straightforward as accurate measurements of particle velocities in a silo is rather difficult. The simple method of marking the trajectory paths of some particles at every 2 s interval during discharge was used to give some approximate measure of the velocity field in the model experiment. The approximate vertical velocities for these particles are obtained by dividing the vertical distance between two adjacent marks with the time interval. Three such measurements are shown in Fig. 8.14(a). A good agreement is found between the experimental observations and the inferred vertical velocity distribution.

The inferred vertical velocity distributions at two other levels (Level 3 and 4) are given in Figs 8.14(b) and 8.14(c). The pattern of the distributions is similar in that the velocity is high and only decreases slightly at small radii, and then decreases much faster to a small value towards the flow boundary. However as it should be, the inferred velocity increases towards the outlet. The central velocity was inferred to be 21.2 mm/s at z=600 mm (Level 6) to 26.3 mm/s at z=400 mm to 35.1 mm/s at z=300 mm.

8.7.2 Comparison with the kinematic prediction

The deduced vertical velocity distributions at Level 3, 4 and 6 are further compared with the kinematic theory in Fig. 8.15. There is some agreement on the magnitudes of the velocity at different levels. However considerable differences exist in the distribution of the velocity at different levels. The velocity predicted by the kinematic theory decreases much faster with increasing radii than the inferred distribution.

The assumption of steady state flow in the kinematic theory is thought to be the cause for the significant under-prediction of velocity. In the process of emptying, the FCB develops with time and most of the particles are stagnant for some time before they start moving. The time in motion for a particle is often less than the measured residence time, and the difference increases with increasing radial coordinate of the particle. This is why the kinematic prediction is close to the inferred values within a radius of say 30 mm, where the residence time of a particle is almost the same as the time in motion. Beyond this region, the kinematic theory predicts smaller velocities as the assumption of steady state flow is getting too severe. The inferred velocity distributions give a more realistic picture of the real phenomenon.

8.8 Concluding remarks

In this chapter, the time-dependent FCB including the fully developed FCB have been inferred using the deduction technique described in Chapter 7. In addition, the inferred trajectory paths and vertical velocity distributions have also been presented. The inferred results have been compared carefully with the experimental observations. The agreement was found to be generally good, and excellent in some cases. Thus, the proposed technique has proved to be reliable and effective for inferring the solids flow pattern in silos from the measured residence times.

Further improvements can be made to the deduction procedure. In particular, a better deduction can be expected by exploring the residence time distribution near the fully developed FCB, determining the level where the top flow layer and the core flow zone meet.

Table 8.1 Average residence times of three concentric discharge tests

Height above base (mm)	Radial coordinates (mm)					
	0.0	60.0	120.0	180.0	240.0	300.0
100.0	1.4	2.6	157.0	216.0		
200.0	2.2	3.8	32.8	199.0	217.0	231.0
300.0	4.3	6.5	21.3	136.0	193.0	206.0
400.0	8.8	9.9	25.8	115.0	168.0	181.0
500.0	13.3	14.8	30.4	104.0	149.0	159.0
600.0	18.6	17.9	38.7	109.0	126.0	137.0
700.0	25.2	27.5	43.3	79.6	103.0	114.0
800.0	34.0	35.3	42.4	58.6	74.4	87.5

Table 8.2: Deduction of FCB at time of 10 s

Initial design								Optimum design								Number of iterations
Design variables							Value of objective (F)	Design variables							Value of objective (F)	
x_1	x_2	x_3	x_4	x_5	x_6	x_7		x_1	x_2	x_3	x_4	x_5	x_6	x_7		
20.0	83.3	76.1	68.0	58.9	48.1	34.0	271.6	22.5	90.0	90.0	90.0	90.0	80.0	62.0	16.1	21
20.0	92.6	84.5	75.6	65.5	53.4	37.8	490.1	18.8	100.0	100.0	99.9	99.9	81.1	62.0	2.5	40
20.0	101.8	93.0	83.2	72.0	58.9	41.6	792.5	16.3	105.3	105.3	105.3	105.3	81.0	62.0	0.7	43
20.0	111.1	101.5	90.7	78.6	64.1	45.4	1180.3	14.3	108.1	106.8	106.8	102.8	80.8	61.9	2.7	47
20.0	120.4	109.9	98.3	85.1	69.5	49.1	1875.0	11.9	121.5	115.1	115.1	109.1	84.3	62.0	3.6	42
20.0	130.0	118.3	105.6	91.7	74.8	52.9	3173.6	9.9	123.8	120.1	110.8	97.6	75.7	62.0	50.0	50

Unit: x_1 (mm/s), x_2 - x_7: (mm), F (s^2)

Table 8.3: Deduction of FCB at time of 20 s

Initial design							Optimum design							Number of iterations
Design variables						Value of objective (F)	Design variables						Value of objective (F)	
x_1	x_2	x_3	x_4	x_5	x_6		x_1	x_2	x_3	x_4	x_5	x_6		
20.0	118.7	106.1	91.9	75.1	53.1	1805.1	14.2	127.7	125.5	124.4	112.7	65.3	2.8	29
20.0	127.8	114.3	99.0	80.8	57.1	3505.3	9.9	132.1	127.9	125.2	103.3	64.9	11.1	50
20.0	136.9	122.4	106.1	86.6	61.2	4819.5	7.7	138.2	131.6	127.0	104.7	65.0	25.9	33
20.0	146.1	130.6	113.1	92.4	65.3	4281.1	6.1	144.3	133.7	128.0	101.7	64.9	52.9	39
20.0	155.2	138.8	120.2	98.1	69.4	4434.5	5.2	148.3	134.0	129.9	103.0	65.0	95.0	16

Unit: x_1 (mm/s), x_2 - x_6: (mm), F (s^2)

Table 8.4: Deduction of vertical velocities of particles at Level 6 at time of 20 s

Initial design							Optimum design							Number of iterations
Design variables						Value of objective (F)	Design variables						Value of objective (F)	
x_1	x_2	x_3	x_4	x_5	x_6		x_1	x_2	x_3	x_4	x_5	x_6		
20.0	9.1	8.2	7.1	5.8	4.1	37.4	21.4	9.9	9.9	5.1	1.6	1.6	0.4	22
20.0	18.2	16.3	14.4	11.5	8.2	32.8	21.4	17.5	14.6	11.3	7.8	7.8	4.5	5
20.0	27.3	24.5	21.2	17.3	12.2	28.6	21.3	29.9	25.0	18.5	11.2	11.2	3.3	3
20.0	36.5	32.7	28.3	23.1	16.3	24.8	21.3	40.0	33.0	24.5	14.3	14.3	2.3	12
20.0	45.6	40.8	35.4	28.9	20.4	21.4	20.8	49.9	41.4	30.6	17.1	17.1	1.9	9
20.0	54.8	49.0	42.4	34.6	24.5	18.3	20.1	60.0	49.4	36.2	19.1	19.1	1.4	27
20.0	63.9	27.2	49.5	40.4	28.6	19.8	20.1	67.5	58.2	45.0	45.0	45.0	2.3	22
20.0	73.0	65.3	56.6	46.2	32.7	57.7	19.6	80.0	79.5	75.0	68.3	60.4	4.5	8
20.0	82.2	73.5	63.6	52.0	36.7	157.0	19.2	90.0	88.9	87.8	74.7	61.1	3.2	23
20.0	91.3	81.6	70.7	57.7	40.8	252.8	18.8	100.0	100.0	100.0	81.1	62.0	2.5	40
20.0	100.4	89.8	77.8	63.5	44.9	578.4	17.5	110.0	110.0	110.0	95.9	62.6	2.2	28
20.0	109.5	98.0	84.9	69.3	49.0	916.3	15.8	119.2	119.2	119.2	89.2	63.0	1.4	37
20.0	118.6	106.1	91.9	75.0	53.1	1805.1	12.0	125.8	123.8	122.6	96.6	63.8	1.0	39
20.0	127.8	114.3	99.0	80.8	57.2	3505.3	9.4	132.2	127.6	124.9	101.7	64.4	6.0	46
20.0	136.9	122.5	106.1	86.6	61.2	4819.5	7.7	138.2	131.6	127.0	104.7	65.1	25.8	

Unit: x_1 (mm/s), x_2 - x_6: (mm), F (s^2)

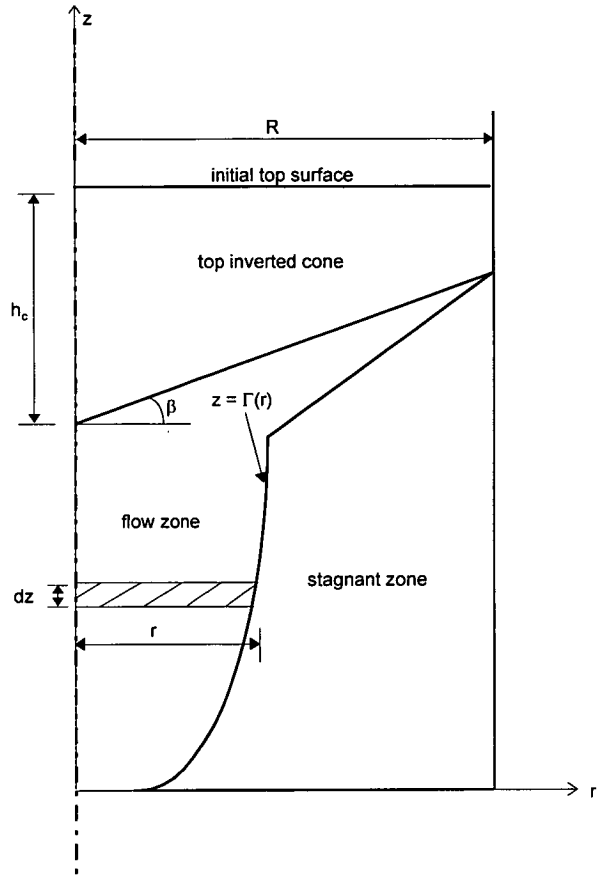

Fig. 8.1: Different zones during solid flow

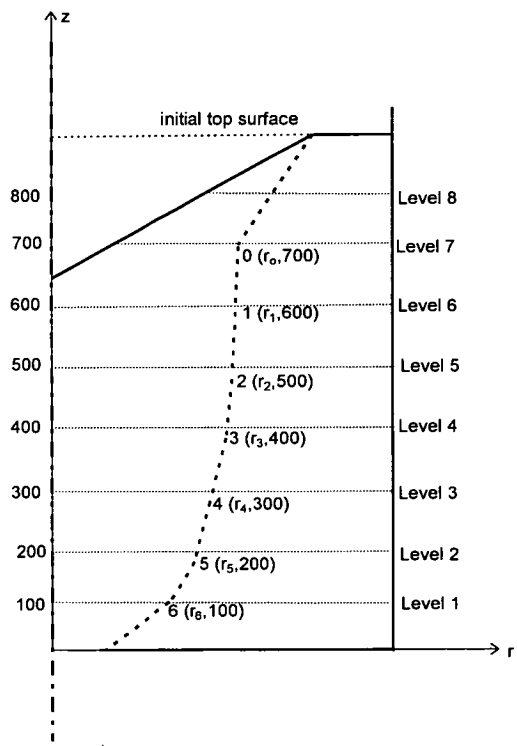

Fig. 8.2: Design variables (r_o, r_1,..., r_6) describing FCB at time of 10 s

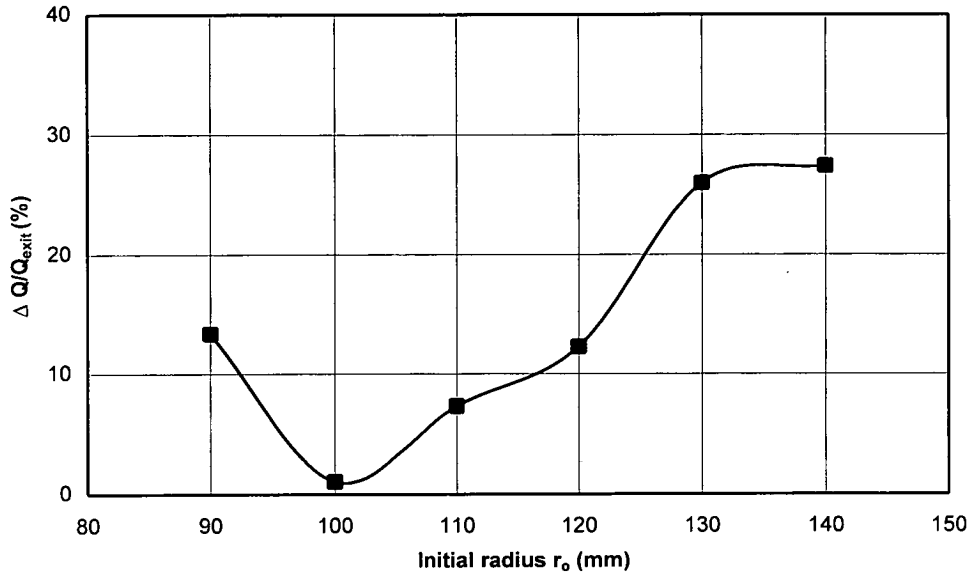

Fig. 8.3: Variation of $\Delta Q/Q_{exit}$ with radial position at time of 10 s

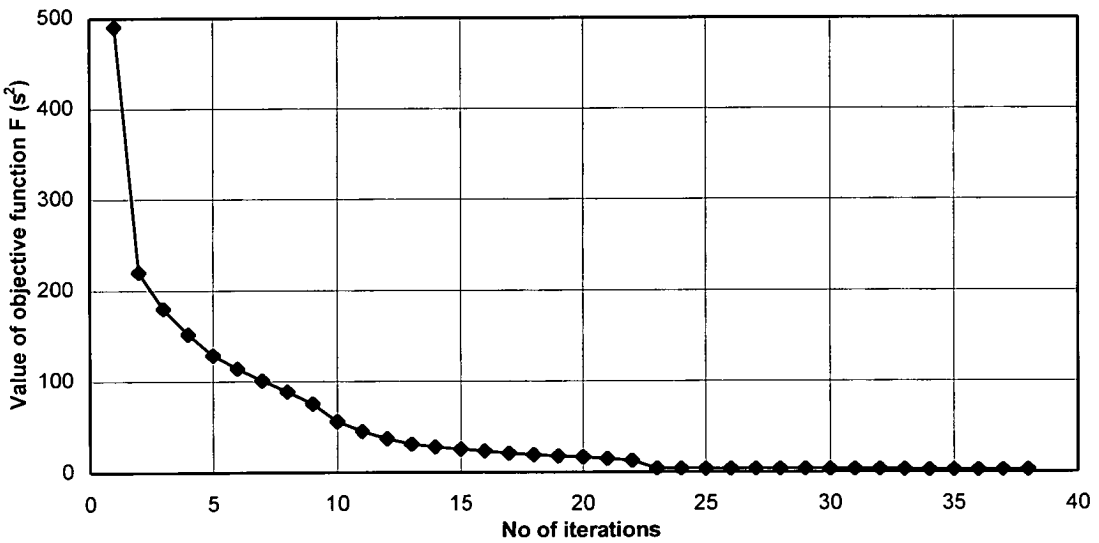

Fig. 8.4: Optimisation history for deducing FCB at time of 10 s

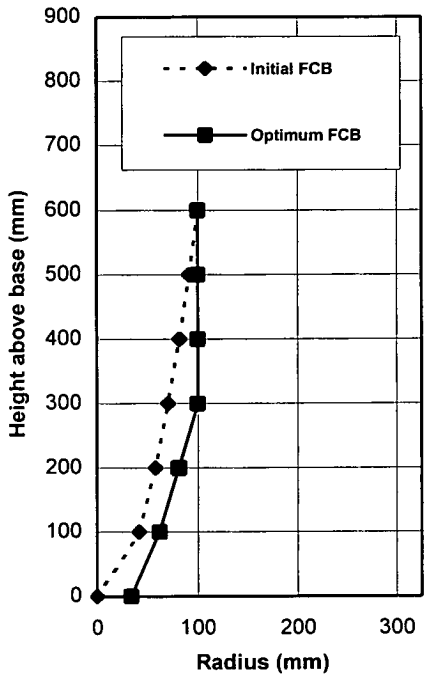

Fig. 8.5: Initial and optimum FCB at time of 10 s

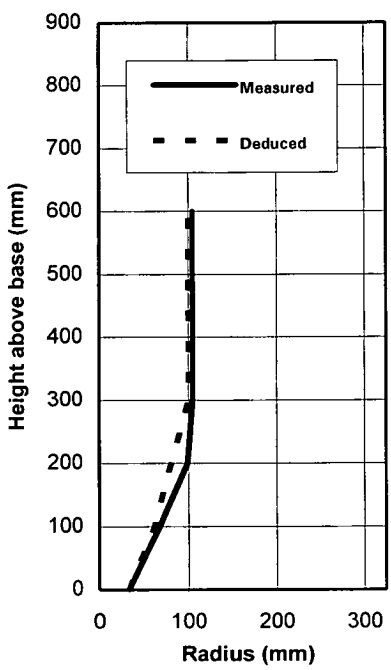

Fig. 8.6: Comparison between deduced and measured FCB at time of 10 s

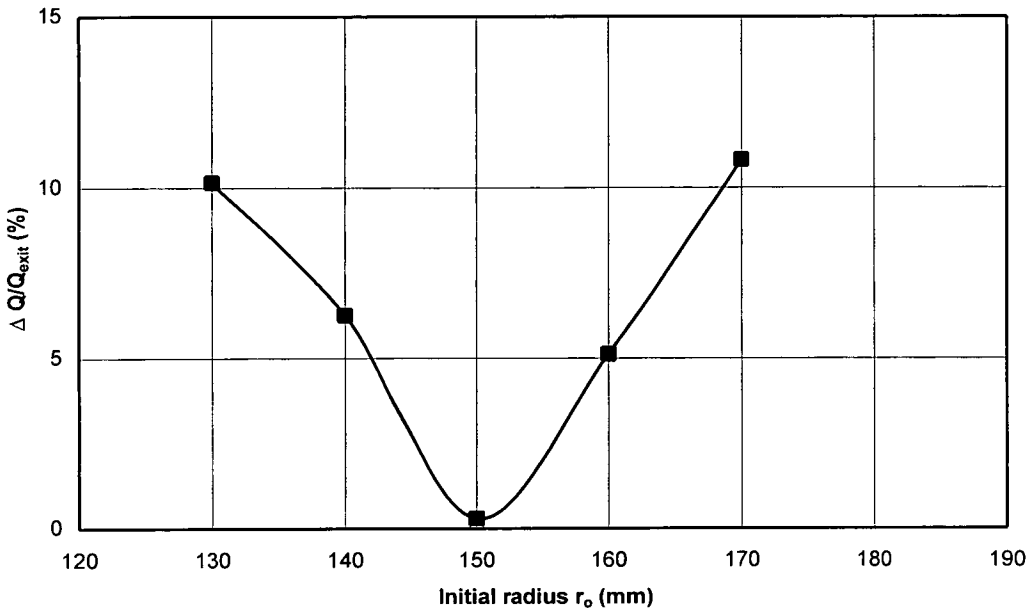

Fig. 8.7: Variation of $\Delta Q/Q_{exit}$ with radial position at time of 20 s

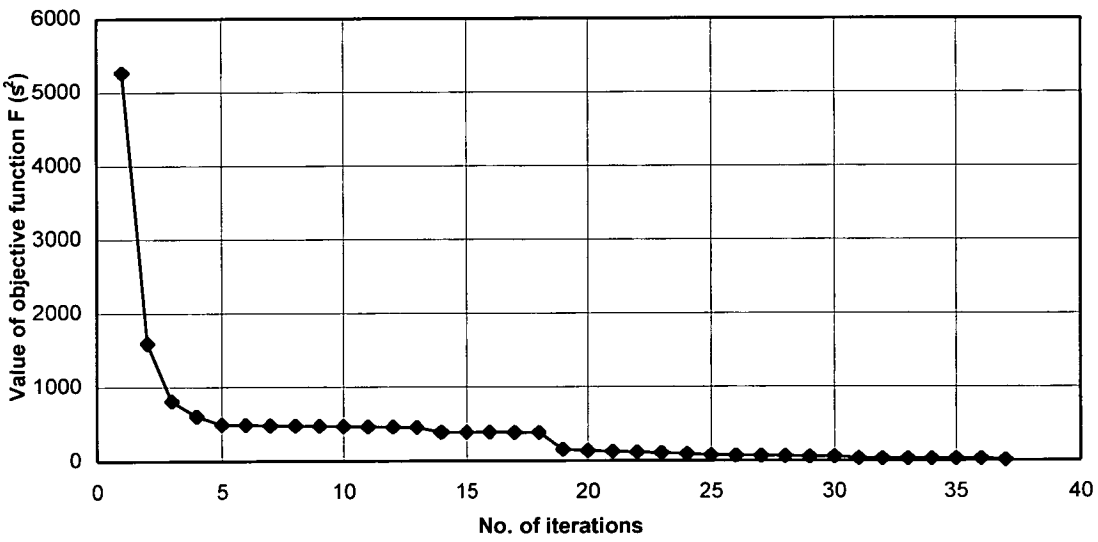

Fig. 8.8: Optimisation history for deducing FCB at time of 20 s

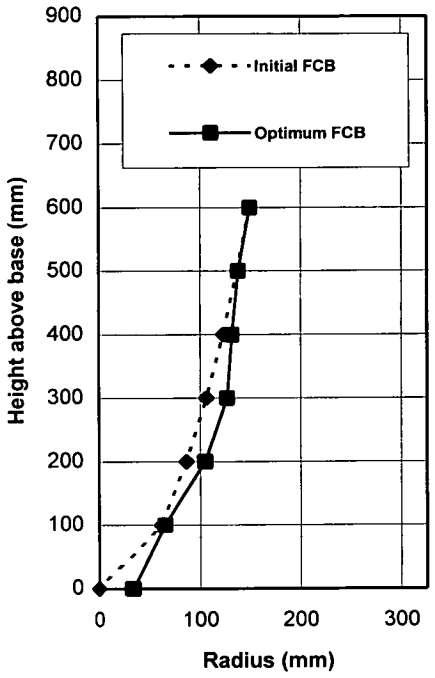

Fig. 8.9: Initial and optimum FCB at time of 20 s

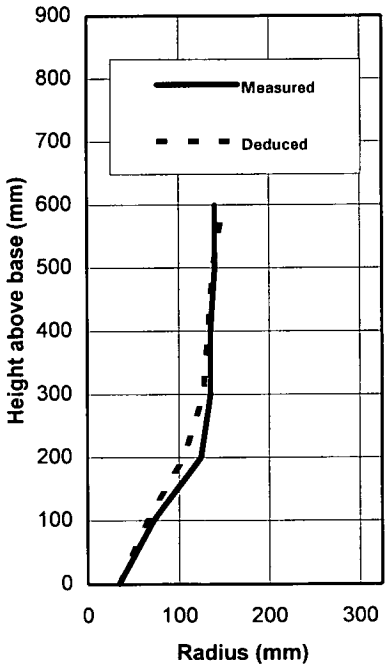

Fig. 8.10: Comparison between deduced and measured FCB at time of 20 s

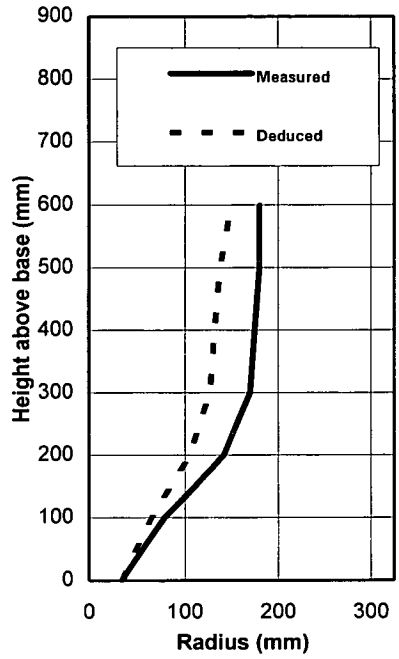

Fig. 8.11: Comparison between deduced and measured fully developed FCB

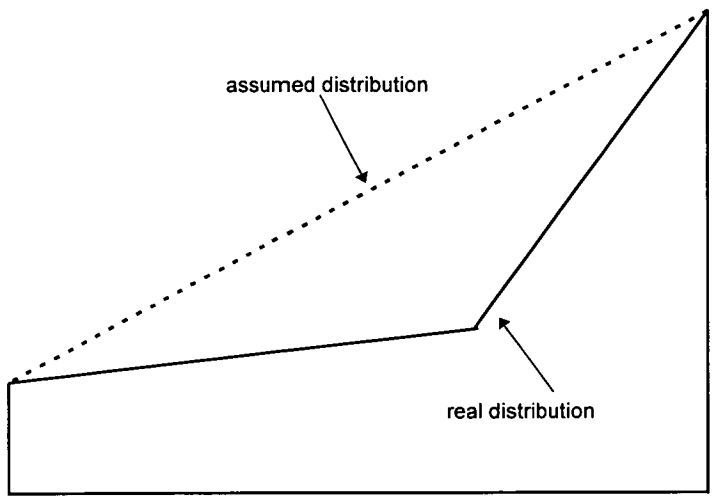

Fig. 8.12: Residence time distribution near fully developed FCB

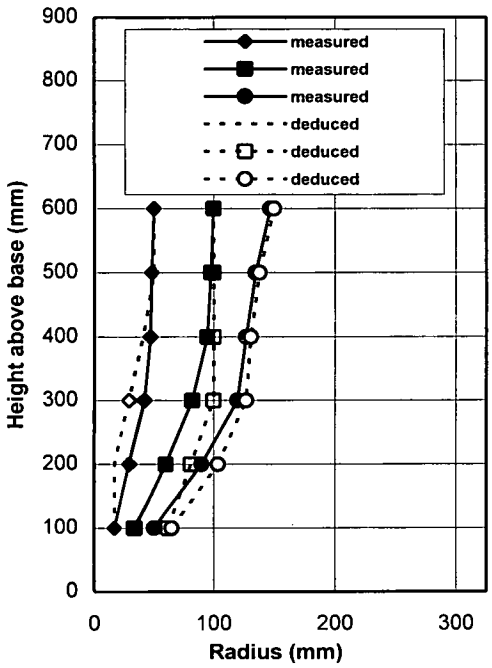

(a) at level 6

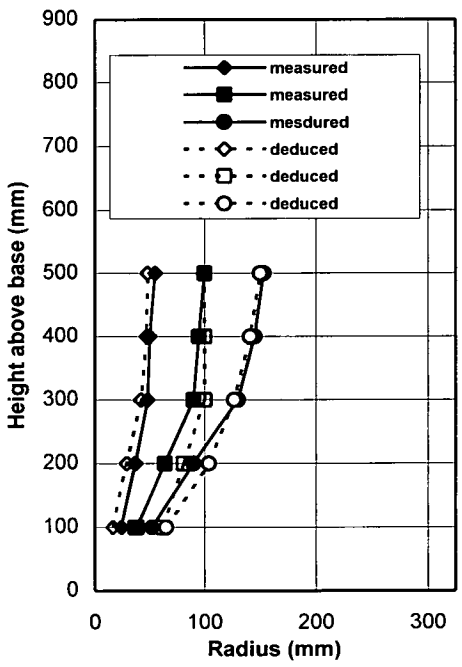

(b) at level 5

Fig. 8.13: Comparison between deduced and measured trajectory paths of particles

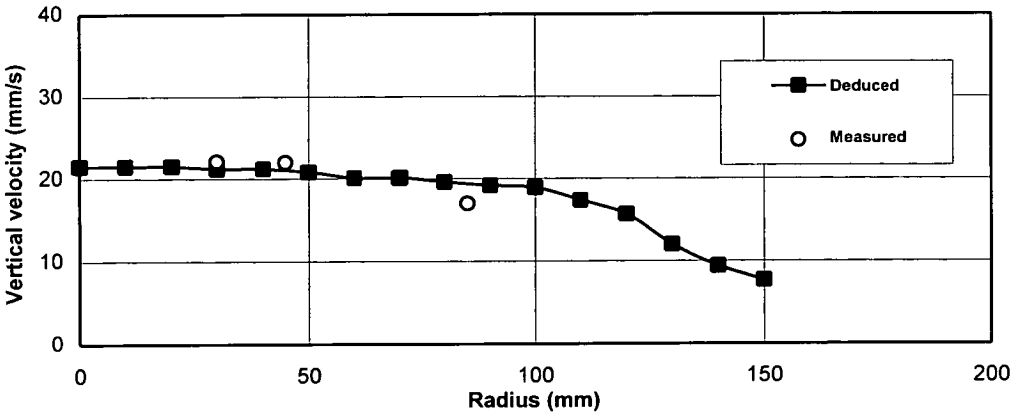

a) at level 6

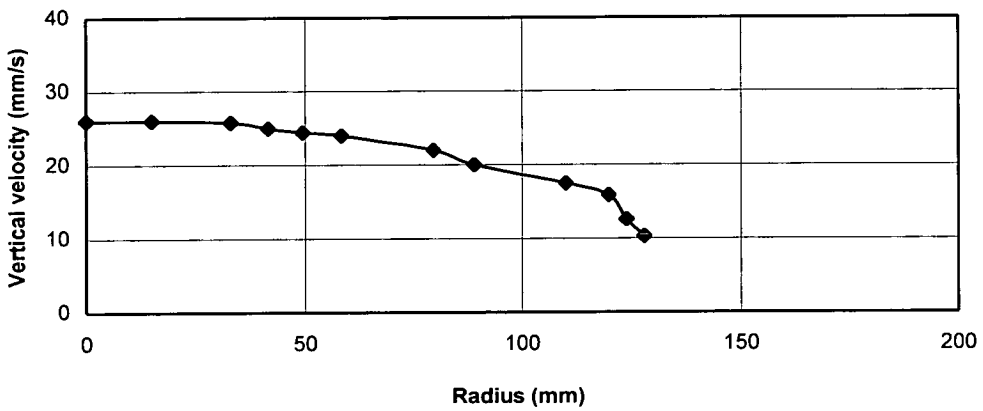

b) at level 4

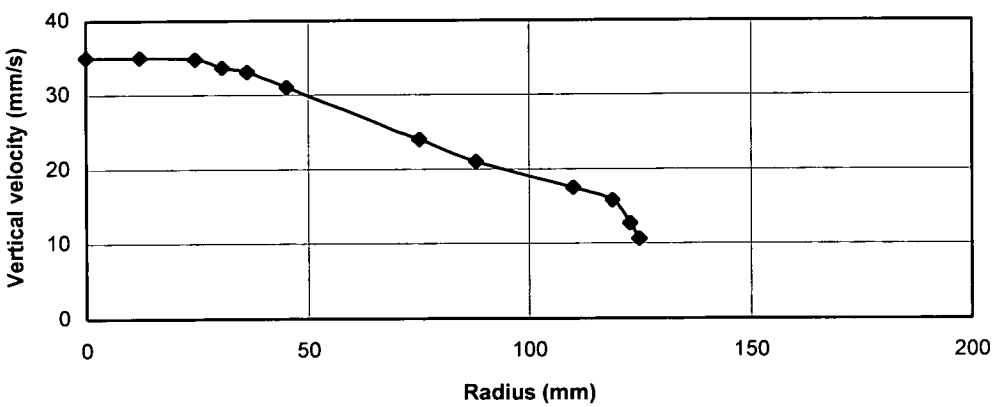

c) at level 3

Fig. 8.14: Deduced vertical velocity distributions

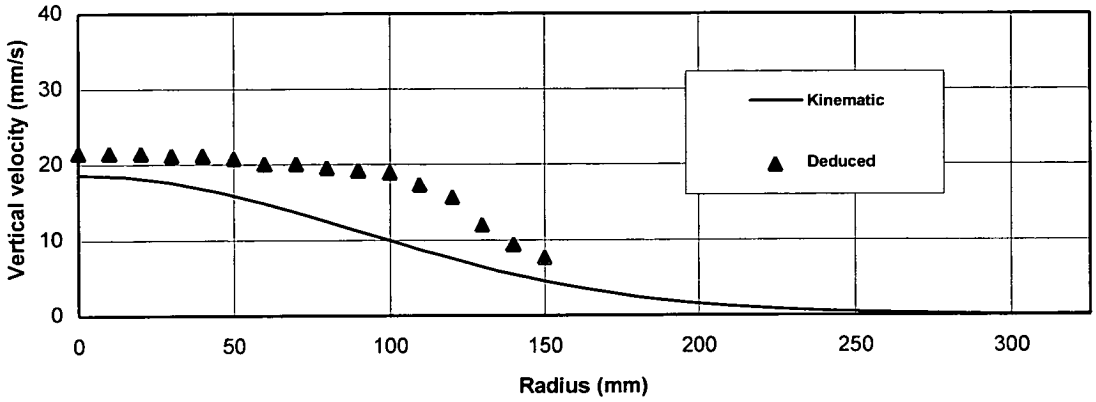

a) at level 6

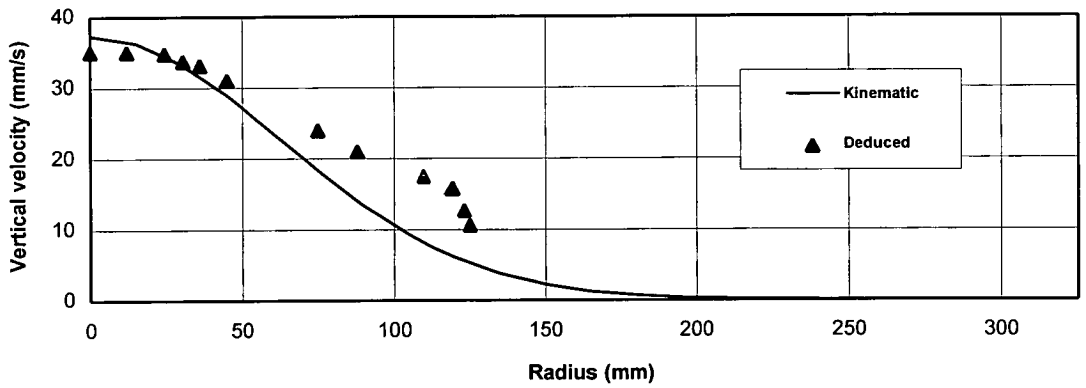

b) at level 4

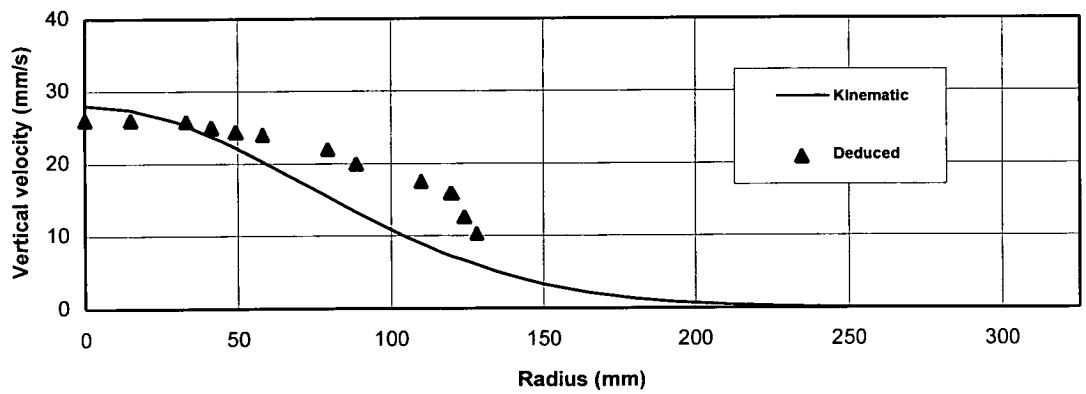

c) at level 3

Fig. 8.15: Comparison between deduced and kinematic vertical velocities of particles

CHAPTER 9

CONCLUSIONS

9.1 General

The flow of particulate solids is a complex phenomenon which is not well understood, but has important applications in many industries. This thesis presents an experimental and theoretical study of the flow of solids in flat-bottomed silos during emptying.

In theoretical work, a simple engineering model to analyse solids flow and a deduction technique to infer the flow behaviour of solids from measured residence measurements were developed. The engineering model was a combination of the kinematic theory for steady state flow and some assumptions concerning about the top flow layer observed in previous experiments. Three parameter are needed in the model: the kinematic constant B, the angle of repose β and the thickness of the top flow layer h_t. The deduction technique, based on the inverse analysis theory, was established using residence time measurements as the input and the continuity equation as the working mechanism of the system.

In experimental work, experiments have been conducted in a half cylindrical model silo to investigate the flow of polypropylene pellets under concentric, half eccentric and fully eccentric discharge. Two experimental techniques have been employed. These are residence time measurements and visual observation through the transparent front wall. Measurements of the residence times of markers,

development of the flow channel boundary (FCB) and the trajectory paths of particles were made.

9.2 Conclusions from experimental work

9.2.1 Full scale silo

The analysis of the full scale silo observations showed that during the emptying process, the top solid surface formed the shape of an inverted cone and the angle of the inclined top surface remained stable throughout the discharge. The flow pattern was found to be highly symmetrical and repeatable, with the coefficient of variation of <5 % for all the residence time measurements at each ring location (a ring consists of a number of markers at a fixed radial coordinate at a level). Further analysis of the residence time measurements showed that an internal funnel flow pattern has occurred during concentric discharge. The approximate location of the fully developed FCB was also inferred from the analyses.

9.2.2 Half cylindrical model silo

First, the retarding effect of the diametral front glass wall was investigated by comparing the residence times of the tracer particles near the front wall with those at the same semi-circle away from the diametral front wall. The retarding effect of the front wall on the residence times was found to be about 8%.

The transparent front wall allows direct observations of the FCB during discharge. It was found that the vertical form of the FCB was close to linear in the lower part of the silo, with the linear region extending to a high level for the fully eccentric case. The angle of inclination between the linear boundary and the vertical axis is about 29^{o} for all three discharge conditions.

The position of the fully developed FCB was determined approximately using three simple approaches of analysing the residence time measurements. The good agreement between the deduced and measured FCBs confirms that these simple methods of plotting statistical measures of the residence time measurements are reasonably good and reliable at finding the approximate location of the fully developed FCB.

In the core flow zone, the trajectory path of a particle generally consisted of a vertical straight line at the upper region and a smooth curve at the lower region. Particles caught by the top flow layer had an inclined trajectory path before entering the fast core flow zone. The angle of inclination of the trajectory path decreased with increasing distance between the position of the particle and the central axis.

Three different zones in which the material possessed different bulk density could be identified. The loosest packing occurred in a small area near the outlet in which the material almost lost contact with each other. In the remaining area of the core flow zone, the material was more loosely packed than in the surrounding stagnant zone where the material had the highest static density. This dilation of bulk density in the flowing solid was found to be quite stable after the initial development of flow channel. An average dilation of 17.7% was evaluated for these experiments.

9.3 Conclusions from numerical work

9.3.1 Prediction model

An engineering model for solids flow in concentrically discharging silos was proposed in Chapter 5 based on the simple kinematic model and some simple assumptions about the top surface profile and top flow layer. As far as is known, the kinematic theory was applied for the first time to model the complete emptying of silos.

For the iron core pellets, a kinematic constant B of 4 times the mean size of the pellets and a top flow layer thickness of 1.0 m gave a good prediction for the flow pattern which occurred in the full scale silo, whilst a kinematic constant B of 2 times the mean size and a top flow layer thickness of 100 mm produced a good prediction for the polypropylene pellets flow in the half model silo. The FCBs and the trajectory paths of particles in different flow zones were predicted. The predicted FCB for polypropylene pellets was found to be in excellent agreement with the measured FCB.

The influence of the kinematic constant B and the thickness of the top flow layer h_t on the FCB was also explored. It has been showed that h_t moderately affects the location of the FCB, while B has a significant influence to that.

9.3.2 Deduction technique

The deduction technique to infer the solids flow pattern in silos by employing the inverse analysis theory was developed in Chapter 7. In this technique, the measured residence time field is treated as the output, and the solids flow is required to satisfy the continuity equation to provide the working mechanism of the system. The unknown velocities and trajectory paths of particles are identified by applying the gradient-based Generalised Reduced Gradient (GRG) method.

The deduction technique was successfully utilised to infer the flow of polypropylene pellets in the half model silo under concentric emptying. The FCBs at the times of 10 and 20 seconds, the fully developed FCB, the trajectory paths of particles and vertical velocity distribution at different levels were inferred and compared with the measured results. The good agreement between the deduced and measured results suggests that the proposed model can reliably be utilised to infer the flow behaviour of solids in silos occurred during concentric emptying.

9.4 Recommendations for further work

Both the prediction model and the deduction technique for solids flow presented in this thesis include some assumptions on the size and shape of the top flow layer during emptying. Whilst the existence of the top flow layer is widely recognised, little is known about its shape and size and how it changes with time. The top flow layer can be expected to be influenced by the geometry and size of silo and the bulk material properties. Further investigations are needed in this area to improve the understanding of the flow behaviour of solids in silos.

In addition to the top flow layer, the prediction model was also based on the kinematic constant B. Simple experiments are needed for a wide range of solids and flow configurations to establish how the magnitude of the kinematic constant varies. Tuzun and Nedderman's (1979b) suggestion that B depends on particle diameter requires further exploration. Simple material tests to measure B must also be devised.

The dilation of solid is an important factor to influence the expansion of the FCB. It is attempted to further investigate the dilation of solid for more materials and try to establish the relationship of the dilation of solid and the material properties.

It is also intended to further improve the deduction technique for concentric discharge and extend the technique to eccentric discharge.

REFERENCES

AL-DIN, N. and GUNN, D.D. (1984) 'The Flow of Non-cohesive Solids Through Orifices', Chemical Engineering Science, Vol. 39, pp 121-127.

ARNOLD, P.C., McLEAN, A.G. and ROBERTS, A.W. (1980) 'Bulk Solids: Storage, Flow and Handling', Tunra Bulk Solids Handling Associates, University of Newcastle, Australia, Sept.

ARORA, J.S, (1989) Introduction to optimum design, McGraw-Hill Book Company.

ARTEAGA, P. and TUZUN, U. (1990) 'Flow of Binary Mixtures of Equal-Density Granules in Hoppers - Size Segregation, Flowing Density and Discharge Rates', Chemical Engineering Science, Vol. 45, No. 1, pp. 205-223.

ATHEY, J.D., CUTRESS, I.O. and PULFER R.F. (1966) 'X-ray Investigations of Flow powders', Chemical Engineering Science, Vol. 21, pp.835-836.

BAGNOLD, R.A. (1954) 'Experiments on a Gravity-free Dispersion of Large Solid Spheres in a Newtonian Fluid under Shear', Proc. R. Soc. London, A225, pp. 49-63.

BARKER, G.C. and MEHTA A. (1992) Physical Review A, pp 3435-3446.

BEVELLO, W.A., LENIGER, H.A. and VAN DE VELDE (1961), 'The Flow of Granular Solids Through Orifices', Chemical Engineering Science, Vol. 15, pp260-269.

BISHARA, A.G. and MAHMOUD, M.H. (1976), 'Using Finite Elements to Analyse Silo Pressure', Agricultural Engineering, Vol. 57, No. 6, pp.12-15.

BASHIR, Y.M. and GODDARD, J.D. (1991) A Novel Simulation Method for the Quasi-static Mechanics of Granular Assemblages, J. Rheol., Vol. 35, pp. 849

BOSLEY, J., SCHOFIELD, C. and SHOOK, C.A. (1969) 'An Experimental Study of Granule Discharge from Model Hoppers', Transactions of the Institute of Chemical Engineers, Vol. 47, pp. T147-T153.

BRANSBY, P.L. and BLAIR-FISH, P.M. (1975) Powder Technology, Vol. 11, pp273.

BROWN, R.L. and HAWKSLEY, P.G.W. (1954) Times Science Review, Vol. 6, No. 12.

BROWN, R.L. and RICHARDS, J.C. (1965) 'Kinematics of the Flow of Dry Powders and Bulk Solids', Rheologica Acta, Band 4, Heft 3, pp. 153-165, Oct.

BROWN, R.L. and RICHARDS, J.C. (1960) 'Profile of Flow of Granules Through Apertures', Transaction-Institution of Chemical Engineers, Vol. 38, pp. 243-256.

BURKETT, R.J., DIXON, C., MORRIS, P.J. and PYLE, D.L. (1971) 'On the Flow of Fluidised Solids Through Orifices', Chemical Engineering Science, Vol. 26, pp.405-417.

CAMPBELL, C.S. and POTAPOV, A.V. (1993) Recent Applications of Computer Simulation to Granular Systems, The First Nisshin Engineering Particle Technology International Seminar, Nisshin Eng. Co. Ltd., Osaka, Japan, pp.27, Jan.

CARSON, J.W., GOODWILL, D.J. and BENGTSON, K.E. (1991) 'Predicting the Shape of Flow Channels in Funnel Flow Bins and Silos', presented at the American Concrete Institute Convention, Boston, Massachusetts, U.S.A, March.

CHATLYNNE, C.J. and RESNICK, W. (1973) 'Determination of Flow Patterns for Unsteady-State Flow of Granular Materials', Powder Technology, Vol. 8, No. 3-4, pp. 177-182.

CHEN J. F. (1996) 'Interpretation of Flow and Pressures in Full Scale Silos', PhD Thesis, University of Edinburgh.

CHEN, J. F., ZHANG, K. F., OOI, J. Y. and ROTTER, J, M. (1995) 'Visualisation of Solids Flow in a Full Scale Silo', PARTEC 95, 3rd European Symposium Storage and Flow of Particulate Solids, Nurnberg, Germany.

CHEN, J. F., OOI, J. Y. and ROTTER, J. M. (1997) 'Flow Pattern Observations in a Full Scale Silo', Research Report R97-004, Department of Civil and Environmental Engineering, University of Edinburgh.

CLEAVER, J.A.S. (1991) 'Velocity Distributions in Conical Hoppers', PhD Thesis, Department of Chemical Engineering, University of Cambridge, May.

CUNDELL, P.A. and STRACK, O.D.L. (1979) 'A Discrete Numerical Model for Granular Assemblies', Geotechnique, Vol. 29, No. 1, pp. 47-65.

CUTRESS, J.O. and PULFER, R.F. (1967) 'X-ray Investigaions of Flowing Powders', Powder Technology, Vol. 1, No. 1, pp. 213-220.

DALANEY, T. and BLAKE, D. (1995) 'Observed Flow Patterns in Eccentrically Discharging Model Silos', Project Report, Dept of Civil and Environmental Engineering, University of Edinburgh.

DEMING, W.E. and MEHRING, A.L. (1929) Industrial and Engineering Chemistry, Vol. 21, pp 661-

DEUTSCH, G.P. and CLYDE, D.H. (1967) 'Flow and Pressure of Granular Materials in Silos', Journal of Engineering Mechanics, ASCE, Vol. 93, No. 6, pp. 103-125, Dec.

DRESCHER, A., COUSENS, T.W., BRANSBY, P.L. (1978) 'Kinematics of the Mass Flow of Granular Material through a Plane Hopper', Geotechnique, Vol. 28, No. 1, pp. 27-42.

EIBL, J. and ROMBACH, G. (1987a) 'Stress and Velocity Fields at Discharging of Silos', Proc. of NUMETA Conference, Swansea, pp. D1-D12.

EIBL, J. and ROMBACH, G. (1987b) 'Numerical Computation of Velocity and Stress Fields in Silos - Theory and Applications', Scientific Papers of the Institute of Building Engineering of the Technical University of Wroclaw.

EIBL, J. and ROMBACH, G. (1988) 'Numerical Investigations on Discharging Silos', ICONMIG, Innsbruck, pp. unknown, Apr.

EFChE (1989) 'Standard Shear Testing Technique for Particulate Solids using the Jenike Shear Cell'.

FOWLER, R.T. and GLASTONBURY, J.R. (1959) 'The Flow of Granular Solids Through Orifices', Chemical Engineering Science, Vol. 10, pp150-156.

GARDNER, G.C. (1966) 'The Region of Flow when Discharging Granular Materials from Bin-Hopper Systems', Chemical Engineering Science, Vol. 21, No. 3, pp. 261-273.

GIUNTA, J.S. (1969) 'Flow Patterns of Granular Materials in Flat-Bottom Bins', Journal of Engineering for Industry, ASME, Vol. 91, No. 2, pp. 406-413, May.

GRAHAM, D.P., TAIT, A.R. and WADMORE, R.S. (1987) 'Measurement and Prediction of Flow Patterns of Granular Solids in Cylindrical Vessels', Powder Technology, Vol. 50, No. 1, pp. 65-76, Mar.

HAFF, P.K. (1983) 'Grain Flow as a Fluid-Mechanical Phenomenon', Journal of Fluid Mechanics, Vol. 134, pp. 401-430, Sept.

HAFF, P.K. and WERNER, B.T. (1986) 'Computer Simulation of the Mechanical Sorting of Grains', Powder Technology, Vol. 48, pp. 239-245.

HANCOCK, A.W. (1970) Ph.D Thesis, University of Cambridge.

HANDLEY, M.F. and PERRY, M.G. (1965) 'Measurements of Stresses in Flowing Granular Materials', Rheological Acta, 4, Heft 3, pp. 225-235.

HANDLEY, M.F. and PERRY, M.G. (1967) 'Stresses in Granular Materials in Converging Hopper Sections', Powder Technology, Vol. 1, pp. 245-251.

HARMENS, A. (1963) 'Flow of Granular Material Through Horizontal Apertures', Chemical Engineering Science, Vol. 18, pp 297-306.

HARTLEN, J., NIELSEN, J., LJUNGGREN, L., MARTENSSON, G. and WIGRAM, S. (1984) 'The Wall Pressure in Large Grain Silos', Swedish Council for Building Res., Stockholm, Document D2:1984.

HAUSSLER, U. and EIBL, J. (1984) 'Numerical Investigations on Discharging Silos', Journal of Engineering Mechanics, ASCE, Vol. 110(1), No. 6, pp. 957-971, June.

HAWKINS, G.W. (1983) Mechanics of Granular Materials: New Models and Constitutive Relations, Edited by Jenkins, J.T. and Satake M., Elsevier , Amsterdam, pp. 305-312.

HUI, K. and HAFF, P.K. (1986) 'Kinetic Grain Flow in a Vertical Channel', International Journal of Multiphase Flow', Vol. 12, No. 2, pp. 289-298, Mar-Apr.

JENIKE, A.W. (1961) 'Gravity Flow of Bulk Solids', Bulletin No. 108, Utah Engineering Experiment Station, University of Utah, Salt Lake City, Utah, October, Vol. 52, No. 29, 309pp.

JENIKE, A.W. (1964) 'Steady Gravity Flow of Frictional-Cohesive Solids in Converging Channels', Journal of Applied Mechanics, ASME, Vol. 31, Ser. E, No. 1, pp. 5-11, Mar.

JENIKE, A.W. and JOHANSON, J.R. (1962) 'Stress and Velocity Fields in Gravity Flow of Bulk Solids', Bulletin No. 116 of the Utah Engineering Experiment Station, May.

JENIKE, A.W., JOHANSON, J.R. and CARSON, J.W. (1973a) 'Bin Loads - Part 2: Concepts', Journal of Engineering for Industry, ASME, Vol. 95, Ser. B, No. 1, pp. 1-5.

JENIKE, A.W., JOHANSON, J.R. and CARSON, J.W. (1973b) 'Bin Loads - Part 4: Funnel-Flow Bins', Journal of Engineering for Industry, ASME, Vol. 95, Ser. B, No. 1, pp. 13-16.

JENIKE, A.W. and SHIELD, R.T. (1959) 'On the Plastic Flow of Coloumb Solids Beyond Original Failure', Journal of Applied Mechanics, ASME, Vol. 26, Ser. E, No. 4, pp. 599-602, Dec.

JOHANSON, J.R. (1964) 'Stress and Velocity Fields in the Gravity Flow of Bulk Solids', Journal of Applied Mechanics, ASME, Vol. 31, Ser. E, No. 3, pp. 499-506, Sept.

KETCHUM, M.S. (1907) 'Design of Walls, Bins and Grain Elevators', 1st edition, McGraw-Hill, New York (2nd edition, 1911, 3rd edition, 1919).

KIRSCH, U. (1981) Optimum structural design - concepts, methods and applications, McGraw - Hill Book Company.

KOTCHANOVA, I.I. (1970) Powder Technology, Vol. 4, pp. 32-37.

KREYSZIG (1993) Advanced Engineering Mathematics, Wayne Anderson.

KVAPIL R. (1959) 'Theorie der Schuttgutbewegung', V.E.B., Verlag Technik, Berlin.

LANGSTON, P.A., TUZUN, U. and HEYES, D.M. (1995) Discrete Element Simulation of Granular Flow in 2D and 3D Hoppers: Dependence of Discharge Rate and Wall Stress on Particle Interactions, Chemical Engineering Science, Vol. 50, No. 6, pp. 967-987.

LAOHAKUL, C. (1979) 'Velocity Distributions in the Wall Region of Flowing Granular Materials', Ph. D. Thesis, University of Cambridge, Feb.

LEE, J., COWIN, S..C. and TEMPLETON, J.S. (1974) 'An Experimental Study of the Kinematics of Flow through Hoppers', Trans. Soc. Rheology, 18:2, pp. 247-269.

LENCZNER, D. (1963) 'An Investigation into the Behaviour of Sand in a Model Silo', The Structural Engineer, Vol. 41, No. 12, pp. 389-398, Dec.

LEVINSON, M., SHMUTTER, B. and RESNICK W. (1977) Powder Technology, Vol. 16, pp.29.

LINK, R.A. and ELWI, A.E. (1987) 'Incipient Flow in Silos: A Numerical Approach', Structural Engineering Report No. 147, Dept. of Civil Engineering, University of Alberta, May.

LITWINISZYN (1963) 'The Model of a Random Walk of Particles Adapted to Researches on Problems of Mechanics of Loose Media', Bulletin de L'Academie Polonaise des Sciences, Series des Sciences Techniques, Vol. 11, No. 10, pp. 61[593]-70[602].

McCABE, R.P. (1974) 'Flow Patterns in Granular Material in Circular Silos', Geotechnique, Vol. 24, No. 1, pp. 45-62.

MAHMOUD, A.A. and ABDEL-SAYED, G. (1981) 'Loading on Shallow Cylindrical Flexible Grain Bins', Journal of Powder and Bulk Solids Tech., Vol. 5, No. 3, pp. 12-19.

MEMON, M.A. and FOSTER, P.J. (1985) PowTech., I. Chem. E, Symp. Series No. 91, Birmingham, UK.

MORIYAMA, R., HAYANO, N. and JOKATI, T. (1983) 'The Effect of Filling Method on the Flow Patterns in a Bin', Proceeding of Second International Conference on the Design of Silos for Strength and Flow, Stratford on Avon, Powder Advisory Centre, September, pp 317-331.

MORRIS, A.J. (1982) Foundations of structural optimization: A unified approach, John Wiley & Sons.

MULLINS, W.W. (1972) 'Stochastic Theory of Particle Flow Under Gravity', Journal of Applied Physics, Vol. 43, No. 2, pp. 665-678, Feb.

MULLINS, W.W. (1974) 'Experimental Evidence for the Stochastic Theory of Particle Flow under Gravity', Powder Technology, Vol. 9, pp. 29-37.

MULLINS, W.W. (1979) 'Critique and Comparison of Two Stochastic Theories of Gravity-Induced Particle Flow', Powder Technology, Vol. 23, No. 1, pp. 115-119.

MUNCH-ANDERSEN, J. and NIELSEN, J. (1990) 'Pressures in Slender Grain Silos - Measurements in Three Silos of Different Sizes', presented at CHISA 1990, Praha, second European Symposium on the Mechanics of Particulate Solids, 26-31 Aug., 9 pp.

MURFITT, P.G. (1980) 'Flow Patterns and Wall Stresses in Core Flow Hoppers', Ph. D. Thesis, University of London.

NEDDERMAN, R.M. (1985) PowTech., I. Chem. E, Symp. Series No. 91, Birmingham, UK.

NEDDERMAN, R.M. (1988) 'The Measurement of the Velocity Profile in a Granular Material Discharging from a Conical Hopper', Chemical Engineering Science, Vol. 43, No. 7, pp. 1507-1516.

NEDDERMAN, R.M. and TUZUN, U. (1979) 'A Kinematic Model for the Flow of Granular Materials', Powder Technology, Vol. 22, No. 2, pp. 243-253, Mar-Apr.

NIELSEN, J. (1983) 'Load Distribution in Silos Influenced by Anisotropic Grain Behaviour', Proceedings of International Conference on Bulk Material Storage Handling and Transportation, Institution of Engineers Australia, August, pp 226-230.

NIELSEN, J. (1984) 'Pressure Measurements in a Full Scale Fly Ash Silo', Fine Particle Society, Pacific Region Meeting, August.

NIELSEN, J. and ASKEGAARD, V. (1977) 'Scale Errors in Model Tests on Granular Media with Special Reference to Silo Models', Powder Technology, No. 1.

NGUYEN, T.V., BRENNEN, C.E. and SABERSKY, R.H. (1980) 'Funnel Flow in Hoppers', Journal of Applied Mechanics, ASME, Vol. 47, No. 4, pp. 729-735, Dec.

NOVOSAD, K. and SURAPATI, K. (1968) 'Flow of Granular Materials: Determination and Interpretation of Flow Patterns', Powder Technology, Vol. 2, No. 2, pp. 82-86.

OKI, K., AKEHATA T. and SHIRAI, T. (1975) Powder Technology, Vol. 11, pp.51.

OKI, K., WALAWENDER W. P. and FAN L.T. (1977) Powder Technology, Vol. 18, pp.171.

OOI, J.Y., ROTTER, J.M. and HULL, T.S. (1988) 'Triaxial testing of dry granular solids at very low stresses', Proc., 11th Australian Conf. on the Mechanics of Structures and Materials, Auckland, New Zealand, Aug., 379-384.

OOI, J.Y. (1990) 'Bulk Solids Behaviour and Silo Wall Pressures', Ph. D. Thesis, University of Sydney.

OOI, J. Y. and ROTTER, J. M. (1990) 'Unsymmetrical Features of Measured Pressures on Prototype Grain Silos', Proceedings of 2nd European Symposium on the Stress and Strain Behaviour of Particulate Solids-Silo Stresses, Prague.

PARISEAU, W.G. (1970) 'Discontinuous Velocity Fields in Gravity Flows of Granular Materials through Slots', Powder Technology, Vol. 3, No. 4, pp. 218-226.

PERRY, M.G., ROTHWELL, E. and WOODFIN, W.T. (1976) 'Model Studies of Mass Flow Bunkers, 2 - Velocity Distributions in the Discharge of Solids from Mass Flow Bunkers', Powder Technology, Vol. 14, No. 1, pp. 81-92.

RAO, V. LAKSHMAN and VENKATESWARLU, D. (1973) 'Determination of Velocities and Flow Patterns of Particles in Mass Flow Hoppers, Powder Technology, Vol. 7, No. 5, pp. 263-265.

RAO, V. LAKSHMAN and VENKATESWARLU, D. (1975) Powder Technology, Vol. 11, pp.133.

RICHARDS, P.C. (1977) 'Bunker Design - Part 1: Bunker Outlet Design and Initial Measurements of Wall Pressures', Journal of Engineering for Industry, ASME, Vol. 99, No. 4, pp. 809-813.

RISTOW, G.H. (1992) Simulating Flow with Molecular Dynamics, J. de Phys. II, Vol. 2, pp. 649

RONG, G., HOLST, M. R., OOI, J. Y. and ROTTER, J. M. (1996) 'An International Comparison of Discrete Element and Finite Element Methods for Predicting Silo Filling Phenomena', 12th International Congress of Chemical and Process Engineering, CHISA'96, Prague.

ROTTER, J. M. (1986) 'The Analysis of Steel Bins Subject to Eccentric Discharge', Proceedings of 2nd International Conference on Bulk Materials Storage, Handling and Transportation, I. E. Australia, Wollongong, pp. 264-271.

ROTTER, J. M. (1987) 'Bending Theory of Shells for Bins and Silos', Trans. Mech. Engng., I. E. Australia, No. 3, pp. 147-159.

ROTTER, J.M., OOI, J.Y., LAUDER, C., COKER, I., CHEN, J.F., and DALE, B.G. (1993) 'A Study of the Flow Patterns in an Industrial Silo', Proc. RELPOWFLO II, Oslo, Aug.

ROTTER, J.M., OOI, J.Y., CHEN, J.F., TILEY, P.J., MAKINTOSH, I. and BENNETT, F.R (1995) Measurement of Flow Pattern in Full Sale Silos, British Materials Handling Board.

ROTTER, J.M., OOI, J.Y., CHEN, J.F., TILEY, P.J., and MAKINTOSH, I. (1996) 'Flow Pattern Measurement in Full Sale Silos', Research Report, Department of Civil and Environmental Engineering, The University of Edinburgh.

ROSATO, A., PRINZ, F., STANDBURG K.J. and SWENSON R (1986) Powder Technology, Vol. 49, pp. 217-224.

ROSE, H.E. and TANAKA, T. (1959), Engineer, Vol. 208, pp 465-.

RUCHENBROD, C. and EIBL, J. (1993) 'Numerical Results to Discharge Processes in Silos', Proc. RELPOWFLO II, Oslo, Aug.

RUNESSON, K. and NILSSON, L. (1986) 'Finite Element Modelling of the Gravitational Flow of a Granular Material', Bulk Solids Handling, Vol. 6, No. 5, pp. 877-884.

SAVAGE, S.B. (1979) 'Gravity Flow of Cohesionless Granular Materials in Chutes and Channels', Journal of Fluid Mechanics, Vol. 92, Part 1, pp. 53-96.

SCHMIDT, L.C. and WU, Y.H. (1989) 'Prediction of Dynamic Wall Pressures on Silos', Bulk Solids Handling, Vol. 9, No. 3, pp. 333-338, Aug.

SMALLWOOD and THORPE (1980) 'Flow of Granular Media', Chemical Engineering Tripos, Undergraduate final year dissertation, University of Cambridge.

SNYDER, R.E. and BALL, R.C. (1994) Self-organised Criticality in Computer Models of Setting Powders, Phys. Rev. E, Vol. 49, pp. 104.

SUGDEN, M.B. (1980) 'Effect of Initial Density on Flow Patterns in Circular Flat-Bottomed Silos', International conference on the design of silos for strength and flow, Lancaster, England.

TAKAHASHI, H. and YANAI, H. (1973) 'Flow Profile and Void Fraction of Granular Solids in a Moving Bed', Powder Technology, Vol. 7, No. 4, pp. 205-214.

THORNTON, C. (1991) Computer Simulation of Hopper Flow, 4th World Congress of Chemical Engineering, Karlsruhe, paper 9.1-27.

THOMPSON, P.A. and GREST, G.S. (1991) Granular Flow: Friction and the Dilatancy Transition, Phys. Rev. Lett., Vol. 67, pp. 1751.

TSUJI, Y., TANAKA, T. and ISHIDA, T. (1992) Powder Technology, Vol. 71, pp.239.

TURNER, M.C. and WOODCOCK L.V. (1993) New Approach to the Constitutive Rheological Relations for Rapid Granular Flow 93, Powders and Grains, Balkema, Rotterdam, pp. 307.

TUZUN, U. and NEDDERMAN, R.M. (1979) 'Experimental Evidence Supporting Kinematic Modelling of the Flow of Granular Media in the Absence of Air Drag', Powder Technology, Vol. 24, No. 2, pp. 257-266, Jan-Feb.

TUZUN, U. and NEDDERMAN, R.M. (1982) 'An Investigation of the Flow Boundary during Steady-State Discharge from a Funnel Flow Bunker', Powder Technology, Vol. 31, No. 1, pp. 27-43, Jan-Feb.

TUZUN, U., HOULSBY, G.T., NEDDERMAN, R.M. and SAVAGE, S.B. (1982) 'The Flow of Granular Materials - 2: Velocity Distributions in Slow Flow', Review Article Number 11, Chemical Engineering Science, Vol. 37, No. 12, pp. 1691-1709.

VAN ZANTEN, D.C., RICHARDS, P.C. and MOOIJ, A. (1977) 'Bunker Design - Part 3: Wall Pressures and Flow Patterns in Funnel Flow', Journal of Engineering for Industry, ASME, Vol. 99, Ser. B, No. 4, pp. 819-823.

WALTON, O. R. (1983) Mechanics of Granular Materials: New Models and Constitutive Relations, Edited by Jenkins, J.T. and Satake M., Elsevier , Amsterdam, pp. 327-338.

WANG, S. Y., YANG, D. Q., LIU, G. H. and ZHANG, K. F. (1991) 'Optimisation, Principles and Applications', Zhejiang University Press, China (in Chinese).

WATSON G.R. (1993) 'Flow Patterns in Flat Bottomed Silos'," Ph.D Thesis, Dept. Civil Engng, Uni. of Edinburgh.

WATSON, G.R. and ROTTER, J.M. (1996), Finite Element Kinematic Analysis of Planar Granular Solids Flow, Chemical Engineering Science, Vol. 51, No. 16, pp. 3967-3978.

WEARE, F. (1989) 'Silo design and construction' Proceeding of Silos: Design, Construction and Repair, Institution of Civil Engrs, Struct. Engng Group Meeting, London, 15 Nov., pp 9-11.

WU, Y.H. (1990) 'Static and Dynamic Analysis of the Flow of Bulk Materials through Silos', PhD thesis, Department of Civil and Mining Engineering, The University of Wollongong, Australia, Feb.

ZHANG, K.F. and OOI, J.Y. (1997) 'A Kinematic Model for Solids Flow in Flat Bottomed Silos, Geotechnique, to appear.

ZHONG, Z., ROTTER, J.M. and OOI, J.Y. (1995) 'Estimation of Eccentric Flow Channel Dimension in Circular Silos', Research Report R 95-013, The University of Edinburgh.

ZHONG, Z., ROTTER, J.M. and OOI, J.Y. (1996) 'The Sensitivity of Silo Flow and Wall Pressures to Filling Method', Submitted to Engineering Structure for publication.